Fishing for genes

Using zebrafish to study the functional genetics of cardiac arrhythmias

Charlotte Dieudonnée Koopman

Layout: Lotte Koopman
Cover design: © 2019 Laurence Garric (EURêKA! Art & Science)
Title: two life lines for a PhD
Printed by: Gildeprint
ISBN: 9789463236638

Fishing for genes

Using zebrafish to study the functional genetics of cardiac arrhythmias

Vissen naar genen

Het gebruik van de zebravis om de functionele
genetica van hartritmestoornissen te bestuderen.
(met een samenvatting in het Nederlands)

Proefschrift

ter verkrijging van de graad van doctor
aan de Universiteit Utrecht
op gezag van de rector magnificus, prof.dr. H.R.B.M. Kummeling,
ingevolge het besluit van het college voor promoties
in het openbaar te verdedigen op

donderdag 13 juni 2019
des middags te 2.30 uur

door
Charlotte Dieudonnée Koopman
geboren op 28 mei 1988
te Rhenen

Promotoren: Prof.dr. J.P.W.M. Bakkers
Prof.dr. M.A. Vos

Copromotor: Dr. T.P. de Boer

The research described in this thesis was performed at the UMC Utrecht and the Hubrecht institute of the Royal Dutch Academy of Arts and Sciences (KNAW), within the framework of the Graduate School of Life Sciences “Cardiovascular Research” (CVR) program of the University Utrecht.

The research described in this thesis was supported by a grant of CardioVasculair Onderzoek Nederland (CVON) formed by: the Dutch Heart Foundation, Dutch Federation of University Medical Centres, the Netherlands Organization for Health Research and Development and the Royal Netherlands Academy of Sciences (CVON-PREDICT).

Financial support by the Dutch Heart Foundation for the publication of this thesis is gratefully acknowledged.

Voor papa en mama

Above all else, guard your heart,
for everything you do flows from it
(Proverbs 4:23)

CONTENTS

CHAPTER 1

General introduction

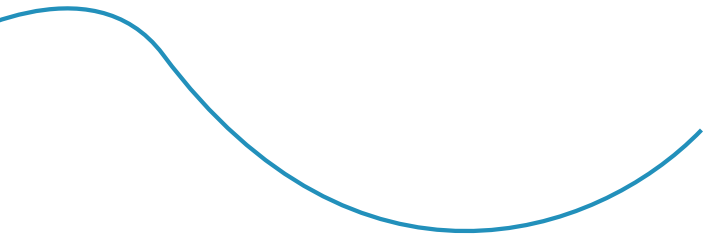

1

The heart is central to life. In an adult person the heart beats approximately 100.000 times a day and pumps about 7.500 liters of blood through the circulation every 24 hours, allowing the delivery of oxygen and nutrients to tissues and the disposal of waste products from the body.[1] The beating of the heart is a highly coordinated and rhythmic event. Every consecutive heartbeat is initiated at the top of the right atrium in the sinoatrial node (SA node). Pacemaker cells in the SA node spontaneously depolarize and generate electrical pulses, which are propagated to adjacent cardiomyocytes. These pulses first travel along the atria towards the atrioventricular node (AV node), resulting in atrial activation and subsequently contraction. After a small delay in the AV node, electrical pulses travel further along the ventricles via the bundles of His and the purkinje fibers, causing the ventricles to contract from apex to base and blood to be expelled into the circulation (Figure 1).[2]

It is not difficult to imagine that perturbations in cardiac electrical conduction can result in arrhythmias; heart rhythms that are too fast (tachycardia), too slow (bradycardia) and/or irregular.[1] Arrhythmias can be life threatening and may cause a complete arrest of the heartbeat, which results in death within minutes if left untreated. Sudden cardiac death (SCD) is one of the leading causes of morbidity and mortality in the Western world. It claims millions of deaths

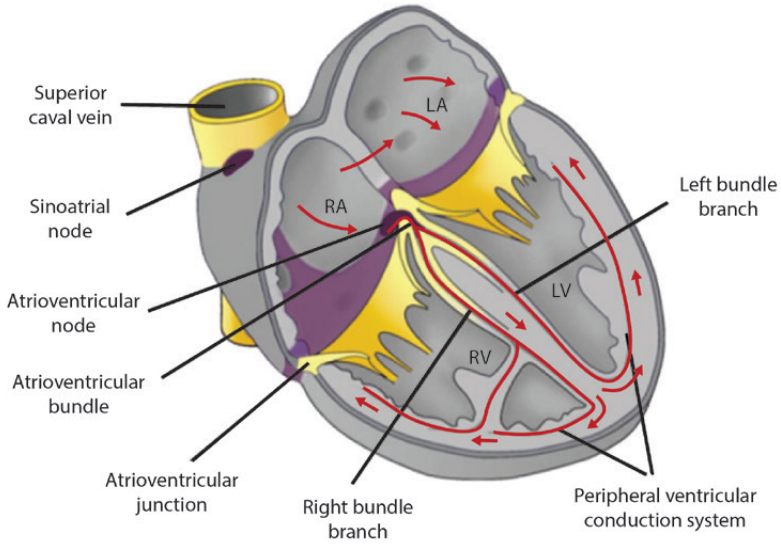

Figure 1. The mammalian heart and the cardiac conduction system. The sinoatrial node generates electrical impulses that travel across the atria, causing their contraction, to the atrioventricular node. In this node the signal is delayed before being propagated through the left and right bundle branches to the peripheral ventricular conduction system, causing contraction of both ventricles. Red arrows represent the direction of action potential propagation, purple and the red lines represent the cardiac conduction system, grey the cardiac chambers, and yellow non-myocardial tissue. RA: right atrium, LA: left atrium, RV: right ventricle, LV: left ventricle. This figure is adapted from Weerd and Christoffels 2016.

annually worldwide, accounting for up to 50% of all cardiovascular deaths.[3] Unfortunately, sudden cardiac arrest occurs out-of-hospital in the vast majority of cases, resulting in a poor survival rate. In addition, cardiac arrhythmias are very poorly understood due to their extremely complex underlying pathophysiology.[4] Thus, a detailed and in-depth examination of the underlying molecular mechanisms of arrhythmias is essential.

In this thesis, we study the genetic basis of cardiac electro(patho)physiology using the zebrafish as a model organism, in order to get a better understanding of the molecular mechanisms of cardiac electrical function.

1. Cardiac electrophysiology

1.1 The cardiac action potential

Electrical signals travel across the heart in the form of action potentials (APs): brief, regenerative changes in voltage across the cell membranes of cardiomyocytes. Different phases, initiated by different ion currents, shape the action potential (Figure 2). During Phase 0 of the AP, membrane voltage rapidly changes from negative (~ -80 mV) to positive (~ +40 mV), a process that is known as depolarization. This is predominantly the result of the fast opening of voltage-gated sodium (Na^+) channels, allowing Na^+ to flow into the cell (I_{Na}). Phase 1 represents the early repolarization phase, and starts with the rapid inactivation of the Na^+ channels, reducing the movement of Na^+ into the cell. At the same time transient outward potassium (K^+) channels open and close rapidly, allowing a brief flow of K^+ out of the cell (I_{to}). Phase 2 is known as the plateau phase, as the membrane potential remains almost constant due to a temporary balance between repolarizing and depolarizing ion currents. Ultra rapid delayed rectifier potassium channels (I_{Kur}) open and allow K^+ ions to leave the cell, while L-type calcium channels allow the movement of Ca^{2+} into the cell. I_{Kur} is highly expressed in atrial myocytes and largely responsible for the much shorter AP duration in the atrium.[5] During phase 3, the rapid repolarization phase, L-type Ca^{2+} channels close, while the potassium channels remain open. The net outward positive current causes repolarization and thereby triggers the opening of more K^+ channels, which are primarily the rapid delayed rectifier K^+ channels (I_{Kr}) followed by the inward rectifying K^+ channels (I_{K1}). The slow delayed rectifier potassium channels (I_{Ks}) come into play when more repolarizing capacity is needed, e.g. under β-adrenergic activation and with increasing heart rates. The acetylcholine-activated K^+ channels ($I_{K,ACh}$) are most abundant in the atria and the SA and AV nodes, and are activated upon vagal stimulation of the heart (as discussed at section 1.3). The rapid and slow delayed rectifier K^+ channels close when the membrane potential is restored to resting membrane potential, but the I_{K1} current remains active during phase 4. At phase 4 the cell is at rest and inward and outward currents are in balance, holding the resting membrane potential more or less constant at -80 mV.[5]

Pacemaker cells don't have a resting membrane potential. During phase 4, the membrane potential slowly becomes more positive until it reaches a threshold potential of approximately

-40mV. One main component of pacemaker cell depolarization is the funny current (I_f), an ion current mediated by the hyperpolarizing-activated cyclic nucleotide-gated (HCN) channels, which open at very negative voltages and facilitate the influx of Na^+. Intracellular Ca^{2+} cycling is proposed as an additional mechanism, as Ca^{2+} sparks are found to precede AP generation. These sparks can trigger the opening of the sodium/calcium exchanger (NCX) channel located at the plasma membrane, thereby promoting membrane depolarization through the exchange of one Ca^{2+} for three Na^+.[5]

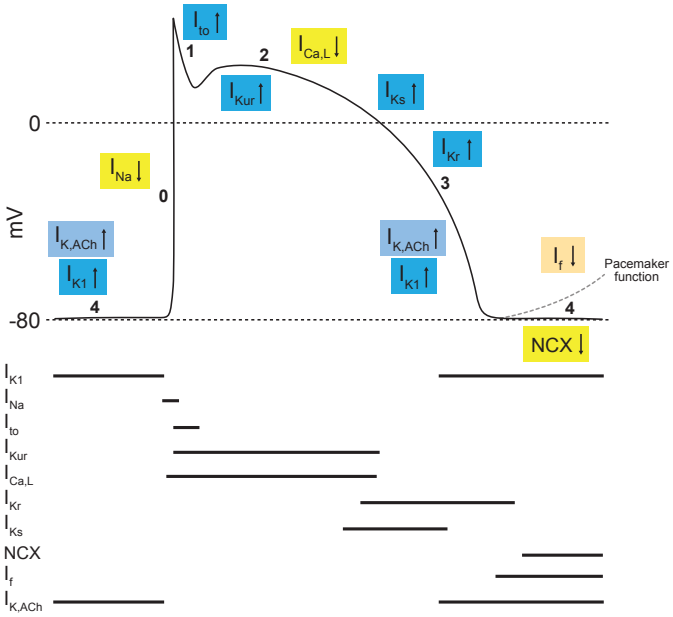

Figure 2. Ion currents that shape the cardiac action potential. The five phases of the action potential are: (4) resting, (0) upstroke, (1) early repolarization, (2) plateau, and (3) final repolarization. In pacemaker cells, the membrane potential slowly becomes more positive during phase 4 (upward dotted line). All inward currents are shown in yellow boxes (I_{Na}, $I_{Ca,L}$, I_f) , all outward currents in blue boxes ($I_{K,ACh}$, I_{K1}, I_{to}, I_{Kur}, I_{Ks}, I_{Kr}). NCX can generate both inward and outward current. Currents that are more abundant in the atria ($I_{K,Ach}$) or only present in pacemaker cells (I_f) are shown in lighter colored boxes. The time of activity of the different currents is represented by the black lines underneath the graph.

1.2 Excitation-contraction coupling

Excitation-contraction coupling is an essential process that translates electrical pulses into contraction of the heart. The second messenger Ca^{2+} plays a central role in this process, as it is a regulator of electrical activity and myofilaments, the contractile elements in cardiomyocytes (Figure 3).

During the plateau phase of the action potential, voltage sensitive L-type calcium channels (LTCCs) are activated, allowing Ca^{2+} ions to flow into the cytosol of the cardiomyocyte. This in turn

results in a small local increase in cytosolic Ca^{2+}, which activates the ryanodine receptors (RyR2) at the membrane of the sarcoplasmic reticulum (SR) and triggers the release of large amounts of Ca^{2+} from the SR into the cytosol. This phenomenon is better known as the calcium-induced calcium release. Next, free cytosolic Ca^{2+} binds the basic contractile elements of the cell, the sarcomeres (part of the myofilaments), activating them and resulting in contraction. During the relaxation phase of the cell, cytosolic Ca^{2+} is taken back up into the SR via the sarco/endoplasmic reticulum ATPase (SERCA2a) pump, which is regulated by phospholamban (PLN). In addition Ca^{2+} is shuttled out of the cell, predominantly through Na^{+}/Ca^{2+} exchanger (NCX) and to a lesser extend through the plasma membrane Ca^{2+} ATPase (PMCA).[6,7] The resulting fluctuation in cytosolic Ca^{2+} triggered by the action potential is referred to as a Ca^{2+} transient.

PLN is a small but essential regulator of SERCA and was discovered in the 1970s. As researchers were unsure of its function but saw that the protein integrated radioactive phosphorus (P^{32}), they named it using the Greek words phosphorous and lambano (receive).[8] After four decades of research, there is a strong understanding of PLN, but at the same time its function remains puzzling and more complex than initially believed.[9] Detailed in vitro studies have demonstrated that PLN regulates SERCA2a activity by affecting its affinity for Ca^{2+}. Initially, it was believed that the function of PLN was restricted to this interaction with SERCA. However, it has become increasingly clear that PLN affects many more processes in the cell and is in fact part of a multimeric regulatome, with interacting partners like HAX-1[10], Hsp90[11], Gm[12], AKAP[13,14], PP1[12], I-1[15], and Hsp20[16]. PLN consists of three domains: a cytoplasmic domain (Ia), a linker domain (Ib), and a SR transmembrane domain (II). Two crucial phosphorylation sites are located within the cytoplasmic Ia domain of PLN: one at Ser^{16} and one at Thr^{17}.[17] Phosphorylation of PLN can be induced at Ser^{16} by cAMP-dependent protein kinase (PKA), or at Thr^{17} by Ca^{2+}/calmodulin-dependent protein kinase II (CaMKII) or protein kinase B (PKB/Akt).[18] Under basal conditions PLN is non-phosphorylated and an inhibitor of SERCA2a activity. This inhibition is reversed during β-adrenergic stimulation when PLN is phosphorylated, resulting in a higher Ca^{2+} affinity of SERCA2a, a higher reuptake of Ca^{2+} into the SR, an enhanced rate of cardiomyocyte relaxation (lusitropic effect) and an increased force of contraction (inotropic effect) due to a higher Ca^{2+} load of the SR.[17] Thus, PLN is a key component at the intersection of two important signal-transduction pathways of the heart: the β-adrenergic pathway and the Ca^{2+} signaling pathway.

PLN exist in a dynamic equilibrium between monomeric and pentameric states. The prevailing theory suggests that the monomer is the “active” form, while the pentamer can be regarded as an “inactive” storage of PLN.[17] While most studies agree that the PLN monomer is the active inhibitory form of SERCA2a, the role of the PLN pentamer has remained more of an anomaly. Some have shown that the channel-like architecture of the pentamer may enable it to conduct ions, such as Ca^{2+} or Cl^{-}.[19,20] In addition, electron microscopy studies have found evidence of a physiological interaction between PLN pentamers and SERCA2a at an accessory site.[21] It was hypothesized that this interaction might facilitate diffusion of monomeric PLN to and from its inhibitory site on SERCA. While the role of PLN oligomerisation is poorly understood, it is clear

that it is important and even necessary for optimal cardiac function. Transgenic mice, expressing a PLN variant (Cys[41]-Phe) that cannot form pentamers, showed defects in cardiac relaxation and a depressed cardiac function, despite the fact that SR Ca^{2+} transport was completely normal.[22]

There is a fraction of SERCA2a pumps that is not functionally regulated by PLN, which is approximately 40% in mice.[23] Data from human and experimental animal models has shown that this ratio changes in heart failure. SERCA2a levels diminish, while PLN levels do not change, resulting in a higher fraction of SERCA2a that is inhibited by PLN.[24] In addition, PLN phosphorylation decreases, adding further to the depression of SERCA2a function in heart failure.[17]

Multiple mutations in *PLN* have been associated with human cardiac disease. One of these mutations, the R14 deletion, will be further discussed in chapter 7.

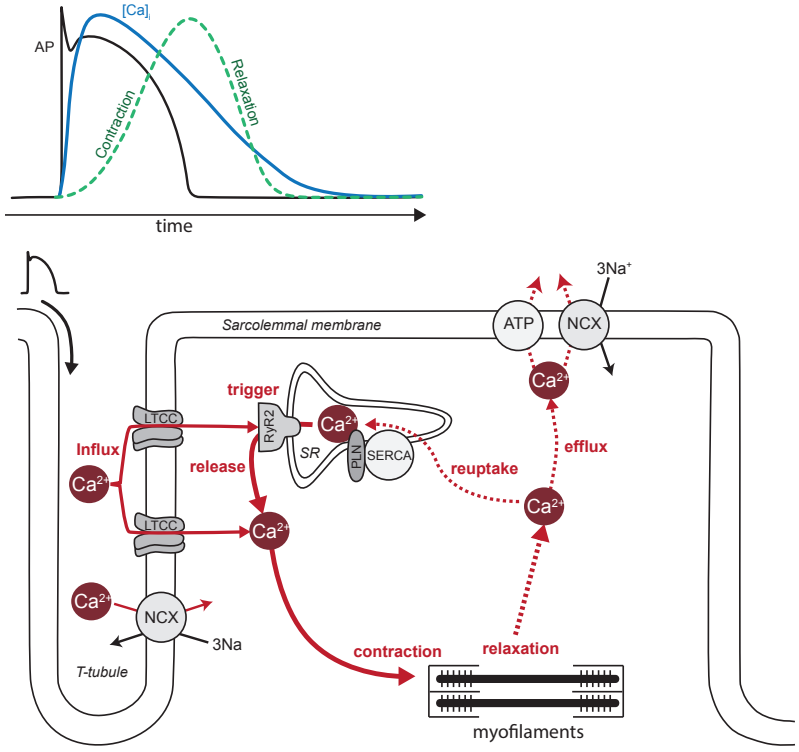

Figure 3. Excitation-contraction coupling and Ca^{2+} transport in ventricular cardiomyocytes. The top panel shows the time course of an action potential, Ca^{2+} transient and contraction curve from a ventricular cardiomyocyte. The bottom panel shows the Ca^{2+} response to an action potential within a ventricular cardiomyocyte. Ca^{2+} flows into the cell via voltage activated LTCCs (L-type Calcium Channels). This Ca^{2+} influx in turn triggers the release of large amounts of Ca^{2+} from the SR (sarcoplasmic reticulum) via RyR2 (ryanodine receptor). Free cytosolic Ca^{2+} binds to the myofilaments, resulting in contraction. During relaxation, Ca^{2+} is released from the myofilaments, and taken back up in the SR via SERCA (sarco/endoplasmic reticulum ATPase) which is regulated by PLN (phospholamban), or transported out of the cell via NCX (Na^{+}/Ca^{2+} exchanger) and PMCA (plasma membrane Ca^{2+} ATPase). This figure is adapted from Bers 2002.

1.3 Autonomic regulation of the heart

The heart is innervated by the autonomic nervous system, which acts largely unconsciously, influencing and regulating the function of internal organs such as the heart, gut and lungs. In the heart, the autonomic nervous system is responsible for the fine-tuning of heart rate, cardiac output and contractility to body demands. There are two different divisions of the autonomic nervous system: the parasympathetic and sympathetic system. Sympathetic nerves innervate the entire heart, including the SA and AV node. Parasympathetic nerves mainly innervate the SA node, AV node, and atrial tissue. The ventricle is only sparsely innervated.[25]

The sympathetic and parasympathetic system have opposing effects on the heart, which are mediated through muscarinic (M_2) and β-adrenergic (β_1/β_2) receptors respectively. Postganglionic sympathetic nerves release the neurotransmitter noradrenaline (NA), which can bind to and activate β-receptors on the heart. β-receptors are 7-transmembrane receptors and have a G-protein attached at their cytoplasmic tail. When the β-receptor is activated, the attached G_s-protein (s for stimulatory) is also activated, initiating a series of reactions that result in the activation of cyclic adenosine monophosphate (cAMP) and PKA. These second messengers exert various effects in the cell, for example through the regulation of ion channels. Overall, they trigger an increased SA node firing rate (positive chronotropic effect), an increased force of contraction of atrial and ventricular cardiomyocytes (positive inotropic effect), increased relaxation of contraction (lusitropic effect) and a faster conduction in the AV node (positive dromotropic effect). A well-known agonist of the β-adrenergic receptors is isoproterenol (also known as isoprenaline). A well-known antagonist is propranolol.[25]

In contrast to the sympathetic system, postganglionic nerves of the parasympathetic system release the neurotransmitter acetylcholine (ACh), which can bind to M_2-receptors on the heart. Like β-receptors, the M_2-receptor is a 7-transmembrane receptor with a G-protein linked to it. Binding of ACh activates the receptor and the G_i-protein (i for inhibitory), initiating a series of reactions that result in a decrease of cAMP in the cell. G_i-proteins can also directly influence muscarinic potassium channels, like Kir3.1/Kir3.4 (responsible for $I_{K,ACh}$). Overall, M_2-receptor activation will result in a decreased SA node firing rate (negative chronotropic effect), a decreased force of contraction of atrial cardiomyocytes (negative inotropic effect) and a slower conduction in the AV node (negative dromotropic effect).[25]

1.4 Arrhythmic mechanisms

Cardiomyocytes communicate with each other via specialized structures called intercalated discs, which contain gap junction channels that connect the cytoplasm of adjacent cells. This way, action potentials that are initiated in one cell can be propagated to the next cell, and so on, ultimately resulting in the activation of the entire heart. Cell-cell communication is a crucial factor in the development of arrhythmias, as arrhythmias involve large parts of the heart. The mechanisms that are responsible for cardiac arrhythmias can be divided into disorders of impulse formation (i.e. focal activity), disorders of impulse conduction (i.e. reentry), or a combination of both.[26,27]

Focal activity can arise from enhanced automaticity or triggered activity.[27] Automaticity refers to the spontaneous activity that some cardiomyocytes possess, such as the SA node pacemaker cells. As mentioned in the previous section, the autonomic nervous system can modulate automaticity. Abnormal automaticity includes both a reduced and an increased automaticity, resulting in bradycardia and tachycardia respectively[26], and can be caused by a disruption of the ion currents that underlie the pacemaker potential, such as the funny current (I_f). Triggered activity is caused by early afterdepolarizations (EADs) or delayed afterdepolarizations (DADs), which are extra depolarizations that accompany or follow the cardiac action potential. When EAD or DAD amplitude is sufficient to bring the membrane to its threshold potential it results in a spontaneous new action potential, referred to as a triggered response. Triggered responses can give rise to premature contractions (ectopic beats or extrasystoles) and tachyarrhythmias. EADs are usually associated with a prolongation of the action potential duration, for example through disrupted Ca^{2+} dynamics or altered repolarizing potassium currents.[27] When the balance in inward/outward currents is tipped towards a higher inward current, the membrane depolarizes and an EAD is formed. DADs are usually associated with conditions of Ca^{2+} overload, which result in spontaneous Ca^{2+} releases from the SR.[27]

Reentry is fundamentally different from focal activity and occurs when an action potential does not extinguish but instead reactivates a region that is no longer refractory (recovering). This results in a continuous circulating electrical wavefront and a rapid and abnormal activation of cardiomyocytes. Requirements for reentry are a unidirectional block, in which impulses can only be conducted in one direction in a section of the heart, and a slowed conduction.[27] Reentry can be measured using electrocardiograms (ECG) or electrodes that are in direct contact with the cardiac tissue.

In this thesis I mainly focus on focal activity as a mechanism for arrhythmias. To determine focal activity we used techniques like optogenetics and patch-clamp to measure membrane voltage, action potential shape, and ion currents (including intracellular Ca^{2+}).

2. The zebrafish as a model to study cardiac arrhythmias

2.1 Advantages of the zebrafish

Zebrafish (*Danio rerio*) are small tropical fish with a remarkable track record in biomedical research. These vertebrates were already used as a genetic model in the 1980s by Streisinger and coworkers.[28] Especially the ease of breeding zebrafish, their low maintenance costs and the unique combination of their transparency (which allows non-invasive in vivo visualization of organs) and their embryological manipulability made it an appealing model for research.[29] In the 1990s and 2000s the zebrafish was used on a large scale in forward genetic screenings to identify genes involved in development and disease. Such investigations have identified thousands of fish mutants and have contributed vastly to our understanding of basic vertebrate biology and

vertebrate development.[30,31] However, over the years the zebrafish has also presented itself as a powerful model for other research areas. It has been increasingly included in studies of human genetic disease, providing independent evidence of gene function and insight into the underlying mechanisms of disease.[32-41] This is mainly the result of the high degree of genetic homology between zebrafish and mammals, and the ease by which the zebrafish can be genetically manipulated, especially since CRISPR/Cas9 became available in 2013. Sequencing of the zebrafish genome was initiated by the Wellcome Trust Sanger Institute in 2001, and resulted in a complete annotation of zebrafish genes and the identification of their human orthologs. A direct comparison of zebrafish and human protein-coding genes revealed that 71.4% of all human genes have at least one zebrafish ortholog, as well as 82% of all human disease causing genes.[42] In addition, when comparing model systems that are accessible for large screens, zebrafish stand out for their highly conserved physiology. They possess fully recognizable organ systems, like liver, heart, kidneys, pancreas and so on, and these organs exhibit very similar functions to their human counterpart. For example, just as in humans, glucose homeostasis in zebrafish is dependent on α, β, δ, and ε cells for the secretion of glucagon, insulin, somatostatin and ghrelin respectively.[43] Also, the hematopoietic system in the zebrafish consists of similar cells types as the human system, and includes erythrocytes, neutrophils, eosinophils, lymphocytes and macrophages.[44].

2.2 Zebrafish heart anatomy

In contrast to the mammalian heart, fish only have one atrium and one ventricle. Nevertheless, human and zebrafish adult hearts resemble each other in many aspects, including basic contractile dynamics, beating rates, the shape of APs and of electrocardiograms (ECGs).[45,46] The zebrafish heart consists of four structures that are connected in series: the sinus venosus, atrium, ventricle,

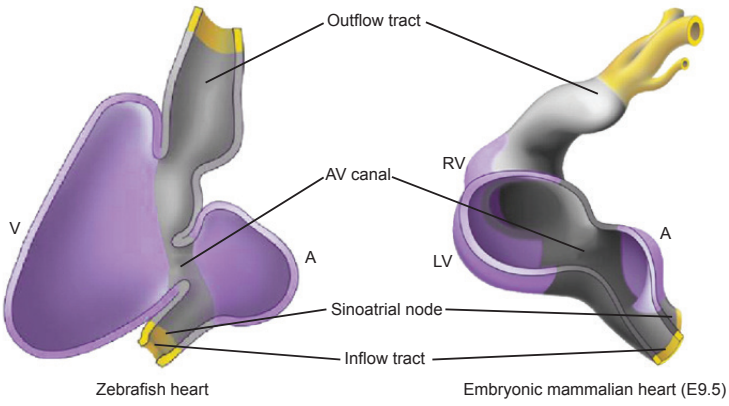

Figure 4. Anatomy of the zebrafish heart and the embryonic mammalian heart. The left panel shows the global structure of the zebrafish heart, the right panel of the embryonic mammalian heart at embryonic (E) day 9.5. Grey represents the cardiac conduction system, purple the cardiac chambers, and yellow non-myocardial tissue. A: atrium, V: ventricle, LV: left ventricle, RV: right ventricle. This figure is adapted from Jensen et al 2013.

and bulbus arteriosus (Figure 4). Venous blood, which is poor in oxygen, is pumped from the cardinal vein into the ventral aorta by the heart. The ventral aorta leads to the gills where the blood is oxygenated and from were the blood is redistributed throughout the body. Like the human heart, the zebrafish heart consists of an endocardial, myocardial and epicardial layer, and has valves separating the different chambers (atrium/ventricle, ventricle/bulbus).[47] A functional equivalent of the cardiac conduction system is present in the zebrafish, since there is synchronized cardiac contraction and a unidirectional blood flow. However, it is good to note that zebrafish do lack a well-defined AV node and the His-Purkinje bundles.[48]

2.3 Development of the zebrafish heart and conduction system

The heart is the first organ to form and function during vertebrate development. In humans, the first heartbeat is observed after a few weeks post fertilization. However, the zebrafish is extra-ordinary when it comes to heart development, as the first heartbeat can be observed within 24 hours post fertilization (hpf).

Development of the heart starts before gastrulation with the specification of myocardial and endocardial progenitor cells.[49] These progenitor cells are localized within the marginal zone, the region in the early embryo that will give rise to the mesoderm.[50] During gastrulation, the cardiac progenitor cells move dorsally towards the mid-line and end up in a bilateral position in the anterior lateral plate mesoderm, the tissue that gives rise to the mesenteries and the major substance of the heart. Homeobox-containing transcription factor Nkx2.5 is the earliest known marker for vertebrate heart development and is required for cardiac differentiation. In zebrafish, Nodal and bone morphogenetic protein (Bmp) signaling induce the expression of Nkx2.5 by inducing gata5 expression at the 1- to 3-somite stage.[49] Cardiac differentiation is initiated at the 12- to 15-somite stage, as Myosin light chain polypeptide 7 (*myl7*, formerly known as *cmlc2*) expression is initiated within a few cells. The number of *myl7* expressing cells increase vastly over time.[51] In addition, future ventricle myocardial cells differentiate and start expressing ventricle myosin heavy chain (*vmhc*). This is followed slightly later by the differentiation of the future atrial myocardial cells which start expressing atrial myosin heavy chain (*amhc*/*myh6*).[49] Expression of sarcomeric genes can be observed as early as the 14-somite stage.[52] The bilateral heart fields fuse at the mid-line and form a cardiac disc structure, with the endocardial cells located at the center. This cardiac disc is transformed into a linear tube during cardiac morphogenesis. Endocardial cells form the inner lining of the heart tube and a distinct venous pole and arterial pole can now be observed.[49] At this stage, myocardial cells are still added to the arterial pole.[51] Cardiac looping and valve formation start at 36 hours post fertilization (hpf). During looping, the ventricle and the atrium become distinct chambers, a process known as chamber ballooning.[53] The ventricle is displaced toward the mid-line, and a constriction appears between the atrium and ventricle, forming the AV canal. The heart tube continues to loop until it forms a distinct S-shape.[49] Extra-cardiac pro-epicardial cells, that are located near the AV canal, start to cover the heart to form an epicardial layer.[54] The valves are fully distinguisable by 105 hpf, showing distinct leaflets composed of two cell layers separated

by a layer of fibronectin-containing extracellular matrix.[55]

Cardiac contractions are first observed when the cardiac tube is formed and are initiated at the venous pole of the heart. Initially these contractions are still irregular and uncoordinated, but they soon become more organized. At this stage, contractions are peristaltic as electrical pulses can only travel slowly through the heart tube. When the heart develops further, heart rate increases and peristaltic movements make place for sequential contraction of the atrium and the ventricle. Pacemaker cells are the last cells that are added to the venous pole of the heart tube.[49] Interestingly, these cells express *isl1*, a LIM-homeodomain-containing transcription factor also expressed in motorneurons. Zebrafish *isl1* mutant embryos display severe bradycardia and arrhythmias, indicating that Islet-1 plays an important role in the function of pacemaker cells.[56] During cardiac looping, a slowing of electrical pulses is observed in the developing AV canal, similar to the delay that occurs in the mammalian AV node. This event likely triggers the transition from peristaltic contraction into sequential contraction, as electrical signals traveling from one pole of the heart to the other are now interrupted. Several signaling pathways and transcription factors are required to maintain a slow-conducting AV canal myocardium. These include the T-box transcription factor Tbx2b and the bone morphogenetic protein Bmp4. [57,58]

While the zebrafish heart looks very distinct from the adult mammalian heart in terms of anatomy and conduction system, it shares many similarities when comparing it with the embryonic mammalian heart. This indicates that the basic building plan of the heart and its structures is very similar between zebrafish and mammals (Figure 4).

2.4 The zebrafish cardiac action potential

The cardiac AP shape in zebrafish shows much resemblance with the human AP shape, indicating that cardiac electrophysiology is highly conserved within the zebrafish. Interestingly, the ventricular AP shape of humans is more similar to zebrafish then it is to rodents, suggesting that the zebrafish could be the preferential model in some electrophysiological studies, especially considering the other benefits of this model.[45] There is indeed a large overlap in cardiac ion currents between zebrafish and human, but there are also some clear differences. Table 1 contains a comparative overview of the cardiac ion channels in human and zebrafish.

Pacemaker currents

Just like humans, the heart rate in zebrafish is controlled by pacemaker cells in the SA node and modulated by the autonomous nervous system. Pacemaker cells express the transcription factor Islet-1 and are organized in a ring-like structure around the inflow region of the atrium.[56] In line with mammals, I_f is one of the main depolarizing currents in zebrafish pacemaker cells.[59] This is well demonstrated within in the zebrafish mutant *slow mo*, which has a marked bradycardia. Patch-clamp experiments revealed that I_f is severely impaired in this mutant as the fast component of I_f is completely abolished.[59,60] In humans, the HCN4 channel (encoded by the *HCN4* gene) is the main channel responsible for I_f, which seems to be the same in zebrafish.[56,61]

Na⁺ channels

Similar to humans, fast Na^+ currents are present in both atrial and ventricular zebrafish cardiomyocytes and are responsible for the AP upstroke phase.[45] In humans $Na_v1.5$ (encoded by the *SCN5A* gene) is the principal cardiac Na^+ channel isoform. *scn5Laa* (*scn12aa*) and *scn5Lab* (*scn12ab*) are the zebrafish orthologues of *SCN5A*.[62] However, in contrast to human $Na_v1.5$, the zebrafish channel is more sensitive to the blocker tetrodotoxin (TTX) due to a replacement of an amino acid in the protein sequence.[63] In a recent study, Huttner and coworkers[64] generated stable transgenic zebrafish lines, which expressed either human wild-type $Na_v1.5$ (*SCN5A*-WT) or a dominant-negative mutant of Nav1.5 (*SCN5A*-D1275N) under the control of the cardiac-specific *myl7*-promoter. Many *SCN5A*-D1275N fish displayed bradycardia, conduction-system abnormalities and premature death. In addition, the *SCN5A*-WT transgene could compensate for the loss of endogenous zebrafish Nav1.5 channels, suggesting that zebrafish Nav1.5 is orthologous to the human Nav1.5.[65] $Na_v1.4$ (*scn4ab gene*) also seems to be expressed in the zebrafish heart, but for now it remains unclear how this channel contributes to I_{Na}.[66]

Ca²⁺ channels

The zebrafish heart contains L-type and T-type Ca^{2+} channels (LTCC and TTCC), similar to the human heart. However, while expression of TTCCs in humans is restricted to the fetal heart and to the pacemaker cells in the adult heart, TTCCs are expressed throughout the zebrafish heart. This could indicate that adult zebrafish cardiomyocytes are more immature compared to mammalian cardiomyocytes.[45] In humans, Cav1.2 (encoded by the *CACNA1C* gene) is the dominant LTCC cardiac isoform and Cav3.2 (encoded by the *CACNA1H* gene) the main TTCC cardiac isoform. In the zebrafish, Cav1.2 and to a lesser extend Cav1.3 (encoded by *cacna1c* and *cacna1da/cacna1db* respectively) are the main LTCC cardiac isoforms[67,68], but zebrafish TTCC composition has not been studied well.[69] Pharmacological and patch-clamp experiments provide robust evidence for a role of LTCC in the plateau phase of atrial and ventricular APs, as LTCC blocker nifedipine shortens the AP duration (APD) in zebrafish atrium and ventricle.[45] In line with this, the *islet beat* zebrafish mutant, which carries a mutation in Cav1.2, displays uncoordinated atrial contraction and has a ventricle that is completely silent.[67]

K⁺ channels

The zebrafish heart shows overlap with the human heart in terms of the types of cardiac K^+ ion channels expressed, but also displays marked differences. As mentioned before, K^+ currents that shape the AP include I_{to}, I_{Kur}, I_{Kr}, I_{Ks}, I_{K1}, $I_{K,ATP}$ and $I_{K,Ach}$ (in order of activation).

The I_{to} current is considered to be absent in the zebrafish heart, as the early rapid repolarization spike (phase 1) is not very prominent in zebrafish APs.[45] In humans I_{to} is formed by the Kv1.4, Kv4.2 and Kv4.3 channels (encoded by the *KCNA4*, *KCND2* and *KCND3* gene respectively). Orthologs for these channels are present in the zebrafish[70], so it is conceivable that one or more of these channels are expressed, but only at low levels.

Table 1. A comparison of ion channels in the adult human and zebrafish heart channels

Current	Organism	α-Subunit	Gene	Expression
I_{Na}	Human Zebrafish	$Na_v1.5$ $Na_v1.5a/b$[62]	*SCN5A* *scn5Laa/ab* (*scn12aa/ab*)[62]	Atrium and ventricle Atrium and ventricle[62]
$I_{Ca,L}$	Human Zebrafish	Cav1.2 Cav1.2, Cav1.3a/b[67,68]	*CACNA1C* *cacna1c, cacna1da/b*[67,68]	Atrium and ventricle Atrium and ventricle[67,68]
$I_{Ca,T}$	Human Zebrafish	Cav3.2 unknown	*CACNA1H* unknown	Fetal heart and SAN Atrium and ventricle[69]
I_{to}	Human Zebrafish	Kv1.4, Kv4.2, Kv4.3 unknown	*KCNA4, KCND2, KCND3* unknown	Atrium and ventricle unknown
I_{K1}	Human Zebrafish	Kir2.1-Kir2.3 Kir2.2a, Kir2.4[77]	*KCNJ2, KCNJ12, KCNJ4* *kcnj12a*[77] *kcnj14*[77]	Atrium and ventricle Atrium[77] Atrium and ventricle[77]
I_{Kr}	Human Zebrafish	Kv11.1 (hERG) Kv11.2 (zERG-3)[71]	*KCNH2* *kcnh6a*[71]	Atrium and ventricle Atrium and ventricle[71]
I_{Ks}	Human Zebrafish	Kv7.1 (KvLQT1) Kv7.1[76]	*KCNQ1* *kcnq1*[76]	Atrium and ventricle Atrium and ventricle[76]
I_{Kur}	Human Zebrafish	Kv1.5 unknown	*KCNA5* unknown	Atrium unknown
$I_{K,ACh}$	Human Zebrafish	Kir3.1, Kir3.4 Kir3.1, Kir3.4[78]	*KCNJ3, KCNJ5* *Kcnj3a, kcnj5*[78]	Atrium, SA node Atrium, SA node[78]
I_f	Human Zebrafish	HCN4 Hcn4[56,61]	*HCN4* *hcn4*[56,61]	SA-node SA-node[56,61]

Baker et al. mentioned the presence of an I_{Kur} in cultured embryonic zebrafish myocytes[59], but no studies have provided further evidence for this. In humans, I_{Kur} is formed by the $K_v1.5$ channel (encoded by the *KCNA5* gene). There is no zebrafish ortholog of *KCNA5* annotated.

I_{Kr} is the main repolarizing current in the zebrafish heart, as it is in humans, but interestingly this current is not formed by Kv11.1 (hERG, encoded by the *KCNH2* gene), but by a channel orthologous to Kv11.2 (zERG or zERG-3, encoded in humans by *KCNH6*; in zebrafish by *kcnh6a*).[71] Despite biophysical differences between the human and zebrafish ERG channel, mutations in zERG do cause similar electrophysiological effects for short and long QT as observed in humans (e.g. zebrafish mutants *breakdance* and *reggae*).[46,72,73] Also, QT prolonging drugs can trigger AP prolongation, bradycardia and AV block in zebrafish embryos, indicating a similar role of hERG and zERG in cardiac electrophysiology.[45,74,75]

In humans, I_{Ks} is formed by the Kv7.1 or KvLQT1 channel (encoded by the *KCNQ1* gene). Zebrafish have cardiac I_{Ks} and express the Kv7.1 channel (encoded by the *kcnq1* gene) both in the atrium and ventricle. 100 µM chromanol 293B, which is a blocker of Kv7.1 and I_{Ks}, was shown to produce a significant prolongation of the AP in the zebrafish ventricle, demonstrating that there is a functional relevance of the channel and of I_{Ks} in zebrafish.[76]

There is a robust background I_{K1} present in atrial and ventricular cardiomyocytes of adult zebrafish (phase 4), and like in humans, the density of I_{K1} is markedly higher in the atrium than the ventricle. But while human I_{K1} is produced by Kir2.1, Kir2.2 and Kir2.3 channels (encoded by the *KCNJ2*, *KCNJ12* and *KCNJ4* gene), zebrafish I_{K1} is predominantly produced by Kir2.4 in the ventricle (92.9% of the total Kir2 population), and by Kir2.2a and Kir2.4 in the atrium (64.7% and 29.3% of the total Kir2 population).[77]

In agreement with findings in human, zebrafish display functional $I_{K,Ach}$, as current amplitude increases in response to carbachol, an agonist of $I_{K,Ach}$. Like humans, this response is only visible in atrial, but not in ventricular zebrafish cardiomyocytes.[45,78] The human channel responsible for $I_{K,Ach}$ is composed of Kir3.1 and Kir3.4 (encoded by the *KCNJ3* and *KCNJ5* gene), which seems to be the same in zebrafish (Kir3.1/3.4, encoded by the *kcnj3a* and *kcnj5* gene).[78]

Excitation-contraction coupling in the zebrafish

In comparison to human cardiomyocytes, zebrafish cardiomyocytes show some important differences in Ca^{2+} handling. Zebrafish cardiomyocytes for example lack transverse tubules and the SR has a lower ability to store and release Ca^{2+}. Crucially, this might make zebrafish cardiomyocytes less susceptible for Ca^{2+} after-transients and delayed afterdepolarizations.[79,80]

Regardless, many proteins that are important in human cardiac Ca^{2+} homeostasis have a functional zebrafish ortholog, indicating that many of the Ca^{2+} pathways are conserved. RyR2 (encoded by the *RYR2* gene) is the main RyR isoform in human hearts, which is similar in zebrafish (RyR2, encoded by the *ryr2* gene). However, in comparison to the human protein, RyR2 in the zebrafish has a very low Ca^{2+} sensitivity, resulting in the release of only a small fraction of SR Ca^{2+} content with each beat.[81] SERCA2a (encoded by the *ATP2A2* gene) is the main cardiac SERCA isoform in both humans and zebrafish, and the SERCA2a regulator PLN (encoded by the *PLN* gene) is also expressed in the zebrafish (Pln, encoded by *plna* on Chr 17 and *plnb* on Chr 20). SERCA2 knockdown in zebrafish causes a reduction in heart rate, weak contractility and hearts fail to loop.[82] Strikingly, the PLN binding site of SERCA2a, as well as the PLN phosphorylation sites are highly conserved, indicating that zebrafish SERCA2a is regulated in a similar fashion by PLN as in human cardiomyocytes.[83] The NCX ion exchanger in humans is encoded by the *SLC8A1* gene and in zebrafish by the *slc8a1b* gene. The zebrafish *tremblor* mutant carries a mutation in NCX and has prominent arrhythmias in the atrium and a completely silent ventricle, demonstrating a functional role of the NCX exchanger in zebrafish.[84]

Overall, zebrafish might not be ideal to study Ca^{2+} modulated arrhythmias, but it is a promising model to study the independent components that regulate Ca^{2+} transients and homeostasis.

Autonomic regulation of the zebrafish heart

The zebrafish heart contains all the essential autonomous nervous system components that are required for the regulation of heart rate and contractility. Like mammals, zebrafish have vagal and sympathetic nerves innervating the heart at the SA node, atrium, AV-region and ventricle.

Stimulation of individual cardiac vagosympathetic nerve trunks as well as direct application of cholinergic and adrenergic agents can evoke bradycardia and tachycardia, indicating that the autonomous nervous system in zebrafish works in a similar fashion as the human autonomous nervous system.[85] In line with this, the zebrafish heart shows expression of M_2-receptors (parasympathetic) and β-adrenoreceptors (sympathetic).[85] The M_2-receptors in humans in encoded by the *CHRM2* gene, and in zebrafish by the *chrm2a* and *chrm2b* genes. The β_1-adrenoreceptor is encoded by the *ADRB1* gene in humans and by the *adrb1* gene in zebrafish.[86]

3. Outline of this thesis

The general aim of the work in this thesis is to study the genetic basis of cardiac electric function and to study the molecular mechanisms underlying arrhythmias. The zebrafish is used as a model organism, exploiting its genetic manipulability and the ease of analysis.

Part I of this thesis is focused on optogenetic sensors and their benefits in studying cardiac cellular electrophysiology. In **chapter 2**, different optogenetic sensors are reviewed and we show that these sensors can be useful tools to study the in vivo dynamics of molecules at a cellular level, without the use of invasive procedures. We critically evaluate these sensors and their suitability for cardiac research. In **chapter 3**, we introduce two zebrafish lines, expressing an optogenetic cardiac voltage sensor (VSFP-butterfly) or a Ca^{2+} sensor (GCaMP6f). With these fish we were able to study cardiac cellular electrophysiology in a detailed and spatiotemporal manner, demonstrating that transgenic VSFP-butterfly and GCaMP6f fish provide a powerful and novel tool for the research of arrhythmias.

In **part II** of this thesis we use the zebrafish to study the effects of different genes on cardiac cellular electrophysiology. **Chapter 4** describes a patient group with a novel multisystem syndrome, in which both cardiac electrophysiology and the nervous system are affected. All patients were found to carry mutations in the *GNB5* gene. A *gnb5* knockout zebrafish line was generated to study the genotype-phenotype relationship, which demonstrated a strong correlation between zebrafish and patient symptoms. This indicated a causal link between *GNB5* mutations and disease, and identified *GNB5* as a novel gene important for cardiac function. In **Chapter 5** we further study the molecular function of GNB5 using human induced pluripotent stem cell-derived atrial cardiomyocytes (iPSC-CMs). We tested the use of I_{KAch} blockers to correct the effect of *GNB5* mutations on cardiac function, both in iPSC-CMs and in the knockout *gnb5* zebrafish model, and show that these drugs can positively affect GNB5 pathology. In **Chapter 6** TMEM161B is introduced as a completely novel component of the cardiac conduction system. A missense mutation in *tmem161b* results in severe arrhythmias in zebrafish embryos. We observed striking changes in the action potentials of these fish, which are likely due to disruption of I_{Kr} and $I_{Ca,L}$. In **Chapter 7** we study the pathology of the phospholamban arginine 14 deletion (PLN R14del) using the zebrafish as a model system. Patients who carry the PLN R14del have a high incidence of arrhythmogenic

right ventricular cardiomyopathy (ARVC) and idiopathic dilated cardiomyopathy (DCM). We show that PLN R14del zebrafish display some cellular changes at a young age and can develop severe cardiomyopathy when they grow older.

Chapter 8 aims to put the results of this thesis in perspective, in the form of a summarizing discussion.

References

1. HeartFoundation.org
2. van Weerd JH & Christoffels VM. The formation and function of the cardiac conduction system. *Development* 2016;143:197–210.
3. Wong CX et al. Epidemiology of Sudden Cardiac Death: Global and Regional Perspectives. *Heart Lung Circ* 2019;28:6–14.
4. Deo R & Albert CM. Epidemiology and genetics of sudden cardiac death. *Circulation* 2012;125:620–637.
5. Grant AO. Cardiac ion channels. *Circ Arrhythm Electrophysiol* 2009;2:185–194.
6. Eisner DA, Caldwell JL, Kistamás K & Trafford AW. Calcium and Excitation-Contraction Coupling in the Heart. *Circ Res* 2017;121:181–195.
7. Bers DM. Cardiac excitation-contraction coupling. *Nature* 2002;415:198–205.
8. Tada M, Kirchberger MA & Katz AM. Phosphorylation of a 22,000-dalton component of the cardiac sarcoplasmic reticulum by adenosine 3':5'-monophosphate-dependent protein kinase. *J Biol Chem* 1975;250:2640–2647.
9. Kranias EG & Hajjar RJ. The Phospholamban Journey 4 Decades After Setting Out for Ithaka. *Circ Res* 2017;120:781–783.
10. Vafiadaki E et al. Phospholamban interacts with HAX-1, a mitochondrial protein with anti-apoptotic function. *J Mol Biol* 2007;367:65–79.
11. Lam CK et al. Novel role of HAX-1 in ischemic injury protection involvement of heat shock protein 90. *Circ Res* 2013;112:79–89.
12. Berrebi-Bertrand I et al. Biophysical interaction between phospholamban and protein phosphatase 1 regulatory subunit GM. *FEBS Lett* 1998;439:224–230.
13. Lygren B et al. AKAP complex regulates Ca^{2+} re-uptake into heart sarcoplasmic reticulum. *EMBO Rep* 2007;8:1061–1067.
14. Rigatti M, Le AV, Gerber C, Moraru II & Dodge-Kafka KL. Phosphorylation state-dependent interaction between AKAP7δ/γ and phospholamban increases phospholamban phosphorylation. *Cell Signal* 2015;27:1807–1815.
15. Nicolaou P et al. Inducible expression of active protein phosphatase-1 inhibitor-1 enhances basal cardiac function and protects against ischemia/reperfusion injury. *Circ Res* 2009;104:1012–1020.
16. Qian J et al. Small heat shock protein 20 interacts with protein phosphatase-1 and enhances sarcoplasmic reticulum calcium cycling. *Circ Res* 2011;108:1429–1438.
17. MacLennan DH & Kranias EG. Phospholamban: a crucial regulator of cardiac contractility. *Nat Rev Mol Cell Biol* 2003;4:566–577.
18. Chu G et al. A single site (Ser^{16}) phosphorylation in phospholamban is sufficient in mediating its maximal cardiac responses to beta-agonists. *J Biol Chem* 2000;275:38938–38943.
19. Kovacs RJ, Nelson MT, Simmerman HK & Jones LR. Phospholamban forms Ca^{2+}-selective channels in lipid bilayers. *J Biol Chem* 1988;263:18364–18368.
20. Oxenoid K & Chou JJ. The structure of phospholamban pentamer reveals a channel-like architecture in

membranes. *Proc Natl Acad Sci U.S.A.* 2005;102:10870–10875.

21. Glaves JP, Trieber CA, Ceholski DK, Stokes DL & Young HS. Phosphorylation and mutation of phospholamban alter physical interactions with the sarcoplasmic reticulum calcium pump. *J Mol Biol* 2011;405:707–723.
22. Chu G et al. Pentameric assembly of phospholamban facilitates inhibition of cardiac function in vivo. *J Biol Chem* 1998;273:33674–33680.
23. Brittsan AG, Carr AN, Schmidt AG & Kranias EG. Maximal inhibition of SERCA2 $Ca^{(2+)}$ affinity by phospholamban in transgenic hearts overexpressing a non-phosphorylatable form of phospholamban. *J Biol Chem* 2000;275:12129–12135.
24. Meyer M et al. Alterations of sarcoplasmic reticulum proteins in failing human dilated cardiomyopathy. *Circulation* 1995;92:778–784.
25. Jamali HK, Waqar F & Gerson MC. Cardiac autonomic innervation. *J Nucl Cardiol* 2017;24:1558–1570.
26. Antzelevitch C & Burashnikov A. Overview of Basic Mechanisms of Cardiac Arrhythmia. *Card Electrophysiol Clin* 2011;3:23–45.
27. Tse G. Mechanisms of cardiac arrhythmias. *J Arrhythm* 2016;32, 75–81.
28. Streisinger G, Walker C, Dower N, Knauber D & Singer F. Production of clones of homozygous diploid zebra fish (*Brachydanio rerio*). *Nature* 1981;291:293–296.
29. Lieschke GJ & Currie PD. Animal models of human disease: zebrafish swim into view. *Nat Rev Genet* 2007;8:353–367.
30. Driever W et al. A genetic screen for mutations affecting embryogenesis in zebrafish. *Development* 1996;123:37–46.
31. Haffter P et al. The identification of genes with unique and essential functions in the development of the zebrafish, *Danio rerio*. *Development* 1996;123:1–36.
32. Berghmans, S. et al. *tp53* mutant zebrafish develop malignant peripheral nerve sheath tumors. *Proc Natl Acad Sci U.S.A.* 2005;102:407–412.
33. Zabinyakov N. et al. Characterization of the first knock-out *aldh7a1* zebrafish model for pyridoxine-dependent epilepsy using CRISPR-Cas9 technology. *PLoS ONE* 2017;12:e0186645.
34. Tessadori F et al. Effective CRISPR/Cas9-based nucleotide editing in zebrafish to model human genetic cardiovascular disorders. *Dis Model Mech* 2018;11(10):dmm035469.
35. Chetaille P et al. Mutations in *SGOL1* cause a novel cohesinopathy affecting heart and gut rhythm. *Nature Genetics* 2014;46:1245–1249.
36. Hendee KE et al. PITX2 deficiency and associated human disease: insights from the zebrafish model. *Hum Mol Genet* 2018;27:1675–1695.
37. Noël ES et al. A Zebrafish Loss-of-Function Model for Human *CFAP53* Mutations Reveals Its Specific Role in Laterality Organ Function. *Hum Mutat* 2016;37:194–200.
38. Golzio C et al. KCTD13 is a major driver of mirrored neuroanatomical phenotypes of the 16p11.2 copy number variant. *Nature* 2012;485:363–367.
39. Liu CX et al. CRISPR/Cas9-induced *shank3b* mutant zebrafish display autism-like behaviors. *Mol Autism* 2018;9:23.
40. Siekierska A et al. Gain-of-function *FHF1* mutation causes early-onset epileptic encephalopathy with

cerebellar atrophy. *Neurology* 2016;86:2162–2170.

41. Panizzi JR et al. *CCDC103* mutations cause primary ciliary dyskinesia by disrupting assembly of ciliary dynein arms. *Nature Genetics* 2012;44:714–719.
42. Howe K et al. The zebrafish reference genome sequence and its relationship to the human genome. *Nature* 2013;496:498–503.
43. Tiso N, Moro E & Argenton F. Zebrafish pancreas development. *Mol Cell Endocrinol* 2009;312:24–30.
44. Jagannathan-Bogdan M & Zon LI. Hematopoiesis. *Development* 2013;140:2463–2467.
45. Nemtsas P, Wettwer E, Christ T, Weidinger G & Ravens U. Adult zebrafish heart as a model for human heart? An electrophysiological study. *J Mol Cell Card* 2010;48:161–171.
46. Arnaout R et al. Zebrafish model for human long QT syndrome. *Proc Natl Acad Sci U.S.A.* 2007:104:11316–11321.
47. Hu N, Sedmera D, Yost HJ & Clark EB. Structure and function of the developing zebrafish heart. *Anat Rec* 2000;260:148–157.
48. Poon KL & Brand T. The zebrafish model system in cardiovascular research: A tiny fish with mighty prospects. *Glob Cardiol Sci Pract* 2013;2013:9–28.
49. Bakkers J. Zebrafish as a model to study cardiac development and human cardiac disease. *Cardiovasc Res* 2011;91:279–288.
50. Keegan BR, Meyer D & Yelon D. Organization of cardiac chamber progenitors in the zebrafish blastula. *Development* 2004;131:3081–3091.
51. de Pater E et al. Distinct phases of cardiomyocyte differentiation regulate growth of the zebrafish heart. *Development* 2009;136:1633–1641.
52. Yelon D, Horne SA & Stainier DY. Restricted expression of cardiac myosin genes reveals regulated aspects of heart tube assembly in zebrafish. *Dev Biol* 1999;214:23–37.
53. Christoffels VM, Burch JBE & Moorman AFM. Architectural plan for the heart: early patterning and delineation of the chambers and the nodes. *Trends Cardiovasc Med* 2004;14:301–307.
54. Serluca FC. Development of the proepicardial organ in the zebrafish. *Dev Biol* 2008;315:18–27 (2008).
55. Beis D et al. Genetic and cellular analyses of zebrafish atrioventricular cushion and valve development. *Development* 2005;132:4193–4204.
56. Tessadori F et al. Identification and functional characterization of cardiac pacemaker cells in zebrafish. *PLoS ONE* 2012;7:e47644.
57. Chi NC et al. Foxn4 directly regulates *tbx2b* expression and atrioventricular canal formation. *Genes Dev* 2008;22:734–739.
58. Verhoeven MC, Haase C, Christoffels VM, Weidinger G & Bakkers J. Wnt signaling regulates atrioventricular canal formation upstream of BMP and Tbx2. *Birth Defects Res Part A Clin Mol Teratol* 2011;91:435–440.
59. Baker K, Warren KS, Yellen G & Fishman MC. Defective 'pacemaker' current (I_h) in a zebrafish mutant with a slow heart rate. *Proc Natl Acad Sci U.S.A*. 1997;94:4554–4559.
60. Stainier DY et al. Mutations affecting the formation and function of the cardiovascular system in the zebrafish embryo. *Development* 1996;123:285–292.
61. Stoyek MR, Croll RP & Smith FM. Intrinsic and extrinsic innervation of the heart in zebrafish (*Danio rerio*).

J Comp Neurol 2015;523:1683–1700.

62. Chopra SS et al. Voltage-gated sodium channels are required for heart development in zebrafish. *Circulation Research* 2010;106:1342–1350.
63. Vornanen M, Hassinen M & Haverinen J. Tetrodotoxin sensitivity of the vertebrate cardiac Na^+ current. *Mar Drugs* 2011;9:2409–2422.
64. Huttner IG et al. A transgenic zebrafish model of a human cardiac sodium channel mutation exhibits bradycardia, conduction-system abnormalities and early death. *J Mol Cell Card* 2013;61:123–132.
65. Vornanen M & Hassinen M. Zebrafish heart as a model for human cardiac electrophysiology. *Channels* 2016;10:101–110.
66. Novak AE et al. Gene duplications and evolution of vertebrate voltage-gated sodium channels. *J Mol Evol* 2006;63:208–221.
67. Rottbauer W et al. Growth and function of the embryonic heart depend upon the cardiac-specific L-type calcium channel alpha1 subunit. *Dev Cell* 2001;1:265–275.
68. Sidi S, Busch-Nentwich E, Friedrich R, Schoenberger U & Nicolson T. *Gemini* encodes a zebrafish L-type calcium channel that localizes at sensory hair cell ribbon synapses. *J Neurosci* 2014;24:4213–4223.
69. Ravens U. Ionic basis of cardiac electrophysiology in zebrafish compared to human hearts. *Prog Biophys Mol Biol* 2018;138:38-44.
70. Zerbino DR et al. Ensembl 2018. *Nucleic Acids Res* 2018;46:D754–D761.
71. Leong IUS, Skinner JR, Shelling AN & Love DR. Identification and expression analysis of *kcnh2* genes in the zebrafish. *Biochem Biophys Res Commun* 2010;396:817–824.
72. Hassel D et al. Deficient zebrafish ether-à-go-go-related gene channel gating causes short-QT syndrome in zebrafish *reggae* mutants. *Circulation* 2008;117:866–875.
73. Kopp R, Schwerte T & Pelster B. Cardiac performance in the zebrafish *breakdance* mutant. *J Exp Biol* 2005;208:2123–2134.
74. Langheinrich U, Vacun G & Wagner T. Zebrafish embryos express an orthologue of HERG and are sensitive toward a range of QT-prolonging drugs inducing severe arrhythmia. *Toxicol Appl Pharmacol* 2003;193:370–382.
75. Milan DJ, Peterson TA, Ruskin JN, Peterson RT & MacRae CA. Drugs that induce repolarization abnormalities cause bradycardia in zebrafish. *Circulation* 2003;107, 1355–1358.
76. Abramochkin DV, Hassinen M & Vornanen M. Transcripts of Kv7.1 and MinK channels and slow delayed rectifier K^+ current (I_{Ks}) are expressed in zebrafish (*Danio rerio*) heart. *Pflugers Arch* 2018;187:329.
77. Hassinen M, Haverinen J, Hardy ME, Shiels HA & Vornanen M. Inward rectifier potassium current (I_{K1}) and Kir2 composition of the zebrafish (*Danio rerio*) heart. *Pflugers Arch* 2015;467:2437–2446.
78. Skarsfeldt MA et al. Atrium-specific ion channels in the zebrafish-A role of I_{KACh} in atrial repolarization. *Acta Physiol (Oxf)* 2018;223:e13049.
79. Xie Y, Ottolia M, John SA, Chen JN & Philipson KD. Conformational changes of a Ca^{2+}-binding domain of the Na^+/Ca^{2+} exchanger monitored by FRET in transgenic zebrafish heart. *Am J Physiol Cell Physiol* 2008;295:C388–93.
80. Verkerk AO & Remme CA. Zebrafish: a novel research tool for cardiac (patho)electrophysiology and ion

channel disorders. *Front Physiol* 2012;3:255.

81. van Opbergen CJM, van der Voorn SM, Vos MA, de Boer TP & van Veen TAB. Cardiac Ca^{2+} signalling in zebrafish: Translation of findings to man. *Prog Biophys Mol Biol* 2018;138:45-58.
82. Ebert AM et al. Calcium extrusion is critical for cardiac morphogenesis and rhythm in embryonic zebrafish hearts. *Proc Natl Acad Sci U.S.A.* 2005;102:17705–17710.
83. Gorski PA, Trieber CA, Ashrafi G & Young HS. Regulation of the Sarcoplasmic Reticulum Calcium Pump by Divergent Phospholamban Isoforms in Zebrafish. *J Biol Chem* 2015;290(11):6777-88.
84. Langenbacher AD et al. Mutation in sodium-calcium exchanger 1 (NCX1) causes cardiac fibrillation in zebrafish. *Proc Natl Acad Sci U.S.A.* 2005;102:17699–17704.
85. Stoyek MR, Quinn TA, Croll RP & Smith FM. Zebrafish heart as a model to study the integrative autonomic control of pacemaker function. *Am J Physiol Heart Circ Physiol* 2016;311:H676–88.
86. Wang Z et al. Zebrafish beta-adrenergic receptor mRNA expression and control of pigmentation. *Gene* 2009;446:18–27.

1

Part 1

Optogenetic sensors

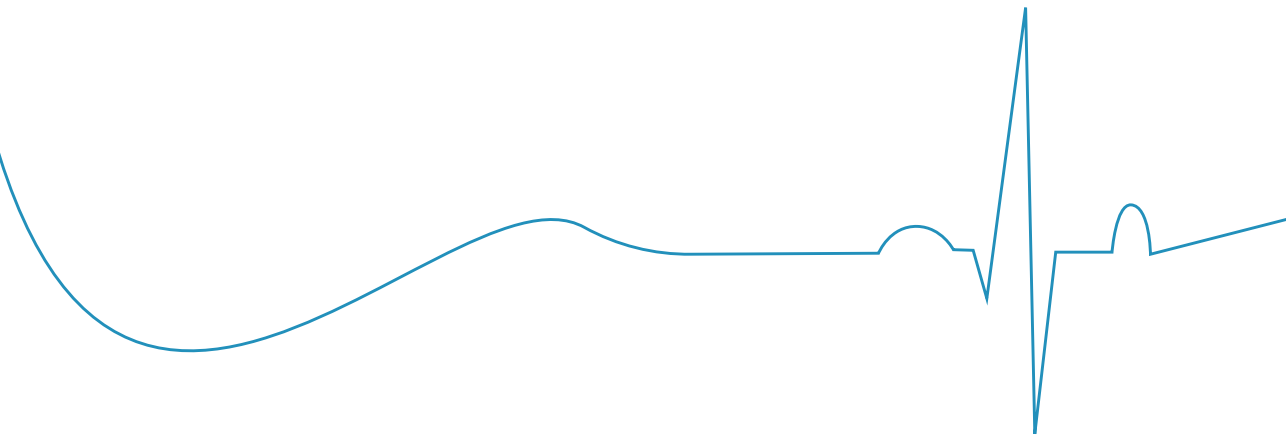

CHAPTER 2

Cardiac optogenetics: using light to monitor cardiac physiology

Charlotte D. Koopman, Wolfram H. Zimmermann, Thomas Knöpfel, Teun P. de Boer

Basic Research in Cardiology 2017;112(5):56

Abstract

Our current understanding of cardiac excitation and its coupling to contraction is largely based on ex vivo studies utilising fluorescent organic dyes to assess cardiac action potentials and signal transduction. Recent advances in optogenetic sensors open exciting new possibilities for cardiac research and allow us to answer research questions that cannot be addressed using the classic organic dyes. Especially thrilling is the possibility to use optogenetic sensors to record parameters of cardiac excitation and contraction in vivo. In addition, optogenetics provide a high spatial resolution, as sensors can be coupled to motifs and targeted to specific cell types and subcellular domains of the heart. In this review, we will give a comprehensive overview of relevant optogenetic sensors, how they can be utilised in cardiac research and how they have been applied in cardiac research up to now.

Keywords: Physiology, calcium cycling/excitation–contraction coupling, ion channels/membrane transport, cell signalling/signal transduction

Introduction

In recent years, the term optogenetics has become synonymous with research that applies channelrhodopsins to trigger depolarisation of cells by exposure to blue light. This is, however, a rather narrow definition that disregards the broad range of possibilities that arises from combining genetic strategies with optical techniques. In this review, we will conform to the wider definition suggested by Gero Miesenböck that optogenetics "combines genetic engineering with optics to observe and control the function of genetically targeted groups of cells with light".[1] While already widely used in neuroscience[2,3], optogenetic methods are now slowly finding their way to cardiac physiology laboratories. In our view, optogenetics has the potential to resolve cardiac physiology in a so far unprecedented way. Cardiac applications of optogenetic actuators such as channelrhodopsin have been covered by several recent reviews.[4-6] Here, we will review optogenetic sensors that are particularly relevant to the cardiac field, studies that have applied optogenetics in the heart, and outline some of the research questions that can be addressed using optogenetic probes and sensors.

1. The unique potential of cardiac optogenetics

Our understanding of cardiac physiology owes much to the development of fluorescent organic dyes that allow the study of intracellular ions (e.g., Ca^{2+}, Mg^{2+}, Na^{+}), transmembrane potential or pH using light microscopy. This optic approach has major advantages over ion-sensitive electrodes that were used before availability of these dyes. It became possible to study many regions of a specimen concurrently without impalement of individual cells and it enabled studies of subcellular mechanisms, including the spatial and temporal resolution of calcium sparks or mitochondrial membrane potential changes, which is impossible with available microelectrodes.

While organic dyes are powerful tools, application of these dyes has practical limits, some of which can be mitigated using an optogenetic approach instead. The main obstacle of using organic dyes is that the experiment can be done only once. After staining a specimen with a dye, the dye will diffuse within the tissue, accumulate in intracellular vesicles or is lost in another way. This results in a decreased specificity of the fluorescent signal, meaning that the staining will typically have to be repeated on a new specimen.

As an additional obstacle, organic dyes can only be used on isolated hearts or isolated cardiomyocytes and are not suitable for in vivo studies. Clearly, in vivo experiments will provide a better understanding of the complex physiology of the heart and the way it functions within the context of the whole body. Also, minimally invasive in vivo experiments may be repeated over time using the same animals, giving the study a greater power to discriminate between experimental groups.

By employing optogenetic sensors and expressing them in the heart, serial in vivo investigation

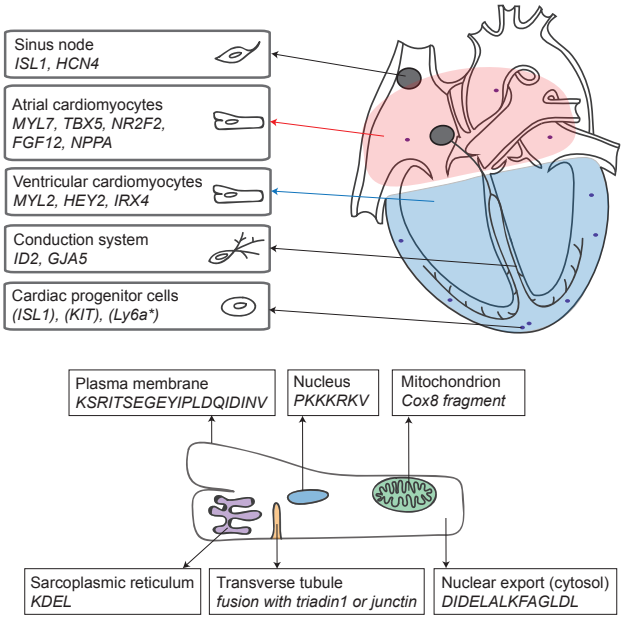

Figure 1. Motifs to target specific cardiac cells or cell organelles. (A) Overview of genes that are higher expressed in subareas of the heart and can be used to target specific cells.[64] The red region indicates atrial cells, the blue region ventricular cells. Genes from cardiac progenitor cells are between brackets, since it is unclear if they are indeed progenitor cell specific. Gene names can differ between species and gene expression may be dependent on developmental stage and specie. **Ly6a* is only found in the mouse. (B) Overview of motifs that can be used to target specific locations within the cell.

of cardiac parameters such as intracellular calcium, pH or membrane potential is conceivable. Moreover, by utilising specific targeting motifs, sensors or actuators can be designed to mark subcellular domains and functions in specific cell types in the heart. Protein targeting motifs for the sarcoplasmic reticulum, plasma membrane, cytoplasm, lysosomes, nucleus, transverse tubule and mitochondrion are readily available. An overview of available cell-specific promoters and compartment-specific motifs can be found in Figure 1.

A clear advantage for the application of optogenetic tools in neuroscience is the lack of gross movements of the brain, opposed to the continuous cardiac cycle that complicates conventional imaging approaches in cardiac physiology. Some possible solutions to this technical challenge will be discussed in later sections of this review.

2. The building plan of optogenetic sensors

Optogenetic sensors are generally composed of a sensing domain linked to one or more fluorescent proteins (FPs). The sensing domain can be activated by the parameter of interest,

causing a conformational change. This in turn affects the optical properties of the FPs, either through altering the fluorescence quantum yield (brightness) of a single FP or by giving rise to changes in Förster resonance energy transfer (FRET) efficacy between two FPs.

This general building plan of optogenetic sensors offers great flexibility and allows numerous sensor compositions. Sensing domains are often based on fragments of endogenous proteins that interact with or respond to the parameter of interest. By altering the sensing domain, its specificity or binding kinetics can be tuned to match the scientific question. Recent advances have increased the number of FPs and the colours that can be used. This has for instance resulted in multiple calcium sensors with different colours[7] and in FPs that provide sensors with stronger FRET responses.[8] Detailed discussion of the structural composition of optogenetic sensors and actuators is beyond the scope of this review, for such information we refer the reader to recent excellent reviews on that topic.[9,10]

3. Optogenetic sensors for cardiac research

An overview of the sensors that will be discussed in this section is given in Figure 2 and Table 1.

3.1. Optogenetic sensors that detect ions

Calcium sensors. Calcium signalling is imperative for cardiomyocyte function and the optogenetic detection of calcium can provide valuable information in cardiac studies. Genetically encoded calcium sensors (GECIs) have improved dramatically in the last 5 years, to the point where they are approaching or exceeding traditional organic dyes in terms of signal-to-noise ratios.[11] It is therefore not surprising that calcium sensors have already made their way into cardiac research. However, some organic dyes still have faster Ca^{2+} binding and unbinding kinetics, something that has to be taken into account when designing experiments. Existing GEVIs include the non-ratiometric CaMP sensors (e.g., GCaMP and RCaMP) and the ratiometric sensors such as cameleon, Twitch and TN-XL.

Excitation–contraction coupling in cardiomyocytes, and thus calcium signalling, is an essential process in cardiac contractility and is strongly influenced by the sympathetic nervous system. However, this interaction is difficult to approach experimentally as it ideally requires an in vivo approach. Tallini et al.[12] demonstrated that expression of the optogenetic calcium sensor GCaMP2 in the mouse heart allows the in situ recording of cardiomyocyte calcium transients. In subsequent work of the same group GCaMP2 has been targeted to endothelial cells to study the in vivo relation between acetylcholine-induced calcium waves in endothelial cells and the subsequent dilation of arterioles.[13] Expression of GCaMP2 was also evident in the cardiac Purkinje fibres, enabling recordings of calcium transients selectively in this cell type. A caveat to the use of GCaMP is the apparent induction of hypertrophy as a result of calmodulin motif overexpression[12], but this can be avoided by an inducible expression system.

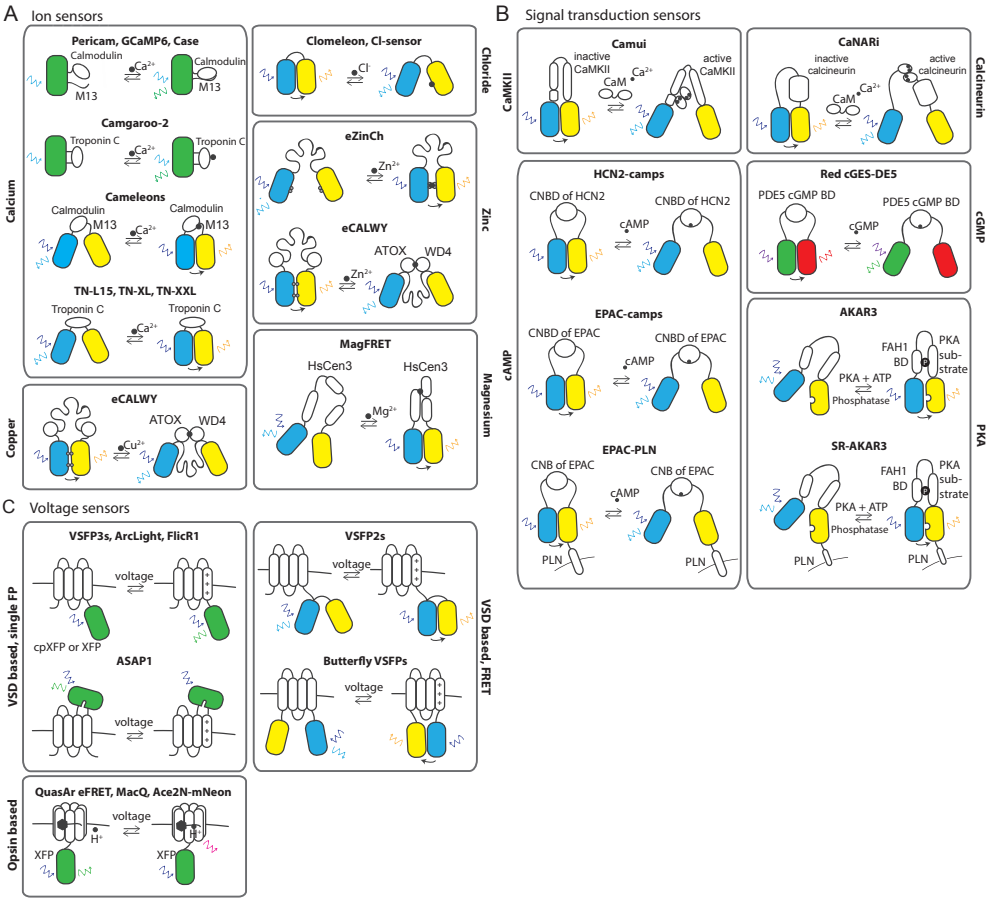

Figure 2. Overview of cardiac optogenetic sensor designs. (A–C) each give an overview of a group of sensors that are relevant for cardiac research. For each sensor its mode of action is schematically visualised. Fluorescent proteins are depicted as coloured barrels, proteins or protein domains as white barrels. Coloured arrows indicate excitation/emission wavelengths. (A) Overview of optogenetic ion sensors. These sensors are based on proteins that can sense and bind the ion of interest with a high affinity. Upon binding, a conformational change occurs within the sensor, inducing or diminishing fluorescence or FRET.[3,8,65-76] (B) Overview of optogenetic signal transduction sensors. These sensors consist of proteins or substrates that can bind the signalling molecule of interest. In case of a substrate, binding will result in activation or deactivation of the substrate. Ultimately, a conformational change of the sensor will induce or diminish fluorescence or FRET.[32-34,36,77-79] (C) Overview of optogenetic voltage sensors. VSD-based sensors are composed of a voltage-sensing transmembrane protein linked to either a single fluorescent protein or to a FRET fluorescent protein pair. When the membrane charges, the VSD displaces, giving rise to a fluorescent response.[53,54,57,59] Opsin-based voltage sensors are based on microbial rhodopsin proton pumps and fluorescence is induced via a voltage-dependent shift in the acid–base equilibrium of the retinal Schiff base located in the proton pump.[60-62]

Another challenge in cardiac research is the analysis of stem cell functionality after transplantation into the heart. Recently, Shiba et al. expressed GCaMP3 in human embryonic stem

Table 1. List of the latest GEVIs apt for cardiac in vivo studies

Name sensor	Year of publication	Design type	Monochromatic or FRET based	Source of voltage-sensing domain or opsin	Expression system for functional characterization	Readout chromophore's peak emission wavelengths	Sensitivity (% ΔR/R per 100 mV)	Response time constant τ (on)	Response time constant τ (off)	Reference
ArcLight A242, Q239	2012	VSD class	Monochromatic	Ci-VSP	HEK293 cells and cultured neurons, fruitfly in vivo	Super ecliptic pHluorin A227D	35%	14.5 ms (122 ms)	44.6 ms (273 ms)	Jin et al.[53]
VSFP2.3	2008, 2015	VSD class	FRET	Ci-VSP	Mouse heart in vivo and ex vivo, PC12 cells	mCerulean: 477 nm mCitrine: 530 nm	15%	3 ms (16 ms)	31 ms	Lundby et al.[54], Liao et al.[42]
Mermaid	2008, 2010	VSD class	FRET	Ci-VSP	Mouse heart ex vivo, zebrafish heart	mUKG: 499 nm mKOk: 563 nm	± 30%	5-20 ms	5-20 ms	Tsutsui et al.[45,55], Kaestner et al.[56]
Chimeric VSFP-butterfly	2014	VSD class	FRET	Ci-VSP/KV3.1 chimera	HEK293 cells, mouse in vivo	mCerulean: 477 nm mCitrine: 529 nm mCitrine: 529 nm mKate2: 633 nm	14.7% 12.7%	2.1 ms (36.7 ms) 2.3 ms (81.2 ms)	14.6 ms 25.1 ms	Mishina et al.[57]
VSFP-CR	2012, 2017	VSD class	FRET	Ci-VSP	Hippocampal neurons, hiPS-CM	Clover: 515 nm mRuby2: 600 nm	12.7%	5.4 ms (59.5 ms)	N.D.	Lam et al.[8], Chen et al.[58]
ASAP-1	2014	VSD class	Monochromatic	Chicken VSP	HEK293 cells and cultured neurons	GFP: 505 nm	±20%	2.1 ms (72 ms)	50.8 ms (2 ms)	St-Pierre et al.[59]
QuasAr eFRET	2014	Microbial opsins	Monochromatic	Archaerhodopsin	HEK293 cells and cultured neurons	EGFP: 505 nm Citrine: 530 nm mOrange: 562 nm mRuby2: 600 nm mKate2: 633 nm	-7.7% -13.1% -10% -8.7% -4.5%	4.3 ms (27 ms) 4.8 ms (21 ms) 4.3 ms (26 ms) 4.3 ms (27 ms) 2.8 ms (35 ms)	3.0 ms (26 ms) 3.1 ms (21 ms) 3.9 ms (27 ms) 3.6 ms (20 ms) 4.0 ms (25 ms)	Zou et al.[60]
MacQ	2014	Microbial opsins	Monochromatic	L. maculans rhodopsin	HEK293T cells, cultured neurons, mouse brain slices, mouse in vivo	mCitrine: 530 nm mOrange2: 562 nm	±20% ±20%	2.8 ms (71 ms) 2.9 ms (115 ms)	5.4 ms (67 ms) 3.4 ms (20 ms)	Gong et al.[61]
Ace2N-mNeon	2015	Microbial opsins	Monochromatic	Acetabularia acetabulum rhodopsin	HEK293T cells and cultured neurons, fruitfly in vivo, mouse in vivo	mNeon/	12%	0.36 ms (4.2 ms)	0.42 ms (5.2 ms)	Gong et al.[62]
FlicR1	2016	VSD class	Monochromatic	Ci-VSP	HeLa cells, HEK293 cells and cultured neurons	cpmApple/597 nm	±3%	3.0 ms (41 ms)	2.8 ms (18 ms)	Abdelfattah et al.[63]

cell-derived cardiomyocytes (SDCs) to evaluate their survival after transplantation into guinea pig hearts.[14] Calcium signals that were detected, demonstrated that the SDCs survived transplantation and displayed calcium transients that were synchronised with the surrounding native myocardium.

Detection of calcium signals at specific subcellular domains in cardiomyocytes such as the dyadic space between T-tubules and the sarcoplasmic reticulum is challenging. Calcium sparks occurring at the dyad are fundamental to excitation–contraction coupling, while whole cell calcium transients are the summation of many nearly simultaneous calcium sparks. The calcium spark has been studied intensively, but mainly as spontaneous events happening in resting cardiomyocytes. This limitation is the result of the inability to resolve calcium sparks (small amplitude), or the dyadic space from the rest of the cytoplasm during whole cell calcium transients (large amplitude). However, in a recent publication, Shang et al. demonstrate that dyadic calcium imaging is feasible in rat cardiomyocytes by targeting a GCaMP6 variant to the dyadic space.[15] This approach resulted in an approximately 50x better spatial specificity compared to organic dyes, high contrast and importantly, the ability to study dyadic calcium signalling during the whole excitation–contraction cycle. Another example of targeted calcium sensor was the use of D1ER, a SR targeted version of Cameleon, in neonatal rat cardiomyocytes. Using this approach, the authors demonstrated the role of AKAP18∂ in the regulation of PKA-mediated phosphorylation of phospholamban.

With the possibility to target calcium sensors to specific domains, availability of sensors with different emission wavelengths becomes important. For example dyadic calcium imaging using a targeted green GCaMP6 sensor could be combined with expression of a red calcium sensor targeted to the sarcoplasmic reticulum or cytoplasm to reveal interaction between compartments. Recently, GECIs with blue, orange or red emission have become available.[7,16-18] Particularly, the red sensors have attracted attention, as they have the advantage that they can be combined with channelrhodopsins, allowing light-induced pacing with blue light and simultaneous study of calcium signalling with green excitation light and red emission.[16] No studies have been published yet that employ red calcium sensors in the heart, but ongoing work in our laboratory has shown that cardiac calcium transients can be well resolved in transfected neonatal rat cardiomyocytes with these sensors (RCaMP1h, R-GECO1, R-CaMP1.07 and R-CaMP2).

The strength of calcium sensors that are derived from GCaMP is the relatively high signal-to-noise ratio. However, these sensors are not ratiometric since they contain only one fluorescent protein, in contrast to FRET sensors (e.g., cameleon, Twitch or TN-XL). Especially in the heart, it is important to take this into consideration when selecting a sensor, as ratiometric approaches provide a way to deal with cardiac contraction artefacts that otherwise confound results. Unfortunately, responses of FRET sensor are much smaller in amplitude than those of GCaMP type sensors (typically max. 15%), which make it more challenging to resolve the optical Ca^{2+} signals. Currently, an interesting hybrid is being developed by fusion of GCaMP3 with the calcium-insensitive FP mCherry.[19] The resulting sensor (GCaMP-GR) promises an optimal combination of a high signal-to-noise single emission sensor with the possibility to correct for movement-related florescence signals. However, application in the heart has not been demonstrated yet. Recently

developed single emission sensors based on CFP variants and reporting PKA activity, membrane voltage or calcium[20,21] may also be combined with, e.g., yellow or green FPs to yield a dual emission sensor with high signal-to-noise ratio.

In conclusion, the toolkit available for studying cardiac calcium handling has greatly advanced, enabling in situ studies of important physiologic calcium processes (i.e., sympathetic influence on the heart), experimental processes (i.e., stem cell transplant functionality) and of calcium handling within cellular compartments. In addition, it is possible to measure different compartments simultaneously by employing differently coloured sensors.

Sensors to detect other ions. Compared to the recent rapid development of GEVIs with improved performance, there are fewer well performing genetically encoded indicators for optogenetic detection of other ions. To our knowledge, there is no sensor available for sodium ions, even though such a sensor would be very interesting given the direct interaction between sodium and other ions (including calcium) via the various sodium co-transporters (Na^+/Ca^{2+}, Na^+/H^+, Na^+/HCO_3^-) and the often increased sodium ion concentration in remodelling cardiomyocytes.[22-24]

Chloride ions can be detected using various optogenetic sensors, which are used in neuroscience given the important role of chloride ions in neuronal excitability.[25] In the heart chloride ions may also play a role in cardiac osmotic balance, excitability and remodelling[26], but their role for now remains elusive.

Magnesium ions influence heart rhythm via potassium and calcium ion channels, and are also relevant in cardiac disease and treatment.[27] Using MagFRET to study intracellular Mg^{2+} in the heart may enhance our insight in the ion's role in normal physiology and cardiac disease.

Other ions that can be detected using optogenetic sensors include Zn^{2+} and Cu^{2+}, which is interesting since both ions are implicated in cardiac disease.[28] However, these sensors have not been used to study cardiomyocytes yet.

3.2. Optogenetic sensors to detect signal transduction

Remodelling of the heart during disease is associated with altered activation of several signal transduction pathways, e.g., CaMKII, calcineurin, cAMP/PKA and cGMP/PKG. The essence of many signal transduction pathways is that they transduce extracellular signals into an intracellular signal, allowing cardiomyocytes to respond their environment. Importantly, extracellular signals typically reach cardiomyocytes via the circulation, from which the heart is disconnected in most conventional experimental settings, meaning that signal transduction pathways are deprived of their physiological input. Application of optogenetic sensors to study signal transduction in vivo could potentially help overcome this limitation.

Calcium-sensitive pathways. Binding of calcium to calmodulin leads to activation of CaMKII by calmodulin. The state of CaMKII is, therefore, strongly influenced by changes in calcium signalling, such as induced by variations in heart rate or neurohumoral factors.[29,30] Interestingly,

CaMKII activity can be affected by phosphorylation or oxidation. By employing the CaMKII activity sensor Camui and two CaMKII variants that are resistant to phosphorylation or oxidation, it was demonstrated that activation of CaMKII by angiotensin-II and endothelin-I largely depends on oxidation, while isoproterenol and phenylephrine affect CaMKII mainly through phosphorylation.[29] In vivo exploration of CaMKII regulation by application of Camui may be instrumental in improving our understanding of its role in cardiac remodelling and arrhythmogenesis.

After binding calcium, calmodulin can also activate calcineurin, which in turn phosphorylates NFAT and causes it to migrate into the nucleus where it functions as a transcription factor. Calcineurin is implicated in cardiac hypertrophy and failure.[30] A FRET sensor to detect calcineurin activity has been developed and employs a fragment of NFAT.[31] Applications have not extended to cardiac cells yet, but experiments in MIN6 β-cells have revealed strong differences between calcium dependence of cytoplasmic and ER calcineurin signalling[32], raising the question how subcellular calcineurin activity is regulated in cardiomyocytes.

Given the essential interaction of CaMKII and calcineurin pathways with intracellular calcium, it would be interesting to simultaneous monitor CaMKII or calcineurin with calcium. Since Camui and CaNAR sensors are based on cyan and yellow fluorescent proteins they may be combined with green or red calcium sensors, though combination with green calcium sensors will require the use of spectral deconvolution approaches to better separate yellow and green emission.

Studying the downstream effects of cardiac innervation. Sympathetic nerve activity and circulating catecholamines are activators of the cardiac β-adrenergic receptor, causing intracellular production of cyclic AMP and PKA-mediated phosphorylation of proteins that subsequently leads to increased heart rate, stronger contractions and faster relaxation of the heart and shortening of the cardiac action potential. FRET sensors detecting cAMP and cGMP have been used to study cardiac adrenergic receptors and their downstream signalling, and are discussed below.

cAMP. Intracellular cAMP/PKA signalling is known to be organised into spatial microdomains.[33] Utilising a transgenic mouse expressing the cAMP sensor HCN2-camps, Nikolaev et al. were able to further specify the contributions of β1 and β2 adrenoceptors[34]: stimulation of β1 adrenoceptors caused a rise in cAMP throughout the cardiomyocyte, while β2 adrenoceptor stimulation caused only a very local increase in cAMP. In another study, the lipid raft protein caveolin-3 was demonstrated to be important for function of β2 adrenergic receptors, by confining β2-AR to the T-tubules it ensures cAMP production upon β2-AR stimulation.[35]

Faster relaxation of the heart upon sympathetic stimulation is the result of enhanced SERCA activity, which pumps Ca^{2+} from the cytoplasm into the sarcoplasmatic reticulum. By targeting Epac1 to SERCA2a through fusion of the sensor with full length phospholamban (PLN), Sprenger et al. were able to demonstrate that SERCA2a and β1-adrenoreceptors communicate via a microdomain that is defined by phosphodiesterase 4 (PDE4) activity.[36] Interestingly, transverse aortic constriction disturbed the communication between the β1-adrenoceptor and SERCA2a

because PDE4 localisation was disturbed, leading to overflow of cAMP beyond the microdomain.

Linking membrane potential to intracellular signalling, a recent study demonstrated that enhancing late Na^+ current in atrial cardiomyocytes induces cAMP production by triggering adenylyl cyclase activity through a Ca^{2+}-dependent mechanism[37], giving insight in a proarrhythmic mechanism that could not have been revealed without an optogenetic sensor.

cGMP. Cardiac remodelling in disease often involves multiple organ systems interacting via circulating hormones, for example the atrial natriuretic factor (ANF) which is released by the atria in response to volume overload.[38] In cardiomyocytes, ANF triggers a cGMP-mediated anti-hypertrophic pathway.[39] cGMP levels can be estimated by measuring cyclic nucleotide gated ion currents, but this approach will only report on subsarcolemmal cGMP levels, and is not feasible in vivo as it requires patch clamp electrophysiology.

In their recent study, Götz et al. employed a transgenic mouse expressing the genetically encoded cGMP sensor red cGES-DE5 to provide a first insight in cGMP signalling in intact adult cardiomyocytes.[40] Basal levels of cGMP are very low in cardiomyocytes (about 10 nM) and can be strongly stimulated by C-type natriuretic peptide and ANF. The resting levels are mostly determined by cGMP generation by NO-sensitive guanylyl cyclases and cGMP degradation by PDE3. After giving the mice a hypertrophic stimulus (mild aortic constriction), PDE5 activity had a greater effect on cGMP levels. Targeting of cGMP sensors to the plasma membrane may give more insight in the importance of particulate versus NO-sensitive GCs.

Concluding, optogenetic cGMP sensors can give novel insights in this important pathophysiological signalling pathway, potentially also in in vivo experiments.

PKA activity. Changed cAMP levels influence the activity of PKA, altering ion channel phosphorylation and function, which is an important mechanism by which the sympathetic nerve system increases heart rate when needed. Direct confirmation of this important mechanism was provided in a recent study using the PKA activity sensor AKAR3.[41] The authors found that interventions that increase cAMP levels in sinoatrial node cardiomyocytes cause increased PKA activity, and that the kinetics and magnitude of the PKA activation underlie increases in beating rate.

Using a variant of AKAR3 fused to phospholamban, SR-AKAR3, Liu et al. investigated β-adrenergic regulation of PKA activity at the SR. Interestingly, the authors found that β-adrenoceptor stimulation with isoproterenol had stronger effects on PKA activity than forskolin or 8-bromo-cAMP, both in neonatal and adult cardiomyocytes[33], suggesting highly localised signalling between the receptor and the SR.

3.3 Optogenetic sensors to detect membrane potential

Like calcium sensors, genetically encoded sensors of membrane potential or GEVIs (genetically encoded voltage indicators) have improved greatly during recent years. The key work in this field

was mainly motivated by the use in neuroscience. Application of GEVIs in the cardiac field started soon afterwards but remained limited to a few studies.[42,43] Existing GEVIs fall into two main classes. One class is based on the bacterial rhodopsin to detect changes in voltage, while the second class relies on a voltage-sensing domain (VSD) derived from voltage-sensing proteins. The fluorescent component of GEVIs often consists of single GFP or the CFP-YFP FRET pair, but other colours have also been reported. An overview of current GEVIs with their main characteristics can be found in Table 1 and in Antic et al.[44]

Clinically used drugs can trigger serious undesirable actions, with one of the most life-threatening responses being cardiac arrhythmias. Many pro-arrhythmic drugs affect the heart directly, but may also influence the heart indirectly through the autonomic nervous system or by activating other physiological mechanisms. Therefore, an in vivo approach is required to gain insight in the full effects that pro-arrhythmic drugs may have on cardiac function. In 2010, Tsutsui et al. reported a novel transgenic zebrafish line with myocardial Mermaid expression, a ratiometric GEVI, in which they were able to measure physiological membrane voltage dynamics in unanesthetized and unrestrained zebrafish embryos. To test the effect of hERG inhibitors on cardiac electrophysiology, embryos were treated with Astemizole. Severe cardiac abnormalities were observed, including a complete absence of ventricular contraction. When performing voltage imaging, it was found that electrical activation first appeared near the atrium–ventricle border and then propagated backward into the atrium, demonstrating in a detailed spatiotemporal manner how cardiac conduction was altered.[45] Models like the Mermaid zebrafish could, thus, provide important new cardiac drug-testing tools.

In addition to their use in drug testing, GEVIs offer the unique possibility to gain more insight into (patho)physiological mechanisms of cardiac conduction, both in the developing and adult heart. Recently, Chang-Liao et al. established a stable-transgenic VSFP2.3 mouse model with cardiac specific expression. In vitro experiments on isolated cardiomyocytes and Langendorff-perfused hearts confirmed that sensor recordings reflected cardiac physiology. To record in vivo action potentials, a minimally invasive fibre optic imaging was developed, in which optical fibres were connected to two high-speed cameras. FRET signals where measured in sedated mice treated without and with blebbistatin, which uncouples excitation and contraction. Interestingly, clear and corresponding signals were identified in both groups indicating that this approach is suitable to study cardiac conduction in the presence of normal contraction and blood perfusion.[42]

Ongoing work in our laboratory demonstrates that VSFP2.3 and the newer VSFP-Butterfly CY can also successfully be expressed and analysed in zebrafish hearts (unpublished data).

The Mermaid zebrafish line and the VSFP2.3 mouse line demonstrate an important proof of principle and provide evidence for the high potential of GEVIs in cardiac research. In contrast to GECIs that have been developed to a stage where fundamental improvements in performance are neither likely nor required for most experimental designs, development of GEVIs is still in a very active phase. To resolve action potentials, ideal membrane potential sensors have to generate robust signals on a millisecond timescale and have optimal targeting to the plasma membrane.

The latest sensors, with improved signal-to-noise ratio and improved kinetics, include VSFP-Butterfly, ASAP1, VSFP-CR, ArchLight, FlicR1 and the FRET-based Arch, Mac and Ace opsins QuasAr eFRET, MacQ eFRET and Ace2N-mNeon (also see Table 1). All are viable candidates for the use in cardiac experiments.

4. In vivo cardiac imaging: challenges and potential solutions

Application of optogenetic sensors in in vitro experiments has already yielded insights that could not have been obtained otherwise. Yet, moving towards using optogenetic sensors in vivo is even more exciting as it will allow us to study cardiac remodelling in the most realistic setting: as an interaction between heart, brain and kidneys. Ideally, application of optogenetic sensors is combined with optogenetic actuators to, e.g., pace the heart at specific locations, or influence protein–protein interactions.[4-6,46,47] Successful use of optogenetic sensors in vivo requires novel approaches in imaging to deal with the continuous movement and contraction of the heart (see figure 3).

4.1. Compensating for myocardial contraction using ratiometric imaging

A tried and tested technique of dealing with cardiac contraction that works well ex vivo is to use ratiometric imaging. In this approach, fluorescent indicators are used that report on the physiological parameter of interest by emitting fluorescence at two wavelengths. Since movement and contractions will affect the fluorescence output equally at the two wavelengths the ratio of the fluorescence intensities at the two wavelengths is therefore, at least theoretically, independent of movement/contraction related indicator signal components. This “rationing” approach is challenging in terms of optical instrumentation since it requires simultaneous imaging at two wavelengths.

Classical examples include FRET dyes like Fura-2 or indo-1, but ratiometric imaging can also be applied to optogenetic sensors, like the FRET sensors Twitch, TN-XL or VSFP2.3. A very interesting approach is to directly fuse a high signal-to-noise optogenetic sensor to a non-sensing fluorescent protein with a different emission wavelength, such as GCaMP-GR.[19]

4.2. Optical fibers

During the cardiac cycle, the heart contracts but also rotates, making registration of the site of recording very challenging, even during an ex vivo, Langendorff-perfused experiment. Several labs have used optical fibres to locally record fluorescent emission of dyes or optogenetic sensors. The key benefit of such fibres is their flexibility and small sizes (down to 100 µm or less). Making use of the flexibility of small fibres, our group recently made recordings of calcium transients in vivo, without opening the thorax.[48] By inserting a 250 µm optical fibre through the carotid artery, it was possible to advance the fibre into the left ventricle and record endocardial calcium transients from

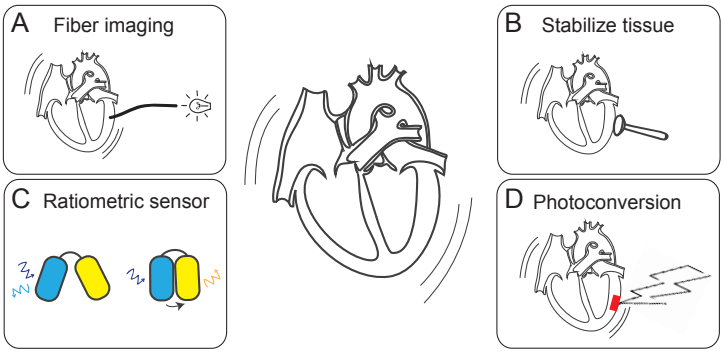

Figure 3. Solutions for cardiac movement artefacts. Solutions for cardiac movement artefacts. (A) Optical fibres are flexible and small, thus allowing the local recording of fluorescence even when movement occurs. The fibre ending is directly positioned against the cardiac tissue. (B) When studies are not limited by opening of the thorax, physical immobilisation of cardiac tissue can be achieved by attaching a rigid ring and applying a gentle vacuum. (C) Ratiometric imaging allows compensation of contraction related increases in fluorescence intensity, since it affects the intensities of both the donor and acceptor fluorophore the same. (D) Photoconversion can be used to convert specific cardiac regions and track these during contraction

transgenic mice overexpressing GCaMP3.

4.3. Immobilisation of the heart

Studies that are not limited by opening of the thorax can benefit from the approaches developed to stabilise the heart in situ. [49-51] The principle of their device is very similar to that of the Octopus heart stabiliser used for human cardiac surgery. Attaching a rigid ring to the heart, either using adhesives or a gentle vacuum, contraction and movement of a small region of the heart is minimised, enabling imaging in living animals. The mechanical stabilisation is combined with electrocardiogram-based triggering, i.e., images are acquired during a selected phase of the cardiac cycle in which the tissue is most stable. While this approach has great potential for in vivo physiology, it is probably not suited for lengthy data acquisition as the tissue may be damaged by prolonged stabilisation.

4.4. Using photoconvertible optogenetic sensors as intrinsic landmarks to track tissue movement.

Dealing with the continuous movement of the heart remains a big challenge, despite the available techniques mentioned above. Especially tracking of a region of interest throughout the cardiac cycle is problematic, the vasculature of the heart can be used as a set of landmarks, but still it is difficult to follow regions. To solve this, extrinsic landmarks can be applied, for instance by injecting black ink into the myocardium, or spraying paint on the heart.

The advent of photoconvertible and photoactivatable calcium sensors enables an attractive alternative approach.[52] The photoconvertible sensors GR-GECO1.1 and GR-GECO1.2 can be

converted from a green emission calcium sensor into a green and red emission calcium sensor by exposure to ~400 nm light. Similarly, the photoactivatable sPA-GCaMP6 emits very little green light, until it is activated by ~400 nm light, after which it will emit green light to report cytoplasmic calcium concentration. Using such sensors, it would be possible to create intrinsic landmarks within the myocardium, which could be very small, down to the size of a single cardiomyocyte. But also for larger regions that have been converted into a landmark, this approach has several benefits. As the shape of the landmark that has been created is known, tracking movement of that specific region is simplified as one only needs to track the boundaries or pattern of the landmark region. Using this information, it should also be possible to use deformation of the boundaries during contraction to correct for contraction artefacts.

Conclusion

Application of optogenetic sensors in cardiac research has only just started. The results from the first studies are exciting, and have provided insights that could not have been obtained by conducting experiments using traditional organic dyes. Especially, the ability to target optogenetic sensors to subcellular regions is expected to provide us with many new mechanistic insights in cardiomyocyte physiology.

Small steps have been made towards application of optogenetic sensors in vivo. Further development of this approach will require optimisation of recording strategies. Especially, the continuous movement and contraction of the heart provide a challenge that is not present in other tissues. Anticipated benefits of in vivo optogenetics are the ability to perform longitudinal studies in individual animals, and importantly the possibility to study cardiomyocyte physiology within the context of whole-body physiology.

Acknowledgements

We acknowledge the support from The Netherlands Cardio Vascular Research Initiative: the Dutch Heart Foundation, Dutch Federation of University Medical Centres, the Netherlands Organisation for Health Research and Development and the Royal Netherlands Academy of Sciences (CVON-PREDICT). W. H. Z. is supported by the DZHK (German Center for Cardiovascular Research), the German Federal Ministry for Science and Education (13GW0007A [CIRM-ET3]), the German Research Foundation (DFG ZI 708/10-1; SFB 937 TP18, SFB 1002 TPs C04, S1; IRTG 1618 RP12) and the Leducq Foundation Transatlantic Network of Excellence (14CVD04).

Conflict of interest

On behalf of all authors, the corresponding author states that there is no conflict of interest.

References

1. Miesenbock G. The Optogenetic Catechism. *Science* 2009 Oct 15;326(5951):395–9.
2. Dombeck DA, Harvey CD, Tian L, Looger LL, Tank DW. Functional imaging of hippocampal place cells at cellular resolution during virtual navigation. *Nat Neurosci* 2010 Oct 3;13(11):1433–40.
3. Mank M, Santos AF, Direnberger S, Mrsic-Flogel TD, Hofer SB, Stein V, et al. A genetically encoded calcium indicator for chronic in vivo two-photon imaging. *Nat Meth* 2008 Sep;5(9):805–11.
4. Ambrosi CM, Klimas A, Yu J, Entcheva E. Cardiac applications of optogenetics. *Prog Biophys Mol Biol* 2014 Aug;115(2-3):294–304.
5. Boyle PM, Karathanos TV, Trayanova NA. "Beauty is a light in the heart": the transformative potential of optogenetics for clinical applications in cardiovascular medicine. *Trends Cardiovasc Med* 2015 Feb;25(2):73–81.
6. Crocini C, Ferrantini C, Pavone FS, Sacconi L. Optogenetics gets to the heart: A guiding light beyond defibrillation. *Prog Biophys Mol Biol* 2017 Nov;130(Pt B):132–9.
7. Zhao Y, Zhao Y, Araki S, Araki S, Wu J, Wu J, et al. An Expanded Palette of Genetically Encoded Ca^{2+} Indicators. *Science* 2011 Sep 29;333(6051):1888–91.
8. Lam AJ, St-Pierre F, Gong Y, Marshall JD, Cranfill PJ, Baird MA, et al. Improving FRET dynamic range with bright green and red fluorescent proteins. *Nature Meth* 2012 Oct; 9(10):1005-12
9. Alford SC, Wu J, Zhao Y, Campbell RE, Knöpfel T. Optogenetic reporters. *Biol Cell* 2013 Jan;105(1):14–29.
10. Knöpfel T. Genetically encoded optical indicators for the analysis of neuronal circuits. *Nat Rev Neurosci* 2012 Oct;13(10):687–700.
11. Yoshiyuki Yamada KM, Yamada Y, Mikoshiba K. Quantitative comparison of novel GCaMP-type genetically encoded Ca^{2+} indicators in mammalian neurons. *Front Cell Neurosci* 2012 Oct;6:41.
12. Tallini YN, Tallini YN, Ohkura M, Ohkura M, Choi BR, Choi BR, et al. Imaging cellular signals in the heart in vivo: Cardiac expression of the high-signal Ca^{2+} indicator GCaMP2. *Proc Natl Acad Sci U.S.A*. 2006 Mar;103(12):4753–8.
13. Tallini YN, Tallini YN, Brekke JF, Brekke JF, Shui B, Shui B, et al. Propagated Endothelial Ca^{2+} Waves and Arteriolar Dilation In Vivo: Measurements in Cx40BAC GCaMP2 Transgenic Mice. *Circ Res* 2007 Dec;101(12):1300–9.
14. Shiba Y, Fernandes S, Zhu W-Z, Filice D, Muskheli V, Kim J, et al. Human ES-cell-derived cardiomyocytes electrically couple and suppress arrhythmias in injured hearts. *Nature* 2012 Aug;489(7415):322–5.
15. Shang W, Shang W, Lu F, Lu F, Sun T, Sun T, et al. Imaging Ca^{2+} Nanosparks in Heart With a New Targeted Biosensor. *Circ Res* 2014 Jan;114(3):412–20.
16. Akerboom J, Carreras Calderón N, Tian L, Wabnig S, Prigge M, Tolö J, et al. Genetically encoded calcium indicators for multi-color neural activity imaging and combination with optogenetics. *Front Mol Neurosci* 2013;6:2.
17. Inoue M, Takeuchi A, Horigane S-I, Ohkura M, Gengyo-Ando K, Fujii H, et al. Rational design of a high-affinity, fast, red calcium indicator R-CaMP2. *Nat Meth* 2014 Nov;12(1):64–70.
18. Ohkura M, Sasaki T, Kobayashi C, Ikegaya Y, Nakai J. An Improved Genetically Encoded Red Fluorescent Ca^{2+} Indicator for Detecting Optically Evoked Action Potentials. Sensi SL, editor. *PLoS ONE* 2012 Jul;7(7):e39933.
19. Shui B, Lee JC, Reining S, Lee FK, Kotlikoff MI. Optogenetic sensors and effectors: CHROMus - the Cornell Heart Lung Blood Institute Resource for Optogenetic Mouse Signaling. *Front Physiol* 2014 Nov;5:428.

20. Bonnot A, Guiot E, Hepp R, Cavellini L, Tricoire L, Lambolez B. Single-fluorophore biosensors based on conformation-sensitive GFP variants. *FASEB J* 2014 Mar;28(3):1375–85.
21. Perron A, Mutoh H, Akemann W, Gautam SG, Dimitrov D, Iwamoto Y, et al. Second and third generation voltage-sensitive fluorescent proteins for monitoring membrane potential. *Front Mol Neurosci* 2009;2:5.
22. Baartscheer A, Schumacher CA, van Borren MMGJ, Belterman CNW, Coronel R, Fiolet JWT. Increased Na^+/H^+-exchange activity is the cause of increased $[Na^+]_i$ and underlies disturbed calcium handling in the rabbit pressure and volume overload heart failure model. *Cardiovasc Res* 2003 Mar;57(4):1015–24.
23. van Borren MMGJ, Vos MA, Houtman MJC, Antoons G, Ravesloot JH. Increased sarcolemmal $Na(^+)/H(^+)$ exchange activity in hypertrophied myocytes from dogs with chronic atrioventricular block. *Front Physiol* 2013;4:322.
24. Verdonck F, Volders PGA, Vos MA, Sipido KR. Increased Na^+ concentration and altered Na/K pump activity in hypertrophied canine ventricular cells. *Cardiovasc Res* 2003 Mar;57(4):1035–43.
25. Doyon N, Vinay L, Prescott SA, De Koninck Y. Chloride Regulation: A Dynamic Equilibrium Crucial for Synaptic Inhibition. *Neuron* 2016 Mar;89(6):1157–72.
26. Duan D-Y, Liu LLH, Bozeat N, Huang ZM, Xiang SY, Wang GL, et al. Functional role of anion channels in cardiac diseases. *Acta Pharmacol Sin* 2005 Mar;26(3):265–78.
27. de Baaij JHF, Hoenderop JGJ, Bindels RJM. Magnesium in man: implications for health and disease. *Physiol Rev* 2015 Jan;95(1):1–46.
28. Alexanian I, Parissis J, Farmakis D, Athanaselis S, Pappas L, Gavrielatos G, et al. Clinical and echocardiographic correlates of serum copper and zinc in acute and chronic heart failure. *Clin Res Cardiol* 2014 Nov;103(11):938–49.
29. Erickson JR, Patel R, Ferguson A, Bossuyt J, Bers DM. Fluorescence Resonance Energy Transfer–Based Sensor Camui Provides New Insight Into Mechanisms of Calcium/Calmodulin-Dependent Protein Kinase II Activation in Intact Cardiomyocytes. *Circ Res* 2011 Sep 16;109(7):729–38.
30. Zarain-Herzberg A, Fragoso-Medina J, Estrada-Avilés R. Calcium-regulated transcriptional pathways in the normal and pathologic heart. López-Casillas F, Vázquez-Prado J, editors. *IUBMB Life* 2011 Oct;63(10):847–55.
31. Newman R, Zhang J. Visualization of phosphatase activity in living cells with a FRET-based calcineurin activity sensor. *Mol Biosyst* 2008 June;4(6):496–501.
32. Mehta S, Aye-Han N-N, Ganesan A, Oldach L, Gorshkov K, Zhang J. Calmodulin-controlled spatial decoding of oscillatory Ca^{2+} signals by calcineurin. *Elife* 2014 Jul;3:e03765.
33. Liu S, Zhang J, Xiang YK. FRET-based direct detection of dynamic protein kinase A activity on the sarcoplasmic reticulum in cardiomyocytes. *Biochem Biophys Res Commun* 2011 Jan 14;404(2):581–6.
34. Nikolaev VO, Bünemann M, Schmitteckert E, Lohse MJ, Engelhardt S. Cyclic AMP imaging in adult cardiac myocytes reveals far-reaching beta1-adrenergic but locally confined beta2-adrenergic receptor-mediated signaling. *Circ Res* 2006 Nov;99(10):1084–91.
35. Wright PT, Nikolaev VO, O'Hara T, Diakonov I, Bhargava A, Tokar S, et al. Caveolin-3 regulates compartmentation of cardiomyocyte beta2-adrenergic receptor-mediated cAMP signaling. *J Mol Cell Cardiol* 2014 Feb;67:38–48.
36. Sprenger JU, Perera RK, Steinbrecher JH, Lehnart SE, Maier LS, Hasenfuss G, et al. In vivo model with targeted cAMP biosensor reveals changes in receptor-microdomain communication in cardiac disease. *Nat Commun* 2015 Apr;6:6965.

37. Fischer TH, Herting J, Mason FE, Hartmann N, Watanabe S, Nikolaev VO, et al. Late I_{Na} increases diastolic SR-Ca^{2+}-leak in atrial myocardium by activating PKA and CaMKII. *Cardiovasc Res* 2015 Jul 1;107(1):184–96.
38. de Bold AJ. Atrial natriuretic factor: a hormone produced by the heart. *Science* 1985 Nov;230(4727):767–70.
39. Nishikimi T, Maeda N, Matsuoka H. The role of natriuretic peptides in cardioprotection. *Cardiovasc Res* 2006 Feb;69(2):318–28.
40. Gotz KR, Götz KR, Sprenger JU, Sprenger JU, Perera RK, Perera RK, et al. Transgenic Mice for Real-Time Visualization of cGMP in Intact Adult Cardiomyocytes. *Circ Res* 2014 Apr;114(8):1235–45.
41. Yaniv Y, Ganesan A, Yang D, Ziman BD, Lyashkov AE, Levchenko A, et al. Real-time relationship between PKA biochemical signal network dynamics and increased action potential firing rate in heart pacemaker cells: Kinetics of PKA activation in heart pacemaker cells. *J Mol Cell Cardiol* 2015 Sep;86:168–78.
42. Liao MLC, de Boer TP, Mutoh H, Raad N, Richter C, Wagner E, et al. Sensing Cardiac Electrical Activity With a Cardiac Myocyte–Targeted Optogenetic Voltage Indicator. *Circ Res* 2015 Aug;117(5):401–12.
43. Liao MLC, Mutoh H, Iwamoto Y, Raad N, Nikolaev V, Luther S, et al. Voltage Sensitive Protein 2.3: A Novel Tool to Study Sarcolemmal Structure and Electrical Activity in Mouse Hearts. *Biophysj* 2011 Feb 2;100(S1):575a–576a.
44. Antic SD, Empson RM, Knöpfel T. Voltage imaging to understand connections and functions of neuronal circuits. *J Neurophysiol* 2016 Jul 1;116(1):135–52.
45. Tsutsui H, Higashijima S-I, Miyawaki A, Okamura Y. Visualizing voltage dynamics in zebrafish heart. *J Physiol* 2010 Jun;588(Pt 12):2017–21.
46. Bruegmann T, Malan D, Hesse M, Beiert T, Fuegemann CJ, Fleischmann BK, et al. Optogenetic control of heart muscle in vitro and in vivo. *Nat Meth*; 2010 Nov;7(11):897–900.
47. van Bergeijk P, Hoogenraad CC, Kapitein LC. Right Time, Right Place: Probing the Functions of Organelle Positioning. *Trends Cell Biol* 2016 Feb;26(2):121–34.
48. L M, van Asten I, MSC F, van Stuijvenberg L, van Veen TAB, M V, et al. Optogenetic Monitoring of Endocardial Calcium Transients in vivo Using a Minimally Invasive Fiber Optic Approach. *Circulation* 2015;(132):A13976.
49. Aguirre AD, Vinegoni C, Sebas M, Weissleder R. Intravital imaging of cardiac function at the single-cell level. *Proc Natl Acad Sci U.S.A*. 2014 Aug;111(31):11257–62.
50. Lee S, Vinegoni C, Feruglio PF, Fexon L, Gorbatov R, Pivoravov M, et al. Real-time in vivo imaging of the beating mouse heart at microscopic resolution. *Nat Commun* 2012;3(1):1054.
51. Vinegoni C, Lee S, Aguirre AD, Weissleder R. New techniques for motion-artifact-free in vivo cardiac microscopy. *Front Physiol* 2015;6:147.
52. Hoi H, Matsuda T, Nagai T, Campbell RE. Highlightable Ca^{2+} Indicators for Live Cell Imaging. *J Am Chem Soc* 2013 Jan;135(1):46–9.
53. Jin L, Han Z, Platisa J, Wooltorton JRA, Cohen LB, Pieribone VA. Single action potentials and subthreshold electrical events imaged in neurons with a fluorescent protein voltage probe. *Neuron* 2012 Sep;75(5):779–85.
54. Lundby A, Mutoh H, Dimitrov D, Akemann W, Knöpfel T. Engineering of a genetically encodable fluorescent voltage sensor exploiting fast Ci-VSP voltage-sensing movements. *PLoS ONE* 2008;3(6):e2514.
55. Tsutsui H, Karasawa S, Okamura Y, Miyawaki A. Improving membrane voltage measurements using FRET with new fluorescent proteins. *Nat Meth* 2008 Aug;5(8):683–5.
56. Kaestner L, Scholz A, Tian Q, Ruppenthal S, Tabellion W, Wiesen K, et al. Genetically encoded Ca^{2+} indicators in

cardiac myocytes. *Circ Res* 2014 May;114(10):1623–39.

57. Mishina Y, Mutoh H, Song C, Knöpfel T. Exploration of genetically encoded voltage indicators based on a chimeric voltage sensing domain. *Front Mol Neurosci*; 2014;7:78.
58. Chen Z, Xian W, Bellin M, Dorn T, Tian Q, Goedel A, et al. Subtype-specific promoter-driven action potential imaging for precise disease modelling and drug testing in hiPSC-derived cardiomyocytes. *Eur Heart J* 2017 Jan ;38(4):292–301.
59. St-Pierre F, Marshall JD, Yang Y, Gong Y, Schnitzer MJ, Lin MZ. High-fidelity optical reporting of neuronal electrical activity with an ultrafast fluorescent voltage sensor. *Nat Neurosci* 2014 Jun;17(6):884–9.
60. Zou P, Zhao Y, Douglass AD, Hochbaum DR, Brinks D, Werley CA, et al. Bright and fast multicoloured voltage reporters via electrochromic FRET. *Nat Commun* 2014;5:4625.
61. Gong Y, Wagner MJ, Zhong Li J, Schnitzer MJ. Imaging neural spiking in brain tissue using FRET-opsin protein voltage sensors. *Nat Commun* 2014;5:3674.
62. Gong Y, Huang C, Li JZ, Grewe BF, Zhang Y, Eismann S, et al. High-speed recording of neural spikes in awake mice and flies with a fluorescent voltage sensor. *Science* 2015 Dec;350(6266):1361–6.
63. Abdelfattah AS, Farhi SL, Zhao Y, Brinks D, Zou P, Ruangkittisakul A, et al. A Bright and Fast Red Fluorescent Protein Voltage Indicator That Reports Neuronal Activity in Organotypic Brain Slices. *J Neurosci* 2016 Feb;36(8):2458–72.
64. Wiencierz AM, Kernbach M, Ecklebe J, Monnerat G, Tomiuk S, Raulf A, et al. Differential Expression Levels of Integrin α6 Enable the Selective Identification and Isolation of Atrial and Ventricular Cardiomyocytes. *PLoS ONE* 2015;10(11):e0143538.
65. Chen T-W, Wardill TJ, Sun Y, Pulver SR, Renninger SL, Baohan A, et al. Ultrasensitive fluorescent proteins for imaging neuronal activity. *Nature* 2013 Jul 18;499(7458):295–300.
66. Griesbeck O, Baird GS, Campbell RE, Zacharias DA, Tsien RY. Reducing the environmental sensitivity of yellow fluorescent protein. Mechanism and applications. *J Biol Chem* 2001 Aug;276(31):29188–94.
67. Heim N, Griesbeck O. Genetically encoded indicators of cellular calcium dynamics based on troponin C and green fluorescent protein. *J Biol Chem* 2004 Apr;279(14):14280–6.
68. Hessels AM, Chabosseau P, Bakker MH, Engelen W, Rutter GA, Taylor KM, et al. eZinCh-2: A Versatile, Genetically Encoded FRET Sensor for Cytosolic and Intraorganelle Zn($^{2+}$) Imaging. *ACS Chem Biol* 2015 Sep;10(9):2126–34.
69. Koay MS, Janssen BMG, Merkx M. Tuning the metal binding site specificity of a fluorescent sensor protein: from copper to zinc and back. *Dalton Trans* 2013 Mar 7;42(9):3230–2.
70. Kuner T, Augustine GJ. A genetically encoded ratiometric indicator for chloride: capturing chloride transients in cultured hippocampal neurons. *Neuron* 2000 Sep;27(3):447–59.
71. Lindenburg LH, Vinkenborg JL, Oortwijn J, Aper SJA, Merkx M. MagFRET: the first genetically encoded fluorescent Mg^{2+} sensor. *PLoS ONE* 2013;8(12):e82009.
72. Markova O, Mukhtarov M, Real E, Jacob Y, Bregestovski P. Genetically encoded chloride indicator with improved sensitivity. *J Neurosci Methods* 2008 May;170(1):67–76.
73. Miyawaki A, Llopis J, Heim R, McCaffery JM, Adams JA, Ikura M, et al. Fluorescent indicators for Ca^{2+} based on green fluorescent proteins and calmodulin. *Nature* 1997 Aug;388(6645):882–7.
74. Nagai T, Sawano A, Park ES, Miyawaki A. Circularly permuted green fluorescent proteins engineered to sense

Ca^{2+}. *Proc Natl Acad Sci U.S.A.* 2001 Mar;98(6):3197–202.

75. Souslova EA, Belousov VV, Lock JG, Strömblad S, Kasparov S, Bolshakov AP, et al. Single fluorescent protein-based Ca^{2+} sensors with increased dynamic range. *BMC Biotechnol* 2007 Jun 29;7(1):37.
76. Vinkenborg JL, Nicolson TJ, Bellomo EA, Koay MS, Rutter GA, Merkx M. Genetically encoded FRET sensors to monitor intracellular Zn^{2+} homeostasis. *Nat Meth* 2009 Oct;6(10):737–40.
77. Allen MD, Zhang J. Subcellular dynamics of protein kinase A activity visualized by FRET-based reporters. *Biochem Biophys Res Commun* 2006 Sep 22;348(2):716–21.
78. Niino Y, Hotta K, Oka K. Simultaneous live cell imaging using dual FRET sensors with a single excitation light. *PLoS ONE* 2009 Jun;4(6):e6036.
79. Takao K, Okamoto KI, Nakagawa T, Neve RL, Nagai T, Miyawaki A, et al. Visualization of synaptic Ca^{2+}/calmodulin-dependent protein kinase II activity in living neurons. *J Neurosci* 2005 Mar;25(12):3107–12.

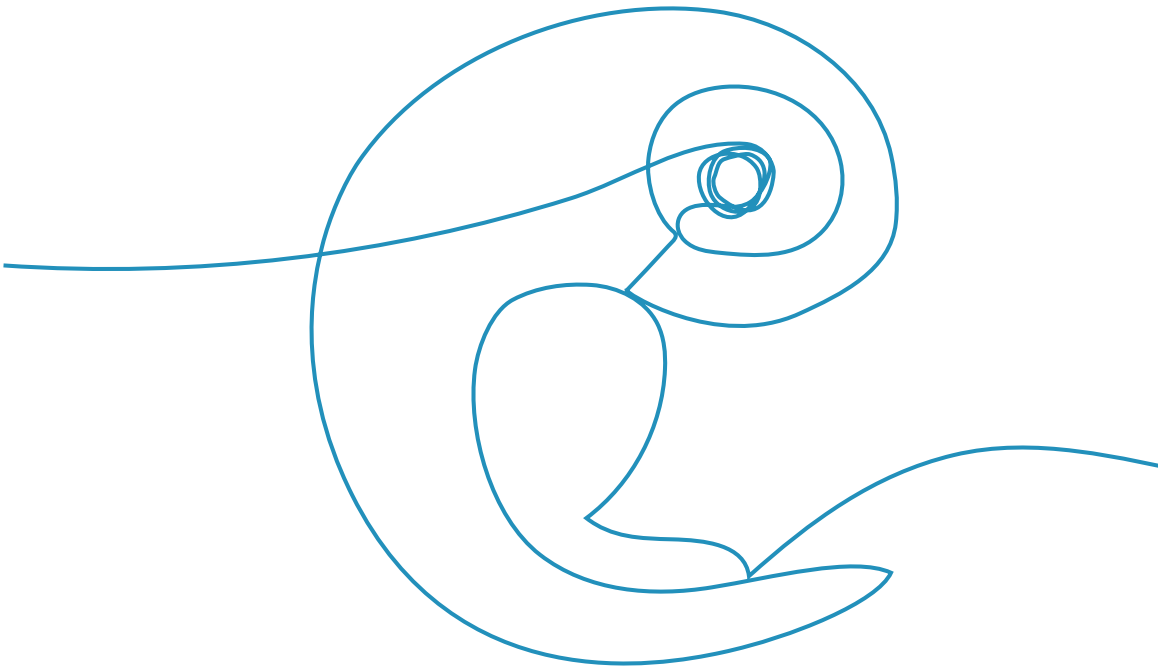

CHAPTER 3

Optogenetic sensors in the zebrafish heart: a novel in vivo electro-physiological tool to study cardiac arrhythmogenesis

Chantal J.M. van Opbergen*, Charlotte D. Koopman*, Bart J.M. Kok, Thomas Knöpfel, Sabine L. Renninger, Michael B. Orger, Marc A. Vos, Toon A.B. van Veen, Jeroen Bakkers#, Teun P. de Boer#

*# contributed equally

Theranostics 2018;8(17):4750-4764

Abstract

Cardiac arrhythmias are among the most challenging human disorders to diagnose and treat due to their complex underlying pathophysiology. Suitable experimental animal models are needed to study the mechanisms causative for cardiac arrhythmogenesis. To enable in vivo analysis of cardiac cellular electrophysiology with a high spatial and temporal resolution, we generated and carefully validated two zebrafish models, one expressing an optogenetic voltage indicator (chimeric VSFP-butterfly CY) and the other a genetically encoded calcium indicator (GCaMP6f) in the heart.

Methods. High-speed epifluorescence microscopy was used to image chimeric VSFP-butterfly CY and GCaMP6f in the embryonic zebrafish heart, providing information about the spatiotemporal patterning of electrical activation, action potential configuration and intracellular Ca^{2+} dynamics. Plotting VSFP or GCaMP6f signals on a line along the myocardial wall over time facilitated the visualization and analysis of electrical impulse propagation throughout the heart. Administration of drugs targeting the sympathetic nervous system or cardiac ion channels was used to validate sensitivity and kinetics of both zebrafish sensor lines. Using the same microscope setup, we imaged transparent juvenile casper fish expressing GCaMP6f, demonstrating the feasibility of imaging cardiac optogenetic sensors at later stages of development.

Results. Isoproterenol slightly increased heart rate, diastolic Ca^{2+} levels and Ca^{2+} transient amplitudes, whereas propranolol caused a profound decrease in heart rate and Ca^{2+} transient parameters in VSFP-Butterfly and GCaMP6f embryonic fish. I_{kr} blocker E-4031 decreased heart rate and increased action potential duration in VSFP-Butterfly fish. $I_{Ca,L}$ blocker nifedipine caused total blockade of Ca^{2+} transients in GCaMP6f fish and a reduced heart rate, altered ventricular action potential duration and disrupted atrial-ventricular electrical conduction in VSFP-Butterfly fish. Imaging of juvenile animals demonstrated the possibility of employing an older zebrafish model for in vivo cardiac electrophysiology studies. We observed differences in atrial and ventricular Ca^{2+} recovery dynamics between 3 dpf and 14 dpf casper fish, but not in Ca^{2+} upstroke dynamics.

Conclusion By introducing the optogenetic sensors chimeric VSFP-butterfly CY and GCaMP6f into the zebrafish we successfully generated an in vivo cellular electrophysiological readout tool for the zebrafish heart. Complementary use of both sensor lines demonstrated the ability to study heart rate, cardiac action potential configuration, spatiotemporal patterning of electrical activation and intracellular Ca^{2+} homeostasis in embryonic zebrafish. In addition, we demonstrated the first successful use of an optogenetic sensor to study cardiac function in older zebrafish. These models present a promising new research tool to study the underlying mechanisms of cardiac arrhythmogenesis.

Keywords: Optogenetics, zebrafish, in vivo cardiac cellular electrophysiology, chimeric VSFP-butterfly CY, GCaMP6f.

Graphical Abstract

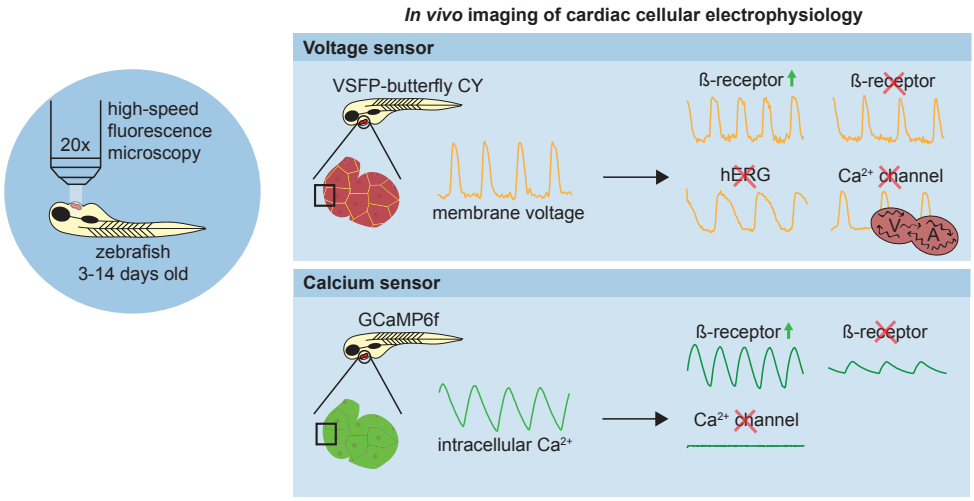

Introduction

Cardiac arrhythmias are among the most challenging human disorders to diagnose and treat due to their complex underlying pathophysiology. To fully understand arrhythmogenic mechanisms, a detailed examination at the multicellular level within the context of the whole body is necessary. While human cardiac electrophysiology has been studied for decades, experimental (animal) models are pivotal to study cellular processes in depth. Unfortunately, as the heart is poorly accessible within a closed thoracic cavity, our current knowledge of cellular electrophysiology is mainly based on in vitro experiments using isolated hearts or cardiomyocytes. Therefore, the ability to conduct in vivo research would provide us remarkable insight into the complex interplay of the heart and other organs to maintain homeostasis.

Small rodent models, like mice and rats, are often used to analyze electrophysiological mechanisms of cardiac arrhythmias as they are affordable, highly available and can be genetically manipulated.[1] However, due to their high heart rates[2], small heart size, and significantly different action potential (AP) shape[3], use (or the application) of these models is usually limited to proof-of-principle studies that can later be extended into larger animal models.[1,4] Large animal models such as the dog, pig, sheep and goat, have hearts that are both anatomically and physiologically more similar to that of a human's. For this reason, large models are more suitable for pre-clinical studies to test safety and efficacy of novel therapies. However, the costs of using these animals are very high, the experimental procedures are complex, and there are more serious ethical concerns.[1] Furthermore, not all large-animal hearts are equally similar to the human heart, thereby reducing the clinical relevance of some disease models.[5] Ultimately, the choice of an animal model has to be determined for each study separately, as it will depend on the specific research goal which animal is most suitable.

During the past few decades, the zebrafish (Danio rerio) has emerged as a powerful, cost-efficient, and easy-to-use vertebrate model to study cardiovascular disease. Due to its optical accessibility, small size, genetic manipulability, rapid development, high offspring numbers, and the possibility of high-throughput chemical screenings, the zebrafish forms an important addition to the existing group of electrophysiological animal models.[6] This especially holds true for the use in high-throughput genotype-phenotype relation studies and in vivo studies. Even though zebrafish hearts have two chambers, their physiology resembles the human heart in multiple aspects.[7] Like mammals, zebrafish have functional pacemaker cells that initiate and regulate cardiac contraction[8,9] and spontaneous heart rates. Furthermore, the relationship between QT interval and heart rate are reported to be comparable to those found in a human.[10,11] In addition, zebrafish cardiac action potentials exhibit a similar shape to human action potentials, with a long plateau phase and substantial correspondence in ion currents.[10,12-14]

Optical mapping with fluorescent dyes has become a fundamental tool to study cardiac cellular electrophysiology and excitation-contraction coupling due to its high spatial and temporal resolution. Unfortunately, dyes are primarily optimized for in vitro experiments - for example, for

use in Langendorff perfused hearts - thereby removing the heart from its context within the body. In vivo experiments with dyes have been performed and are achievable[15,16], but the approaches are usually invasive (due to required surgery or high DMSO concentrations) and lack cell type specificity. Optogenetic sensors form an appealing alternative, as they can be genetically targeted to specific subsets of cells, have low phototoxicity and can be used for in vivo (longitudinal) studies.[17-19] Genetically encoded voltage indicators (GEVI's) and Ca^{2+} indicators (GECI's) are two groups of optogenetic sensors that allow the detection of membrane depolarization and intracellular Ca^{2+} dynamics respectively. To accurately reflect the short action potentials and Ca^{2+} fluxes in the heart, it is essential that optogenetic sensors have robust, high-resolution signals and fast kinetics. The novel voltage sensor Chimeric VSFP-butterfly CY (cyan-yellow: mCitrine/mCerulean) has unprecedented kinetics in comparison to earlier differential dual emission ("FRET'') voltage sensors like VSFP2.3 and Mermaid. Off kinetics in particular have improved vastly, allowing for an accurate reflection of action potential shape.[20] Similarly, the Ca^{2+} sensor GCaMP6f has excellent kinetics and was the first GCaMP sensor to surpass the sensitivity and speed of the classic synthetic Ca^{2+} dyes.[21]

Here we describe a novel cardiac voltage sensor zebrafish line, chimeric VSFP-butterfly CY, and the validation of this voltage sensor line together with a GCaMP6f Ca^{2+} sensor line to study cellular membrane voltage and intracellular Ca^{2+} dynamics in the heart in a spatiotemporal manner. We show that both chimeric VSFP-butterfly CY and GCaMP6f accurately reflect cardiac electrophysiology and that parallel use of these zebrafish lines provides a powerful tool to study in vivo excitation-contraction coupling and cardiac arrhythmogenesis in zebrafish. In addition, we demonstrate for the first time the possibility to perform in vivo imaging of cardiac optogenetic sensors in juvenile zebrafish.

Methods

Zebrafish husbandry

Fish used in this study were housed under standard conditions as previously described.[22] All experiments were conducted in accordance to the ethical guidelines and approved by the local ethics committee at the Royal Dutch Academy of Sciences (KNAW).

Development of transgenic zebrafish

To generate the *tg(myl7:chimeric VSFP-butterfly CY)* line (VSFP: voltage sensitive fluorescent protein), we first cloned the chimeric VSFP-butterfly sequence from its original vector pCAG-Chimeric_Butterfly_CY_1.0 (Addgene plasmid #59800) into pGEM-T easy using PCR-based cloning. After validation through sequencing, chimeric VSFP-butterfly was cloned into pCR8/GW/TOPO using EcoRI restriction. Multisite Gateway cloning was used to combine chimeric VSFP-butterfly CY (pME) with the cardiac-specific *myl7* promoter (p5E) and a SV40 late polyA signal (p3E) into

the pDestTol2pA (http://tol2kit.genetics.utah.edu) destination vector. To obtain transgenic zebrafish, wild-type Tupfel Long fin (TL) strain zebrafish embryos were injected with 1 nL of 100 ng/µL pDestTol2pA *myl7*:chimeric VSFP-butterfly CY and 24 ng/µL tol2 transposase mRNA at the 1-cell stage. Tol2 sequences flanking the expression cassette facilitated stable genomic integration (Kawakami 2007). Injected embryos (F0) were screened for mCitrine and mCerulean expression in the heart and grown to adulthood. The adult F0 generation was outcrossed to wild-type TL strain zebrafish and F1 embryos were screened for bright and homogeneous mCitrine and mCerulean expression in the heart to generate a stable *tg(myl7:chimeric-VSFP-butterfly-CY)* line.

To generate the UAS:GCaMP6f construct, ten repeats of the Upstream Activation Sequence (10x UAS), were placed upstream of GCaMP6f[21], in the Gateway destination vector pDestTol2pA, using Gateway LR recombination. 12 ng/µL plasmid DNA with 40 ng/µL Tol2 transposase mRNA and 0.02% Phenol Red was injected into 1-cell stage embryos. An outcrossed stable UAS:GCaMP6f line was crossed to *myl7*:Gal4FF fish, and progeny was screened for GCaMP6f expression in the heart to identify *tg(myl7:Gal4FF; UAS:GCaMP6f)* fish.

Confocal imaging

At 24 h post-fertilization (hpf), embryos were placed in 1-phenyl-2-thiourea (PTU) to keep them transparent. Embryos at 3 days post-fertilization (dpf) were treated with 40 µM of 2,3-Butanedione 2-monoxime (BDM) (Sigma-aldrich, B0753) dissolved in E3 containing 16 mg/mL Tricaine until the heart stopped beating. BDM was used in this experiment, since it is highly effective in blocking cardiac contraction, but was not used in any other experiments in this study due to its interference with cardiac electrophysiology. Subsequently, these embryos were embedded in 0.3% agarose (UltraPure agarose, Invitrogen) prepared in E3 medium containing 16 mg/mL Tricaine and a maintenance dose of 20 µM BDM. To establish expression patterns of chimeric VSFP-butterfly CY and GCaMP6f, recordings were performed at 20 °C using an inverted TCS SP8 confocal laser-scanning microscope (Leica microsystems, Germany) and a 20x objective. Images were processed using ImageJ (U. S. National Institutes of Health, Bethesda, Maryland, USA).

High-speed fluorescence imaging in embryos

A morpholino (MO) oligomer targeted against *tnnt2a* (5'-CATGTTTGCTCTGATCTGACACGCA-3') was used to uncouple contraction from excitation in embryos, thereby preventing contraction artifacts in our recordings of cardiac electrophysiology and Ca^{2+} dynamics. This 'silent heart' ATG morpholino was applied as described previously.[23] At 24 hpf, embryos were placed in PTU to keep them transparent. Embryos at 3 dpf were embedded in 0.3% agarose prepared in E3 medium containing 16 mg/mL Tricaine and placed in a heated (28 °C) recording chamber. Recordings were performed using a custom-build upright widefield microscope (Cairn research, Kent, UK) equipped with a 20x 1.0 NA objective (Olympus XLUMPLFLN20X W). White LED excitation light was filtered using a 438/24 nm filter (Semrock FF02-438/24-25) and reflected towards the objective using a 458 nm dichroic mirror (Semrock FF458-Di02-25x36). Emitted fluorescence

was directed to an emission splitter unit (OptoSplit II ByPass Image Splitter) fitted with a 509 nm dichroic mirror (Semrock FF509-FDi01-25x36) and 483/32 nm and 514 long-pass emission filters (Semrock FF01-483/32-25 and LP02-514RU-25, respectively). Images were projected on a high-speed camera (Andor Zyla 4.2 plus sCMOS). Recordings were performed at 100 fps, for 1000-2000 frames. Basal parameters were recorded first. Subsequently, drug stocks were diluted in 28°C E3-Tricaine medium (isoproterenol hydrochloride 1, 10 or 100 µM, Sigma-Aldrich I6504; propranolol hydrochloride 1, 10 or 100 µM, Sigma-Aldrich P0884; E4031 100, 250, or 500 µM, Sigma-Aldrich M5060; nifedipine 1, 10, or 100 µM, Sigma-Aldrich N7634) and the medium was mixed vigorously to assure a homogeneous concentration of the drug. Embryos were incubated for 30 min in normal E3-Tricaine medium (Placebo experiments) or E3-Tricaine-drug mixture and parameters were measured again. Isoproterenol experiments were recorded in both a 25°C and 28°C heated solution. For nifedipine washout experiments, embryos were removed from agarose gel and incubated 180 min in E3-Tricaine medium at 28°C. Subsequently embryos were fixed again in 0.3% agarose and parameters were measured for a third time. Recordings were analyzed using Image J and Matlab (Version R2015a, Mathworks, Natick, MA, USA).

High-speed fluorescence imaging in PAB-treated embryos and juveniles

14 dpf juvenile casper *tg(myl7:Gal4FF; UAS:GCaMP6f)* fish were embedded and imaged using the same approach as was employed in 3 dpf embryos. In contrast to embryos, we used para-amino-blebbistatin (PAB), a highly soluble and non-phototoxic blebbistatin derivative, to inhibit contraction.[24] PAB was used as an alternative, as fish cannot be raised to adulthood once injected with the tnnt2a morpholino due to a lack of blood flow. Fish were incubated in E3 medium containing 16 mg/mL Tricaine and 100 µM PAB for 15 min before embedding them in 0.3% agarose. To enable the comparison between embryonic and juvenile fish, we also treated 3 dpf casper fish with PAB instead of the *tnnt2a* MO. These fish were incubated in E3 medium containing 16 mg/mL Tricaine and 75 µM PAB for 90 min before embedding them in 0.3% agarose. Recordings were performed at 28°C. While hearts never fully stopped beating, contraction was inhibited sufficiently to prevent major movement artifacts. To correct for remaining movement, we used the 'Template Matching' plugin from ImageJ.

Statistical analysis

Statistical analysis and drawing of graphs and plots were carried out in GraphPad Prism (version 6 for Mac OS X, GraphPad Software, San Diego California USA). Differences between two groups were analyzed using the paired Student's t-test, and comparisons between experimental groups were analyzed by one-way ANOVA for non-parametric variables with Tukey's post-test for intergroup comparisons. Correlation between changes in diastolic Ca^{2+} levels and transient amplitude was analyzed using linear regression. All data is presented as mean±SEM, and $p<0.05$ was considered significant. * $p\leq0.05$, ** $p\leq0.01$, *** $p\leq0.001$, **** $p\leq0.0001$, n.s. $p>0.05$. N denotes the number of fish used per dataset.

Results

Expression of chimeric VSFP-butterfly CY and GCaMP6f in the zebrafish heart

We generated a transgenic zebrafish line expressing the voltage-sensitive fluorescent protein (VSFP) chimeric VSFP-butterfly CY (cyan-yellow: mCitrine/mCerulean), and placed it under the control of the cardiac-specific *myl7* promoter to generate the *tg(myl7:chimeric VSFP-butterfly CY)* line, referred to as VSFP-butterfly fish (Figure 1A). Fish expressing the sensor developed normally and high magnification in vivo confocal images of embryonic zebrafish hearts expressing chimeric VSFP-butterfly at 3 days post-fertilization (dpf) showed correct localization of the sensor to the plasma membrane, with very little cytosolic fluorescence (Figure 1B). In parallel, we generated a transgenic zebrafish line expressing GCaMP6f under the control of the cardiac-specific *myl7* promoter and the Gal4-UAS system: *tg(myl7:Gal4FF; UAS:GCaMP6f)*, referred to as GCaMP6f fish (Figure 1C). Fish expressing this sensor also developed normally and in vivo- confocal images of 3 dpf embryonic zebrafish hearts expressing GCaMP6f showed correct localization of the sensor to the cytosol, with very little nuclear fluorescence (Figure 1D).

VSFP-butterfly and GCaMP6f report voltage and Ca^{2+} dynamics in the embryonic zebrafish heart

To study in vivo spatiotemporal patterning of electrical activity in 3 dpf embryonic VSFP-butterfly zebrafish hearts, we used high-speed widefield epifluorescence microscopy (Figure 2A). Fish were injected with an antisense morpholino oligomer (MO) against *tnnt2a* at the one-cell stage to stop cardiac contractions and to avoid motion artifacts during imaging. Individual analysis of the mCitrine and mCerulean channels demonstrated a decrease in mCerulean signal and a simultaneous increase in mCitrine signal with every consecutive membrane depolarization, signifying an increase in FRET efficacy during membrane depolarization (Figure 2B and Movie S1). Ratiometric processing of the mCitrine and mCerulean channels provided spatial information about action potential (AP) configuration and propagation across the whole heart. Characteristics that could be extracted from our analysis were: heart rate (interval between action potentials) and repolarization parameters (action potential duration (APD) as measured from the start of the upstroke, in which APD_{10} indicates 10% of the APD, APD_{20} 20%, APD_{50} 50% and APD_{90} 90%) (Figure 2C). We obtained a clear depiction of electrical impulse propagation throughout the heart by plotting ratiometric signals along a trajectory defined by the myocardial wall as a line versus time (analogous to the line scan approach). APs that originated in the atrium demonstrated a small delay at the AV canal and then rapidly spread throughout the ventricle. These line plots also revealed a difference in AP duration between the atrium and ventricle, and provided information about the regularity of the activation intervals (Figure 2D).

The same high-speed widefield epifluorescence imaging setup and analysis procedure was used to obtain detailed information of in vivo cytosolic Ca^{2+} dynamics in 3 dpf embryonic GCaMP6f zebrafish hearts (Movie S2). Analysis of GCaMP6f (cpEGFP) signal intensity over time allowed examination of diastolic Ca^{2+} levels, the speed of intracellular Ca^{2+} release and reuptake/clearance

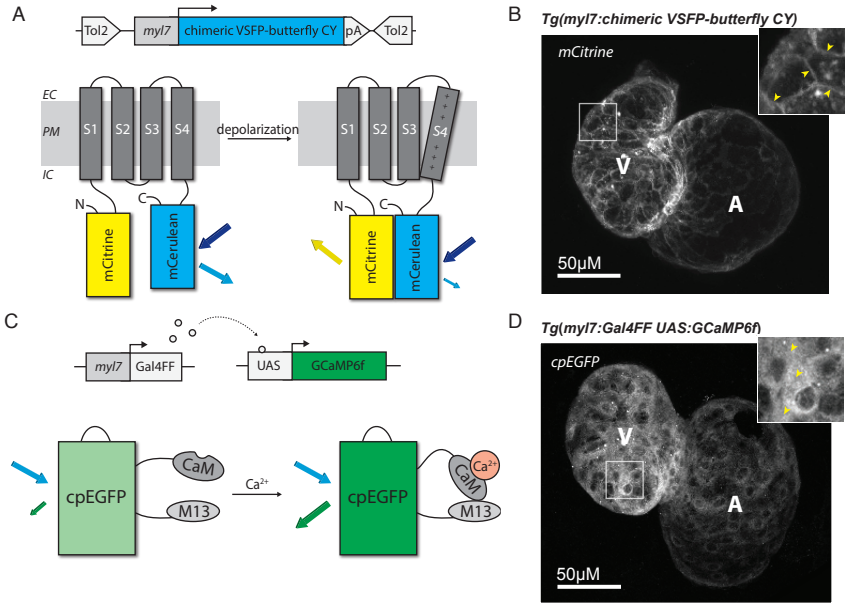

Figure 1. Development of voltage- and Ca^{2+}-reporting zebrafish lines. (A) DNA construct and concept of the sensing mechanism of chimeric VSFP-butterfly CY. Chimeric VSFP-butterfly CY was placed under control of the *myl7* promoter to restrict its expression to the heart. The sensor consists of a voltage sensitive domain with transmembrane segments S1-S4, sandwiched between a fluorescence resonance energy transfer (FRET) pair of the fluorescent proteins mCitrine and mCerulean. Movement of S4 upon membrane depolarization translates into a change of FRET efficiency. (B) 3D projection of a confocal image of a 3 dpf zebrafish *tg(myl7:chimeric VSFP-butterfly CY)* heart. Only the mCitrine channel is displayed. Insert shows a magnification of the selected ventricular area; arrowheads highlight the membrane targeting of chimeric VSFP-butterfly CY. (C) DNA construct and sensor dynamics of GCaMP6f. GCaMP6f was placed under the control of the *myl7* promoter to restrict its expression to the heart. The Gal4FF-UAS system amplifies its expression. GCaMP6f consists of a circularly permutated enhanced green fluorescence protein (cpEGFP) fused to calmodulin (CaM) and the M13 peptide. When intracellular Ca^{2+} rises, CaM binds to M13, causing increased brightness of cpEGFP. (D) 3D projection of a confocal image of a 3dpf zebrafish *tg(myl7:Gal4FF;UAS:GCaMP6f)* heart. Insert shows a magnification of the selected ventricular area; arrowheads highlight cytosolic expression of GCaMP6f. CaM: calmodulin; EC: extracellular; IC: intracellular; pA: poly(A); PM: plasma membrane; tg: transgenic; UAS: upstream activation sequence.

as well as maximal Ca^{2+} amplitudes (Figure 2C). Individual analysis of the atrial and ventricular myocardium demonstrated differences in Ca^{2+} dynamics along the heart tube such as a faster Ca^{2+} release in the atrium as reflected by the steeper upstroke phase (Figure 2C). We obtained a clear depiction of Ca^{2+} propagation over the zebrafish heart by plotting fluorescence signals of the myocardial wall as a line versus time. These line plots clearly showed that (like voltage signals) Ca^{2+} release starts in the atrium, has a slight delay in the AV-canal and then rapidly spreads throughout the ventricle (Figure 2E).

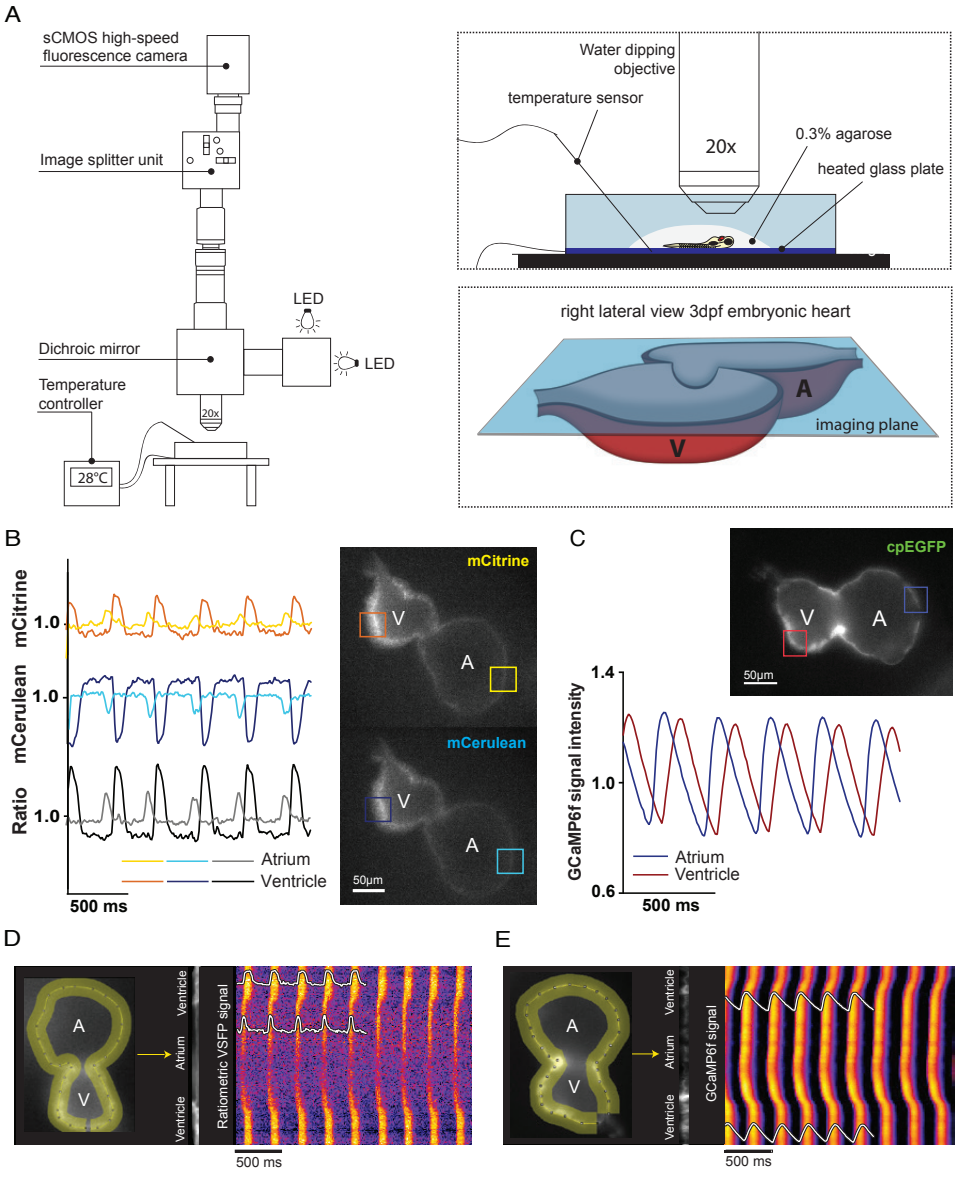

Figure 2. In vivo recording of voltage and Ca^{2+} dynamics in the embryonic zebrafish heart. (A) Recordings were performed using a custom-built upright widefield microscope equipped with a 20x objective, LED excitation light, an emission splitter unit and a high-speed fluorescence camera. Embryos were embedded in 0.3% agarose and placed in a temperature-controlled water bath. Temperature was regulated using a heated glass plate and a temperature sensor. A schematic depiction of the focal plane through the embryonic heart is visible in the right bottom frame. (B) Using the high-speed epifluorescence microscope, movies of 3 dpf non-contracting chimeric VSFP-butterfly CY embryonic hearts were recorded. Signal analysis demonstrated an increase in mCitrine (top panel) and decrease in mCerulean (bottom panel) every consecutive excitation

cycle, starting in the atrium and followed by the ventricle. From these signals, a ratiometric signal could be calculated to study action potential (AP) configuration in both chambers. The selected atrial or ventricular regions are indicated by square boxes superimposed on the fluorescence images. (C) Movies of 3 dpf non-contracting GCaMP6f embryonic hearts were recorded and signal analysis demonstrated a clear oscillatory Ca^{2+} signal, starting in the atrium and followed by the ventricle. (D-E) Line plots of both chimeric VSFP-butterfly CY and GCaMP6f signals illustrating electrical impulse (D) and Ca^{2+} propagation (E) throughout the heart. Background-corrected fluorescence intensities were averaged across the width of the myocardial wall and along a trajectory defined by the course of the wall. Signal heat maps of trajectory against time depict depolarizations of the membrane (D) or increases in intracellular Ca^{2+} (E). The chimeric VSFP-butterfly CY line plot (D) clearly shows that APs originate in the atrium, have a small delay at the atrioventricular canal (AVC) and then rapidly spread throughout the ventricle. White insets represent the spatial AP traces, visible is the longer AP duration in the ventricle as compared to the atrium, as well as the regularity of the activation intervals. Analysis of GCaMP6f signal intensity versus time (E) also shows a clear activation pattern from atrium to ventricle. White insets represent the spatial Ca^{2+} transients, showing a faster speed of intracellular Ca^{2+} release in the atrium versus ventricle, similar speed in Ca^{2+} reuptake/clearance between chambers and nice regularity of activation intervals. A: atrium; cpEGFP: circularly permutated enhanced green fluorescent protein; V: ventricle.

VSFP-butterfly and GCaMP6f accurately report the in vivo effects of cardiac sympathetic intervention

To validate the functionality and sensitivity of our VSFP-butterfly and GCaMP6f lines, we used two pharmacological agents to target the sympathetic sensitivity of the heart: the β-adrenergic agonist isoproterenol and the β-adrenergic antagonist propranolol. Placebo experiments demonstrated that incubation without pharmacological agents did not influence cardiac parameters (Figure S1). Optimal concentrations of isoproterenol and propranolol were determined via dose-response measurements in VSFP-butterfly fish (Figure S2A-B). β-adrenergic stimulation is known to increase heart rate and force of contraction by enhancing intracellular Ca^{2+} dynamics. Incubation with 100 µM isoproterenol seemed to have a limited effect in both the VSFP-butterfly and GCaMP6f zebrafish lines at 28°C (average increase in heart rate: VSFP 7.6%, $p \leq 0.001$; GCaMP 5.4%, n.s.) (Figure S3). We lowered the environmental temperature from 28°C to 25°C, in order to reduce the sympathetic tone of the heart. This resulted in a more pronounced effect of isoproterenol on heart rate (average increase: VSFP 19.9%, $p \leq 0.001$; GCaMP 8.8%, $p \leq 0.05$) (Figure 3A, C) and Ca^{2+} transient amplitudes (Figure 3D-E). Isoproterenol significantly increased AP frequency (25°C: 124.3 ± 24.2 bpm vs. 144.5 ± 22.2 bpm, $p \leq 0.001$; 28°C: 172.9 ± 22.6 bpm vs 182.2 ± 16.4 bpm, $p \leq 0.001$) in VSFP-butterfly embryos without affecting APD (Figure 3A-B and Figure S1A), and significantly increased the number of Ca^{2+} transients per minute (147.8 ± 24.1 vs 160.9 ± 20.9, $p \leq 0.05$), diastolic Ca^{2+} levels and Ca^{2+} transient amplitudes in GCaMP6f embryos at 25°C (Figure 3C-E). In contrast, treatment with 100 µM of the β-receptor antagonist propranolol very effectively decreased AP frequency (197.2 ± 21.8 bpm vs 149,2 ± 26.4 bpm, $p \leq 0.001$) without affecting APD in chimeric VSFP-butterfly CY fish (Figure 3A-B), and significantly decreased Ca^{2+} transient frequency (185.9 ± 21 bpm – 137.5 ± 20.7 bpm, $p \leq 0.0001$), diastolic Ca^{2+} levels and the amplitude

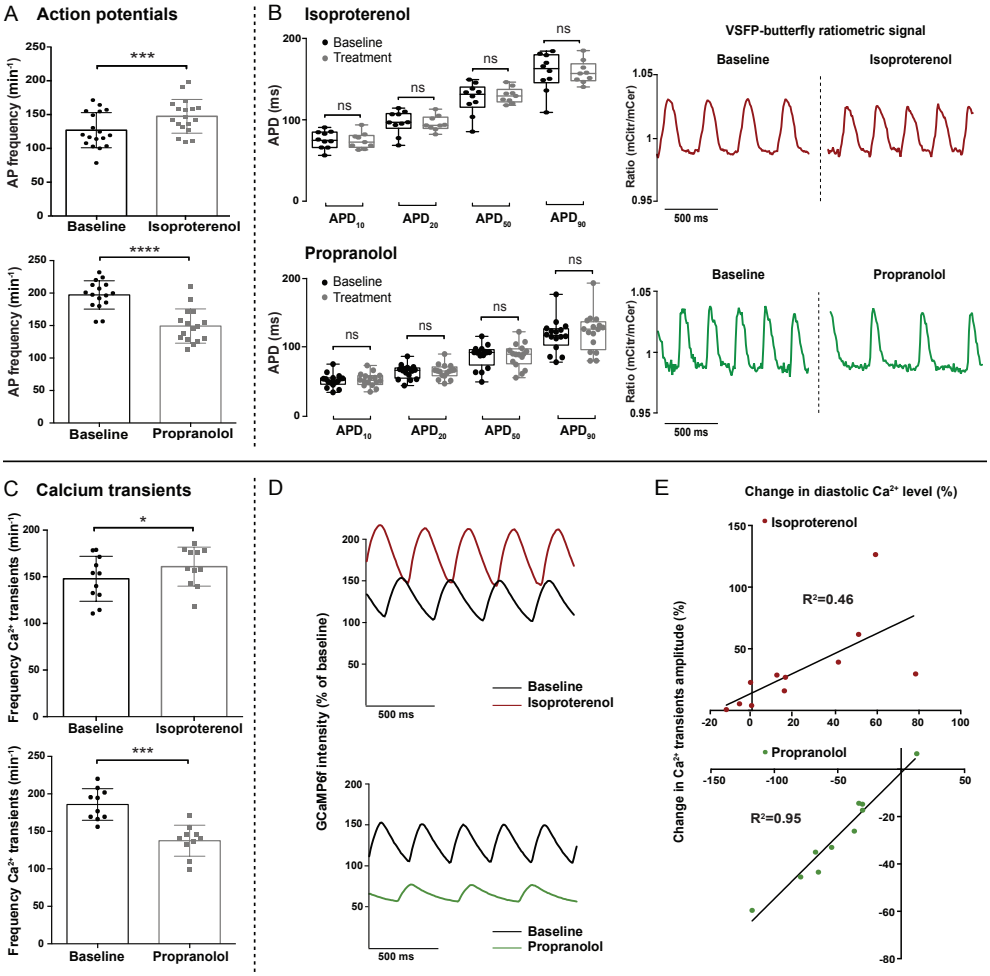

Figure 3. In vivo effect of sympathetic intervention on ventricular electrophysiology and Ca^{2+} dynamics in embryonic zebrafish. 3 dpf VSFP-butterfly and GCaMP6f fish were treated for 30 min with β-adrenergic receptor agonist isoproterenol (100 µM) or antagonist propranolol (100 µM). Isoproterenol experiments were recorded at 25°C to decrease sympathetic tone and propranolol experiments at 28°C. (A-B) VSFP-butterfly fish treated with isoproterenol (n=18) or propranolol (n=17). (A) Bar graphs demonstrating a significant increase in AP frequency (heart rate) after isoproterenol treatment ($p \leq 0.001$) and a decrease after propranolol treatment ($p \leq 0.0001$) (mean ± SEM). (B) Boxplots demonstrating action potential duration (APD) parameters. No significant changes were found in $APD_{10,20,50}$ and APD_{90} after treatment. Representative examples of normalized VSFP-butterfly ratiometric signals of the same fish before and after treatment showing the clear effect on AP frequency by isoproterenol and propranolol treatment, without affecting the AP configuration. (C-E) GCaMP6f fish treated with isoproterenol (n=11) or propranolol (n=10). (C) Bar graphs (mean ± SEM) demonstrating a significant increase in Ca^{2+} transient frequency after treatment with isoproterenol ($p \leq 0.05$) and a decrease after treatment with propranolol ($p \leq 0.001$). (D) Representative examples of the effect of isoproterenol and propranolol on Ca^{2+} transient amplitude and GCaMP6f signal intensity compared to baseline. Clear changes in Ca^{2+} transient frequency, Ca^{2+} transient amplitude and baseline

GCaMP6f signal intensity (diastolic Ca^{2+} level) are visible. GCaMP6f intensity is represented as percentage change compared to baseline, setting the lowest value of the baseline measurement at 100%. (E) Correlation plots of the change in diastolic Ca^{2+} level versus the change in Ca^{2+} transient amplitude after sympathetic stimulation (p=0.02, R2=0.46) and sympathetic inhibition (p≤0.0001, R2=0.95), presenting significant positive correlations.

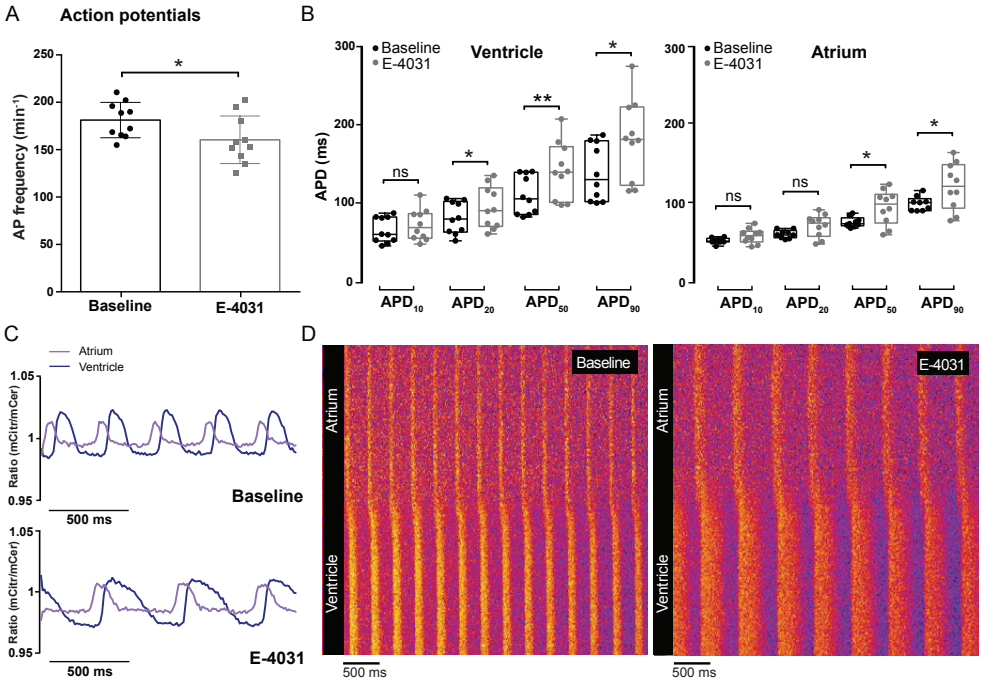

Figure 4. In vivo effect of I_{Kr} block on cardiac electrophysiology in embryonic VSFP-butterfly CY fish. 3 dpf VSFP-butterfly CY fish were treated for 30 min with I_{kr} antagonist E-4031 (500 µM; n=10). (A) Bar graphs demonstrating a significant decrease in AP frequency after E-4031 treatment (p≤0.05) (mean ± SEM). (B) Boxplots demonstrating APD parameters of the ventricle and atrium at baseline and after treatment with E-4031. A significant increase in $APD_{20,50}$ and APD_{90} in the ventricle and significant increase in APD_{50} and APD_{90} in the atrium was found (* p≤0.05, ** p≤0.01). (C) A representative example of the ratiometric AP signals recorded in the atrium and ventricle before and after treatment with E-4031. Clear broadening of the AP shape after treatment is visible. (D) Line plots of the ratiometric AP signals versus time showing a decreased AP frequency and increase of AP duration in the atrium as well as the ventricle. The pattern of atrial-ventricular electrical conduction seems unaffected after treatment with E-4031.

of Ca^{2+} transients in GCaMP6f fish (Figure 3C-E). To visualize the effect of adrenergic intervention on intracellular Ca^{2+} kinetics, we plotted the change in diastolic Ca^{2+} levels against the change in Ca^{2+} transient amplitude in each individual fish after treatment with 100 µM isoproterenol or 100 µM propranolol (Figure 3E). Isoproterenol treatment at 28 °C shows a strong correlation (R^2=0.80, p=0.0004) between the diastolic Ca^{2+} levels and Ca^{2+} transient amplitude, although these

parameters did not always increase (Figure S3B). When lowering the environmental temperature, isoproterenol treatment induced a clear positive correlation between diastolic Ca^{2+} levels and Ca^{2+} transient amplitude (R^2=0.46, p=0.02). In contrast, propranolol shows a strong negative correlation (R^2=0.95, p≤0.0001) (Figure 3E and Figure S4).

VSFP-butterfly and GCaMP6f fish are sensitive to I_{Kr} and to LTCC blockade

To validate whether VSFP-butterfly is sensitive enough to pick up changes in APD and AP morphology, we used classic pharmacological agents to target cardiac ion channels. The hERG channel blocker E-4031 is known to block the rapid delayed rectifier K^+ channel (I_{Kr}), thereby decreasing K^+ efflux and increasing APD. The optimal dose of E-4031 was determined via dose-response measurements in VSFP-butterfly fish (Figure S2C). Incubation with 500 µM E-4031 induced a significant reduction of AP frequency (181.3 ± 18.6 vs 160.4 ± 25.1 bpm, p≤0.05) in the zebrafish heart (Figure 4A). APD_{50} and APD_{90} were significantly increased in both the atrium (APD_{50}: 72.7 ± 7.2 vs 92.7 ± 21.8 ms, p≤0.05; APD_{90}: 95.3 ± 10.5 vs 119 ± 29.4 ms, p≤0.05) and the ventricle (APD_{50}: 110.9 ± 24.8 vs 142.1 ± 36.4 ms, p≤0.01; APD_{90}: 139.2 ± 36.1 vs 181 ± 51.6 ms, p≤0.05), while APD_{20} only showed an increase in the ventricle (81.8 ± 20.2 vs 95.2 ± 26.8 ms, p≤0.05) (Figure 4B). APD_{10} was unaffected in both chambers (Figure 4B). This decrease in AP frequency and lengthening of APD was clearly exposed when visualized by line graphs and line plots (Figure 4C-D).

The voltage-sensitive L-type Ca^{2+} ion channel is essential for the influx of Ca^{2+} after a membrane depolarization and for the maintenance of the AP plateau phase. The L-type Ca^{2+} antagonist nifedipine (100 µm) induced a total block of Ca^{2+} transients in the entire heart, which was visible by the complete disappearance of GCaMP6f fluorescence (Figure 5B-C). The effect of nifedipine on GCaMP6f signal intensity appeared to be dose dependent: 100 µM nifedipine induced a total Ca^{2+} block in 100% of the fish treated (Figure 5A-B), 10 µM nifedipine only resulted in a total Ca^{2+} block in 41.7% of embryos treated, while 1 µM was not able to induce a total block in any of the fish (Figure S5A-C). Nifedipine did cause a clear reduction in frequency of Ca^{2+} transients with all the different concentrations (1, 10, 100 µM: 19% (p≤0.01), 56% (p≤0.001), 100% (p≤0.0001) decrease, respectively) (Figure 5B and Figure S5B-C). Washout experiments were performed in all 3 conditions to exclude that toxicity (death of the embryos) could have been the reason for the disappearance of the GCaMP6f signal. Washout after treatment with 1 µM and 10 µM nifedipine completely restored frequency of Ca^{2+} transients to baseline levels in all fish (Figure S5B-C). Washout after treatment with 100 µM nifedipine reversed the Ca^{2+} block in 65% of the fish, restoring frequency of Ca^{2+} transients, and Ca^{2+} transient amplitudes to levels near to baseline (Figure 5B-C).

Strikingly, in contrast with GCaMP6f signals, VSFP-butterfly signals could still be recorded after 100 µM nifedipine treatment. Nifedipine treatment in VSFP-Butterfly fish did, however, significantly reduce the AP frequency (198.9 ± 24.7 vs 156.8 ± 25.2 bpm, p≤0.0001) (Figure 6A-B), which is in line with the effect on Ca^{2+} transient frequency in GCaMP6f fish at 1 µM and 10 µM

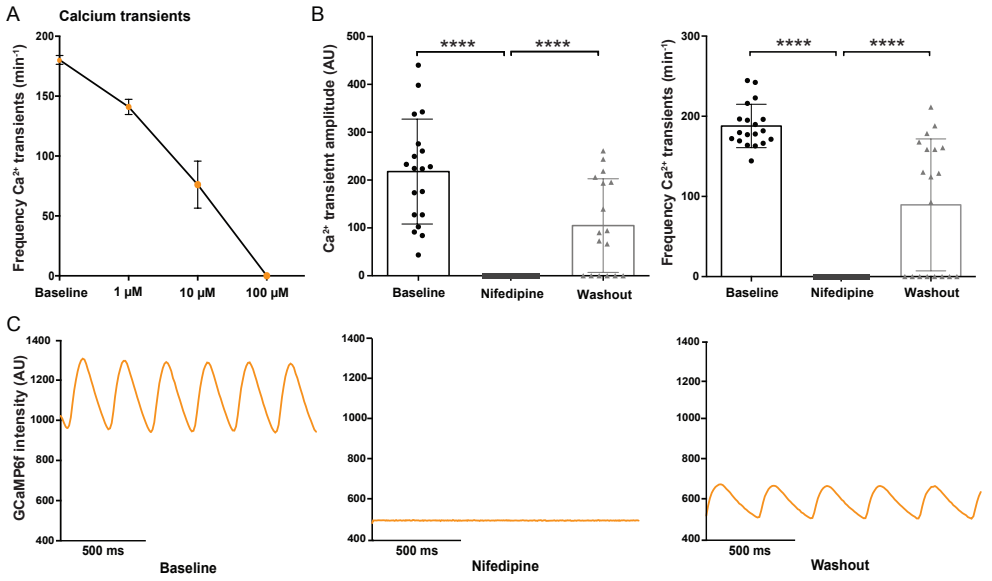

Figure 5. In vivo effect of L-type calcium channel block on ventricular Ca^{2+} dynamics in embryonic GCaMP6f fish. 3 dpf GCaMP6f fish were treated for 30 min with the L-type calcium channel (LTCC) antagonist nifedipine. (A) Dose-response curve showing that increased concentrations of nifedipine (1-100 µM) result in a decreased frequency of Ca^{2+} transients in the ventricle (representative of frequencies over the entire heart tube). Baseline measurements of the 3 treatment groups are pooled in one group (mean ± SEM, 10 and 100 µM p≤0.0001, baseline: n=43, 1 µM: n=12, 10 µM: n=12, 100 µM: n=19). (B) Bar graphs showing that treatment with 100 µM nifedipine completely diminished Ca^{2+} amplitude and frequency (p≤0.0001), which was partly reversed after washout in E3 medium (p≤0.0001) (mean ± SEM, baseline n=19, treatment n=19, washout n=17). (C) A visual representation of the total block in GCaMP6f signal intensity in one representative fish after treatment with 100 µM nifedipine and the rescue of Ca^{2+} amplitude and frequency after washout in E3 medium. AU: arbitrary units.

nifedipine, but not at 100 µM nifedipine, as the GCaMP6f signal completely disappeared at this concentration (Figure 5B-C). In the ventricle, APD was slightly, but significantly increased after treatment with 100 µM nifedipine (APD_{10}: 54.1 ± 6.3 vs 60.8 ± 6.3 ms, p≤0.01; APD_{20}: 67.2 ± 7.1 vs 77.2 ± 6.8 ms, p≤0.01; APD_{50}: 92.5 ± 9.3 vs 105.4 ± 10.7 ms, p≤0.001; APD_{90}: 114.1 ± 11 vs 130 ± 13.8 ms, p≤0.01) (Figure 6B). In the atrium, only APD_{10} was significant increased (43.1 ± 4 vs 47 ± 3.4 ms, p≤0.05), while APD_{20}, APD_{50} and APD_{90} were not affected (Figure 6B). Strikingly, in 20% of the treated fish (100 µM) we observed a desynchronized atrial-ventricular (A-V) electrical impulse propagation (Figure 6C and Movie S3).

GCaMP6f reports Ca^{2+} dynamics in the juvenile zebrafish heart

To study in vivo cardiac Ca^{2+} dynamics in older fish, we developed a transparent casper *tg(myl7:Gal4FF;UAS:GCaMP6f)* zebrafish line. Due to mutations in the genes *mitfa* and *mpv17*[25], casper zebrafish lack two skin pigments and remain transparent even into adulthood.[26] We

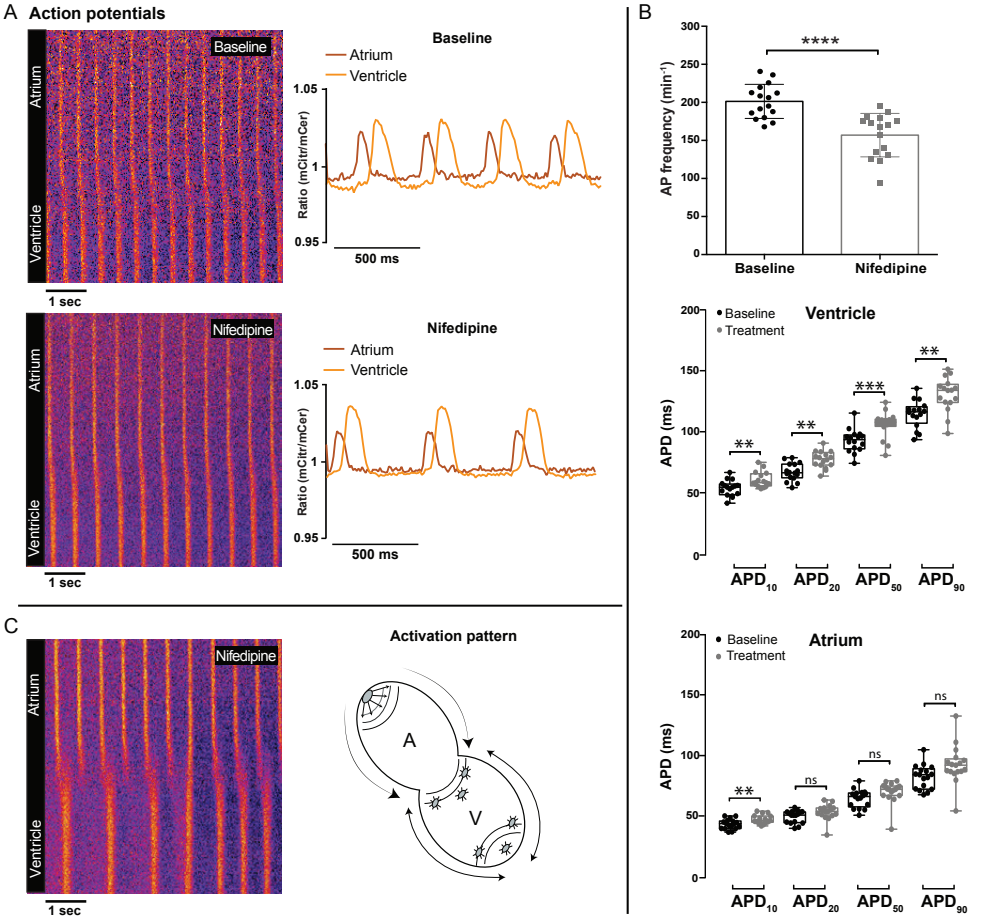

Figure 6. In vivo effect of LTCC blockage on cardiac electrophysiology in embryonic VSFP-butterfly CY fish. 3 dpf VSFP-butterfly fish were treated for 30 min with 100 µM nifedipine. (A) Line plots of the ratiometric VSFP-butterfly signal versus time in one representative fish before and after treatment, along with a visual representation of the AP configuration. The line plots show a decrease in AP frequency and slight increase in ventricular APD after treatment with nifedipine. Line plots and adjacent ratiometric graphs are from the same fish. (B) APD parameters before and after treatment with 100 µM nifedipine (n=16). Bar graphs show a significant decrease in the AP frequency (mean ± SEM, p≤0.0001) and boxplots show a significant increase in APD10,20,50 and APD90 in the ventricle (middle panel; ** p≤0.01, *** p≤0.001), but only an increase of APD10 in the atrium (bottom panel; p≤0.05). (C) A line plot of one representative fish showing a disturbed atrial-ventricular electrical conductance after treatment with 100 µM nifedipine, which occurred in 20% of the fish. Atrial firing is regular, but there is ectopic activation at the apex as well at the base of the ventricle, which is clarified in the schematic picture. A: atrium; V: ventricle.

used the same high-speed widefield epifluorescence microscopy setup employed in 3 dpf VSFP-butterfly and GCaMP6f embryos (Figure 2A and Figure 7A). 3 dpf and 14 dpf casper *tg(myl7:Gal4FF;UAS:GCaMP6f)* zebrafish were treated with 75 µM and 100 µM para-amino-

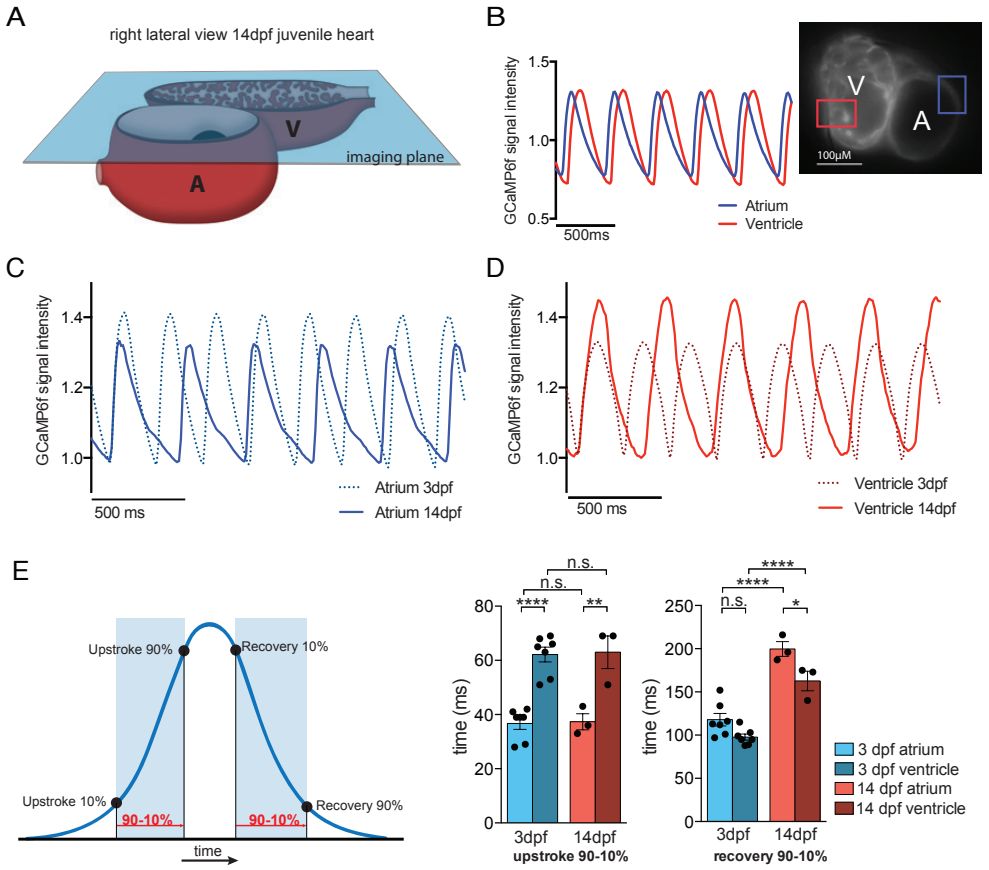

Figure 7. In vivo recording of Ca^{2+} dynamics in embryonic and juvenile casper GCaMP6f fish. (A) Visual representation of the imaging plane in 14 dpf juvenile casper-GCaMP6f hearts. The same widefield high-speed epifluorescence microscopy setup was used as in 3 dpf embryos. (B) Movies of almost silent GCaMP6f juvenile hearts were recorded and signal analysis demonstrated a clear oscillatory cpEGFP (GCaMP6f) Ca^{2+} signal in the selected atrial or ventricular region. (C-D) Representative examples of normalized oscillatory atrial (C) and ventricular (D) GCaMP6f signals from 3 and 14 dpf PAB-treated casper hearts, showing the Ca^{2+} transient dynamics over time. (E) Schematic representation of analyzed Ca^{2+} transient parameters. Bar graphs (mean ± SEM) demonstrating the speed in Ca^{2+} transient upstroke and recovery phase, compared between chambers and age (3 dpf n=7, 14 dpf n=3), showing a significant faster Ca^{2+} transient upstroke in the atrium compared to the ventricle, in both 3 dpf ($p \leq 0.0001$) and 14 dpf casper fish ($p \leq 0.01$). The recovery phase is significantly slower in 14 dpf casper fish compared to 3dpf casper fish, both in the atrium ($p \leq 0.0001$) and the ventricle ($p \leq 0.0001$). Also, the Ca^{2+} transient recovery phase is slower in the atrium compared to the ventricle, both in 3 dpf and 14 dpf fish ($p \leq 0.05$) (mean ± SEM, one-way ANOVA).

blebbistatin (PAB) respectively, to inhibit contraction. While hearts never fully stopped beating with PAB, contraction was inhibited sufficiently to prevent major movement artifacts (Movie S4). Analysis of the oscillatory GCaMP6f (cpEGFP) signal over time allowed examination of Ca^{2+} transient dynamics in both cardiac chambers (Figure 7B). Similar to 3 dpf embryos, individual analysis of the

atrial and ventricular myocardium demonstrated differences in Ca^{2+} dynamics between chambers, with again a faster rise of cytosolic Ca^{2+} levels in the atrium (Figure 7B-E). Interestingly, when comparing Ca^{2+} dynamics between 3 dpf and 14 dpf zebrafish, we found significant differences in the recovery phases of atrial and ventricular Ca^{2+} transients (Figure 7C-E). Cytosolic Ca^{2+} clearance was significantly slower in the atrium of 14 dpf fish (90-10%: 117.9 ± 7.3 ms at 3 dpf vs. 199.7 ± 8.6 ms at 14 dpf, $p \leq 0.0001$), as well in the ventricle of 14 dpf fish (90-10%: 97.7 ± 3.5 ms at 3 dpf vs. 162.7 ± 11.4 ms at 14 dpf, $p \leq 0.0001$) (Figure 7E), which could be an effect of the overall slower heart rate at 14 dpf (Figure S6A). To investigate whether genetic background and type of contraction block affects Ca^{2+} dynamics, two zebrafish strains (TL and casper) and two types of contraction blockers (*tnnt2a* MO and PAB) were compared (Figure S6). We did observe an effect of zebrafish strain, as we found higher heart rates in casper fish compared to embryonic TL fish (Ca^{2+} transient frequency; TL MO 216.6 ± 3.1 bpm vs. casper MO 238.4 ± 4.2 bpm, $p \leq 0.001$; TL PAB 223.5 ± 2.9 bpm vs. casper PAB 242.1 ± 3.9 bpm, $p \leq 0.001$) (Figure S6A), as well as a shorter Ca^{2+} transient recovery time in casper fish, both in the atrium (TL MO 137.6 ± 2.5 ms vs. casper MO 123.3 ± 2.6 ms, $p \leq 0.05$; TL PAB 138.6 ± 2.1 ms vs casper PAB 117.9 ± 7.2 ms, $p \leq 0.01$) and in the ventricle (TL MO 120.8 ± 2.9 ms vs. casper MO 98.20 ± 2.9 ms, $p \leq 0.0001$; TL PAB 119.8 ± 1.7 ms vs casper PAB 97.71 ± 3.5 ms, $p \leq 0.001$) (Figure S6C). No difference in Ca^{2+} transient upstroke time between embryonic casper and TL fish was observed (Figure S6B). In addition, the type of contraction block seemed to have no effect on Ca^{2+} dynamics, as MO- and PAB-treated fish of the same strain demonstrated a similar Ca^{2+} transient frequency, Ca^{2+} transient upstroke time and Ca^{2+} transient recovery time (Figure S6A-C).

Discussion

Experimental animal models have been instrumental for the development of our understanding of cardiac cellular electrophysiology and the pathophysiology of cardiac arrhythmias. In general, in vivo assays are mainly used to study global multicellular cardiac electrophysiology, while in vitro and ex vivo experiments allow detailed research into cardiac cellular electrophysiology. Unfortunately, it is extremely difficult to study cardiac cellular electrophysiology in the context of the whole body, as the heart is simply not accessible within a closed thoracic cavity. Here, we describe the generation and validation of two transgenic zebrafish lines that can be used to study in vivo cardiac cellular electrophysiology by reporting cardiac membrane voltage (via the chimeric VSFP-butterfly CY sensor) and cytosolic Ca^{2+} dynamics (via the GCaMP6f sensor).

During the past decades, the zebrafish has emerged as a powerful model to study human disease due to its small size, optical accessibility and ease of genetic engineering. Zebrafish can be used to test mechanisms of disease in vivo, especially through genotype-phenotype screens, and they also are an efficient and suitable model to screen large libraries of chemical compounds.[6] Large-scale chemical screens are very appealing, as they would allow for fast and economical

surveys to identify novel compounds that could benefit patients. Mutagenesis in zebrafish has improved markedly in the past few years due to development of the CRISPR/Cas9 technique and it is even possible to generate fish carrying patient-specific mutations.[27] In future studies, combining the VSFP-butterfly and/or the GCaMP6f transgenic line with zebrafish carrying a loss of function or a specific patient mutation could provide unique information about the impact of mutations on cardiac electrophysiology.

In this study, we validated the reliability and robustness of both the VSFP-butterfly and GCaMP6f sensor lines through treatment of 3 dpf embryos with well-studied (golden standard) drugs. The β-adrenergic agonist isoproterenol and the β-adrenergic antagonist propranolol were used to test the sensitivity of the 3 dpf embryonic zebrafish heart to modulation of sympathetic tone. In line with literature, isoproterenol increased heart rate and enhanced intracellular Ca^{2+} dynamics[28], while propranolol had the opposite effect. In general, β-adrenergic stimulation in human cardiomyocytes also decreases APD[29], which we did not observe in the zebrafish heart. However, this could be due to baseline heterogeneity in AP contour between species.[30] Strikingly, the response to propranolol was much more prominent than the response to isoproterenol in 3 dpf embryos (especially at 28°C), possibly indicating that at this developmental stage the sympathetic tone is higher than the parasympathetic tone. In line with this, Schwerte et al. demonstrated that the vagal tone is not very pronounced in zebrafish embryos until ±11-12 dpf[31], and heart rates recorded in adult zebrafish (100 days, 28°C) are reported to be around 130 bpm, which is much lower than the 180-200 bpm average we find in 3 dpf embryos[32] suggesting that the vagal tone is not fully developed at 3 dpf.

In line with literature, the hERG ion channel blocker E-4031 clearly prolonged APD.[33] A similar response has been described in isolated atrial and ventricular cardiomyocytes from adult zebrafish.[13] E-4031 also significantly decreased heart rate, an observation we did not expect as the hERG channel is not typically associated with mammalian SA node electrophysiology. However, literature provides more reports of bradycardia-inducing effects by QT-prolonging drugs in zebrafish embryos, as well as reports of LQT2 patients with bradycardia carrying a hERG mutation.[12,34,35]

Nifedipine largely blocked Ca^{2+} transients, disrupted atrial-ventricular electrical conduction and mainly affected action potential configuration in the ventricle, with relatively little effect in the atrium. It is known that zebrafish express both L-type (LTCC) and T-type Ca^{2+} channels (TTCC), which distinguishes them from mammals, as mammals only express LTCC in the working myocardium of the heart. Dominance of the LTCC in the zebrafish ventricle, but not in the atrium, could explain why we see a more pronounced effect of nifedipine on the ventricle. Indeed, island beat zebrafish embryos with a loss of function mutation in the gene encoding the zebrafish LTCC, have a chaotically beating atrium but a completely silent ventricle.[36] In addition tomo-seq, a technique that provides spatial information on RNA expression, indeed demonstrated a clear expression dominance of LTCC in the ventricle, but not in the atrium at 2 dpf.[37]

In this study, we also demonstrated the first successful use of optogenetic sensors in 14 dpf juvenile zebrafish by crossing our *tg(myl7:Gal4FF;UAS:GCaMP6f)* line with transparent casper fish.

While 3 dpf embryos remain easier to manipulate and provide a fast way to screen for the effects of mutations or drugs, juvenile fish provide an excellent tool to measure electrophysiology in a more mature system. This can be extremely helpful, for instance when a mutation only results in a phenotype after the embryonic stages. Our data demonstrate that the Ca^{2+} transient upstroke time is similar in both the atrium and ventricle of 3 dpf and 14 dpf fish, but the Ca^{2+} transient recovery time is significantly longer in 14 dpf fish. One possible explanation is the physiological decrease in heart rate from 200-250 bpm at 3 dpf to approximately 150-180 bpm at 14 dpf, as it may influence the speed of Ca^{2+} release and recovery. It is also possible that this decrease in Ca^{2+} transient recovery time is an effect of cardiomyocyte maturation, but this can only be confirmed with recordings that have similar Ca^{2+} transient frequencies.

Ultimately, it would be favorable to combine these high-sensitivity voltage and Ca^{2+} sensors into one zebrafish line, as it will allow for a one-on-one comparison and it will diminish the influence of genetic heterogeneity between zebrafish lines on experimental outcomes. In terms of fluorescence spectra, it would be a possibility to combine chimeric VSFP-butterfly with RCaMP2, a red variant of GCaMP. The concept of a dual-sensor fish is not novel, as Hou et al. presented simultaneous mapping of membrane voltage and Ca^{2+} using a genetically encoded dual-function Ca^{2+} and voltage reporter (CaViar).[38] This dual-sensor fish is very promising; however, its dim opsin voltage signal (30-80 times dimmer than EGFP) makes imaging highly challenging and detailed APD analyses complicated.

Another previously reported zebrafish line used the VSFP2 type voltage indicator termed Mermaid. While it was shown that Mermaid can report in vivo cardiac membrane voltage[39], this voltage sensor has slow kinetics, with a τ_{off} of >60 ms[40] as compared to 14.6±0.5 ms in the chimeric VSFP-butterfly[20] used here, resulting in reduced temporal resolution of the voltage report.

In conclusion, by introducing the optogenetic sensors chimeric VSFP-butterfly CY and GCaMP6f into the zebrafish heart we successfully generated two tools capable of reporting in vivo cellular electrophysiological characteristics. Parallel use of both sensors showed the ability to study heart rate, cardiac AP configuration, spatiotemporal patterning of electrical activation and intracellular Ca^{2+} dynamics. In addition, we demonstrated the first successful use of an optogenetic sensor in juvenile zebrafish, opening new possibilities for electrophysiological research. Due to the fast kinetics and high-resolution signals of both sensors, chimeric VSFP-butterfly CY and GCaMP6f zebrafish provide promising models to study electro(patho)physiology and to search for novel drugs that could aid patients with cardiac arrhythmias.

Limitations

Validation of the sensors via side-by-side comparison to an established method, such as current clamp recording, was not performed in this study. However, these recordings are very challenging when performed in vivo and the temporal resolution of chimeric VSFP-butterfly CY and GCaMP6f have been characterized in several earlier studies. Another limitation of our study is the use of

a total contraction block to prevent movement artifacts, despite its necessity for the accurate assessment of fluorescence signals over time. The effects of normal cardiac contractile function and hemodynamic load on electrophysiological and Ca^{2+} transient properties via e.g., mechano-electrical feedback mechanisms could therefore not be taken into account. Another challenge is the very fast nature of the AP upstoke phase (less than 2 ms). While chimeric VSFP-butterfly CY has excellent kinetics (τ_{on} 2.3±0.2 ms), the upstroke phase is simply too fast for accurate tracing with the imaging strategy used in this study (for example the camera exposure time (10 ms) is longer than the AP upstroke time). Consequently, we have not addressed AP upstroke velocity in this study.

Abbreviations

A: atrium; AP: action potential; APD: action potential duration; AU: arbitrary units; BDM: 2,3-Butanedione 2-monoximel; bpm: beats per minute; Ca^{2+}: calcium; CY: cyan-yellow: mCitrine/mCerulean; dpf: days post-fertilization; GECI: genetically encoded calcium indicator; GEVI: genetically encoded voltage indicator; MO: morpholino; PAB: para-amino-blebbistatin; PTU: 1-phenyl-2-thiourea; TL: Tupfel long fin; V: ventricle; VSFP: voltage-sensitive fluorescent protein.

Acknowledgements

We acknowledge the support from The Netherlands Cardio Vascular Research Initiative (CVON): the Dutch Heart Foundation, Dutch Federation of University Medical Centres, the Netherlands Organization for Health Research and Development and the Royal Netherlands Academy of Sciences (CVON-PREDICT). This work was supported by the Champalimaud Foundation, ZonMW grant 40-00812-98-12086, the ERA-NET Cofund action N° 643578 under the European Union's Horizon 2020 research and innovation programme and national funding organisations Canadian Institutes for Health Research (CIHR), the Netherlands Organization for Health Research and Development (ZonMw), Belgium (Flanders) Research Foundation Flanders (FWO), and French National Research Agency (ANR). We thank Mr. Jiuru Li for carefully proofreading the manuscript.

Competing interests

The authors have declared that no competing interests exist.

References

1. Kang C, Brennan JA, Kuzmiak-Glancy S, Garrott KE, Kay MW, Efimov IR. Technical advances in studying cardiac electrophysiology - Role of rabbit models. *Prog Biophys Mol Biol* 2016 Jul;121(2):97–109.
2. Kass DA, Hare JM, Georgakopoulos D. Murine cardiac function: a cautionary tail. *Circ Res* 1998 Mar;82(4):519–22.
3. Glukhov AV, Flagg TP, Fedorov VV, Efimov IR, Nichols CG. Differential K(ATP) channel pharmacology in intact mouse heart. *J Mol Cell Cardiol* 2010 Jan;48(1):152–60.
4. Milani-Nejad N, Janssen PML. Small and large animal models in cardiac contraction research: advantages and disadvantages. *Pharmacol Ther* 2014 Mar;141(3):235–49.
5. Lelovas PP, Kostomitsopoulos NG, Xanthos TT. A comparative anatomic and physiologic overview of the porcine heart. *J Am Assoc Lab Anim Sci* 2014 Sep;53(5):432–8.
6. Lieschke GJ, Currie PD. Animal models of human disease: zebrafish swim into view. *Nat Rev Genet* 2007 May;8(5):353–67.
7. Hu N, Sedmera D, Yost HJ, Clark EB. Structure and function of the developing zebrafish heart. *Anat Rec* 2000 Oct;260(2):148–57.
8. Stoyek MR, Croll RP, Smith FM. Intrinsic and extrinsic innervation of the heart in zebrafish (*Danio rerio*). *J Comp Neurol* 2015 Apr 9;523(11):1683–700.
9. Tessadori F, van Weerd JH, Burkhard SB, Verkerk AO, de Pater E, Boukens BJ, et al. Identification and functional characterization of cardiac pacemaker cells in zebrafish. *PLoS ONE* 2012;7(10):e47644.
10. Arnaout R, Ferrer T, Huisken J, Spitzer K, Stainier DYR, Tristani-Firouzi M, et al. Zebrafish model for human long QT syndrome. *Proc Natl Acad Sci USA* 2007 Jul;104(27):11316–21.
11. Milan DJ, Jones IL, Ellinor PT, MacRae CA. In vivo recording of adult zebrafish electrocardiogram and assessment of drug-induced QT prolongation. *Am J Physiol Heart Circ Physiol* 2006 Jul;291(1):H269–73.
12. Milan DJ, Peterson TA, Ruskin JN, Peterson RT, MacRae CA. Drugs that induce repolarization abnormalities cause bradycardia in zebrafish. *Circulation* 2003 Mar;107(10):1355–8.
13. Nemtsas P, Wettwer E, Christ T, Weidinger G, Ravens U. Adult zebrafish heart as a model for human heart? An electrophysiological study. *J Mol Cell Cardiol* 2010 Jan;48(1):161–71.
14. Verkerk AO, Remme CA. Zebrafish: a novel research tool for cardiac (patho)electrophysiology and ion channel disorders. *Front Physiol* 2012 Jul;3:255.
15. Muntean BS, Horvat CM, Behler JH, Aboualaiwi WA, Nauli AM, Williams FE, et al. A Comparative Study of Embedded and Anesthetized Zebrafish in vivo on Myocardiac Calcium Oscillation and Heart Muscle Contraction. *Front Pharmacol* 2010 Dec;1:139.
16. Stosiek C, Garaschuk O, Holthoff K, Konnerth A. In vivo two-photon calcium imaging of neuronal networks. *Proc Natl Acad Sci U.S.A*. 2003 Jun;100(12):7319–24.
17. Liao MLC, de Boer TP, Mutoh H, Raad N, Richter C, Wagner E, et al. Sensing Cardiac Electrical Activity With a Cardiac Myocyte–Targeted Optogenetic Voltage Indicator. *Circ Res* 2015 Aug;117(5):401–12.
18. Koopman CD, Zimmermann WH, Knöpfel T, de Boer TP. Cardiac optogenetics: using light to monitor cardiac physiology. *Basic Res Cardiol* 2017 Aug;112(5):56.

19. Kaestner L, Scholz A, Tian Q, Ruppenthal S, Tabellion W, Wiesen K, et al. Genetically encoded Ca^{2+} indicators in cardiac myocytes. *Circ Res* 2014 May;114(10):1623–39.
20. Mishina Y, Mutoh H, Song C, Knöpfel T. Exploration of genetically encoded voltage indicators based on a chimeric voltage sensing domain. *Front Mol Neurosci* 2014;7:78.
21. Chen TW, Wardill TJ, Sun Y, Pulver SR, Renninger SL, Baohan A, et al. Ultrasensitive fluorescent proteins for imaging neuronal activity. *Nature* 2013 Jul;499(7458):295–300.
22. Westerfield M. The Zebrafish Book. 4 ed. University of Oregon Press, Eugene.
23. Sehnert AJ, Huq A, Weinstein BM, Walker C, Fishman M, Stainier DYR. Cardiac troponin T is essential in sarcomere assembly and cardiac contractility. *Nat Genet* 2002 May;31(1):106–10.
24. Várkuti BH, Képiró M, Horváth IÁ, Végner L, Ráti S, Zsigmond Á, et al. A highly soluble, non-phototoxic, non-fluorescent blebbistatin derivative. *Sci Rep* 2016 May;6(1):26141.
25. D'Agati G, Beltre R, Sessa A, Burger A, Zhou Y, Mosimann C, et al. A defect in the mitochondrial protein Mpv17 underlies the transparent casper zebrafish. *Dev Biol* 2017 Oct;430(1):11–7.
26. White RM, Sessa A, Burke C, Bowman T, LeBlanc J, Ceol C, et al. Transparent adult zebrafish as a tool for in vivo transplantation analysis. *Cell Stem Cell* 2008 Feb;2(2):183–9.
27. Liu J, Zhou Y, Qi X, Chen J, Chen W, Qiu G, et al. CRISPR/Cas9 in zebrafish: an efficient combination for human genetic diseases modeling. *Hum Genet* 2017 Jan;136(1):1–12.
28. Shen JX. Isoprenaline enhances local Ca^{2+} release in cardiac myocytes. *Acta Pharmacol Sin* 2006 Jul;27(7):927–32.
29. Taggart P, Sutton P, Chalabi Z, Boyett MR, Simon R, Elliott D, et al. Effect of adrenergic stimulation on action potential duration restitution in humans. *Circulation* 2003 Jan;107(2):285–9.
30. Sala L, Hegyi B, Bartolucci C, Altomare C, Rocchetti M, Váczi K, et al. Action potential contour contributes to species differences in repolarization response to β-adrenergic stimulation. *Europace* 2017 Oct;67:615.
31. Schwerte T, Prem C, Mairösl A, Pelster B. Development of the sympatho-vagal balance in the cardiovascular system in zebrafish (*Danio rerio*) characterized by power spectrum and classical signal analysis. *J Exp Biol* 2006;209(Pt 6):1093–100.
32. Barrionuevo WR, Burggren WW. O2 consumption and heart rate in developing zebrafish (*Danio rerio*): influence of temperature and ambient O2. *Am J Physiol* 1999 Feb;276(2 Pt 2):R505–13.
33. Sanguinetti MC, Tristani-Firouzi M. hERG potassium channels and cardiac arrhythmia. *Nature* 2006 Mar;440(7083):463–9.
34. Yoshida H, Horie M, Otani H, Kawashima T, Onishi Y, Sasayama S. Bradycardia-induced long QT syndrome caused by a de novo missense mutation in the S2-S3 inner loop of HERG. *Am J Med Genet* 2001 Feb;98(4):348–52.
35. Melong N, Steele S, MacDonald M, Holly A, Collins CC, Zoubeidi A, et al. Enzalutamide inhibits testosterone-induced growth of human prostate cancer xenografts in zebrafish and can induce bradycardia. *Sci Rep* 2017 Oct;7(1):14698.
36. Rottbauer W, Baker K, Wo ZG, Mohideen MA, Cantiello HF, Fishman MC. Growth and function of the embryonic heart depend upon the cardiac-specific L-type calcium channel alpha1 subunit. *Dev Cell* 2001 Aug;1(2):265–75.
37. Burkhard SB, Bakkers J. Spatially resolved RNA-sequencing of the embryonic heart identifies a role for Wnt/β-catenin signaling in autonomic control of heart rate. *Elife* 2018 Feb;7:971.

38. Hou JH, Kralj JM, Douglass AD, Engert F, Cohen AE. Simultaneous mapping of membrane voltage and calcium in zebrafish heart in vivo reveals chamber-specific developmental transitions in ionic currents. *Front Physiol* 2014;5(42):344.
39. Tsutsui H, Higashijima SI, Miyawaki A, Okamura Y. Visualizing voltage dynamics in zebrafish heart. *J Physiol* 2010 Jun;588(Pt 12):2017–21.
40. Mutoh H, Perron A, Dimitrov D, Iwamoto Y, Akemann W, Chudakov DM, et al. Spectrally-resolved response properties of the three most advanced FRET based fluorescent protein voltage probes. *PLoS ONE* 2009;4(2):e4555.

Supplemental figures

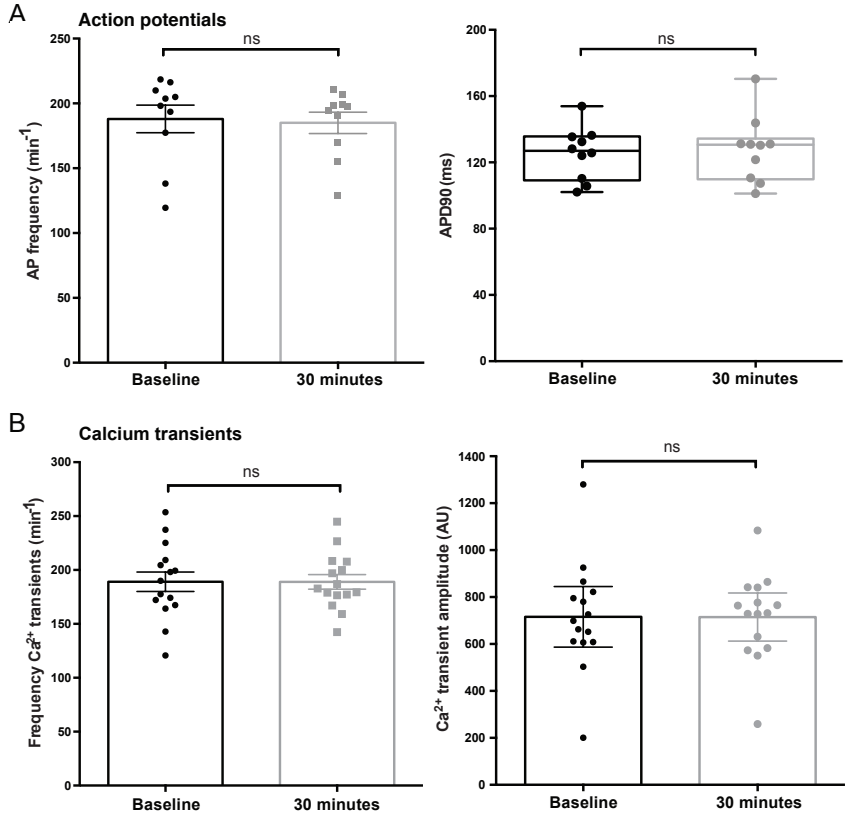

Figure S1. No effects of placebo treatment on cardiac electrophysiology and Ca^{2+} dynamics in embryonic zebrafish. Ventricular signals of 3 dpf chimeric VSFP-butterfly CY and GCaMP6f fish were recorded at baseline and after 30 min incubation in normal E3-Tricaine solution without added drugs, at 28°C. (A) Bar graphs of AP-frequency, and boxplots of APD90 demonstrate no significant effect on both parameters in VSFP-butterfly CY fish, after 30 min incubation (mean ± SEM, n=10). (B) Bar graphs on frequency of Ca^{2+} transients, and Ca^{2+} transient amplitude demonstrates no significant effect on both parameters in GCaMP6f fish, after 30 min incubation (mean ± SEM, n=15). AU: arbitrary units.

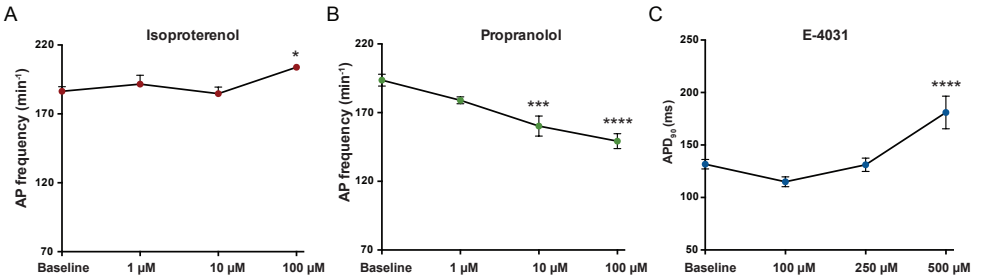

Figure S2. Dose-response effects of isoproterenol, propranolol and E-4031 in VSFP-butterfly CY fish. The effect of different concentrations (1-100 µM) isoproterenol and propranolol on AP frequency. (A) Showing a significant increase in AP frequency after treatment with 100 µM isoproterenol (mean ± SEM, $p<0.05$, one-way ANOVA, baseline: n=40, 1 µM: n=9, 10 µM: n=16, 100 µM: n=15). (B) Gradual decrease of AP frequency with increasing propranolol concentrations (mean ± SEM, ***$p\leq0.001$, ****$p\leq0.0001$, one-way ANOVA, baseline: n=39, 1 µM: n=11, 10 µM: n=12, 100 µM: n=16). (C) The effect of different concentrations (100-500 µM) E-4031 on ventricular APD90 showing a significant increase in APD_{90} after treatment with 500 µM (mean ± SEM, $p\leq0.0001$, one-way ANOVA, baseline: n=30, 100 µM: n=9, 250 µM: n=11, 500 µM: n=10). Baseline measurements of the different concentration groups were pooled into one group.

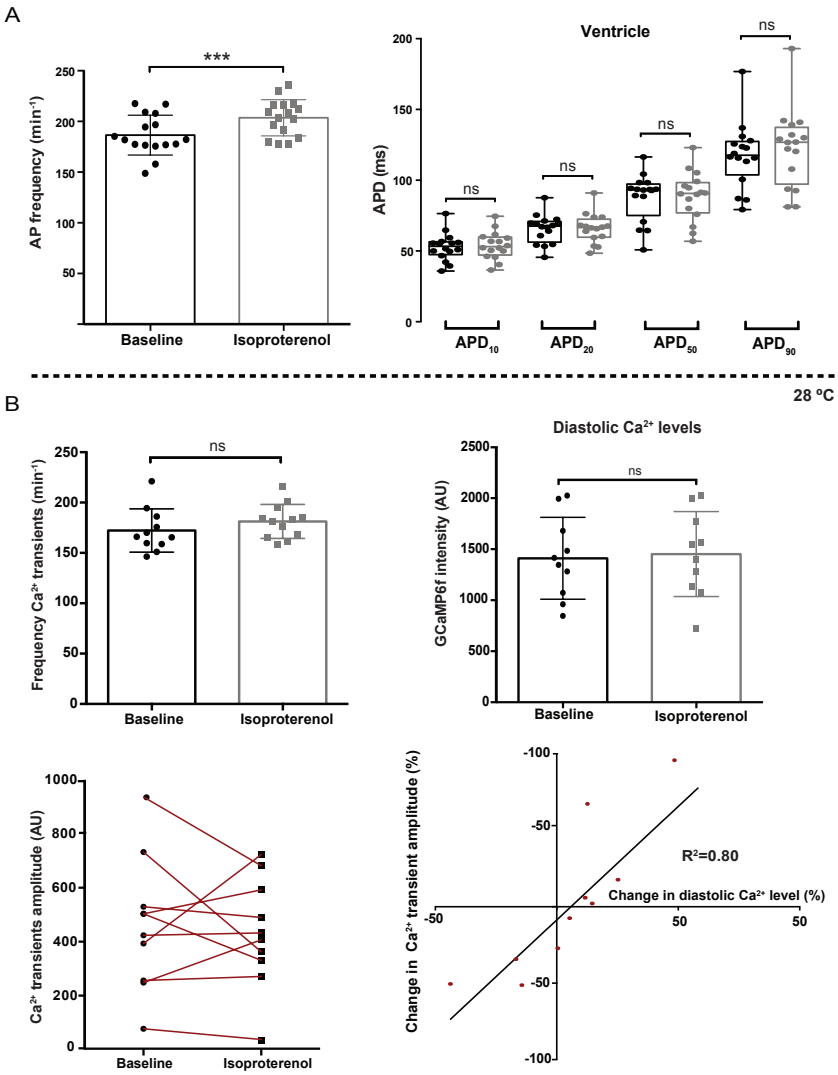

Figure S3. In vivo effect of sympathetic stimulation on cardiac electrophysiology and Ca^{2+} dynamics at 28°C. 3 dpf VSFP-butterfly and GCaMP6f fish were treated for 30 min with β-adrenergic receptor agonist isoproterenol (100 µM), experiments were performed at 28°C. (A) Bar graphs demonstrate a significant increase in AP frequency after isoproterenol treatment (mean ± SEM, p≤0.001, n=15). Boxplots show action potential duration (APD) parameters at baseline and after isoproterenol treatment. No significant changes were found in $APD_{10,20,50}$ and APD_{90} after treatment. (B) Effect of isoproterenol on Ca^{2+} dynamics at the physiological temperature of 28°C, n=15. Bar graphs demonstrating no significant increase in the frequency of Ca^{2+} transients and no change in diastolic Ca^{2+} levels (mean ± SEM). The change in Ca^{2+} transient amplitude is plotted per individual fish, demonstrating no consistent positive response towards treatment. The correlation plot of the change in diastolic Ca^{2+} level versus the change in Ca^{2+} transient amplitude after sympathetic stimulation presents a significant correlation, which is positive as well as negative (p=0.0004, R2=0.80). AU: arbitrary units.

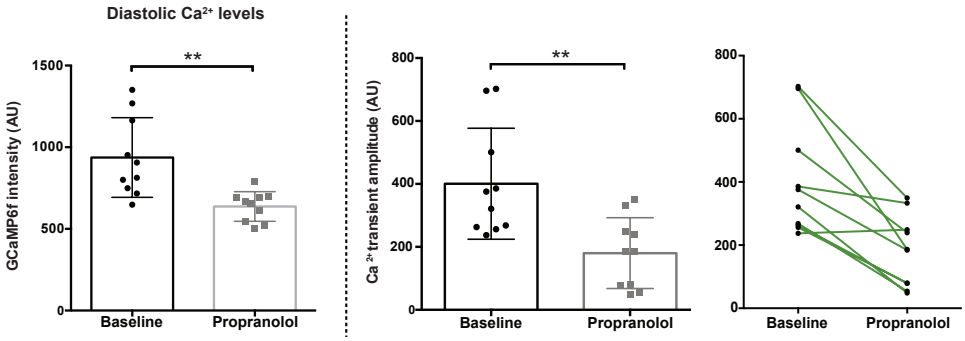

Figure S4. In vivo effect of sympathetic inhibition on Ca^{2+} dynamics in GCaMP6f fish. 3 dpf GCaMP6f fish were treated for 30 min with β-adrenergic receptor antagonist propranolol (100 μM), n=10. Bar graphs demonstrating a significant decrease in diastolic Ca^{2+} levels ($p \leq 0.01$) (left panel) and Ca^{2+} transient amplitude ($p \leq 0.01$) (middle panel) after treatment (mean ± SEM). Change in Ca^{2+} transient amplitude is plotted per individual fish (right panel), demonstrating a clear decrease in 9/10 fish after treatment (right panel). AU: arbitrary units.

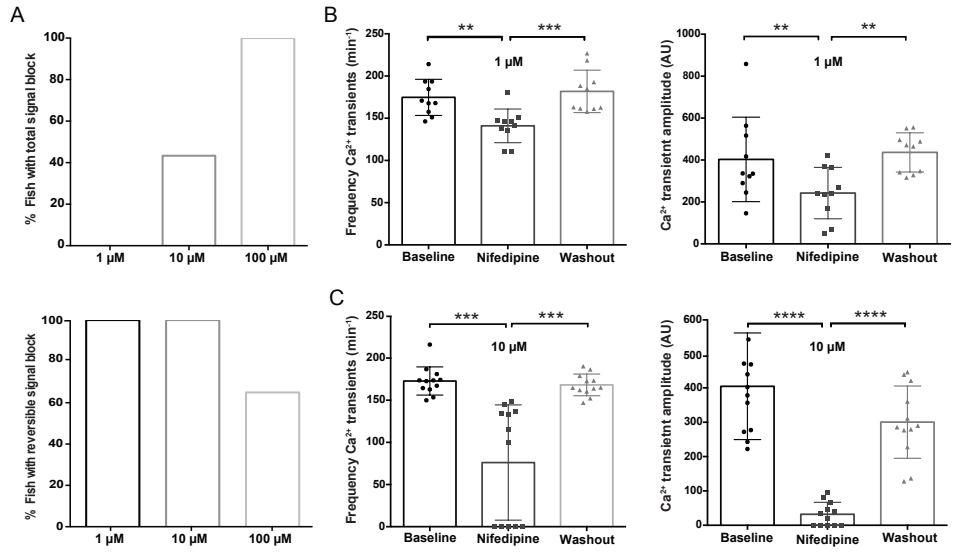

Figure S5. Dose-response effect of nifedipine on ventricular Ca^{2+} dynamics in GCaMP6f fish. 3dpf GCaMP6f fish were treated for 30 min with 1, 10 and 100 µM nifedipine. (A) Bar graphs demonstrating the percentage of fish in which the ventricular GCaMP6f signal was blocked 100% after treatment (top panel) and the percentage of fish in which this block was reversible after washout in E3 medium for 180 min (bottom panel). Y-axis numbers are representable for the signal intensity across the entire heart tube. No total signal block was observed after 1 µM treatment, but there was a total block in 41.7% of fish when treated with 10 µM and total block in 100% of the fish when treated with 100 µM nifedipine. In addition, this total block was reversible in all fish after treatment with 10 µM and in 65% of fish treated with 100 µM nifedipine (data are presented as mean, 1 µM: n=10, 10 µM: n=12, 100 µM: n=19). (B) Bar graphs demonstrating a significant decrease in Ca^{2+} transient frequency ($p \leq 0.01$) and Ca^{2+} transient amplitude ($p \leq 0.01$) after 1 µM nifedipine treatment. These parameters recovered to baseline levels after washout (mean ± SEM, frequency $p \leq 0.001$, amplitude $p \leq 0.01$). (C) Bar graphs demonstrating a significant decrease in Ca^{2+} transient frequency ($p \leq 0.001$) and Ca^{2+} transient amplitude ($p \leq 0.0001$) after 10 µM nifedipine treatment. These parameters significantly recovered after washout (mean ± SEM, frequency $p \leq 0.001$, amplitude $p \leq 0.0001$). AU: arbitrary units.

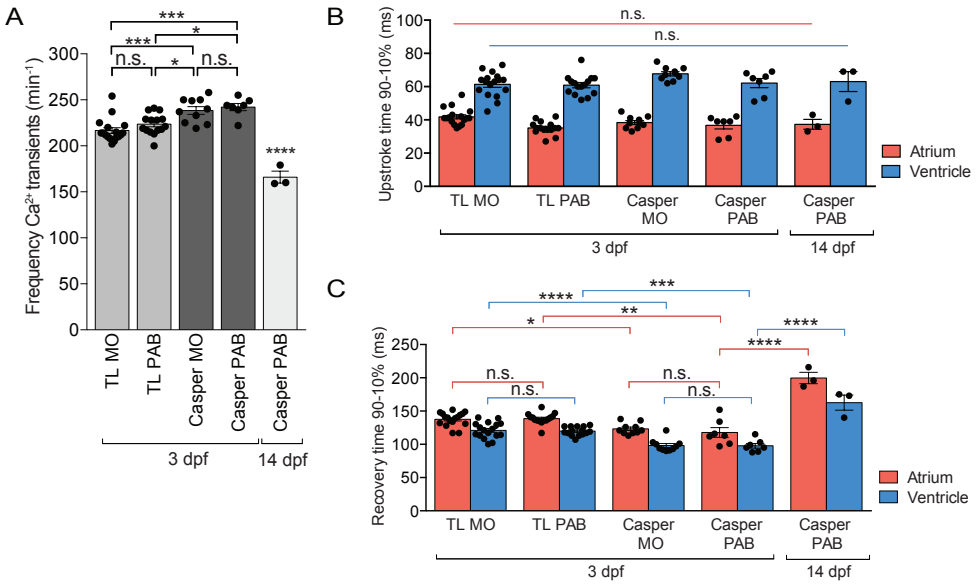

Figure S6. In vivo Ca^{2+} dynamics of embryonic zebrafish with different genetic backgrounds and different types of contraction block. Comparison in Ca^{2+} transient dynamics between different experimental groups (TL MO n=17, TL PAB n=15, casper MO n=10, casper PAB n=7, 14 dpf casper PAB n=3). (A) Bar graphs demonstrating no significant difference in Ca^{2+} transient frequency between MO and PAB treated fish within the TL or casper background. Embryonic casper fish have a higher Ca^{2+} transient frequency compared to embryonic TL fish. Ca^{2+} transient frequency is significant lower in 14 dpf juvenile fish compared to both 3 dpf casper and TL fish (mean ± SEM, * p≤0.05, *** p≤0.001, one-way ANOVA). (B) Bar graphs demonstrating no significant differences in atrial and ventricular upstroke time between TL and casper fish, between 3 dpf and 14 dpf, nor between MO and PAB treated fish (mean ± SEM, one-way ANOVA). (C) Bar graphs demonstrating a significant difference in atrial and ventricular Ca^{2+} transient recovery time in 3 dpf TL versus 3 dpf casper fish, as well as a significant difference in atrial and ventricular Ca^{2+} transient recovery time of 3 dpf versus 14 dpf casper fish (mean ± SEM, * p≤0.05, ** p≤0.01, *** p≤0.001, **** p≤0.0001, one-way ANOVA). No significant differences were observed between MO and PAB treated fish (mean ± SEM, one-way ANOVA). MO: morpholino; PAB: para-amino-blebbistatin; TL: Tupfel long fin.

Supplemental movie legends

Supplemental movies can be found at journal website: http://www.thno.org/v08p4750.htm

Movie S1. In vivo recording of chimeric VSFP-butterfly CY signals in the embryonic zebrafish heart. Using the high-speed epifluorescent microscope, a movie of the 3 dpf non-contracting chimeric VSFP-butterfly CY embryonic heart was recorded. Fluorescence was recorded in two channels, the mCitrine signal can be seen in the top panel and mCerulean in the bottom panel. Upon each membrane depolarization a slight increase of mCitrine intensity and a slight decrease of mCerulean intensity can be detected. Signal intensity changes are hard to detect by eye, but easily collected via signal analysis in imageJ (see Figure 2). A: atrium; V: ventricle.

Movie S2. In vivo recording of GCaMP6f signals in the embryonic zebrafish heart. Using the high-speed epifluorescent microscope, a movie of the 3 dpf non-contracting GCaMP6f embryonic heart was recorded. Upon the increase in cytosolic Ca^{2+} levels an increase of cpEGFP intensity can be detected. Atrial-ventricular activation is easily visible by eye. A: atrium; V: ventricle.

Movie S3. Desynchronized electrical impulse propagation after nifidipine treatment in the embryonic zebrafish heart. Using the high-speed epifluorescent microscope, a movie of the 3 dpf non-contracting chimeric VSFP-butterfly CY embryonic heart, treated with 100 µM nifedipine, was recorded. Ratiometric mCitrine and mCeruelan signals over the atrium and ventricle were converted into a color-coded movie, presented by a 32-color gradient. The disturbed atrial-ventricular electrical impulse propagation is detectable by an asynchronous activation pattern. A: atrium; V: ventricle.

Movie S4. In vivo recording of GCaMP6f signals in the juvenile zebrafish heart. Using the high-speed epifluorescent microscope, a movie of the 14 dpf GCaMP6f juvenile heart was recorded, contraction is partly inhibited using para-amino-blebbistatin (PAB). Upon the increase in cytosolic Ca^{2+} levels an increase of cpEGFP intensity can be detected. Atrial-ventricular activation is visible by eye. A: atrium; V: ventricle.

Part 2

Using zebrafish to study the genetics of cardiac arrhythmias

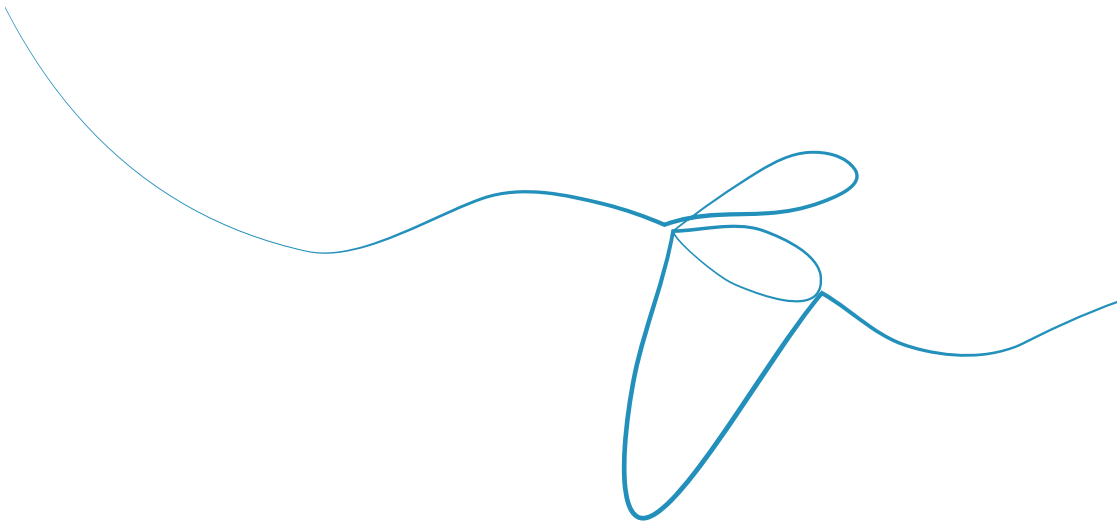

CHAPTER 4

GNB5 Mutations Cause an Autosomal-Recessive Multisystem Syndrome with Sinus Bradycardia and Cognitive Disability

Lodder E.M.*, De Nittis P.*, Koopman CD*, Wiszniewski W., Moura de Souza CF, Lahrouchi N., Guex N., Napolioni V., Tessadori F., de Boer T., Beekman L., Nannenberg E.A., Boualla L., Blom NA, de Graaff W., Kamermans M., Cocciadiferro D., Malerba N., Mandriani B., Coban Akdemir ZH, Fish RJ, Eldomery MK, Ratbi I., Wilde AAM, de Boer TP, Simonds WF, Neerman-Arbez M., Sutton VR, Kok F., Lupski JR, Reymond A.#, Bezzina CR#, Bakkers J#, Giuseppe Merla#

*# contributed equally

American Journal of Human Genetics 2016;99(3):786

Abstract

GNB5 encodes the G protein β subunit 5 and is involved in inhibitory G protein signaling. Here, we report mutations in *GNB5* that are associated with heart-rate disturbance, eye disease, intellectual disability, gastric problems, hypotonia, and seizures in nine individuals from six families. We observed an association between the nature of the variants and clinical severity; individuals with loss-of-function alleles had more severe symptoms, including substantial developmental delay, speech defects, severe hypotonia, pathological gastro-esophageal reflux, retinal disease, and sinus-node dysfunction, whereas related heterozygotes harboring missense variants presented with a clinically milder phenotype. Zebrafish *gnb5* knockouts recapitulated the phenotypic spectrum of affected individuals, including cardiac, neurological, and ophthalmological abnormalities, supporting a direct role of GNB5 in the control of heart rate, hypotonia, and vision.

Keywords: whole-exome sequencing, heart rate, intellectual disability, hypotonia, G-protein signaling, parasympathetic system

Main text

Heterotrimeric G proteins trigger a signal transduction cascade composed of α, β, and γ subunits. They are associated with G protein-coupled receptors (GPCRs) in modulating an array of cellular functions, including release of a multitude of hormones and growth factors, regulation of cell contraction and migration, and cell growth and differentiation during development.[1,2,3,4] G protein-coupled signaling plays a crucial role in neuronal communication, including regulation of the antagonistic effects of the parasympathetic and sympathetic branches of the autonomic nervous system throughout the body. We report a genetic disorder caused by mutations affecting *GNB5* (MIM:604447), encoding guanine nucleotide-binding protein subunit beta-5, and with disease manifestation in multiple systems.

We identified nine affected individuals (six females and three males) from six unrelated families presenting with a clinical overlap of neurological and cardiac conduction defects; all subjects were found to have variation in the same gene, *GNB5*, and share a similar rare phenotype. This work results from exome and phenotype data aggregation among independent groups engaged in studying the molecular basis of yet unsolved human genetic rare disease traits. Shared phenotypic features representing the cardinal characteristics of the syndrome include global developmental delay, seizures, generalized hypotonia, retinal disease, and the uncommon feature of early-onset sinus-node dysfunction (Table 1). Additional clinical investigations and diagnostic studies did not show any evidence of structural CNS, ocular, or cardiac anomalies. Affected individuals from four of the six families (families A–D) demonstrated the severe end of the disease spectrum, including substantial cognitive deficits, delayed motor development, severe hypotonia, retinal disease, pathological gastro-esophageal reflux, and sinus-node dysfunction. Affected individuals in families E and F presented with a milder phenotype, including mild intellectual impairment, language delay, and bradycardia (Figure 1, Table 1, Supplemental Note).

Given that no potentially pathogenic genomic structural abnormalities were identified by array comparative genomic hybridization and karyotyping of the affected subjects, we applied whole-exome sequencing to all the affected individuals and their healthy parents. Families were recruited in Italy (family A), Brazil (B and F), the United States (C and D), and the Netherlands (E). The institutional review boards of the IRCCS Casa Sollievo Della Sofferenza Hospital, the Hospital das Clínicas da Universidade de São Paulo, the Baylor College of Medicine, the Amsterdam Academic Medical Center, and the University of Lausanne approved this study. Participants were enrolled after written informed consent was obtained from parents or legal guardians. The clinical evaluation included medical history interviews, a physical examination, and review of medical records. To uncover genetic variants associated with the complex phenotype shown by the nine affected subjects, we sequenced their exomes and those of their parents. DNA libraries were prepared from blood-derived genomic DNAs according to standard procedures. Exomes were captured and sequenced with different platforms to reach 50- to 120-fold coverage on average. Variants were called as previously described.[5,6,7] Variants were filtered on the basis of inheritance

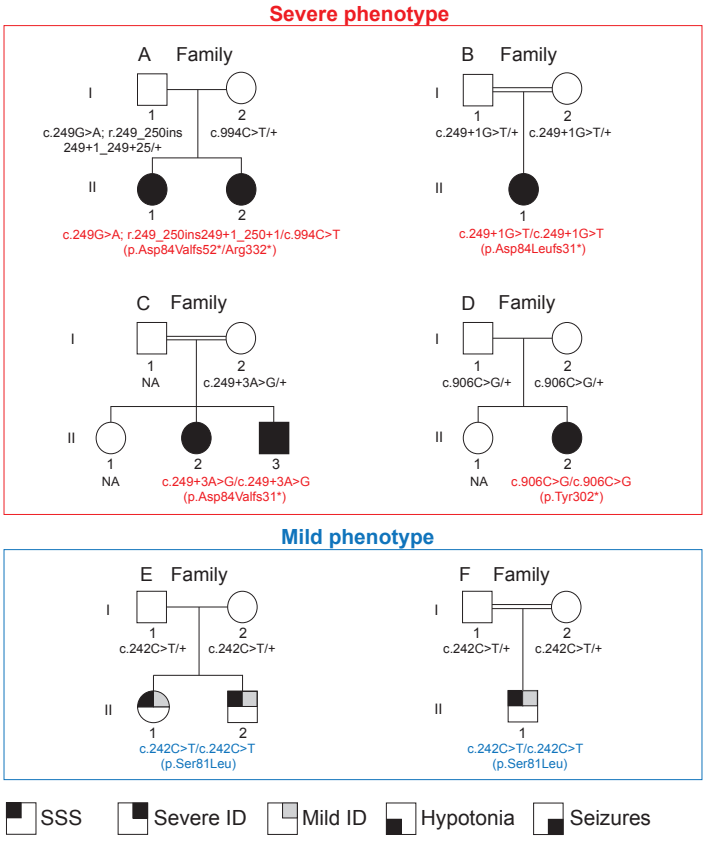

Figure 1. Pedigrees from the Six Families Investigated in this Study. Affected members of families A to D (upper red-lined panel) and E to F (lower blue-lined panel) show severe and mild manifestation of the core symptoms of the syndrome defined in this study. Filled symbols represent individuals with severe sinus sick syndrome (SSS; top left quarter), intellectual disability (ID; top right quarter), hypotonia (bottom left quarter), and seizures (bottom right quarter), whereas a light-gray top left quarter indicates the presence of mild ID. Genotypes are specified according to GenBank: NM_006578.3.

patterns, including autosomal recessive, X-linked, and de novo and/or autosomal dominant. Variants with MAF < 0.05% in control cohorts (dbSNP, the 1000 Genome Project, NHLBI GO Exome Sequencing Project, the Exome Aggregation Consortium database, and our in-house databases) and predicted to be deleterious by SIFT,[8] PolyPhen-2,[9] and/or UMD-Predictor[10] were prioritized.

Given a potential history of consanguinity reported in some families (families B, C, and F (Figure 1, Table 1), we filtered variants by using Mendelian expectations for the assumption of

Table S1. Affected individual numbers refer to those in the pedigree in Figure 1. Complete pedigree charts, consanguinity status, variants, and related homozygous and/or compound heterozygous alleles are reported in Figure 1 and Table S1. Abbreviations are as follows: M, male; f, female; NA, not available; +, clinical trait present; –, clinical trait not present; PFO, patent foramen ovale; bpm, beats per minute; implant., implantation; abn., abnormalities.

Table 1: Overlapping clinical features of individuals with *GNB5* Mutations

	Family A		Family B	Family C		Family D	Family E		Family F
	II.1	II.2	II.1	II.2	II.3	II.2	II.1	II.2	II.1
Gender, Age	F, 22	F, 20	F, 6	F, 11	M, 9	F, 12	F, 13	M, 8	M, 23
Birth weight	3580 g (50th percentile)	NR	2980 g (15th percentile)	2751 g (15 th percentile)	NA	2845 g (15th percentile)	NR	NR	NR
Ethnicity	Italy	Italy	Jordan	Puerto Rico	Puerto Rico	India	Morocco	Morocco	Brazil
Consanguinity	-	-	+	+	+	-	-	-	+
Altered speech development	+	+	+	+	+	+	+	+	NA
- Verbal understanding	NA	NA	nonverbal	unremarkable	unremarkable	NA	NA	NA	NA
- Lexical production	NA	NA	nonverbal	delayed	delayed	nonverbal	delayed	delayed	NA
Intellectual disability (ID)	+	+	+	+	+	+	mild	mild	Mild
Epilepsy	+	+	+	-	-	+	-	-	-
Sinus Sick Syndrome (SSS)	+	+	+	+	+	increased PR interval (intermittent Weckenbach)	+	+	+
- Minimum heart rate	24	39	NA	paced	paced	NA	20	16	
- Maximum heart rate	163	192	NA	paced (27% heartbeats on Holter)	paced (20% heartbeats on Holter)	NA	176	180	NA
- Chronotropic response	NA	NA	NA	+	+	NA	unremarkable	unremarkable	NA
- Escape beats	+	+	NA	paced	paced	NA	+	+	NA
- Pacemaker implant.	-	-	-	+	+	-	-	+	NA
- Heart structural abn.	-	PFO	NA	-	-	-	-	-	NA
Hypotonia	+	+	+	+	+	+	-	impaired fine motor skills	-
Pathological gastric reflux	+	+	-	+	+	+	-	-	NA
Nystagmus	+	+	+	+	+	+	NA	-	NA
Metabolic work-up									
- Plasma amino acids chromatography	938 µm/l (restored)	+ (restored)	unremarkable	unremarkable	unremarkable	unremarkable	444 µm/l	unremarkable	NA
- Urine organic acids	unremarkable	unremarkable	increased excretion of 3-methyl-glutaconic acid	unremarkable	unremarkable	unremarkable	NA	NA	NA

a rare autosomal-recessive trait. We found *GNB5* to be compliant with Mendelian expectations and bearing bi-allelic putative deleterious variants in all affected individuals (Figure 1, Table S1). Sanger sequencing in each family confirmed the anticipated segregation of the *GNB5* variants. Strikingly, the variants found in the severely affected individuals (families A–D) were predicted to be loss-of-function (LoF) alleles, whereas the more mildly affected individuals from families E and F were homozygous for the same missense variant, c.242C>T (p.Ser81Leu [GenBank: NM_006578.3]) (Figures 1 and S1A). In families B, C, and D the affected individuals were homozygous for splice variants (c.249+1G>T [p.Asp84Leufs31*] and c.249G+3A>G [p.Asp84Valfs31*]) and a nonsense variant (c.906C>G [p.Tyr302*]), respectively (Figures 1 and S1A, Table S1). In family A, the affected siblings were compound heterozygous for a maternally inherited nonsense variant (c.994C>T [p.Arg332*]) and a paternally inherited splice-site change (c.249G>A [p.(=)]), which gives rise to an aberrantly spliced isoform containing an additional 25 nucleotides of the intervening intron 2 (Figure S2A). We experimentally show that the transcripts from both alleles are targeted by nonsense-mediated mRNA-decay (Figure S2B).

The five *GNB5* LoF variants identified in families A–D are either not present or present with MAF ≤ 8.25×10^{-6} in ExAC (Exome Aggregation Consortium, v.0.3.1) (Table S1). Correspondingly, LoF variants in *GNB5* are underrepresented in comparison to expectation in this database; specifically, ExAC reports 8 LoF variants whereas 19 were expected. The c.242C>T (p.Ser81Leu) missense variant identified in family E, of Moroccan ancestry, and family F, of Brazilian ancestry, has a MAF < 5×10^{-5} (6/121,000) in the human population and 4.3×10^{-4} in Latinos (5/11,574). A sample of individuals from Morocco identified a prevalence of 1 out of 1,260 (7.94×10^{-4}) for this allele. We estimated the prevalence of the c.242C>T (p.Ser81Leu) variant in the Moroccan population by genotyping a total of 630 Moroccan individuals, including 394 Moroccans and 235 Dutch citizens of Moroccan descent by real-time PCR. Pathogenicity of this variant is further supported by three-dimensional representation of the encoded protein complexed with RGS9, a member of the R7 subfamily of regulators of G-protein signaling (RGS) proteins and common binding partner of GNB5. GNB5 is folded into essentially identical seven-bladed β-propellers (WD40 repeated domains) with equivalent N-terminal helical extensions.[11] Replacement of the evolutionarily conserved serine 81 (Figure S1B) by leucine will induce localized structural changes in the immediate vicinity of this residue, which could impair both the central pore of the β-propeller and the binding kinetics of RGS proteins (Figures S3– S5).

In line with the clinical presentation of affected individuals, Gnb5 ablation in mice resulted in marked neurobehavioral abnormalities, including learning deficiencies, hyperactivity, impaired gross motor coordination, abnormal gait,[12] defective visual adaptation,[13] and perturbed development and functioning of retinal bipolar cells.[14] Correspondingly, mice lacking Rgs6, the GNB5-dependent RGS protein enriched in heart tissue, exhibit bradycardia and hypersensitivity to parasympathomimetics.[15,16] To independently investigate the functional effects of variation of GNB5 in the full phenotypic spectrum of subjects reported herein, we engineered a zebrafish model knocked out for *gnb5*.

CRISPR/Cas9 genome editing was used to generate zebrafish with LoF mutations in *gnb5a* and *gnb5b*. This teleost has two *GNB5* paralogs as a result of an ancient genome duplication event[17] (Figure S6). We identified stable lines with a 7 bp insertion in *gnb5a* and a 8 bp deletion and 15 bp insertion in *gnb5b*, causing a frameshift and premature truncation of the encoded proteins, respectively (Figure S7). It was anticipated that *gnb5a* and *gnb5b* might have redundant functions, which was confirmed by the absence of overt phenotypes in embryos homozygous for either LoF mutations. As a consequence, a double knockout was generated to ensure complete loss of functional Gnb5. In-crosses of *gnb5a* and *gnb5b* double heterozygotes resulted in clutches of embryos containing the expected 6.25% of *gnb5a*$^{-/-}$/*gnb5b*$^{-/-}$ double mutants (henceforth referred to as *gnb5* mutants). Consistent with syndrome manifestations of affected individuals, zebrafish mutant embryos had no striking dysmorphologic features (Figure S7D). However, the

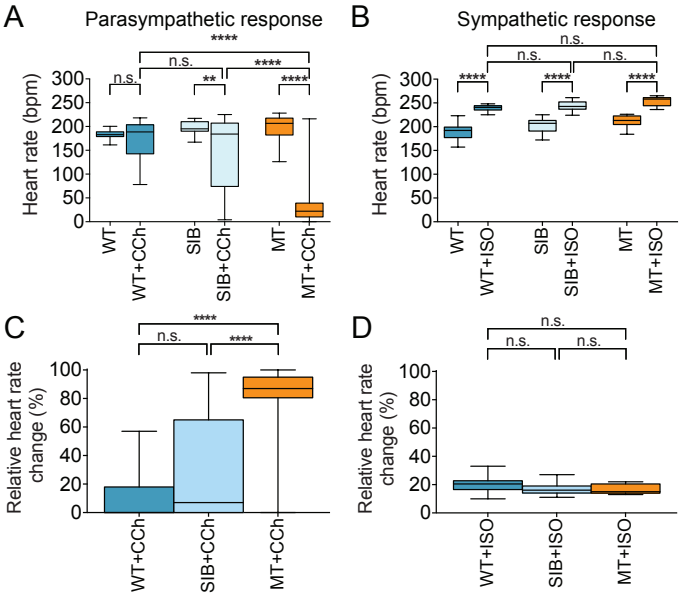

Figure 2. Cardiac Function in *gnb5* Mutant Zebrafish. (A–D) Box-whisker plots demonstrate the heart rate response and the relative heart rate change of 5 dpf wild-type (WT), sibling (SIB), and *gnb5* mutant (MT) larvae. Embryos at 5 dpf were embedded in 0.3% agarose prepared in E3 medium containing 16 mg/ml Tricaine. Basal heart rates were recorded first. Then, (A and C) 400 µM of the parasympathetic agonist carbachol (CCh; Sigma-Aldrich C4382) (WT n = 10, SIB n = 39, MT n = 14) or (B and D) 100 µM of the sympathetic agonist isoproterenol hydrochloride (ISO; Sigma-Aldrich 1351005) (WT n = 12, SIB n = 22, MT n = 9) was added and incubated for 30 min and heart rates were measured. Recordings were performed at 150 frames per second and were analyzed with ImageJ. The relative heart rate change is the percentage change between the basal heart rate measured and the heart rate after addition of CCh or ISO. n denotes the number of fish used per dataset. Differences between two groups were analyzed via the Student's t test. Differences between more than two groups were analyzed via one-way ANOVA with Tukey's post-hoc test. Data are shown as mean ± SEM, and $p < 0.05$ was considered significant. $^{*}p < 0.05$, $^{**}p \leq 0.01$, $^{***}p \leq 0.001$, $^{****}p \leq 0.0001$. $p > 0.05$ was considered not significant (n.s.). bpm, beats per minute.

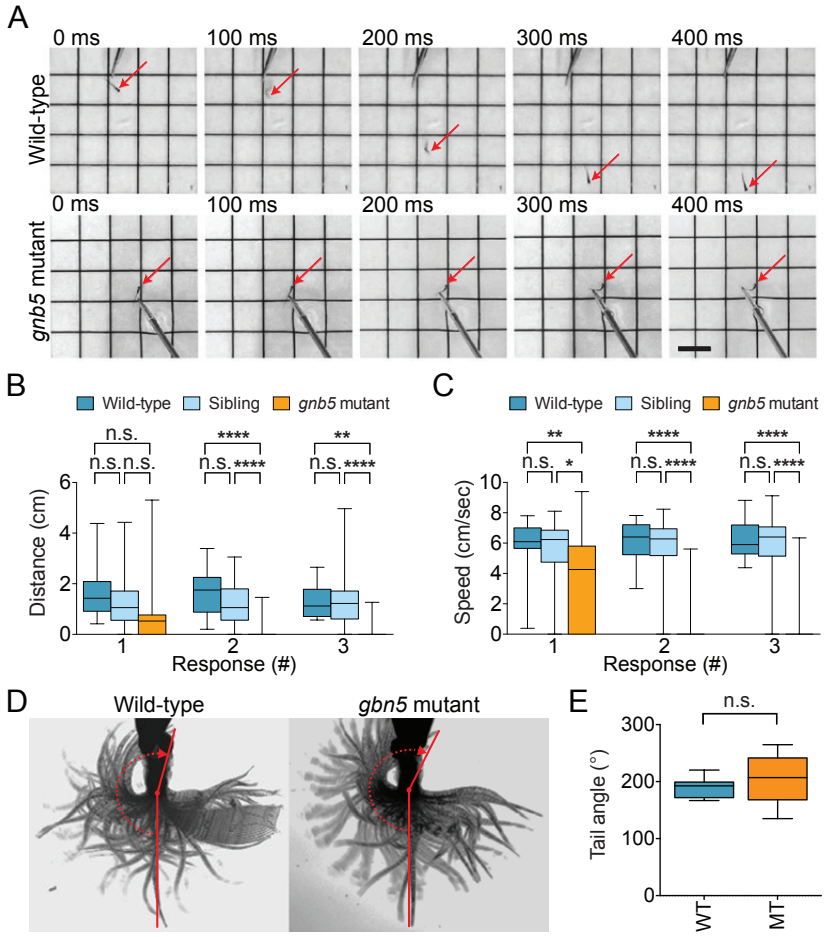

Figure 3. Neurologic Function in *gnb5* Mutant Zebrafish. (A–C) Touch-evoked escape response assay in which three consecutive tactile stimuli were applied. Embryos at 3 dpf were placed in the middle of a standard 88 mm petri dish containing E3 medium. Three consecutive tactile stimuli were applied by touching the tail of the embryo with an insect pin. Stimuli were only applied when the embryo was still. Behavior was recorded with a standard camera (30 fps) and analyzed with ImageJ (NIH) and the plugin MTrackJ.19 (A) shows representative responses of 3 dpf wild-type and *gnb5* mutant embryos to a touch stimulus. Scale bar, 0.5 cm. Box-whisker plots show quantification of the (B) swimming distance and (C) swimming speed in TL wild-types (n = 19), siblings (n = 46), and *gnb5* mutants (n = 27). (D and E) Analysis of maximum tail movement at 5 dpf. Larvae at 5 dpf were sedated in E3 containing 16 mg/ml Tricaine and embedded in 0.5% UltraPureTM agarose (Invitrogen 16500-500) in a 35 mm glass bottom dish. After setting, the agarose was cut away caudal to the swimming bladder, leaving the tail free to move. The dish was filled with E3 medium and embryos were left to recover from the sedation for 10 min at 28°C. Next, a maximal escape response was elicited by repeatedly touching the head of the embryo with an insect pin. Recordings were performed at 280 fps, for 30 s, with a high-speed CCD camera (Hamamatsu Photonics K.K., C9300-221) and analyzed with ImageJ (angle tool). (D) shows representative minimum projection images of tail movement in wild-type and *gnb5* mutant embryos, including tail angle analysis. The tail angle represents the angle between the head-tail midline axis in resting state

and a line that was drawn from just caudal of the swimbladder to the tip of the tail at maximal tail movement. (E) Tail angle quantification is displayed in box-whisker plots (wild-type n = 10, *gnb5* mutants n = 10). fps, frames per second. n denotes the number of fish used per dataset. Differences between two groups were analyzed via the Student's t test. Differences between more than two groups were analyzed via one-way ANOVA with Tukey's post-hoc test. Data are shown as mean ± SEM, and $p < 0.05$ was considered significant. *$p < 0.05$, **$p \leq 0.01$, ***$p \leq 0.001$, ****$p \leq 0.0001$. $p > 0.05$ was considered not significant (n.s.).

larvae showed impaired swimming activity, remained small, and generally died 7–14 days post fertilization (dpf), most likely as a result of their inability to feed.

To assess the putative involvement of GNB5 in autonomic nervous system functions, we investigated the GNB5-RGS-GIRK channel pathway. As GNB5 recruits RGS proteins to G protein-coupled inward rectifier potassium (GIRK) channels involved in the hyperpolarization of cell membranes,[16,18] we investigated whether LoF of GNB5 could delay GIRK channel deactivation kinetics, increase hyperpolarization time of cell membranes, and impair cell responsiveness to new stimuli. Carbachol (PubChem CID: 5831) is a parasympathomimetic compound that activates acetylcholine receptors of the heart and the GNB5-RGS-GIRK channel pathway. Treatment of *gnb5* mutant larvae with carbachol resulted in a strong decrease of the heart rate, whereas it had little effect on wild-type and sibling larvae (Figure 2), consistent with loss of negative regulation of the cardiac GIRK channel by GNB5-RGS. In contrast, treatment with the sympathetic agonist isoproterenol resulted in an increased heart rate that was similar in wild-type, sibling, and *gnb5* mutant larvae (Figure 2). These results indicate that GNB5 is crucial for parasympathetic control of heart rate, but not for sympathetic control, suggesting that lack of GNB5 is associated with extreme bradycardia at rest. Correspondingly, affected individuals present with severe bradycardia at rest (minimal observed heart rates of <25 bpm [beats per minute]) combined with a normal chronotropic response (maximum heart rates >150 bpm).

The severe muscle hypotonia reported in affected individuals could result from GIRK-mediated hyperpolarization of neurons controlling skeletal muscle tone. *gnb5* mutant embryos hatched normally from their chorion, a process that requires muscle contraction, but their swimming behavior appeared abnormal at 3 dpf. To investigate whether this abnormal behavior was linked to neurologic dysfunction and hypotonia, we examined the touch-evoked escape response. We anticipated that neurons would only become fully hyperpolarized after an initial stimulus and thus presented the embryos with three consecutive tactile stimuli. Whereas wild-type larvae rapidly swam away in response to repeated tactile stimuli, *gnb5* mutants showed a significant decrease in swimming distance and swimming speed at stimuli two ($p \leq 0.0001$) and three ($p \leq 0.01$), but not after the first stimulus (Figures 3A–3C). Accordingly, *gnb5* mutant larvae were predominantly unresponsive to repeated tactile stimuli (Movies S1 and S2). To test whether this abnormal escape response is the consequence of neurologic dysfunction rather than reduced muscle function, we performed a tail movement assay. 5 dpf larvae were given a strong tactile stimulus while we recorded the movement of the tail (Figures 3D and 3E). No significant difference in the maximum

tail angle was detected between wild-type and *gnb5* mutant larvae (Figure 3E). These results indicate that the tail muscles of *gnb5* mutants are fully functional and that the abnormal escape response is associated with neurological dysfunction and possibly muscle hypotonia.

Given that affected individuals have visual problems, including nystagmus, we investigated the visual system by measuring the optokinetic response (OKR) of *gnb5* mutant larvae. When wild-type larvae were placed in a drum with a rotating light stimulus (Figure S8A), the OKR consisted of smooth pursuit eye movements followed by rapid rest saccades in the opposite direction (Figure S8B, Movie S3). In contrast, OKR was completely absent in *gnb5* mutant larvae although their eyes showed no morphological abnormalities and could make eye movements (Figure S8C, Movie S4). This indicates that the eye muscles are functional in *gnb5* mutants but that proper eye-movement control depends on GNB5. Overall these data show that *gnb5* mutants faithfully recapitulate the phenotypic spectrum of affected individuals, including cardiac, neurologic, and ophthalmologic abnormalities.

These results provide evidence for a direct role of GNB5 in the control of heart rate, motor capacity, and vision. Whereas GNB1 (MIM: 139380), GNB2 (MIM: 139390), GNB3 (MIM: 139130), and GNB4 (MIM: 610863) are widely expressed and encode highly homologous proteins,[20] GNB5 is preferentially expressed in the brain and nervous system and encodes a peptide with less homology with its four paralogs.[21,22]

Germline de novo *GNB1* variants cause severe neurodevelopmental disability,[23] hypotonia, and seizures. *GNB3* bi-allelic LoF has been linked to congenital stationary night blindness (MIM: 610445, 163500, 610444, 613830, 616389, 310500, 257270, 613216, 614565, 615058, 300071, and 610427) and recessive retinopathy in humans,[24,25] retinal degeneration in chickens,[26] and reduced cone sensitivity and mild bradycardia in mice.[27,28] A SNP in *GNB3* was associated with postural tachycardia syndrome[29] and incidence of cardiovascular disease and stroke.[30] Similarly, *GNB2* and *GNB4* map to loci governing heart rate on chromosomes 7 and 3, respectively.[31,32] We hereby demonstrate that bi-allelic LoF and missense variants in *GNB5* cause a multisystem syndrome with features that include global developmental delay, sinus-node dysfunction, seizures, eye abnormalities, gastric problems, and generalized hypotonia. We highlight the importance of GNB5 for neuronal signaling, including the regulation of the antagonistic effects of the parasympathetic and sympathetic nervous system.

Supplemental Data

Supplemental Data includes supplemental acknowledgments, a supplemental note, eight figures, one table, and four movies and can be found with this article online at http://dx.doi.org/10.1016/j.ajhg.2016.06.025.

Conflicts of interest statement

JRL has stock ownership in 23andMe, is a paid consultant for Regeneron Pharmaceuticals, has stock options in Lasergen, Inc., is a member of the Scientific Advisory Board of Baylor Miraca

Genetics Laboratories, and is a co-inventor on multiple United States and European patents related to molecular diagnostics for inherited neuropathies, eye diseases and bacterial genomic fingerprinting. Baylor College of Medicine (BCM) and Miraca Holdings Inc. have formed a joint venture with shared ownership and governance of the Baylor Miraca Genetics Laboratories (BMGL), which performs clinical exome sequencing. The Department of Molecular and Human Genetics at Baylor College of Medicine derives revenue from the chromosomal microarray analysis (CMA) and clinical exome sequencing offered in the Baylor Miraca Genetics Laboratory (BMGL; http://www.bmgl.com/BMGL/Default.aspx website). GM is a paid consultant for Takeda Pharmaceutical Company Limited.

References

1. Daly AF, Lysy PA, Desfilles C, Rostomyan L, Mohamed A, Caberg JH, Raverot V, Castermans E, Marbaix E, Maiter D. GHRH excess and blockade in X-LAG syndrome. *Endocr Relat Cancer* 2016;23:161–170.
2. Daly AF, Yuan B, Fina F, Caberg JH, Trivellin G, Rostomyan L, de Herder WW, Naves LA, Metzger D, Cuny T. Somatic mosaicism underlies X-linked acrogigantism syndrome in sporadic male subjects. *Endocr Relat Cancer* 2016;23:221–233.
3. Trivellin G, Daly AF, Faucz FR, Yuan B, Rostomyan L, Larco DO, Schernthaner-Reiter MH, Szarek E, Leal LF, Caberg JH. Gigantism and acromegaly due to Xq26 microduplications and GPR101 mutation. *N Engl J Med* 2014;371:2363–2374.
4. Krishnan A, Mustafa A, Almén MS, Fredriksson R, Williams MJ, Schiöth HB. Evolutionary hierarchy of vertebrate-like heterotrimeric G protein families. *Mol Phylogenet Evol* 2015;91:27–40.
5. Alfaiz AA, Micale L, Mandriani B, Augello B, Pellico MT, Chrast J, Xenarios I, Zelante L, Merla G, Reymond A. *TBC1D7* mutations are associated with intellectual disability, macrocrania, patellar dislocation, and celiac disease. *Hum Mutat* 2014;35:447–451.
6. Borck G, Hög F, Dentici ML, Tan PL, Sowada N, Medeira A, Gueneau L, Holger T, Kousi M, Lepri F. *BRF1* mutations alter RNA polymerase III-dependent transcription and cause neurodevelopmental anomalies. *Genome Res* 2015;25:609.
7. Yuan B, Pehlivan D, Karaca E, Patel N, Charng WL, Gambin T, Gonzaga-Jauregui C, Sutton VR, Yesil G, Bozdogan ST. Global transcriptional disturbances underlie Cornelia de Lange syndrome and related phenotypes. *J Clin Invest* 2015;125:636–651.
8. Ng PC, Henikoff S. Predicting deleterious amino acid substitutions. *Genome Res* 2001;11:863–874.
9. Adzhubei IA, Schmidt S, Peshkin L, Ramensky VE, Gerasimova A, Bork P, Kondrashov AS, Sunyaev SR. A method and server for predicting damaging missense mutations. *Nat Methods* 2010;7:248–249.
10. Salgado D, Desvignes JP, Rai G, Blanchard A, Miltgen M, Pinard A, Lévy N, Collod-Béroud G, Béroud C. UMD-Predictor: A High-Throughput Sequencing Compliant System for Pathogenicity Prediction of any Human cDNA Substitution. *Hum Mutat* 2016;37:439–446.
11. Cheever ML, Snyder JT, Gershburg S, Siderovski DP, Harden TK, Sondek J. Crystal structure of the multifunctional Gbeta5-RGS9 complex. *Nat Struct Mol Biol* 2008;15:155–162.
12. Zhang JH, Pandey M, Seigneur EM, Panicker LM, Koo L, Schwartz OM, Chen W, Chen CK, Simonds WF. Knockout of G protein β5 impairs brain development and causes multiple neurologic abnormalities in mice. *J Neurochem* 2011;119:544–554.
13. Krispel CM, Chen CK, Simon MI, Burns ME. Novel form of adaptation in mouse retinal rods speeds recovery of phototransduction. *J Gen Physiol* 2003;122:703–712.
14. Rao A, Dallman R, Henderson S, Chen CK. Gbeta5 is required for normal light responses and morphology of retinal ON-bipolar cells. *J Neurosci* 2007;27:14199–14204.
15. Yang J, Huang J, Maity B, Gao Z, Lorca RA, Gudmundsson H, Li J, Stewart A, Swaminathan PD, Ibeawuchi SR. RGS6, a modulator of parasympathetic activation in heart. *Circ Res* 2010;107:1345–1349.
16. Posokhova E, Wydeven N, Allen KL, Wickman K, Martemyanov KA. RGS6/Gβ5 complex accelerates I_{KACh}

gating kinetics in atrial myocytes and modulates parasympathetic regulation of heart rate. *Circ Res* 2010;107:1350–1354.

17. Meyer A, Schartl M. Gene and genome duplications in vertebrates: the one-to-four (-to-eight in fish) rule and the evolution of novel gene functions. *Curr Opin Cell Biol* 1999;11:699–704.
18. Xie K, Allen KL, Kourrich S, Colón-Saez J, Thomas MJ, Wickman K, Martemyanov KA. Gbeta5 recruits R7 RGS proteins to GIRK channels to regulate the timing of neuronal inhibitory signaling. *Nat Neurosci* 2010;13:661–663.
19. Meijering E, Dzyubachyk O, Smal I. Methods for cell and particle tracking. *Methods Enzymol* 2012;504:183–200.
20. Gautam N, Downes GB, Yan K, Kisselev O. The G-protein betagamma complex. *Cell Signal* 1998;10:447–455.
21. Watson AJ, Katz A, Simon MI. A fifth member of the mammalian G-protein beta-subunit family. Expression in brain and activation of the beta 2 isotype of phospholipase C. *J Biol Chem* 1994;269:22150–22156.
22. Witherow DS, Slepak VZ. A novel kind of G protein heterodimer: the G beta5-RGS complex. *Receptors Channels* 2003;9:205–212.
23. Petrovski S, Kury S, Myers CT, Anyane-Yeboa K, Cogne B, Bialer M, Xia F, Hemati P, Riviello J, Mehaffey M. Germline De Novo Mutations in *GNB1* Cause Severe Neurodevelopmental Disability, Hypotonia, and Seizures. *Am J Hum Genet* 2016 May;98(5):1001-1010
24. Vincent A, Audo I, Tavares E, Maynes JT, Tumber A, Wright T, Li S, Michiels C, Consortium GNB, Condroyer C. Biallelic Mutations in *GNB3* Cause a Unique Form of Autosomal-Recessive Congenital Stationary Night Blindness. *Am J Hum Genet* 2016 May;98(5):1011-1019
25. Arno G, Holder GE, Chakarova C, Kohl S, Pontikos N, Fiorentino A, Plagnol V, Cheetham ME, Hardcastle AJ, Webster AR. Recessive Retinopathy Consequent on Mutant G-Protein beta Subunit 3 (GNB3). *JAMA Ophthalmol* 2016 Aug;134(8):924-7
26. Tummala H, Ali M, Getty P, Hocking PM, Burt DW, Inglehearn CF, Lester DH. Mutation in the guanine nucleotide-binding protein beta-3 causes retinal degeneration and embryonic mortality in chickens. *Invest Ophthalmol Vis Sci* 2006;47:4714–4718.
27. Nikonov SS, Lyubarsky A, Fina ME, Nikonova ES, Sengupta A, Chinniah C, Ding XQ, Smith RG, Pugh EN Jr, Vardi N, Dhingra A. Cones respond to light in the absence of transducin β subunit. *J Neurosci* 2013;33:5182–5194.
28. Ye Y, Sun Z, Guo A, Song LS, Grobe JL, Chen S. Ablation of the *GNB3* gene in mice does not affect body weight, metabolism or blood pressure, but causes bradycardia. *Cell Signal* 2014;26:2514–2520.
29. Nakao R, Tanaka H, Takitani K, Kajiura M, Okamoto N, Kanbara Y, Tamai H. *GNB3* C825T polymorphism is associated with postural tachycardia syndrome in children. *Pediatr Int* 2012 Dec;54(6):829-37
30. Zhang L, Zhang H, Sun K, Song Y, Hui R, Huang X. The 825C/T polymorphism of G-protein beta3 subunit gene and risk of ischaemic stroke. *J Hum Hypertens* 2005;19:709–714.
31. den Hoed M, Eijgelsheim M, Esko T, Brundel BJ, Peal DS, Evans DM, Nolte IM, Segrè AV, Holm H, Handsaker RE, et al. Identification of heart rate-associated loci and their effects on cardiac conduction and rhythm disorders. *Nat Genet* 2013 Jun;45:621–631.

32. Smolock EM, Ilyushkina IA, Ghazalpour A, Gerloff J, Murashev AN, Lusis AJ, Korshunov VA. Genetic locus on mouse chromosome 7 controls elevated heart rate. *Physiol Genomics* 2012;44:689–698.

Supplemental text

Case Reports

Family A: The proband (A.II.2, Figure 1) is a 20-year-old woman born from healthy non-consanguineous parents of Italian ancestry. Clinical synopsis includes severe ID and speech disorder, nystagmus, bradyarrhythmia, postural defects, epilepsy, hypotonia, and pathological gastric reflux. Brain magnetic resonance imaging (MRI) at 2 years of age was normal. Electroencephalography (EEG) reported signs of disordered electrogenesis and changes in vigil-state brain bioelectric activity. Episodes of sudden sinus pauses followed by junction escape beats were observed. Cardiac echocardiogram (ECHO) revealed Patent Foramen Ovale (PFO). Ophthalmology records reported retinal degeneration; ISCEV standard Electroretinogram (ERG) was electronegative. Amniotic fluid chromosome analysis was normal.

The proband's 22-year-old sister (A.II.1, Figure 1) presented with severe ID hypotonia, nystagmus, epilepsy, and pathological gastric reflux. Brain MRIs, at 14 months and 9 years of age, revealed no clinically substantial alterations. Electroretinography and Visually Evoked Potentials (PEV) recording sessions revealed electronegative ERG and retinal degeneration with rods' involvement, respectively. Fundus photography documented thinned retinal vessels, oblique implantation of the optic nerve head, and no macular abnormalities or pigment accumulation. Electrocardiography (ECG) and Holter monitoring identified bradycardic sinus rhythm. Genomic array using the Affymetrix CytoScan HD (Affymetrix, Santa Clara, CA, USA) revealed no pathological CNVs.

Family B: The 6-year-old proband is the only child born to Jordanian first-cousin parents. She was born in Brazil by caesarean section after an uneventful pregnancy. At 2 months of age, she presented with infantile spasms with EEG demonstrating hypsarrhythmia. Treatments with vigabatrin and valproic acid were unsuccessful in controlling the seizures. When evaluated at 6 months of age, she had a profound developmental delay and, because of apneic spells and desaturation episodes, she was admitted in the Intensive Care Unit. She was not dysmorphic and internal organs were normal. A brain MRI performed at 1 year of age showed T2 hyperintensities in thalamus, globus pallidus and brainstem tegmentum (likely related to vigabatrin use). A second brain MRI performed two years later failed to show remarkable abnormalities. Acylcarnitine and plasma amino acids analyses were normal, whereas urine organic acid analysis showed an increase in 3-methyl-glutaconic acid. At 5 years of age, she was unable to support her head and had no eye contact.

Family C: The proband is an 11-year-old female (Figure 1). She presented with absent speech, severe ID, hyporeflexia and nystagmus. She is hypotonic with no head control and has never sat independently. ECG detected prolonged cardiac pauses and symptomatic chronotropic

incompetence that were treated with a pacemaker. EEG was normal. Brain MRI showed supratentorial volume loss anterior>posterior in a watershed distribution, attributed to episodes of hypotension. Skeletal muscle biopsy histopathology revealed focal z-band streaming and type 1 fiber predominance, with enlarged and abnormally shaped mitochondria, and increased glycogen as free particles. Severely decreased levels of ubiquinol cytochrome c-oxidoreductase (complex III) were reported, whereas PAA, UOA, and ACP were normal. Oligonucleotide/SNP array detected no pathogenic CNVs. Parents are consanguineous and of Puerto Rican Roma ancestry. There is a 9-year-old affected brother who was born at term by normal vaginal delivery after an uneventful pregnancy. He showed global developmental delay, nystagmus, sinus node dysfunction and gastric reflux. EEG investigation showed no disturbance of brain function. No structural abnormalities were identified by echocardiography (ECHO). A progressive cardiac arrhythmia with prolonged cardiac pauses resulted in the implantation of a pacemaker. Metabolic work-up (plasma amino acids (PAA), urine organic acids (UOA), and plasma acylcarnitine profile (ACP) was normal. Oligonucleotide and SNP arrays did not identify CNVs.

Family D: The proband is a female currently 12-years-old. She was born after a pregnancy characterized by decreased fetal movements. Her healthy parents are non-consanguineous individuals of Indian descent. She presented with severe cognitive and psychomotor delay, epilepsy and hypotonia. When awake, she has normal rhythm and PR intervals (i.e. time from the onset of the atrial depolarization to the start of the ventricular depolarization). In contrast when asleep she starts to increase her PR interval, suggestive of intermittent Wenckebach (i.e. progressive atrio-ventricular block resulting in irregular cardiac rhythm). No structural heart abnormalities were demonstrated on conventional ECHO. She has nystagmus and ophthalmological evaluation demonstrated abnormal ERG studies (both photopic and scotopic) and grossly normal funduscopic examination. She has a history of gastric reflux. The laboratory workup included metabolic studies, chromosome analysis and aCGH studies – all normal.

Family E: The proband was born to non-consanguineous, healthy parents of Moroccan ancestry after an uneventful pregnancy. He presented at the age of 1 year with an episode of prolonged syncope, which prompted his father to start cardiopulmonary resuscitation. Electrocardiographic monitoring showed severe sinus node dysfunction with sinus bradycardia, marked sinus arrhythmia, and multiple sinus pauses up to 4.4 seconds, requiring pacemaker implantation (AAI). The patient also presents with mild learning delay mainly characterized by late speech development, as well as impaired fine motor skills. No brain MRI or EEG were performed. No cardiac structural abnormality was seen on echocardiography. His older sister was similarly affected with sinus node dysfunction including multiple sinus pauses up to 3.2 seconds, mild mental retardation and late speech development. Echocardiography of her heart did not show any substantial abnormality. None of the siblings suffers from epilepsy and no abnormality was observed in the sister on either brain MRI and EEG. Both siblings had normal eyesight, no hearing problems and no involvement

of the gastro-intestinal tract. ECG and Holter monitoring of the parents did not reveal any signs of sinus node dysfunction.

Family F: The proband is a 23-year-old male born from consanguineous parents. His phenotypic manifestations range from borderline/mild ID, to keratoconus, and sinus arrhythmia.

Acknowledgments

We thank the families of affected individuals for their contribution. We are grateful to R. Tadros, K.Y. van Spaendonck-Zwarts and the members of the Lausanne Genomic Technologies Facility for exome sequencing support and B. Augello B and M.T. Pellico for technical support. We dedicate this study to Dr. Leopoldo Zelante who headed for 40 years the Medical Genetics Unit, Casa Sollievo della Sofferenza, San Giovanni Rotondo and recently passed away. Leopoldo's devotion to the families who nurture affected children and passion for medical genetics was, is and will remain exemplar for all of us. We are grateful to the Genomic Disorder Biobank and Telethon Network of Genetic Biobanks (Telethon Italy grant GTB12001G) for banking of biospecimens. This work was supported by grants from the Swiss National Science Foundation (31003A_160203) to AR; the US National Human Genome Research Institute (NHGRI)/National Heart Lung and Blood Institute (NHLBI) grant number HG006542 to the Baylor-Hopkins Center for Mendelian Genomics and the National Institute of Neurological Disorders and Stroke (NINDS) NS058529 to JRL; Career Development Award K23NS078056 from NINDS to WW; the Italian Ministry of Health (Ricerca Corrente) to GM; the Dutch Heart Foundation (CVON 2012-10 Predict project and CVON 2014-18 CONCOR-genes project) to CRB, AAMW and JB and JB and CRB, respectively. The Intramural Research Program of NIDDK (WFS), as well as the Genomic Disorder Biobank and Telethon Network of Genetic Biobanks (grant GTB12001G) also supported this research. The funders had no role in study design, data collection and analysis, decision to publish, or preparation of the manuscript. The authors declare no conflicts of interest with the exception of JRL and GM whose competing interests are detailed in the Conflicts of interest statement.

Supplemental References

1. Dombrovski L, Wasney GA, Tempel W, Senisterra G, Bolshan Y, Smil D, Nguyen KT, Hajian T, Poda G, Al-Awar R, Bountra C, Weigelt J, Edwards AM, Brown PJ, Schapira M, Arrowsmith CH, Vedadi M, Wu H. Crystal structure of human wd repeat domain 5 with compound.
2. Thomas LR, Wang Q, Grieb BC, Phan J, Foshage AM, Sun Q, Olejniczak ET, Clark T, Dey S, Lorey S, et al. Interaction with WDR5 promotes target gene recognition and tumorigenesis by MYC. *Molecular cell* 2015;58:440-452.
3. Cavaliere P, Levi-Acobas F, Mayer C, Saul FA, England P, Weber P, Raynal B, Monteil V, Bellalou J, Haouz A, et al. Structural and functional features of Crl proteins and identification of conserved surface residues required for interaction with the RpoS/sigmaS subunit of RNA polymerase. *The Biochemical journal* 2014;463:215-224.

4. Cheever ML, Snyder JT, Gershburg S, Siderovski DP, Harden TK, and Sondek J. Crystal structure of the multifunctional Gbeta5-RGS9 complex. *Nature structural & molecular biology* 2008;15:155-162.
5. Lovell SC, Word JM, Richardson JS, and Richardson DC. The penultimate rotamer library. *Proteins* 2000;40:389-408.
6. Guex N, and Peitsch MC. SWISS-MODEL and the Swiss-PdbViewer: an environment for comparative protein modeling. *Electrophoresis* 1997;18:2714-2723.

Table S1: In silico pathogenic prediction of all detected variants in *GNB5* gene

GNB5 Variations	Mode of inheritance	dbSNP138	ExAC AF	SIFT/Provean prediction	PolyPhen-2	MutationTaster	NNSPLICE	NetGene2	UMD-Predictor
Splice site change									
c.249G>A r.[249G>A;249-250ins25] p.(D84Vfs52X)	Compound heterozygous	-	-	Tolerated/ Neutral	NR	Disease causing	Reduced splicing efficiency in donor site (score = 0.78)	Reduced splicing efficiency in donor site (score = 0.70)	Pathogenic
c.249+1G>T p.(D84Lfs31X)	Recessive	-	-	NR	NR	Disease causing	Loss of the canonical splice site	Loss of the canonical splice site	NS
c.249+3A>G p.(D84Vfs31X)	Recessive	-	-	NR	NR	Disease causing	Slight reduced splicing efficiency in donor site (score = 0.97)	No change	NS
Nonsense									
c.994C>T p.(R332X)	Compound heterozygous	-	8,24E-06	NS	NS	Disease causing	NR	NR	Pathogenic
c.906C>G p.(Y302X)	Recessive	-	8,24E-06	NS	NS	Disease causing	NR	NR	Pathogenic
Missense									
c.242C>T p.(S81L)	Recessive	-	4,96E-05	Damaging (score = 0)	Possibly damaging (score = 0.867)	Disease causing	NR	NR	Pathogenic

NS = Not scored

NR = Not relevant

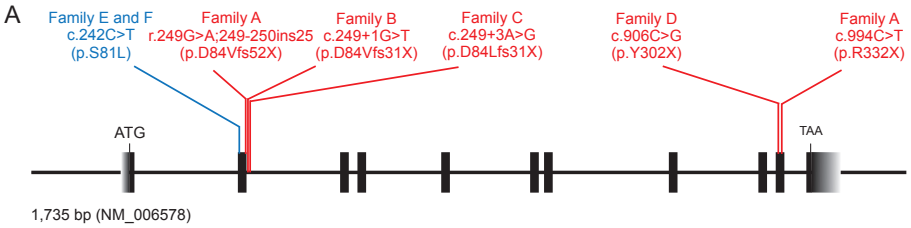

B

Figure S1. *GNB5* mutational landscape. (A) Schematic representation of the exon-intron structure of human *GNB5* gene (NM_006578). Loss-of-function (red) and missense (blue) variants detected in the six studied families. Their respective positions are indicated on the corresponding exons. The predicted protein changes are shown in brackets. (B) Conservation across vertebrates of the first WD40 domain of GNB5 and Serine 81 residue that is altered by a missense substitution (p.(Ser81Leu)) in families E and F.

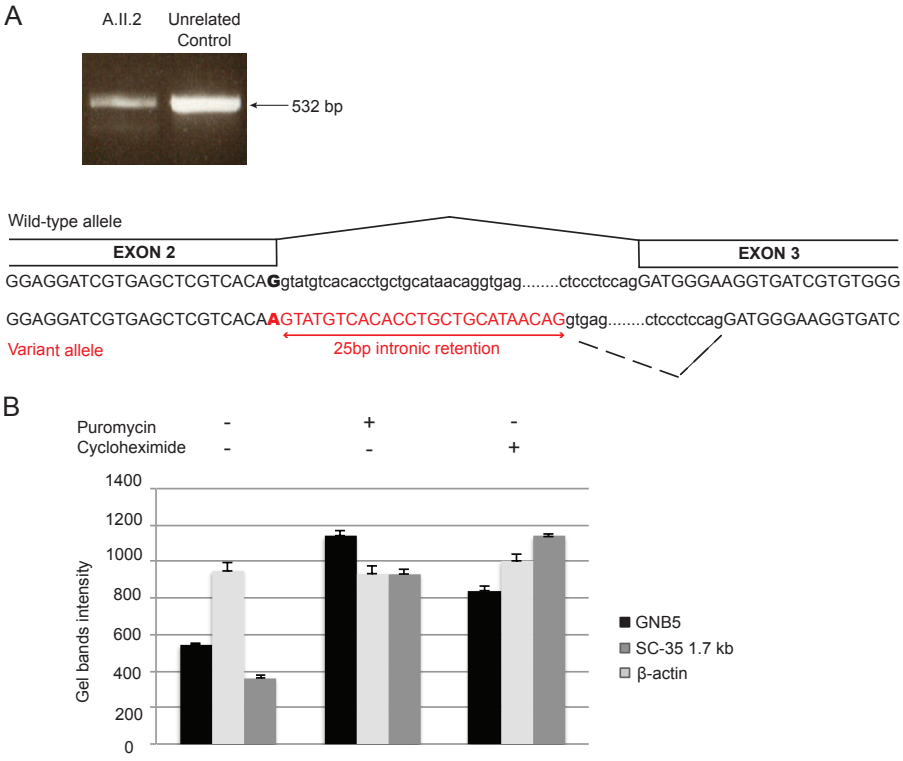

Figure S2. Molecular characterization of Family A variants. (A) The synonymous substitution c.249G>A (p.(=)), affecting the last nucleotide of the second exon of *GNB5*, is predicted to alter splicing accuracy by both NetGene 2 and NNSPLICE (Table S1). To clarify the nature of this variant we RT-PCR amplified and sequenced the allele carrying the splice-site change from total RNA from primary fibroblasts of individual A.II.2. *GNB5* exon 1 to 6 amplification (top) and sequencing (bottom) from RNA of the II.2 affected individual of family A who carries the c.249G>A splice site variant are shown. The variant transcript contains an additional 25 bp (red), corresponding to the intervening intron 2. (B) The r.249_250ins249+1_249+25 allele is predicted to encode a truncated polypeptide containing a stretch of 52 incorrect amino acids starting with an Asp to Val substitution at position 84 (p.(Asp84Valfs52X)). Cloning and sequencing of amplicons from individual A.II.1 and A.II.2 further revealed that all transcripts containing the paternal allele were aberrantly spliced. Using the same approach, we examined the relative abundance of the c.249G>A and c.994C>T alleles. Both altered transcripts are less frequent than their unchanged counterpart in parents' cells of father (A.I.1) and mother (A.I.2) (5 out of 14 amplicons (35.7%) for the paternal allele and 2 out of 15 (13.3%) for the maternal one). These results prompted us to hypothesize that both mutant alleles of family A might be targeted by the nonsense-mediated mRNA-decay (NMD) pathway. We measured by RT-PCR the levels of *GNB5* mRNA in proband's fibroblasts after treatment with Puromycin of Cycloheximide. The mRNA level of GNB5 was restored after treatment with both of these known indirect NMD inhibitors suggesting that the c.249G>A and c.994C>T variants trigger NMD of the corresponding transcripts and thus represent LoF alleles. The physiological NMD substrate SC-35 1.7 Kb was included as positive control (dark grey bars). β- actin (light grey bars) was used as internal control.

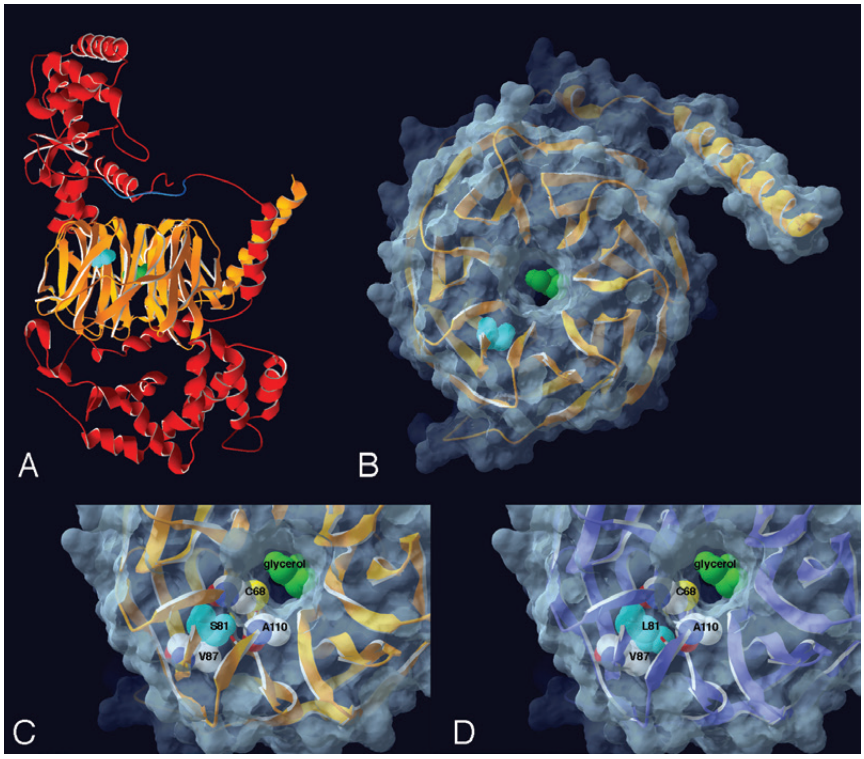

Figure S3. 3D model of the GNB5-RGS complex. (A) To gain independent support for the pathogenicity of the *GNB5* Ser81Leu missense substitution, we used a three-dimensional representation of the GNB5 encoded protein (orange) complexed with RGS9 (red, MIM: 604067), a member of the R7-subfamily of Regulators of G-protein Signaling (RGS) proteins. The evolutionarily conserved Serine 81 (cyan) is located in a β-strand very close to the central pore, where a glycerol molecule (green) is displayed in 2pbi and various molecules have been shown to bind in related structures (pdb entries 3smr, 4y7r, 4q11)[1,2,3]. A loop of RGS9 (blue) blocks the access to the central pore of GNB5. (B) Top view of the GNB5 molecular surface. The evolutionary conserved Ser81 (cyan) is located in a β-strand, very close to the central pore of the β-propeller, but not directly solvent accessible. The glycerol molecule is shown in green (RGS9 and Cys111 have been removed for clarity). (C) Detailed views of the Ser81 aminoacidic context. The replacement of Serine 81 by a Leucine will induce localized structural changes in the immediate vicinity of this residue. The positioning of Cys68 could also be altered potentially permitting the formation of a disulphide bridge with Cys111. Additionally, the rearrangements occurring between Leu81 and Ala110, Met109 and Try107 could impair the binding kinetics of RGS proteins, given that both these residues contribute to the contact surface between GNB5 and RGS9. (D) These Leu81-induced structural changes can be accommodated after a few cycles of energy minimization (see Figure S5 for rotamer modeling).

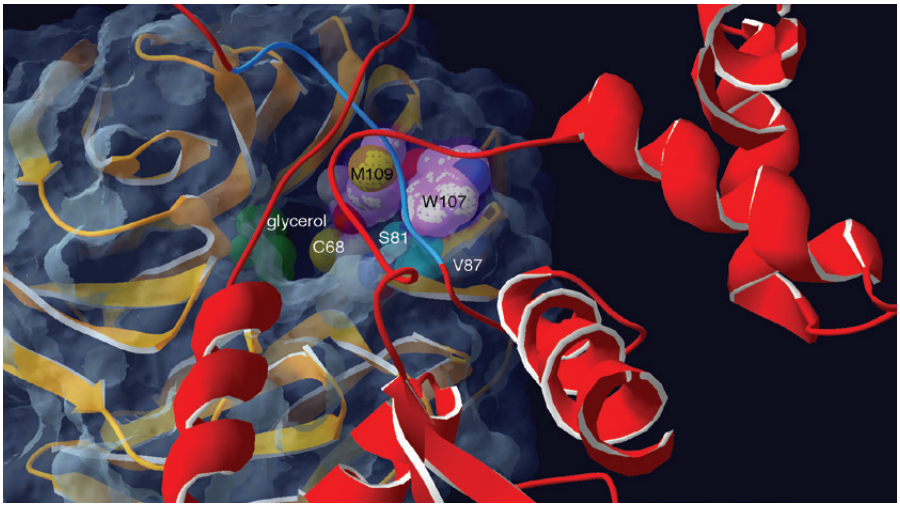

Figure S4. Ser81Leu protein modeling. GNB5 (red) complexed to RGS9 (orange) 3D model showing the proximity of residue Ser81 (cyan) with Cys68 (yellow), Met109, Trp107 and Val87 (white), as well as with the glycerol molecule (green) included in the PDB entry 2pbi4. The RGS9 loop (blue) blocks the access to the central pore of GNB5. Highlighted in purple are the side-chains of Trp107 and Met109 that directly contribute to the contact surface between GNB5 and RGS9.

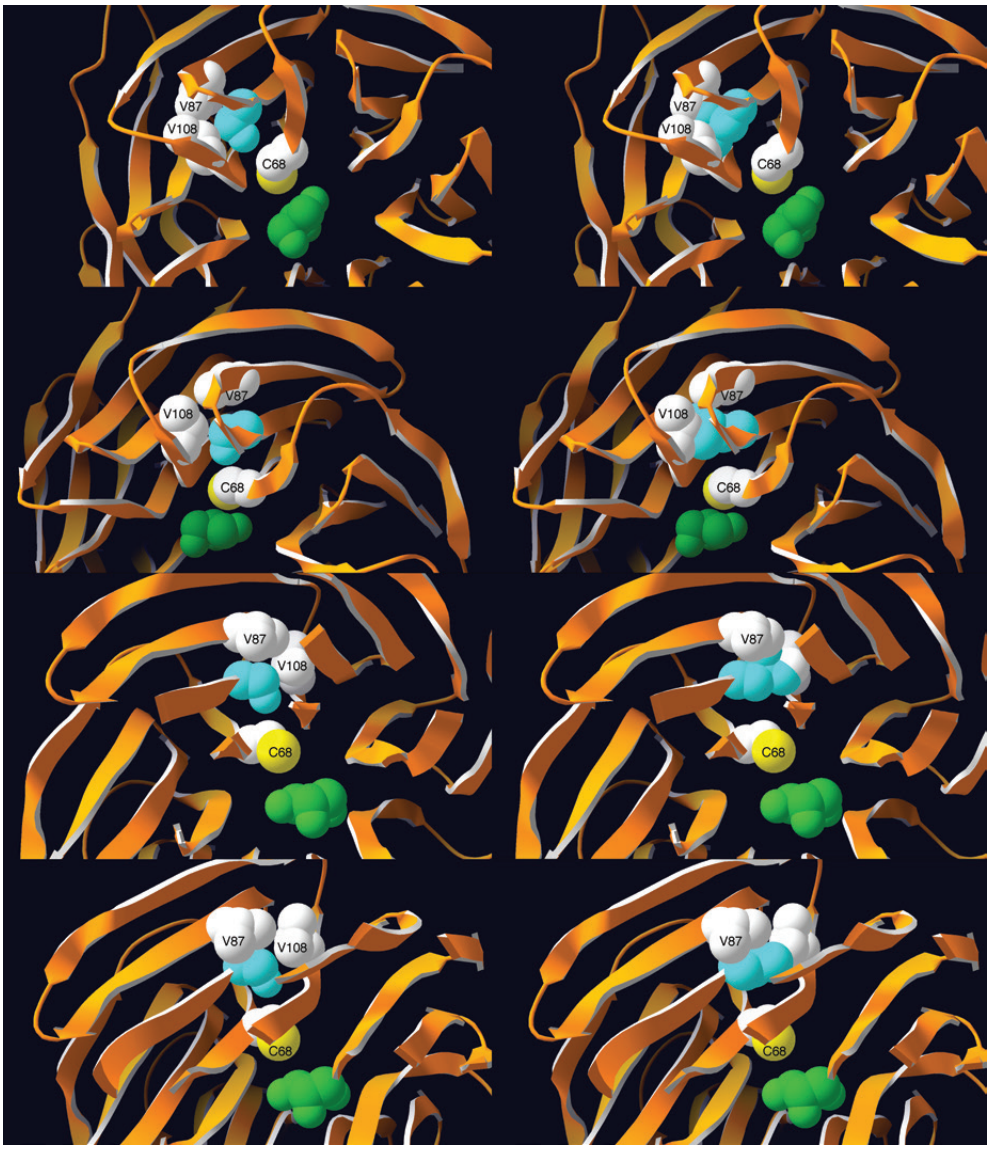

Figure S5. Ser81Leu protein rotamers modeling. Diverse views of the GNB5 3D model showing the Ser81 residue (cyan) compared to the glycerol molecule in the pore (green) and nearby residues (left column). Related rotamers emphasizing the steric hindrances-induced local rearrangements associated with the Leucine replacement identified in families E and F are shown for comparison on the right. Perturbations of the rotamers were evaluated using the backbone dependent rotamer library5 implemented in the Swiss-PdbViewer6.

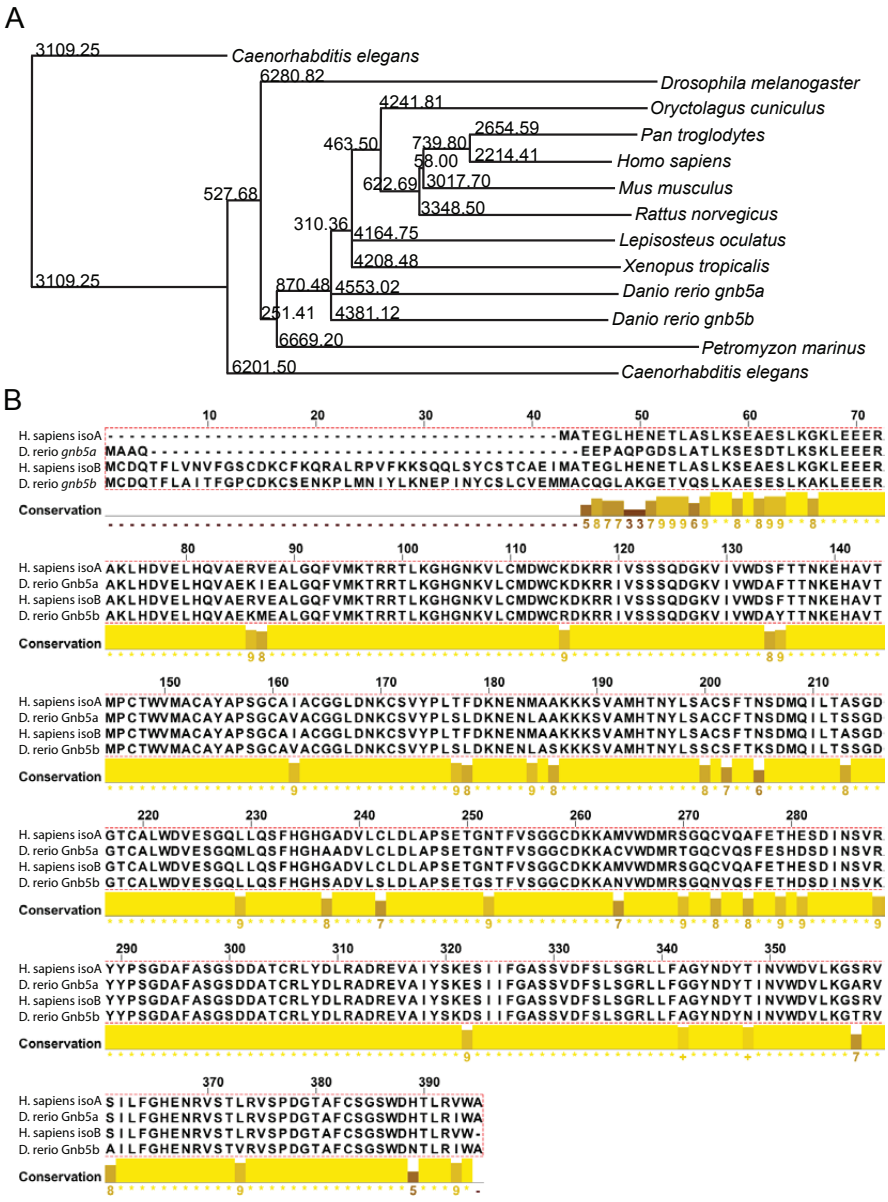

Figure S6. Evolutionary conservation of *GNB5* genomic sequences across species. (A) Phylogenetic tree based on the genomic sequences of 13 different species. For each species the longest or most validated coding transcript was selected. Linkage is based on neighbor joining. Values represent the branch lengths. (B) Conservation of zebrafish Gnb5a and Gnb5b compared to the human GNB5 proteins. Human *GNB5* is translated into two protein isoforms; isoform A is the shorter variant (353 aa), while isoform B is the longer variant (395 aa). Gnb5a aligns with GNB5 isoform A, Gnb5b with GNB5 isoform B. Yellow indicates full conservation between the four proteins. H. sapiens, Homo sapiens; D. rerio, Danio rerio.

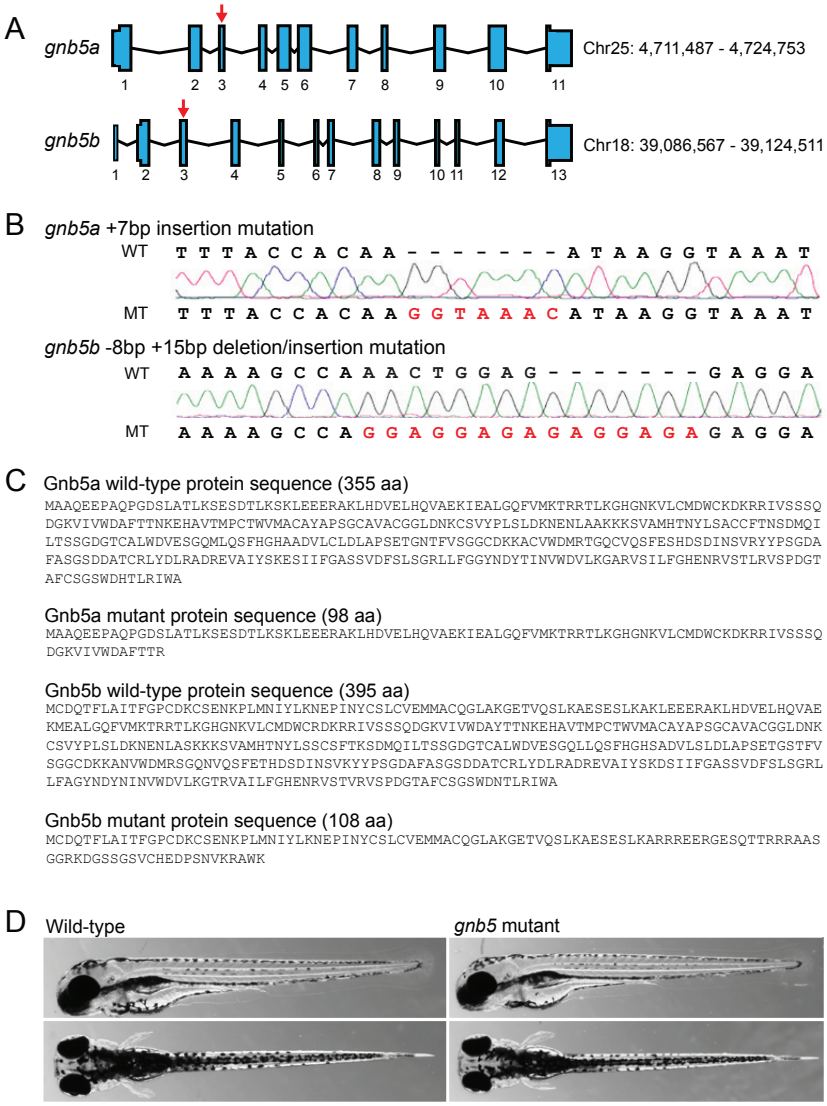

Figure S7. Genomic editing of zebrafish *gnb5a* and *gnb5b*. (A) *gnb5a* and *gnb5b* exons, introns and chromosomal location. Red arrows indicate the sitesof CRISPR/Cas9-induced mutations. (B) Partial sequences of *gnb5a* and *gnb5b* demonstrating the specific mutations that were generated; *gnb5a* +7bp insertion of GGTAAAC; *gnb5b* -8bp deletion of AACTGGAG and +15bp insertion of GGAGGAGAGAGGAGA. WT, wild-type *gnb5* sequence; MT, *gnb5* mutant sequence. (C) Gnb5 wild-type and mutant protein sequences. Both mutations result in an early stop codon and truncation of the protein. (D) Representative images illustrating the morphology of 3 dpf wild-type and *gnb5* mutants as seen from a left lateral view (top) and dorsal view (bottom).

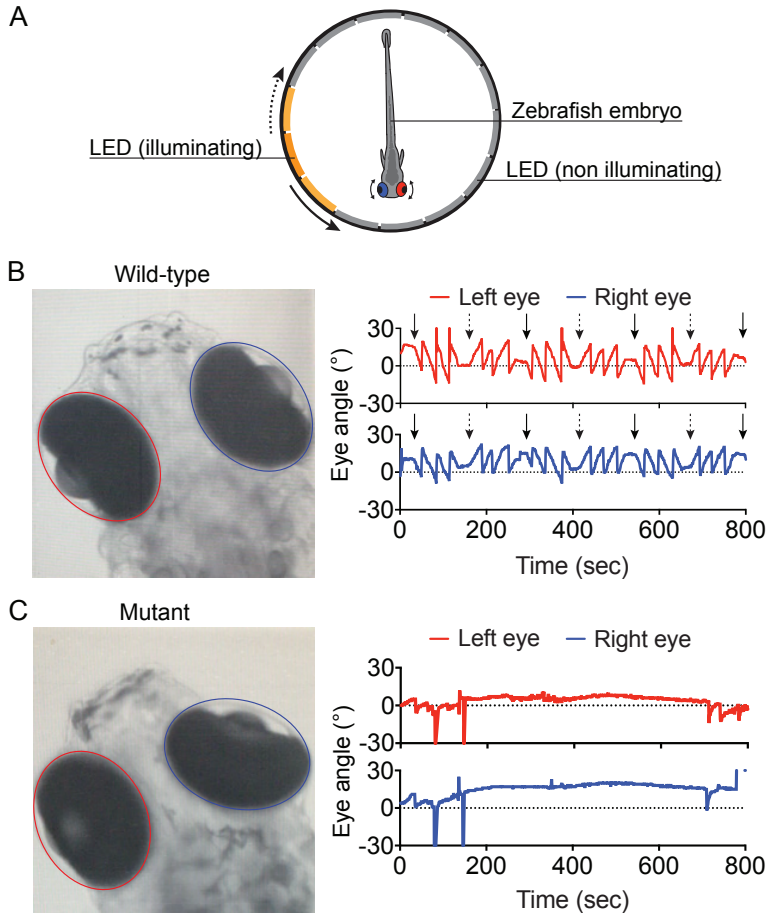

Figure S8. Optokinetic response in *gnb5* double mutant zebrafish larvae. (A) Schematic of the optokinetic response set-up. Larvae at 7 dpf were embedded dorsal side up in a petri dish and placed in the center of an optokinetic drum containing circularly-placed plexiglass slides, each illuminated by 5 LEDs at the top and 5 LEDs at the bottom. 2 LEDs were red (630 nm), 4 LEDs were green (526 nm), and 4 LEDs were blue (458 nm). A light stimulus was rotated around the embryo, and changed direction periodically. The intensities of the LEDs were adjusted such that each stimulus wavelength delivered an equal amount of quanta, thus generating a white stimulus. Sinusoids with 100% contrast, a spatial frequency of 0.014 cycles/deg were rotated around the fish with an angular velocity of 18 deg/sec. This resulted in a temporal frequency of 0.25 cycles/sec. The average intensity was 16 lux. To avoid habituation of the optokinetic response, the stimulus changed direction periodically. It first moved counterclockwise for 12 sec, then held still for 3 sec before it moved clockwise for another 12 sec. Eye position and angle were automatically tracked over time and translated into graphs. Dashed arrow, rightward rotation; solid arrow, leftward rotation. (B, C) Representative optokinetic images and graphs of a wild-type and *gnb5* mutant embryo (total recordings wild-type N=6, mutants N=6). Red, left eye; blue, right eye.

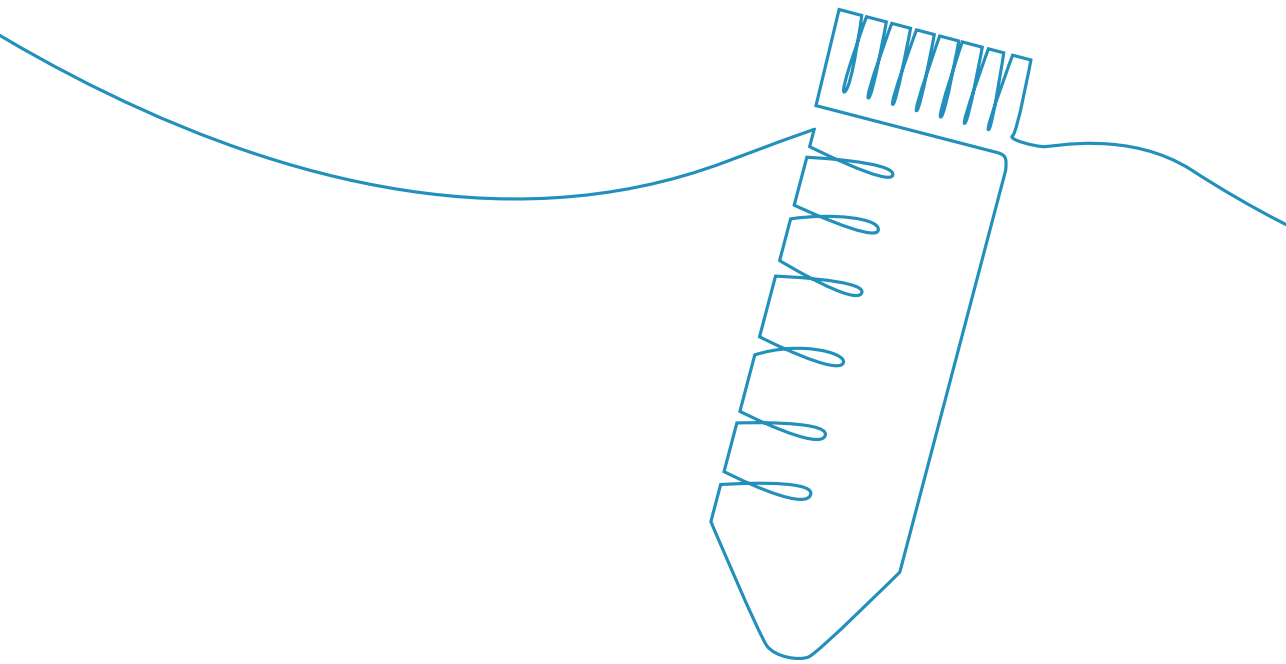

CHAPTER 5

Genetic variation in *GNB5* causes bradycardia by increasing $I_{K,ACh}$ augmenting cholinergic response

Christiaan C. Veerman*, Isabella Mengarelli*, Charlotte D. Koopman, Ronald Wilders, Shirley C. van Amersfoorth, Diane Bakker, Rianne Wolswinkel, Mariam Hababa, Teun P. de Boer, Kaomei Guan, James Milnes, Elisabeth M. Lodder, Jeroen Bakkers, Arie O. Verkerk#, Connie R. Bezzina#

*# contributed equally

Under revision

Abstract

Mutations in *GNB5*, encoding the G-protein β5 subunit (Gβ5), have been recently linked to a multisystem disorder that includes severe bradycardia. We here investigated the mechanism underlying bradycardia caused by the recessive p.S81L Gβ5 variant. Using CRISPR/Cas9-based targeting we generated an isogenic series of human induced pluripotent stem cell (hiPSC) lines that were respectively wild-type, heterozygous and homozygous for the *GNB5* p.S81L variant. These were differentiated into cardiomyocytes (hiPSC-CMs) that robustly expressed the acetylcholine-activated potassium current ($I_{K,ACh}$). Baseline electrophysiological properties of the lines did not differ. Upon application of carbachol (CCh), homozygous p.S81L hiPSC-CMs displayed an increased $I_{K,ACh}$ density and a more pronounced decrease of spontaneous activity as compared to wild-type and heterozygous p.S81L hiPSC-CMs, explaining the bradycardia in homozygous carriers. Application of the specific $I_{K,ACh}$ blocker XEN-R0703 resulted in near-complete reversal of the phenotype. Our results provide mechanistic insights and proof of principle for potential therapy in patients carrying *GNB5* mutations.

Key words: Electrophysiology, Mechanisms, Ion Channels/Membrane Transport, Genetically Altered and Transgenic Models, Treatment

Introduction

Inherited ion channel mutations are an important cause of sinoatrial node (SAN) dysfunction in the young.[1] The recent identification of rare genetic variants in genes encoding G-protein β (Gβ) subunits has expanded the repertoire of causal genes involved in SAN dysfunction beyond the previously described ion channel subunit genes.[2-5] Gβ subunits are components of heterotrimeric G-protein complexes that mediate G-protein coupled receptor signaling involved in many processes including slowing of heart rate (HR). Acetylcholine (ACh), released from post-ganglionic parasympathetic neurons, binds to M_2 muscarinic receptors on pacemaker cells and atrial myocytes, triggering activation of heterotrimeric G-proteins that dissociate into Gα-GTP and Gβγ subunits. Of central importance is the effect of the Gβγ complex on the G protein-coupled inwardly rectifying K^+ (GIRK) channel, which underlies the ACh-activated K^+ current ($I_{K,ACh}$). This channel is predominantly expressed in pacemaker cells and atrial myocytes,[6] and is a heterotetramer consisting of Kir3.1 (encoded by *KCNJ3*) and Kir3.4 (encoded by *KCNJ5*) ion channel subunits.[7] The Gβγ complex activates $I_{K,ACh}$,[8] which, due to its permeability of K^+ ions and inwardly rectifying properties,[9] results in membrane potential hyperpolarization and slowing of diastolic depolarization in SAN cells, thereby decreasing spontaneous activity.[10]

Recently, we and others reported mutations in *GNB5*, encoding Gβ5, as a cause of an autosomal recessive multisystem disorder including severe bradycardia at young age, necessitating pacemaker implantation.[2,4,5] As opposed to the other Gβ-subunits, Gβ5 has an inhibitory effect on GIRK channels, thereby dampening the parasympathetic response, an effect that involves interaction with Regulator of G-protein Signaling (RGS) proteins.[11,12] In patients carrying pathogenic variants in *GNB5* the maximal HR during exercise is unaffected, while severe bradycardia occurs at rest, indicating a relation between the mutant *GNB5* and parasympathetic state.[2] Of the eight families described, the majority harbored recessive loss-of-function variants (i.e. nonsense, splice-site and frameshift),[2,4,5] whereas the recessive missense variant c.242C>T p.S81L (NM_006578.3, rs761399728) was found in two independent families.[2] This missense variant is a low-frequency variant in individuals of Latin descent (minor allele frequency ~$3.2x10^{-4}$) where 1 in ~1500 individuals is a heterozygous carrier.[13]

The mechanism by which inherited genetic variation in *GNB5* causes excessive bradycardia remains unclear. By CRISPR/Cas9-based genome editing, we here generated an isogenic series of human induced pluripotent stem cell (hiPSC) lines (wild-type, heterozygous and homozygous for Gβ5-S81L), which we differentiated into cardiomyocytes (hiPSC-CMs) that robustly express the $I_{K,ACh}$ channel by applying a retinoic acid (RA)-based protocol. We demonstrate that in the homozygous state the S81L variant results in an increased $I_{K,ACh}$ density and in excessive slowing of spontaneous activity upon stimulation with the cholinergic agonist carbachol (CCh). We also show reversibility of the phenotype by a specific blocker of $I_{K,ACh}$ (XEN-R0703), both in homozygous Gβ5-S81L hiPSC-CMs and in vivo in a zebrafish gnb5 knockout model, thus presenting proof of principle for pharmacological treatment of bradycardia as a consequence of genetic variants in *GNB5*.

Methods

Genetic modification and differentiation of hiPSCs lines into cardiomyocytes

The study was approved by the Medical Ethics Committee of the Amsterdam UMC, location AMC, and the University Medical Center Göttingen (Az 21/1/11). Written informed consent was obtained from the control individual from whom the hiPSC line was generated. The (*GNB5* c.242C>T) Gβ5-S81L variant was introduced in heterozygous and homozygous state into a previously characterized control hiPSC line[37] by means of CRISPR/Cas9-based genome editing.[38] A detailed description of the genetic modification is provided in the Supplemental Methods. The generated isogenic hiPSC lines were subject to quality control including the evaluation of expression of the pluripotency markers TRA1-81, OCT-4, NANOG, and SSEA4 by immunocytochemistry, the verification of integrity of karyotype, and the assessment of sequences at candidate gRNA off-target loci. Details are provided in the Supplemental Methods.

HiPSCs were differentiated into cardiomyocytes that robustly express $I_{K,ACh}$ using a previously described protocol in chemically defined medium and serum-free and feeder-free conditions.[39] One µmol/l all-trans-retinoic acid (RA; Sigma) was applied during day 4-7 of differentiation to promote acquisition of atrial-like fate and expression of the $I_{K,ACh}$ channel.[14,15] A metabolic selection-based enrichment for hiPSC-CMs was used by applying glucose-depleted culture medium containing 4 mmol/l lactate during day 20-26 of differentiation.[40] For electrophysiological experiments, hiPSC-CM cultures were enzymatically dissociated into single cells and plated at a low density on matrigel-coated coverslips.[17] All experiments were performed on cells from at least 3 independent differentiation replicas.

RT-qPCR

RNA was isolated from the three isogenic hiPSC lines using the Macherey-Nagel NucleoSpin RNA II isolation kit following the manufacturer's instructions. RNA (500 ng) was retro-transcribed using SuperScript II Reverse Transcriptase (Life Technologies) and oligo dT primers. To determine transcript abundance, quantitative PCR (qPCR) was conducted with SYBR green on a Roche LightCycler 480 Real-Time PCR System. RNA samples were obtained from three biological differentiation replicas with triplicate measurements (technical replicas). Gene expression levels were analyzed using the LinReg PCR program.[41] TBP (TATA Binding Protein) was used as a reference gene. Primers are listed in Supplemental Table S1

Cellular electrophysiology in hiPSC-CMs

Data acquisition. $I_{K,Ach}$ APs were measured using an Axopatch 200B amplifier (Molecular Devices, Sunnyvale, CA, USA). Voltage control, data acquisition, and analysis were realized with custom software. Pipettes (resistance 2–3 MΩ) were pulled from borosilicate glass capillaries (Harvard Apparatus, UK). Cell membrane capacitance (C_m) was calculated and potentials were corrected for calculated liquid junction potentials.[42] Signals were low-pass-filtered with a cut-off of 5 kHz,

and digitized at 40 and 20 kHz for APs and $I_{K,ACh}$, respectively.

$I_{K,ACh}$ measurements. $I_{K,ACh}$ was measured at 21±0.2°C using the ruptured patch-clamp technique. Bath solution contained (in mmol/l): 145 KCl, 1.0 $MgCl_2$, 1.8 $CaCl_2$, 10 glucose, 5 HEPES, pH 7.4 (KOH). Pipettes were filled with solution containing (in mmol/l): 105 K-gluc, 20 KCl, 5 NaCl, 1 $MgCl_2$, 10 BAPTA (pre-dissolved in KOH), 5 MgATP, 0.3 Na-GTP, 10 HEPES, pH 7.2 (NMDG-OH). $I_{K,ACh}$ was elicited at –50 mV by rapidly applying 100 µmol/l CCh (Sigma) using a puffer pipette system in close proximity to the patched cell. $I_{K,ACh}$ deactivation time kinetics were measured in the presence of 1 mmol/l of atropine, a muscarinic receptor antagonist. Current density was calculated by dividing the CCh-elicited current by C_m. Time dependence of activation and deactivation were determined by fitting the mono-exponential functions $I/I_{max}=A\times[1-\exp(-t/\tau)]$ and $I/I_{max}=A\times\exp(-t/\tau)$, respectively, in which τ is the time constant of activation and deactivation, respectively. Desensitization was defined as the percentage of current decay during continuous exposure to CCh. Cells that virtually lacked $I_{K,ACh}$ were excluded from analysis. The proportion of excluded cells was similar in all groups.

AP measurements. APs were recorded at 36±0.2°C using the amphotericin-perforated patch-clamp technique and solutions as described previously.[14,15,17,43] APs were elicited at an overdrive stimulus frequency of 1 Hz with 3-ms, 1.2× threshold current pulses through the patch pipette. APs were recorded under control conditions and after 4-5 minutes of application of 10 µmol/l CCh. We analyzed cycle length, MDP, AP amplitude (APA_{max}), AP plateau amplitude ($APA_{plateau}$; measured 20 ms after initiation of the AP upstroke), maximum AP upstroke velocity (V_{max}), and AP duration at 20, 50 and 80% repolarization (APD_{20}, APD_{50} and APD_{80}, respectively). Parameters from 10 consecutive APs were averaged.

Heart rate analysis in *gnb5* knockout zebrafish

Zebrafish experiments were conducted in accordance with the local ethical guidelines and approved by the Ethics Committee of the Royal Netherlands Academy of Arts and Sciences. Fishes were housed under standard conditions as previously described.[44] Fish with a homozygous loss-of-function mutation in *gnb5a* and a heterozygous loss-of-function mutation in *gnb5b* (*gnb5a*$^{-/-}$ *gnb5b*$^{+/-}$) were crossed to obtain double knockout mutants (*gnb5a*$^{-/-}$ *gnb5b*$^{-/-}$; referred to as *gnb5* knockout) as described previously.[2] Embryos at 5 days post-fertilization were embedded in 0.3% agarose (UltraPure, ThermoFisher) prepared in E3 medium containing 16 mg/ml Tricaine. Measurements were performed at 28°C using an inverted light microscope with climate chamber and a high-speed CCD camera (Hamamatsu Photonics K.K., Hamamatsu City, Japan). HR was analyzed using ImageJ (National Institutes of Health, Bethesda, Maryland, USA).

Computer simulations

The spontaneous electrical activity of a single human SAN pacemaker cell was simulated using the comprehensive mathematical model that was recently developed by Fabbri et al.[ref] The electrical activity of a single human atrial cell was simulated using the model by Maleckar et al.,[45] which was

selected because it includes well-validated equations for $I_{K,ACh}$.[22] Further details are provided in the Supplemental Methods.

Statistical analyses

Statistical analysis was performed in IBM SPSS statistics 24 and GraphPad Prism 7. Data are presented as mean±SEM, unless stated otherwise. For non-normally distributed parameters, data are presented as boxplots, in which boxes represent lower quartile, median and upper quartile and whiskers 1.5x interquartile range. Parameters were tested for normal distribution and equality of variance with the Shapiro-Wilk and Levene's test, respectively. In case of normally distributed data, two-sided t-tests or paired t-tests were performed for 2 groups and one-way ANOVA, followed by post-hoc Holm-Sidak tests for >2 groups. In case of a non-normal distribution, Mann-Whitney U tests or Wilcoxon rank tests were used for 2 groups and Kruskal-Wallis tests, followed by Bonferroni corrected pairwise comparisons for >2 groups. To test for differences in proportions, a Chi-Square test was used. In hiPSC-CMs, drug effects and effects of CCh were tested by one-way or two-way repeated measures ANOVA, respectively, followed by Holm-Sidak post-hoc tests or Bonferroni corrected pairwise comparisons, respectively. In zebrafish, the effect of XEN-R0703 was evaluated by two-way repeated measures ANOVA, followed by post-hoc Bonferroni corrected pairwise comparisons. $P<0.05$ defines statistical significance.

Results

Generation of Gβ5-S81L heterozygous and homozygous hiPSCs

To evaluate the electrophysiological consequences of the Gβ5-S81L variant we introduced it into a control hiPSC line by means of CRISPR/Cas9 based genome editing, generating an isogenic series consisting of wild-type, heterozygous and homozygous Gβ5-S81L hiPSC lines (hereafter annotated as WT, $S81L^{het}$ and $S81L^{homo}$, respectively) (Supplemental Figure 1A-C). All cell lines maintained expression of the pluripotency markers TRA1-81, OCT4, NANOG and SSEA4 (Supplemental Figure 1D-E, Table S2), exhibited a normal karyotype (Supplemental Figure 1F-G) and showed unmodified sequences at candidate gRNA off-target loci (Supplemental Table S3). Data were generated from one clone per each kind of genotype. Relevant results were also confirmed in a second $S81L^{homo}$ clone.

Generation of hiPSC-CMs in presence of RA results in a functional $I_{K,ACh}$

To study the effect of the Gβ5-S81L variant on $I_{K,ACh}$, we differentiated the three isogenic hiPSC lines into hiPSC-CMs using an RA-based differentiation protocol that promotes acquisition of atrial-like fate with robust expression of $I_{K,ACh}$. In line with our previous observations[14,15], we found in WT hiPSC-CMs that the atria-enriched transcripts *NPPA* and *NR2F2* were upregulated upon RA treatment, as was the transcript of *KCNJ3*, encoding Kir3.1 (Figure 1A). In both DMSO- and

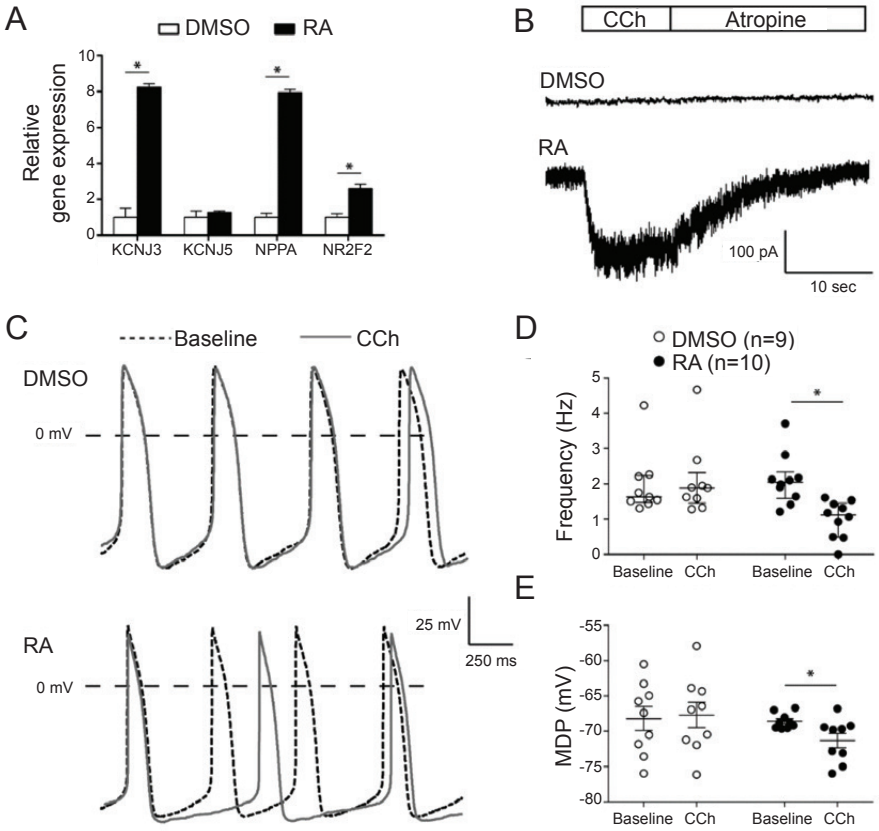

Figure 1. Application of retinoic acid (RA) to differentiating hiPSCs results in cardiomyocytes (CMs) that exhibit a robust acetylcholine-activated K^+ current ($I_{K,ACh}$). A, Transcript expression of genes in RA-treated hiPSC-CMs relative to expression in DMSO-treated hiPSC-CMs using 3 biological replicates, normalized to TBP. RA-treatment enhanced expression of the genes *KCNJ3, NPPA,* and *NR2F2*. *P<0.05 (two-sided t-tests). B, Typical $I_{K,ACh}$ traces in DMSO- and RA-treated hiPSC-CMs initiated by fast application of 100 µmol/l carbachol (CCh). After reaching steady-state, addition of 1 mmol/l atropine achieves instant removal of CCh from muscarinic receptors and deactivation of the current. In DMSO-treated hiPSC-CMs, $I_{K,ACh}$ was not detected, while RA-treated hiPSC-CMs all demonstrated a robust current (for average data, see Figure 2). C, Typical spontaneous action potentials (APs) of DMSO- and RA-treated hiPSC-CMs at baseline and upon addition of 10 µmol/l CCh. D and E, Frequency of spontaneous APs (D) and maximal diastolic potential (MDP; E) of each cell at baseline and in presence of CCh in DMSO- and RA-treated hiPSC-CMs. *P<0.05 (two-way ANOVA)

RA-treated WT hiPSC-CMs, we observed spontaneously active cells. Spontaneous activity is a consistent finding in hiPSC-CMs[16] due to an (almost) complete lack of inwardly rectifying K^+ current (I_{K1})[17] and presence of the hyperpolarization-activated inward current (I_f)[18] and 'Ca^{2+} clock'.[19] For action potential (AP) measurements, we selected cells with a high beating rate (>1 Hz) to evaluate

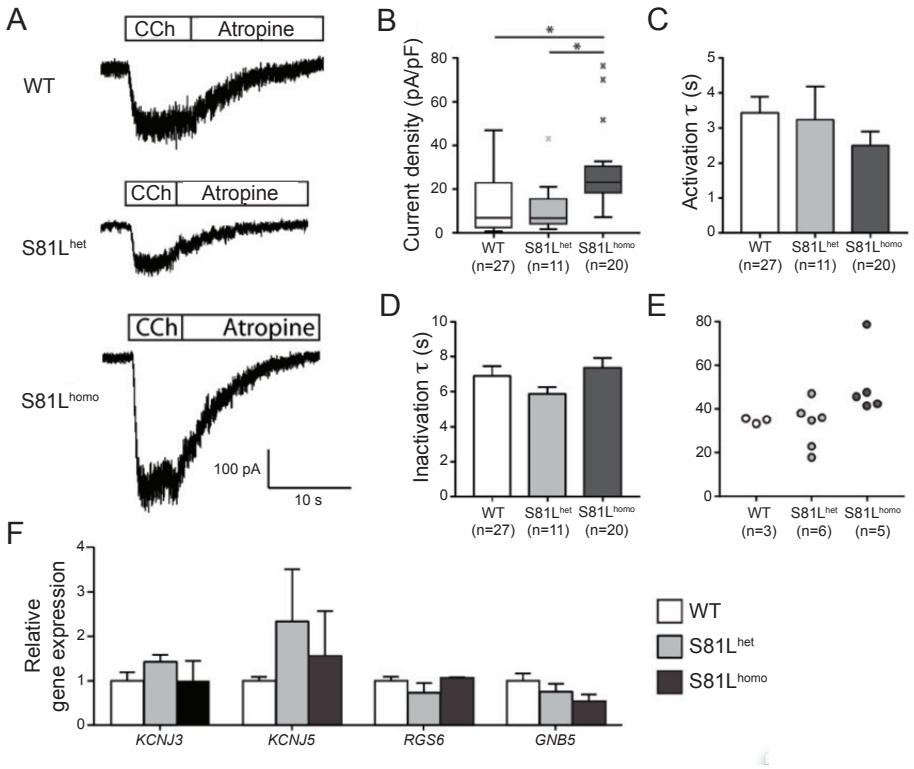

Figure 2. Impact of the Gβ5-S81L variant on $I_{K,ACh}$ in RA-treated hiPSC-CMs. (A) Typical recordings and (B) average $I_{K,ACh}$ density in WT, S81L^{het}, and S81L^{homo} hiPSC-CMs. Average $I_{K,ACh}$ density is increased in S81L^{homo} hiPSC-CMs compared to WT and S81L^{het} hiPSC-CMs. *P<0.05 (Kruskal-Wallis non-parametric test, followed by Bonferroni post-hoc analysis). (C) Time constant (τ) of $I_{K,ACh}$ activation and (D) deactivation. (E) Percentage of desensitization, measured as the percentage of $I_{K,ACh}$ decrease at steady-state upon continuous CCh application. (F) Transcript level of the genes involved in G-protein-coupled activation of $I_{K,ACh}$. Data are from 3 biological differentiation replicas and expression level of each gene is indicated as relative to its expression in WT hiPSC-CMs of each gene.

the effects of CCh on beating frequency and cells with a low beating rate (< 1 Hz) to assess AP properties with and without CCh at a fixed pacing rate of 1 Hz. As reported previously,[15] RA-treated WT hiPSC-CMs displayed shorter APs with a lower plateau as compared to DMSO-treated WT hiPSC-CMs, both during spontaneous activity and when paced at 1 Hz, thus showing a more atrial-like AP morphology. In voltage-clamp experiments, we confirmed the presence of $I_{K,ACh}$ in RA-treated WT hiPSC-CMs. By applying CCh, a robust current could be evoked in RA-treated and not in DMSO-treated WT hiPSC-CMs (Figure 1B). This $I_{K,ACh}$ deactivated upon rapid addition of the muscarinic antagonist atropine (Figure 1B). Functional $I_{K,ACh}$ effects on spontaneous activity were subsequently demonstrated by AP measurements in spontaneously fast beating hiPSC-CMs. Figure 1C shows typical examples; effects on frequency and maximal diastolic potential (MDP)

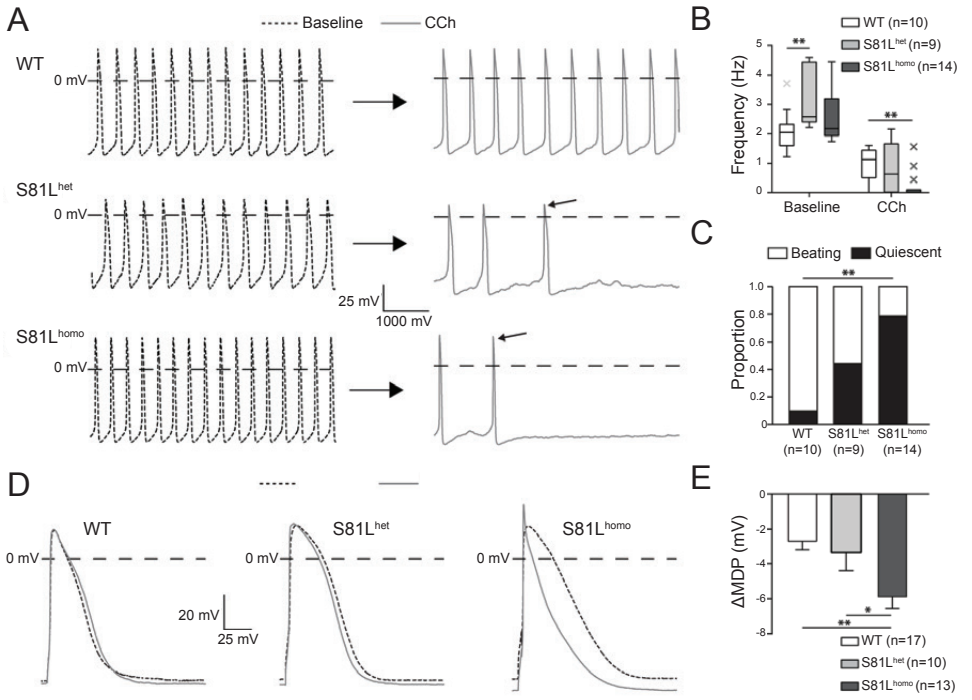

Figure 3. CCh induces more pronounced effects in S81L^{homo} compared to WT and S81L^{het} RA-treated hiPSC-CMs. (A) Representative spontaneous APs at baseline (left) and upon 10 µmol/l CCh (right) in WT, S81L^{het} and S81L^{homo} RA-treated hiPSC-CMs. The slanted arrows near the APs in presence of CCh indicate the last AP before cessation of spontaneous activity. (B) Average beating frequencies before and during application of CCh. **P<0.01 (two-way repeated measures ANOVA and post-hoc Bonferroni corrected pairwise comparison). (C) Proportion of WT, S81L^{het} and S81L^{homo} hiPSC-CMs that became quiescent upon application of CCh. **P<0.01 (Chi-Square test, followed by Bonferroni corrected pairwise comparisons). (D) Representative APs (1 Hz) before and after the application of CCh. (E) Average change in MDP upon addition of CCh. *P<0.05 and **P<0.01 (one-way ANOVA, post-hoc Holm-Sidak test).

are summarized in Figure 1, D and E, respectively. In RA-treated hiPSC-CMs, but not in DMSO-treated hiPSC-CMs, application of CCh caused a significant slowing of spontaneous activity due to hyperpolarization of the maximal diastolic potential (MDP) and a slower diastolic depolarization rate. Thus, RA-treated hiPSC-CMs display an atrial-like phenotype with functional presence of $I_{K,ACh}$ in line with previous observations,[14,15] confirming that these cells are indeed suitable to study the electrophysiological effects of the Gβ5-S81L variant on $I_{K,ACh}$.

$I_{K,ACh}$ density is increased in S81L^{homo} hiPSC-CMs

Having established the presence and relevance of $I_{K,ACh}$ in our RA-treated hiPSC-CM model, we next compared the properties of $I_{K,ACh}$ in the isogenic WT, S81L^{het} and S81L^{homo} hiPSC-CMs. Figure

	WT (n=12)	S81L^{het} (n=10)	S81L^{homo} (n=13)
MDP (mV)	−68.5±0.6	−69.3±1.3	−70.2±1.8
APA (mV)	94.7±4.6	86.5±4.9	85.6±4.9
V_{max} (V/s)	40.9±9.9	28.3±8.2	32.9±8.9
APD_{20} (ms)	45.3±5.7	49.4±12.7	39.0±4.4
APD_{50} (ms)	81.5±9.7	82.4±19.2	66.6±6.5
APD_{80} (ms)	109.0±12.6	103.8±19.5	88.8±8.4
$APA_{plateau}$ (mV)	86.1±4.8	75.0±7.7	77.9±5.5

Table 1. Action potential (AP) parameters in WT, S81L^{het} and S81L^{homo} at baseline in spontaneously fast beating hiPSC-CMs. Data are mean±SEM. MDP, maximal diastolic potential; APA_{max}, maximal AP amplitude; V_{max}, maximal upstroke velocity; APD_{20}, APD_{50}, APD_{80}, AP duration at 20, 50, and 80% of repolarization, respectively; $APA_{plateau}$, AP plateau amplitude.

	Baseline			**10 µmol/l CCh**		
	WT	S81L^{het}	S81L^{homo}	WT	S81L^{het}	S81L^{homo}
MMDP* (mV)	-69.8±1.4	-69.1±1.8	-70.2±1.7	-72.5±1.4$^{\#}$	-72.4±1.7$^{\#}$	-76.1±1.6$^{\#}$
$AAPA_{max}$ (mV)	83.4±4.5	84.9±5.0	88.6±3.1	88.7±4.3$^{\#}$	88.0±4.7	98.3±3.2$^{\#}$
VV_{max} (V/s)	65±17	28±15	59±18	97±21$^{\#}$	52±20	124±27$^{\#}$
$AAPD_{20}$ * (ms)	23.2±36.4	30.4±33.3	30.5±7.2	23.7±46.7	29.8±33.3	23.1±20.8$^{\#}$
$AAPD_{50}$ (ms)	49.6±47.0	50.3±46.2	55.8±15.2	41.2±57.6	48.9±51.0	44.0±37.5$^{\#}$
$AAPD_{80}$ (ms)	79.3±63.6	69.5±63.1	73.6±19.5	73.4±74.0	66.8±58.3	60.0±34.8
$AAPA_{plateau}$ (mV)	64.2±6.4	70.8±8.5	79.2±2.7	65.4±6.6	71.3±8.7	76.1±3.9

Table 2. Action potential (AP) parameters (1 Hz) in WT, S81L^{het} and S81L^{homo} hiPSC-CMs. Data are mean±SEM, except AP durations which are median±IQR. Number of cells are and 17, 10, 13 for WT, S81L^{het}, S81L^{homo}, respectively. MDP, maximal diastolic potential; APAmax, maximal AP amplitude; Vmax, maximum upstroke velocity; APD_{20}, APD_{50}, APD_{80}, AP duration at 20, 50 and 80% of repolarization, respectively; APAplateau, AP plateau amplitude. #P<0.05 compared to baseline (paired t-test or Wilcoxon Signed Rank test); *P<0.05 interaction effect for CCh (two-way repeated measures ANOVA).

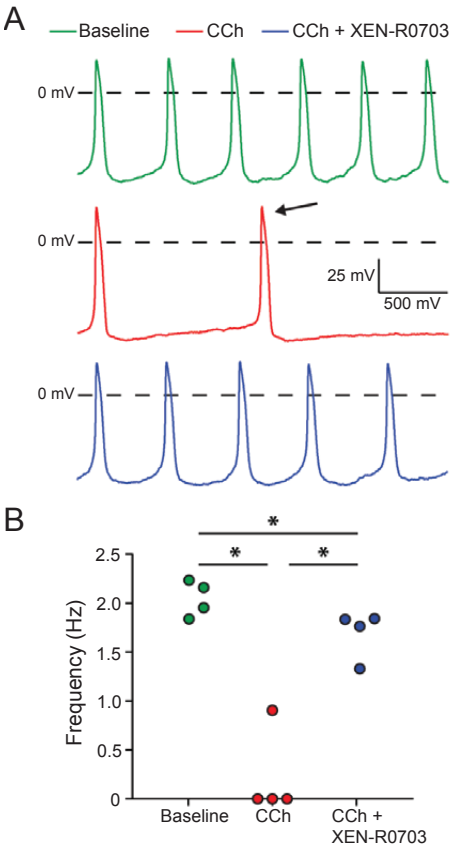

Figure 4. CCh induces an extreme slowing of spontaneous beating in S81L^{homo} hiPSC-CMs, which is largely suppressed by $I_{K,ACh}$ blockade through XEN-R0703. (A) Typical APs of an S81L^{homo} hiPSC-CM at baseline (top), upon application of 10 µmol/l CCh (middle), and upon addition of 1 µmol/l XEN-R0703 in presence of 10 µmol/l CCh (bottom). (B) Effects of CCh and XEN-R0703 on spontaneous AP frequency in four S81L^{homo} hiPSC-CMs. *P<0.05 (one-way repeated measures ANOVA followed by post-hoc Holm-Sidak test).

2A shows typical examples of $I_{K,ACh}$ measurements. $I_{K,ACh}$ density was significantly higher in S81L^{homo} hiPSC-CMs compared to S81L^{het} and WT (Figure 2B). Moreover, activation and deactivation time constants were not significantly different between groups (Figure 2C-D). In addition, desensitization was similar between groups (Figure 2E). No significant differences were observed in *KCNJ3, KCNJ5, RGS6,* and *GNB5* transcript abundance across the WT, S81L^{het} and S81L^{homo} lines, indicating that the increased $I_{K,ACh}$ density in S81L^{homo} hiPSC-CMs was not due to altered expression of these genes (Figure 2F). Thus, homozygous presence of the Gβ5-S81L variant increases $I_{K,ACh}$ density without changes in transcript level or kinetics.

S81L^{homo} hiPSC-CMs demonstrate a severe reduction in beating frequency upon CCh application

Subsequently, we evaluated the effects of $I_{K,ACh}$ activation on APs of WT, S81L^{het} and S81L^{homo} hiPSC-CMs. Figure 3A shows typical APs of spontaneously fast beating hiPSC-CMs. Baseline AP parameters, i.e. in absence of CCh, were similar between the three groups (Figure 3A, and Table 1), with exception of a slightly higher spontaneous beating frequency in S81L^{het} hiPSC-CMs (Figure

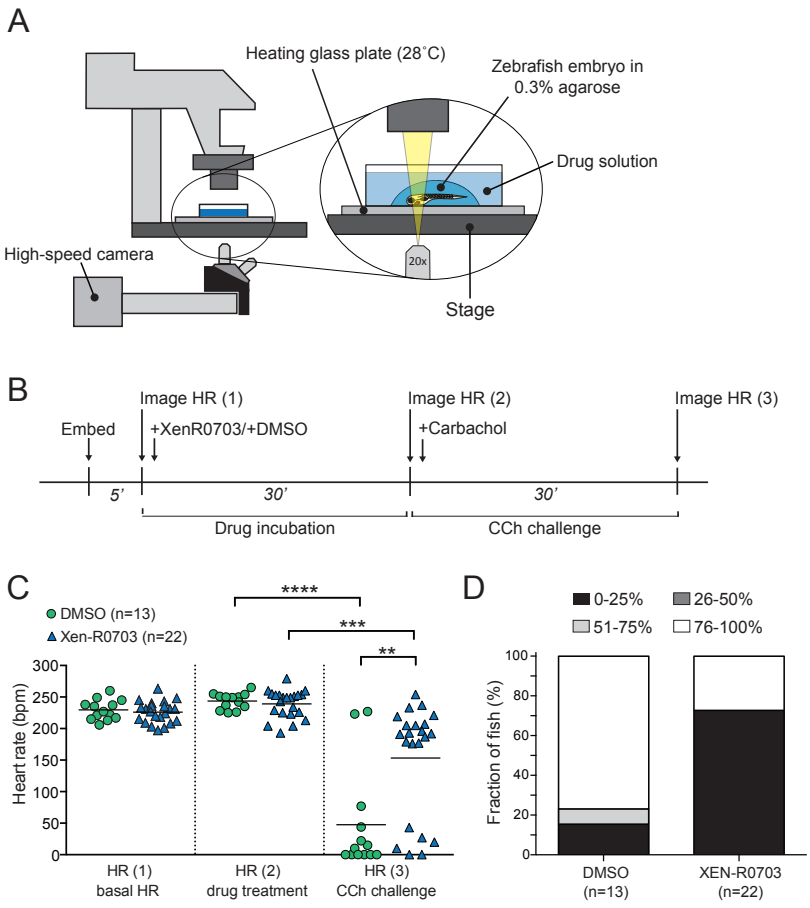

Figure 5. Effect of $I_{K,ACh}$ blockade on heart rate (HR) in *gnb5* knockout zebrafish. (A) Experimental setup for high-speed imaging of the zebrafish heart. HR was recorded at 150 fps for 10 seconds. (B) Time schedule of drug treatment and CCh challenge in *gnb5* knockout larvae. (C) Scatter dot plots with mean of HR of *gnb5* knockout larvae 5 days post-fertilization at basal level, after treatment with 50 µmol/l XEN-R0703 or DMSO, and upon application of 500 µmol/l CCh. **P<0.01, ***P<0.001, ****P<0.0001 (two-way repeated measures ANOVA followed by Bonferroni corrected pairwise comparisons). D, Percentage of *gnb5* knockout larvae that responded to 500 µmol/l CCh with a decrease in HR of 0-25, 26-50, 51-75, or 76-100%.

3B, indicating that baseline electrophysiological properties are unaffected by the Gβ5 S81L variant. $I_{K,ACh}$ activation by CCh induced a reduction in spontaneous beating frequency in all three hiPSC-CM lines, which was much more pronounced in S81L^{homo} compared to WT hiPSC-CMs (Figure 3A-C). In fact, 79% of the S81L^{homo} hiPSC-CMs became quiescent, while S81L^{het} and WT hiPSC-CMs reached a quiescent state in 44 and 10% of the cells, respectively (Figure 3C). This main finding in S81L^{homo} hiPSC-CM was confirmed in a second independent S81L^{homo} clone. In this independent clone, 71% of the spontaneously beating S81L^{homo} hiPSC-CMs (n=7) became quiescent upon application of CCh.

The higher amount of spontaneous activity cessation in S81L^{homo} hiPSC-CMs is in agreement with the observed increased $I_{K,ACh}$ density. Due to the termination of the spontaneous activity, however, we were unable to determine the effects on AP characteristics. Therefore, we also assessed the effects of $I_{K,ACh}$ activation on APs in slow beating hiPSC-CMs stimulated at an overdrive stimulus frequency of 1 Hz. In absence of CCh, AP parameters were not different between WT, S81L^{het} and S81L^{homo} hiPSC-CMs (Table 2). This further shows that the Gβ5-S81L variant does not affect electrophysiological properties at baseline conditions. Upon addition of CCh, a significant MDP hyperpolarization was observed in all three groups (Figure 3D; Table 2). In S81L^{homo} hiPSC-CMs however, hyperpolarization was more pronounced as compared to the other two groups (Figure 3E; Table 1). Furthermore, S81L^{homo} hiPSC-CMs displayed a more pronounced shortening of APD_{20} (Table 2. This suggests that the AP configuration is only seriously affected by $I_{K,ACh}$ in hiPSC-CMs if

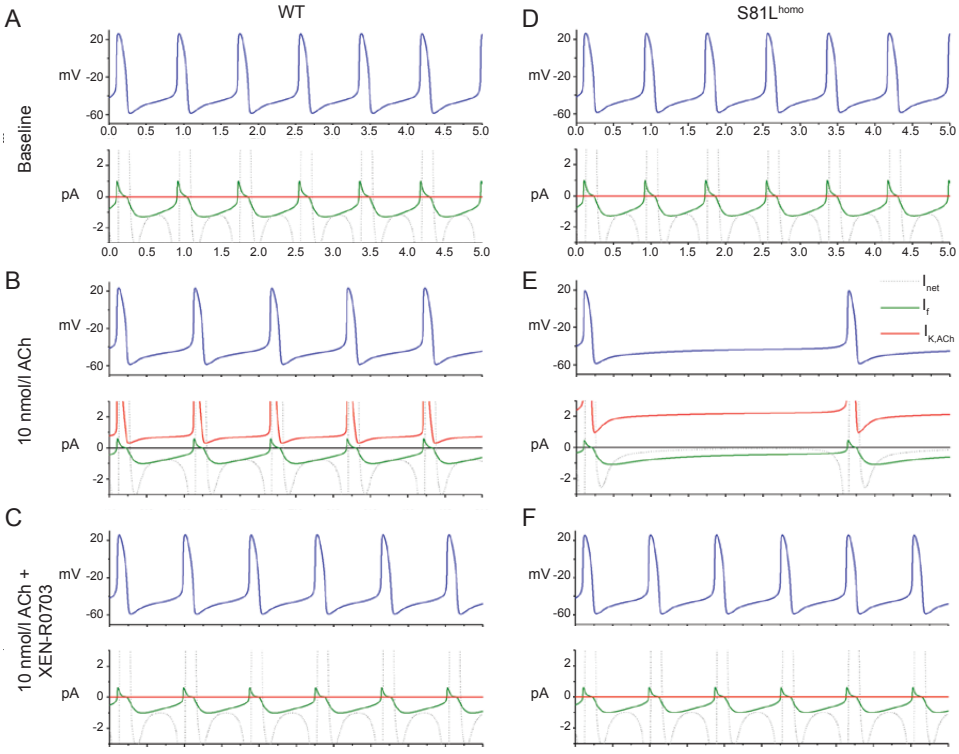

Figure 6. ACh induces more pronounced effects in S81L^{homo} compared to WT simulated human SAN pacemaker cells. (A–C) Spontaneous action potentials (blue lines) and associated net membrane current (I_{net}, grey lines), hyperpolarization-activated 'funny current' (I_f, green lines), and $I_{K,ACh}$ (red lines) in (A) a WT human SAN pacemaker cell at baseline, (B) upon addition of 10 nmol/l ACh, and (C) upon addition of 10 nmol/l ACh in the presence of XEN-R0703. (D–F) Spontaneous action potentials and associated I_{net}, I_f, and $I_{K,ACh}$ in an S81L^{homo} human SAN pacemaker cell at (D) baseline, (E) upon addition of 10 nmol/l ACh, and (F) upon addition of 10 nmol/l ACh in the presence of XEN-R0703 (F).

$I_{K,ACh}$ densities are large. Thus, while AP parameters in absence of CCh were largely identical in the three hiPSC-CMs lines, the S81L^{homo} line demonstrated a more pronounced effect of CCh in terms of cellular hyperpolarization, AP shortening, and slowing of spontaneous beating, which is in line with both the increased $I_{K,ACh}$ density and the bradycardia exhibited only by homozygous Gβ5 S81L patients.[2]

Pharmacological $I_{K,Ach}$ blockade rescues bradycardia in S81L^{homo} hiPSC-CMs and *gnb5* knockout zebrafish

Given the observed increased $I_{K,ACh}$ density in S81L^{homo} hiPSC-CMs, selective blockers of $I_{K,ACh}$ may provide a useful pharmacological treatment for patients with Gβ5 genetic defects. We tested this hypothesis in our hiPSC-CMs as well as in vivo in *gnb5* knockout zebrafish that we generated previously.[2]

$I_{K,ACh}$ blockade in hiPSC-CMs. We evaluated possible pharmacological rescue of the phenotype in S81L^{homo} hiPSC-CMs using the selective $I_{K,ACh}$ blocker XEN-R0703.[14] Figure 4A shows typical examples of spontaneous activity at baseline (top panel), in presence of CCh (middle panel), and in presence of CCh and XEN-R0703 (bottom panel). Addition of 1 µmol/l XEN-R0703 in presence of 10 µmol/l CCh resulted in an almost complete reversal of the effects of CCh on spontaneous activity. This indicates that the drug is efficient in reversing the enhanced reduction of automaticity in S81L^{homo} hiPSC-CMs (Figure 4B).

$I_{K,ACh}$ blockade in zebrafish. We also tested XEN-R0703 in an in vivo *gnb5* knockout zebrafish model that faithfully recapitulated the phenotypical spectrum of patients with pathogenic variants in *GNB5*, including bradycardia (for details, see Lodder et al.[2]). In short, CCh led to a strong decrease in HR in *gnb5* knockout zebrafish, while little effect was observed in wild-type and sibling larvae.[2] To study the effect of XEN-R0703, HR of *gnb5* knockout zebrafish was first recorded at baseline, then after the administration of 50 µmol/l XEN-R0703 or DMSO, and lastly after challenging larvae with 500 µmol/l CCh (Figure 5B). The used concentrations are higher than in our patch-clamp assay because the zebrafish assay is considerably less sensitive.[20] While most larvae in the DMSO control group responded to CCh with a severe decrease in HR, the larvae pretreated with XEN-R0703 had a markedly lower sensitivity to CCh (Figure 5C). The response to CCh was calculated for each individual fish and the outcomes subdivided into categories of 0-25%, 26-50%, 51-75% and 75-100% decrease in HR. A 0-25% decrease in HR was considered physiological, whereas 26-100% was considered pathological. While 85% of the DMSO treated *gnb5* knockout fish showed a pathological decrease in HR, only 27% of fish pretreated with XEN-R0703 showed such a reduction (Figure 5D). Together, these results demonstrate that $I_{K,ACh}$ blockade largely rescues CCh-induced bradycardia in *gnb5* knockout zebrafish.

Predicted effects of the homozygous Gβ5-S81L variant in computational models of a SAN and an atrial cell

To evaluate whether the observed increase in $I_{K,ACh}$ density, associated with the homozygous

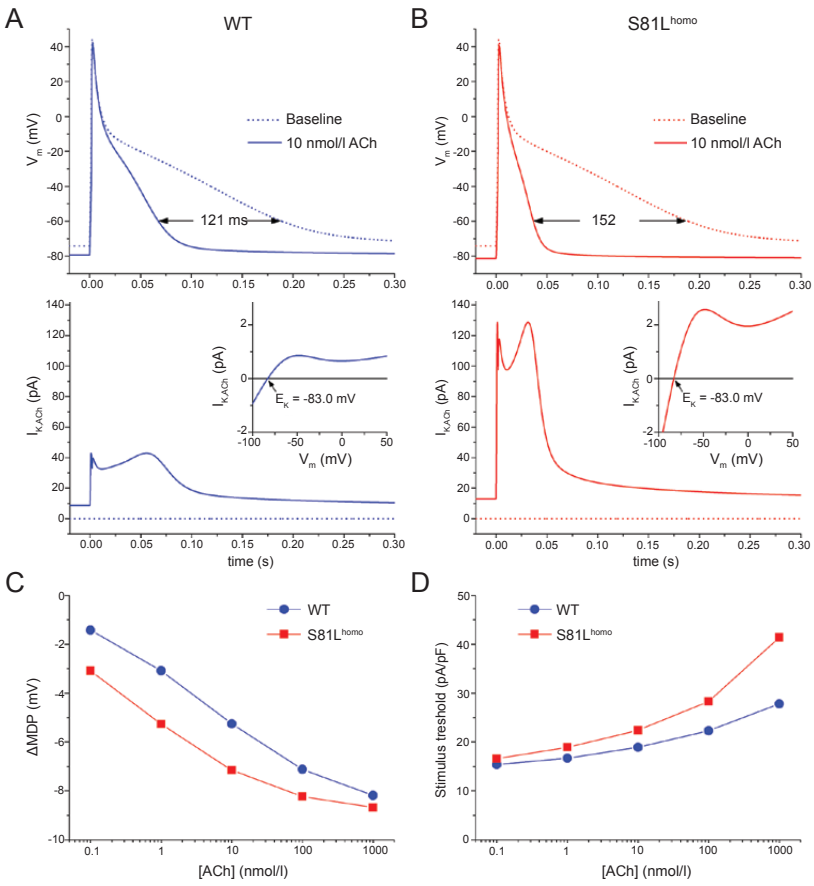

Figure 7. ACh induces more pronounced AP effects in S81L^{homo} compared to WT simulated human atrial myocytes. (A-B) APs elicited at 1 Hz (top panels) and associated $I_{K,ACh}$ (bottom panels) at baseline (dotted lines) and upon addition of 10 nmol/l ACh (solid lines) in (A) WT and (B) S81L^{homo} human atrial myocytes. The horizontal double-headed arrows in panel A indicate the ACh-induced shortening of AP duration. The 'wobbles' in the time course of $I_{K,ACh}$ in panel B are caused by the N-shape of the $I_{K,ACh}$ current-voltage relationship (insets). The slanted arrows in the insets point to the $I_{K,ACh}$ reversal potential (EK) of −83.0 mV. (C-D) Shift in maximum (C) diastolic potential (ΔMDP) and (D) threshold stimulus current amplitude at ACh concentrations ranging from 0.1 nmol/l to 1 µmol/l. Note the logarithmic abscissa scale.

variant, is the major contributor to the generation of excessive bradycardia, we conducted computer simulations using mathematical models of both a SAN pacemaker cells and an atrial cell[21,22]. We implemented a threefold increase in $I_{K,ACh}$ density, as observed in our experiments in S81L^{homo} hiPSC-CMs (Figure 2B). In the wild-type human SAN model, application of ACh at a concentration of 10 nmol/l activated $I_{K,ACh}$ and inhibited the hyperpolarization-activated current (I_f), resulting in a decrease in depolarizing net current (I_{net}) during diastole. Consequently, beating rate

decreased from 74 to 58 bpm (Figure 6A-B). However, implementing a threefold increased $I_{K,ACh}$ density, which simulates the homozygous Gβ5-S81L variant effects, resulted in a dramatic slowing of beating rate (from 74 to 17 bpm) (Figure 6D-E). Additionally, $I_{K,ACh}$ blockade, which simulates the pharmacological effects of XEN-R0703, largely, but incompletely, reversed ACh effects (Figure 6C, F). These findings closely resemble those obtained in $S81L^{homo}$ hiPSC-CMs, demonstrating that the threefold increase in $I_{K,ACh}$ density is sufficient to induce the bradycardic phenotype. Furthermore, the effect of ACh/CCh on I_f, as also exists in real SAN cells,[23] may explain the incomplete rescue of beating frequency by XEN-0703 in the mutant zebrafish and hiPSC-CMs.

One may argue that the Gβ5 S81L variant further suppresses pacemaker activity by reducing the excitability of the atrial tissue surrounding the SAN through a more pronounced membrane hyperpolarization by CCh/ACh, as we observed in $S81L^{homo}$ hiPSC-CMs (Figure 3E). This was assessed in simulations of a human atrial cardiomyocyte. At baseline, the wild-type model cell exhibits an MDP of −74.1 mV, which becomes hyperpolarized by 5.3 mV upon application of 10 nmol/l ACh (Figure 7A, top, and Figure 7C) as a result of the activation of $I_{K,ACh}$ (Figure 7A, bottom). Due to the hyperpolarization, the threshold stimulus current amplitude increases by 29% (from 14.6 pA/pF at baseline to 18.9 pA/pF) (Figure 7D). After implementing the threefold increase in $I_{K,ACh}$ density (Figure 7B), the ACh-induced hyperpolarization is larger (7.2 mV) as is the increase in threshold stimulus current (53%). Qualitatively similar observations are made at other concentrations of ACh (Figure 7C-D). Thus, the homozygous Gβ5-S81L variant likely does not only slow pacemaker activity of SAN cells, but also reduces excitability of atrial cells, as such contributing to the bradycardic phenotype in patients.

Discussion

Genetic variants in *GNB5*, encoding Gβ5, have been linked to an autosomal recessive multisystem disorder that includes severe bradycardia at rest. The mechanism by which inherited genetic variation in *GNB5* causes bradycardia has remained unexplored. We here conducted electrophysiological studies in hiPSC-CMs that were genome-edited for the Gβ5-S81L variant to uncover the cellular mechanism underlying the bradycardia. We demonstrated that this variant causes a more pronounced slowing of beating rate by means of an increase $I_{K,Ach}$ density in response to cholinergic stimulation. Furthermore, we showed that this effect in hiPSC-CMs, as well as the effect of cholinergic-induced bradycardia in *gnb5* knockout zebrafish, can be rescued by the specific $I_{K,ACh}$ blocker XEN-R0703.

The cholinergic-gated K^+ current $I_{K,ACh}$ is involved in the negative chronotropic effect of the parasympathetic nervous system on heart rate.[24] It is an inwardly rectifier K^+ current,[9] and its activation results in an outward current leading to membrane hyperpolarization, AP shortening, and slowing of beating rate.[10] The increased $I_{K,Ach}$ density that we observed in $S81L^{homo}$ hiPSC-CMs in response to cholinergic stimulation is thus a plausible explanation for the more pronounced

slowing of beating rate and hyperpolarization we observed in these cells. Besides SAN cells, $I_{KA,Ch}$ is also expressed in atrial cardiomyocytes.[6] This raises the possibility that the increase in $I_{K,ACh}$ as a consequence of Gβ5-S81L homozygosity may also contribute to bradycardia during increased vagal tone by reducing the excitability of the atrium. Decreased atrial excitability favours SAN-exit block due to source-to-sink mismatch, eventually resulting in SAN pauses and bradycardia.[25] Indeed, the computer simulation studies that we conducted in an atrial cardiomyocyte model revealed a decreased excitability in cells in which the experimentally observed increase in $I_{K,ACh}$ was implemented. Thus, apart from a direct effect on intrinsic pacemaker function, a more pronounced atrial hyperpolarization due to increased $I_{K,ACh}$ may also contribute to the phenotype of homozygous Gβ5-S81L variant carriers. The fact that the defect associated with the Gβ5-S81L variant in hiPSC-CMs became apparent only upon cholinergic stimulation is in line with clinical findings. Patients homozygous for this variant suffer from severe reduction of minimum HR (dependent on the parasympathetic tone) while maximum HR (chronotropic competence) is normal.[2] Furthermore, the finding that $S81L^{het}$ hiPSC-CMs exhibit a similar $I_{K,ACh}$ density and a similar response to CCh compared to WT hiPSC-CMs is in line with the unaffected heterozygous carriers.[2]

The binding of ACh to M2 muscarinic receptors triggers the activation of heterotrimeric G-proteins that dissociate into Gα-GTP and Gβγ subunits. While Gβ1-β4/γ complexes function to activate GIRK channels, Gβ5 has an inhibitory effect on these channels.[11] Gβ5 associates with RGS proteins of the R7 family, with RGS6 being the most abundant RGS in cardiomyocytes. Gβ5-RGS complexes promote the hydrolysis of Gα-GTP to Gα-GDP which then reassociates with Gβ1-β4/γ, likely relieving the activatory effect of the Gβ1-β4/γ on the GIRK channel.[26] In a heterologous model of neuronal dopamine receptor-mediated signalling, Shamseldin and colleagues showed that Gβ5-S81L leads to loss-of-function of Gβ5-RGS complexes, which presumably decreases the inhibitory reassociation of Gα-GDP with the βγ complexes during the termination response.[27] Conversely, a decreased rate of $I_{K,ACh}$ deactivation was previously reported in both *Rgs6*$^{-/-}$ and *Gnb5*$^{-/-}$ mice[12,28,29], however the mechanism by which decreased deactivation rate of $I_{K,ACh}$ affects HR in the absence of changes in density remains unclear. In the present study, we did not find kinetic changes in $I_{K,Ach}$ as a consequence of the Gβ5-S81L variant. Notwithstanding, the augmented $I_{K,ACh}$ that we observe is in line with the HR-reducing effect of the variant, as substantiated by our computer simulations.

$I_{K,ACh}$ augmentation as a disease mechanism is also operative during atrial fibrillation.[30] $I_{K,ACh}$ blockers have been developed to treat atrial fibrillation, though so far with disappointing results.[31] We demonstrated the potential of the $I_{K,ACh}$ blocker XEN-R0703 by showing an almost complete rescue of the CCh-triggered decrease in beating frequency in $S81L^{homo}$ hiPSC-CMs and by demonstrating rescue of CCh-induced bradycardia in vivo in *gnb5* knockout zebrafish. Therefore, as previously suggested in mice,[32] our current study provides a possible new application for I_{KACh} blockers as a therapy for bradycardia in patients carrying mutations in *GNB5*, which may substitute or postpone pacemaker treatment.

hiPSC-CMs have become increasingly used to study ion channel variants causing inherited arrhythmia syndromes.[33,34] Yet, differentiation protocols that have been used thus far in disease

modelling generate primarily ventricular-like cardiomyocytes.[14] We here investigated for the first time the effects of a human genetic variant in a signal transduction component utilizing a specific differentiation protocol that enriches for hiPSC-CMs expressing $I_{K,ACh}$, a current active in SAN and atrial cells. This cellular model enabled us to study the effect of genetic variation in a component of a G-protein coupled receptor signalling cascade that impacts on ion channel function, rather than genetic variation within the ion channel itself, further underscoring the potential of this model. The introduction of the genetic variant in both the heterozygous and the homozygous state allowed us to compare the effect of different dosages of the variant, which matched the phenotype observed in heterozygous and homozygous S81L^{homo} carriers.

While the effect of the mutation on the $I_{K,ACh}$ current that we uncovered can explain the bradycardia phenotype of the patients, we have not studied the effect of the Gβ5-S81L variant in 'pacemaker-like' cells derived from hiPSCs.[35,36] Furthermore, we focused on the effects of the Gβ5-S81L variant on intrinsic cardiomyocyte electrophysiological properties. *GNB5* is also expressed in neurons and we therefore cannot exclude the possibility of an effect of the variant on the beating rate through its effect in central or peripheral neurons. Finally, baseline AP properties were not different between groups, suggesting that the Gβ5-S81L variant does not affect ion currents at baseline. However, we cannot exclude effects on other ion currents which are modulated by CCh that may contribute to the bradycardic phenotype as well. Nonetheless, our modelling study demonstrated that the effect of the variant on $I_{KA,Ch}$ density is the main contributor to the reduction of the beating rate at the cardiomyocyte level and that blockade of the channel almost completely reverses the bradycardic phenotype.

We studied for the first time the cellular electrophysiological consequences of human genetic variation in *GNB5*. We demonstrated that the Gβ5-S81L variant in the homozygous state results in an increased $I_{K,ACh}$ density upon muscarinic receptor stimulation and excessive slowing of spontaneous activity, a plausible mechanism for the bradycardia observed in the patients. Pharmacological $I_{K,ACh}$ blockade rescues the phenotype in a cellular and an in vivo model, pointing to a possible therapy for bradycardia in patients carrying pathogenic variants in *GNB5*.

Non-standard abbreviations and acronyms

ACh – acethylcholine
AP – action potential
APA_{max} – AP amplitude
$APA_{plateau}$ – AP plateau amplitude
APD_{20} – AP duration at 20% repolarization
APD_{50} – AP duration at 50% repolarization
APD_{80} – AP duration at 80% repolarization
CCh – carbachol
E_K – reversal potential for K^+ ions

GNB5 – G-protein subunit β5 (gene)
Gβ5 – guanine nucleotide-binding protein subunit β5 (protein)
GAP – GTPase-activating
GIRK channel – G protein-coupled inwardly-rectifying K^+ channel
hiPSC-CMs – human induced pluripotent stem cell-derived cardiomyocytes
HR – heart rate
$I_{K,ACh}$ – acetylcholine-activated K^+ current
I_f – hyperpolarization-activated inward current
$I_{Ca,L}$ – L-type Ca^{2+} current
I_{K1} – inwardly rectifying K^+ current
I_{net} – net membrane current
MDP – maximal diastolic potential
RA – retinoic acid
RGS – Regulator of G-protein
SAN – sinoatrial node
V_{max} – maximum AP upstroke velocity

Sources of funding

This study was funded by a grant from the Netherlands Heart Foundation (CVON-Predict project), an Innovation Grant from the Academic Medical Center, and an E-Rare-3 grant (JTC 2015). KG is supported by the Deutsche Forschungsgemeinschaft (SFB 1002A04 and GU 595/3-1).

Disclosures

None

Author contributions

CCV, IM, CDK, MH, TPdB, AOV, JM, EML, JB and CRB designed the experiments. CCV, IM, CDK, MH, TPdB, AOV, RW, SCvA, and DB performed the experiments. KG generated the control line. CCV, IM, CDK, AOV, EML and CRB wrote the manuscript. CRB and JB obtained funding. AOV, JB and CRB supervised the study.

References

1. Verkerk AO, Wilders R. Pacemaker activity of the human sinoatrial node: an update on the effects of mutations in *HCN4* on the hyperpolarization-activated current. *Int J Mol Sci* 2015;16:3071-94.
2. Lodder EM, De Nittis P, Koopman CD, et al. *GNB5* Mutations Cause an Autosomal-Recessive Multisystem Syndrome with Sinus Bradycardia and Cognitive Disability. *Am J Hum Genet* 2016;99:704-10.
3. Stallmeyer B, Kuss J, Kotthoff S, Zumhagen S, Vowinkel KS, Rinne S, Matschke LA, Friedrich C, Schulze-Bahr E, Rust S, Seebohm G, Decher N, Schulze-Bahr E. A Mutation in the G-Protein Gene *GNB2* Causes Familial Sinus Node and Atrioventricular Conduction Dysfunction. *Circ Res* 2017;120:e33–e44.
4. Turkdogan D, Usluer S, Akalin F, Agyuz U, Aslan ES. Familial early infantile epileptic encephalopathy and cardiac conduction disorder: A rare cause of SUDEP in infancy. *Seizure* 2017;50:171-172.
5. Vernon H, Cohen J, De Nittis P, Fatemi A, McClellan R, Goldstein A, Malerba N, Guex N, Reymond A, Merla G. Intellectual developmental disorder with cardiac arrhythmia syndrome in a child with compound heterozygous *GNB5* variants. *Clin Genet* 2018;93:1254-1256.
6. Dobrzynski H, Marples DD, Musa H, Yamanushi TT, Henderson Z, Takagishi Y, Honjo H, Kodama I, Boyett MR. Distribution of the muscarinic K^+ channel proteins $Kir_{3.1}$ and $Kir_{3.4}$ in the ventricle, atrium, and sinoatrial node of heart. *J Histochem Cytochem* 2001;49:1221-34.
7. Krapivinsky G, Gordon EA, Wickman K, Velimirovic B, Krapivinsky L, Clapham DE. The G-protein-gated atrial K^+ channel I_{KACh} is a heteromultimer of two inwardly rectifying K^+-channel proteins. *Nature* 1995;374:135-41.
8. Wickman KD, Iniguez-Lluhl JA, Davenport PA, Taussig R, Krapivinsky GB, Linder ME, Gilman AG, Clapham DE. Recombinant G-protein beta gamma-subunits activate the muscarinic-gated atrial potassium channel. *Nature* 1994;368:255-7.
9. Sakmann B, Noma A, Trautwein W. Acetylcholine activation of single muscarinic K^+ channels in isolated pacemaker cells of the mammalian heart. *Nature* 1983;303:250-3.
10. DiFrancesco D, Ducouret P, Robinson RB. Muscarinic modulation of cardiac rate at low acetylcholine concentrations. *Science* 1989;243:669-71.
11. Lei Q, Jones MB, Talley EM, Garrison JC, Bayliss DA. Molecular mechanisms mediating inhibition of G protein-coupled inwardly-rectifying K^+ channels. *Mol Cells* 2003;15:1-9.
12. Wydeven N, Posokhova E, Xia Z, Martemyanov KA, Wickman K. RGS6, but not RGS4, is the dominant regulator of G protein signaling (RGS) modulator of the parasympathetic regulation of mouse heart rate. *J Biol Chem* 2014;289:2440-9.
13. Lek M, Karczewski KJ, Minikel EV, et al. Analysis of protein-coding genetic variation in 60,706 humans. *Nature* 2016;536:285-91.
14. Devalla HD, Schwach V, Ford JW, Milnes JT, El-Haou S, Jackson C, Gkatzis K, Elliott DA, Chuva de Sousa Lopes SM, Mummery CL, Verkerk AO, Passier R. Atrial-like cardiomyocytes from human pluripotent stem cells are a robust preclinical model for assessing atrial-selective pharmacology. *EMBO Mol Med* 2015;7:394-410.
15. Marczenke M, Piccini I, Mengarelli I, Fell J, Ropke A, Seebohm G, Verkerk AO, Greber B. Cardiac Subtype-Specific Modeling of Kv1.5 Ion Channel Deficiency Using Human Pluripotent Stem Cells. *Front Physiol* 2017;8:469.
16. Veerman CC, Kosmidis G, Mummery CL, Casini S, Verkerk AO, Bellin M. Immaturity of human stem-cell-derived

cardiomyocytes in culture: fatal flaw or soluble problem? *Stem Cells Dev* 2015;24:1035-52.

17. Meijer van Putten RM, Mengarelli I, Guan K, Zegers JG, van Ginneken AC, Verkerk AO, Wilders R. Ion channelopathies in human induced pluripotent stem cell derived cardiomyocytes: a dynamic clamp study with virtual I_{K1}. *Front Physiol* 2015;6:7.
18. Ma J, Guo L, Fiene SJ, Anson BD, Thomson JA, Kamp TJ, Kolaja KL, Swanson BJ, January CT. High purity human-induced pluripotent stem cell-derived cardiomyocytes: electrophysiological properties of action potentials and ionic currents. *Am J Physiol Heart Circ Physiol* 2011;301:H2006-17.
19. Kim JJ, Yang L, Lin B, Zhu X, Sun B, Kaplan AD, Bett GC, Rasmusson RL, London B, Salama G. Mechanism of automaticity in cardiomyocytes derived from human induced pluripotent stem cells. *J Mol Cell Cardiol* 2015;81:81-93.
20. Barros TP, Alderton WK, Reynolds HM, Roach AG, Berghmans S. Zebrafish: an emerging technology for in vivo pharmacological assessment to identify potential safety liabilities in early drug discovery. *Br J Pharmacol* 2008;154:1400-13.
21. Fabbri A, Fantini M, Wilders R, Severi S. Computational analysis of the human sinus node action potential: model development and effects of mutations. *J Physiol* 2017;595:2365-2396.
22. Maleckar MM, Greenstein JL, Trayanova NA, Giles WR. Mathematical simulations of ligand-gated and cell-type specific effects on the action potential of human atrium. *Prog Biophys Mol Biol* 2008;98:161-70.
23. DiFrancesco D, Tromba C. Muscarinic control of the hyperpolarization-activated current (I_f) in rabbit sino-atrial node myocytes. *J Physiol* 1988;405:493-510.
24. Wickman K, Nemec J, Gendler SJ, Clapham DE. Abnormal heart rate regulation in GIRK4 knockout mice. *Neuron* 1998;20:103-14.
25. Joyner RW, van Capelle FJ. Propagation through electrically coupled cells. How a small SA node drives a large atrium. *Biophys J* 1986;50:1157-64.
26. Slepak VZ. Structure, function, and localization of Gbeta5-RGS complexes. *Prog Mol Biol Transl Sci* 2009;86:157-203.
27. Shamseldin HE, Masuho I, Alenizi A, Alyamani S, Patil DN, Ibrahim N, Martemyanov KA, Alkuraya FS. *GNB5* mutation causes a novel neuropsychiatric disorder featuring attention deficit hyperactivity disorder, severely impaired language development and normal cognition. *Genome Biol* 2016;17:195.
28. Posokhova E, Wydeven N, Allen KL, Wickman K, Martemyanov KA. RGS6/Gbeta5 complex accelerates I_{KACh} gating kinetics in atrial myocytes and modulates parasympathetic regulation of heart rate. *Circ Res* 2010;107:1350-4.
29. Yang J, Huang J, Maity B, et al. RGS6, a modulator of parasympathetic activation in heart. *Circ Res* 2010;107:1345-9.
30. Nattel S, Burstein B, Dobrev D. Atrial remodeling and atrial fibrillation: mechanisms and implications. *Circ Arrhythm Electrophysiol* 2008;1:62-73.
31. Podd SJ, Freemantle N, Furniss SS, Sulke N. First clinical trial of specific I_{KACh} blocker shows no reduction in atrial fibrillation burden in patients with paroxysmal atrial fibrillation: pacemaker assessment of BMS 914392 in patients with paroxysmal atrial fibrillation. *Europace* 2016;18:340-6.
32. Mesirca P, Bidaud I, Briec F, et al. G protein-gated I_{KACh} channels as therapeutic targets for treatment of sick sinus syndrome and heart block. *Proc Natl Acad Sci U.S.A.* 2016;113:E932-41.

33. Bellin M, Marchetto MC, Gage FH, Mummery CL. Induced pluripotent stem cells: the new patient? *Nat Rev Mol Cell Biol* 2012;13:713-26.
34. Hoekstra M, Mummery CL, Wilde AA, Bezzina CR, Verkerk AO. Induced pluripotent stem cell derived cardiomyocytes as models for cardiac arrhythmias. *Front Physiol* 2012;3:346.
35. Birket MJ, Ribeiro MC, Verkerk AO, Ward D, Leitoguinho AR, den Hartogh SC, Orlova VV, Devalla HD, Schwach V, Bellin M, Passier R, Mummery CL. Expansion and patterning of cardiovascular progenitors derived from human pluripotent stem cells. *Nat Biotechnol* 2015;33:970-9.
36. Protze SI, Liu J, Nussinovitch U, Ohana L, Backx PH, Gepstein L, Keller GM. Sinoatrial node cardiomyocytes derived from human pluripotent cells function as a biological pacemaker. *Nat Biotechnol* 2017;35:56-68.
37. Dudek J, Cheng IF, Balleininger M, Vaz FM, Streckfuss-Bomeke K, Hubscher D, Vukotic M, Wanders RJ, Rehling P, Guan K. Cardiolipin deficiency affects respiratory chain function and organization in an induced pluripotent stem cell model of Barth syndrome. *Stem Cell Res* 2013;11:806-19.
38. Ran FA, Hsu PD, Wright J, Agarwala V, Scott DA, Zhang F. Genome engineering using the CRISPR-Cas9 system. *Nat Protoc* 2013;8:2281-308.
39. Lian X, Zhang J, Azarin SM, Zhu K, Hazeltine LB, Bao X, Hsiao C, Kamp TJ, Palecek SP. Directed cardiomyocyte differentiation from human pluripotent stem cells by modulating Wnt/beta-catenin signaling under fully defined conditions. *Nat Protoc* 2013;8:162-75.
40. Tohyama S, Hattori F, Sano M, et al. Distinct metabolic flow enables large-scale purification of mouse and human pluripotent stem cell-derived cardiomyocytes. *Cell Stem Cell* 2013;12:127-37.
41. Ramakers C, Ruijter JM, Deprez RH, Moorman AF. Assumption-free analysis of quantitative real-time polymerase chain reaction (PCR) data. *Neurosci Lett* 2003;339:62-6.
42. Barry PH, Lynch JW. Liquid junction potentials and small cell effects in patch-clamp analysis. *J Membr Biol* 1991;121:101-17.
43. Verkerk AO, Veerman CC, Zegers JG, Mengarelli I, Bezzina CR, Wilders R. Patch-Clamp Recording from Human Induced Pluripotent Stem Cell-Derived Cardiomyocytes: Improving Action Potential Characteristics through Dynamic Clamp. *Int J Mol Sci* 2017;18:1873.
44. Westerfield M. The zebrafish book. A guide for the laboratory use of zebrafish (Danio rerio). 2000;Eugene, Oregon, USA: University of Oregon Press.
45. Maleckar MM, Greenstein JL, Giles WR, Trayanova NA. K^+ current changes account for the rate dependence of the action potential in the human atrial myocyte. *Am J Physiol Heart Circ Physiol* 2009;297:H1398-410.

Supplemental Methods

Genetic modification of hiPSCs

The c.242C>T S81L *GNB5* mutation was inserted into a control hiPSC line by means of clustered regularly interspaced short palindromic repeat (CRISPR)/Cas9 technology according to a previously published protocol. Briefly, we inserted the *GNB5*-targeting gRNA sequence into the pSPCas9(BB)-2a-GFP vector as described previously.[1] Next, 4 μg of the gRNA expressing vector and 4 μg of a single strand-oligodeoxynucleotide (ssODN) carrying: (1) the c.242C>T mutation, (2) a total of 96 nucleotides of homologous sequence flanking the mutation site, and (3) a synonymous mutation that generates a HindIII restriction site (Supplemental Figure 1B), were inserted into hiPSCs by nucleofection using the Lonza Amaxa 2b Nucleofector Device and the Stem Cell Nucleofector I Kit according to manufacturer's protocol (Supplemental Figure 1A). Restriction analysis was used to verify the presence of cells carrying the homologous recombination event in the whole population of transfected cells. Transfected cells were subsequently selected by fluorescent-activated cell sorting (FACS) and seeded at a low density (limiting dilution) to achieve monoclonal growth. Separate clones were isolated, expanded and screened for the presence of the *GNB5* mutation by Sanger sequencing. Both heterozygous and homozygous clones carrying the S81L *GNB5* mutation were expanded and stored. Of the successfully targeted clones that we subsequently used in our study, a region of approximately 1000 nucleotides surrounding the gRNA target site was screened by sequencing. To screen for specific mutations caused by the Cas9 protein, putative off-targets were identified using the CRISPR Finder online tool,[2] which, based on the gRNA sequence, proposed 3 candidate genomic loci that exhibited 3 mismatches with the gRNA, while no off-target loci with 2 or 1 mismatches were found. Screening of these regions was performed by Sanger sequencing and found to be unaltered. Moreover, we confirmed the expression of pluripotency markers (see Supplemental Table S1 for the applied antibodies) in the targeted hiPSC clones by immunocytochemistry (Supplemental Figure 1D-E) as described previously.[3] Karyotype analysis was performed by COBRA Fish technique[4] for the wild-type (WT) and $S81L^{het}$ hiPSC line and by G-banding for the $S81L^{homo}$ hiPSC line.

Computer simulations

The spontaneous electrical activity of a single human SA nodal pacemaker cell was simulated using the comprehensive mathematical model that was recently developed by Fabbri et al.4 In this Fabbri-Severi model, acetylcholine (ACh) does not only activate the ACh-activated K^+ current ($I_{K,ACh}$), but also inhibits the hyperpolarization-activated 'funny current' (I_f), through a hyperpolarizing shift in its voltage dependence of activation (thus shifting the half-activation voltage of If to a more negative value). Furthermore, ACh inhibits the L-type Ca^{2+} current ($I_{Ca,L}$) and the sarco/endoplasmic reticulum Ca^{2+}-ATPase (SERCA pump), which regulates the Ca^{2+} uptake into the sarcoplasmic reticulum. Under control conditions, the simulated administration of 10 nmol/l ACh leads to a 21% reduction in pacemaking rate from 74 to 58 beats/min. Of note, the inhibition of

If and activation of $I_{K,ACh}$ are the major determinants of this rate slowdown, whereas the inhibiting effects on $I_{Ca,L}$ and the SERCA pump only play a minor role.[5]

For simulations of a single human atrial cell, we used the model by Maleckar et al.6 The latter model, which is also known as the 'human atrial myocyte with new repolarization' (hAMr) model, was selected because it includes well-validated equations for $I_{K,ACh}$.[7] Action potentials were elicited with a 2 ms, ≈50% suprathreshold stimulus current at a frequency of 1 Hz. The threshold stimulus current amplitude was determined by increasing the stimulus current amplitude in 0.1 pA/pF steps until a train of 100 action potentials could successfully be elicited. To prevent slow drifts in ion concentrations, the intracellular Na^+ and K^+ concentrations were fixed, as were the cleft ion concentrations.

The CellML code of both models, as available from the CellML Model Repository,[8] was edited and run in version 0.9.31.1409 of the Windows based Cellular Open Resource (COR) environment.[8] In both models, the $S81L^{homo}$ mutation was simulated through a threefold increase in the conductance of $I_{K,ACh}$, based on the experimental observations of Figure 2. All simulations were run for a sufficiently long time, i.e. for the duration of a train of 200 action potentials, to reach steady-state behavior.

Supplemental figures and tables

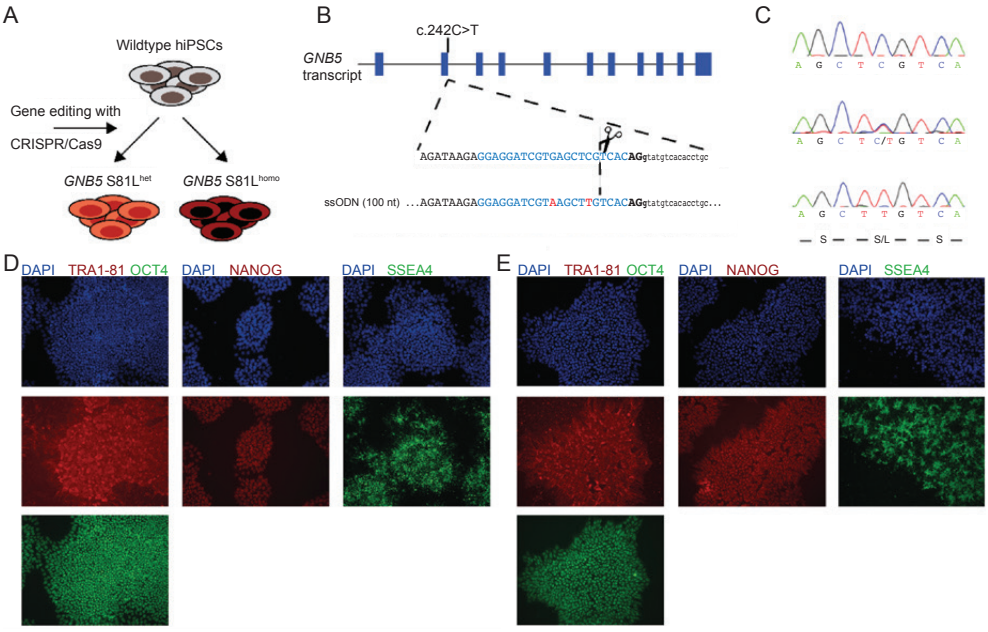

Figure S1. Generation of genome-edited hiPSC lines. (A) Using CRISPR/Cas9 technology, the c.242C>T p.S81L *GNB5* mutation was inserted into a control hiPSC line in heterozygous and homozygous state. (B) Location of the c.242C>T mutation in the *GNB5* transcript and the surrounding sequence. The gRNA sequence that was used is indicated in blue, the PAM sequence in bold. In the single-stranded oligonucleotide (ssODN) that was applied for homologous recombination the c.242C>T mutation is indicated in red and bold, whereas red and italic indicates the synonymous mutation generating a restriction site used for colony screening. (C) Sanger sequences of wildtype (upper panel), S81L heterozygous (middle panel) and S81L homozygous (lower panel) clones. (D-E) Immunocytochemistry of the pluripotency markers OCT4, TRA1-81, NANOG, and SSEA4 in the (D) S81L heterozygous and (E) homozygous lines. Scale bars are 100 µm.

Gene	Forward 5' to 3'	Reverse 5' to 3'
TBP	GCTCACCCACCAACAATTTAG	TCTGCTCTGACTTTAGCACCTG
NR2F2	GCCATAGTCCTGTTCACCTCA	AATCTCGTCGGCTGGTTG
NPPA	GCTCCTTCTCCACCACCAC	GGGCACGACCTCATCTTCTA
KCNJ3	ACCTATCCCAGCGAAGCAT	AAAACGATGACCCCAAAGAA
KCNJ5	GAGCCCTTTCTGGGAGATGT	TTTCCAAGGTGAGGACTGGTG
GNB5	CGTGTCGCCTCTATGACCTG	CTTTGAGAACATCCCAGACG
RGS6	AAATCTGGCAAGAGTTTCTGG	GGGCATAGCTGTCACTCTTCA

Table S1. Primer sequences used for quantitative PCRs.

Antigen	Isotype	Company
OCT3/4	Mouse IgG2b	Santa Cruz Biotechnology
TRA 1-81	Mouse IgM	Abcam
SSEA-4	Mouse Ig3	Santa Cruz Biotechnology
NANOG	Goat IgG	R&D Systems

Table S2. Antibodies used for immunochemistry.

Location	Genomic sequence	Mismatches	Strand	Type
22:19979742-19979764	GAGG**T**C**C**GTGAGC**T**TGTCAC ***TGG***	3	–	Exonic
16:77913475-77913497	GAGGATCG**A**GAGCT**GA**TCAC ***TGG***	3	–	Intronic
1:160408628-160408650	GAGGAT**G**GTGAGCTC**A**TC**T**C ***TGG***	3	+	Intronic

Table S3. Putative genomic off-target sites for the gRNA used to introduce mutation p.S81L in *GNB5*. Sequence in italic depicts the PAM site (NGG), in bold and red depicts mismatches with the gRNA. Original gRNA: GAGGATCGTGAGCTCGTCACAGG.

Supplemental references

1. Ran FA, Hsu PD, Wright J, Agarwala V, Scott DA, Zhang F. Genome engineering using the CRISPR-Cas9 system. *Nat Protoc* 2013;8:2281-308.
2. Hodgkins A, Farne A, Perera S, Grego T, Parry-Smith DJ, Skarnes WC, Iyer V. WGE: a CRISPR database for genome engineering. *Bioinformatics* 2015;31:3078-80.
3. Veerman CC, Mengarelli I, Guan K, Stauske M, Barc J, Tan HL, Wilde AA, Verkerk AO, Bezzina CR. hiPSC-derived cardiomyocytes from Brugada Syndrome patients without identified mutations do not exhibit clear cellular electrophysiological abnormalities. *Sci Rep* 2016;6:30967.
4. Szuhai K, Tanke HJ. COBRA: combined binary ratio labeling of nucleic-acid probes for multi-color fluorescence in situ hybridization karyotyping. *Nat Protoc* 2006;1:264-75.
5. Fabbri A, Fantini M, Wilders R, Severi S. Computational analysis of the human sinus node action potential: model development and effects of mutations. *J Physiol* 2017;595:2365-2396.
6. Maleckar MM, Greenstein JL, Trayanova NA, Giles WR. Mathematical simulations of ligand-gated and cell-type specific effects on the action potential of human atrium. *Prog Biophys Mol Biol* 2008;98:161-70.
7. Maleckar MM, Greenstein JL, Giles WR, Trayanova NA. K^+ current changes account for the rate dependence of the action potential in the human atrial myocyte. *Am J Physiol Heart Circ Physiol* 2009;297:H1398-410.
8. Lloyd CM, Lawson JR, Hunter PJ, Nielsen PF. The CellML Model Repository. *Bioinformatics* 2008;24:2122-3.
9. Garny A, Kohl P, Noble D. Cellular open resource (COR): a public CellML based environment for modelling biological function. *Int J Bifurcat Chaos* 2003;13:3579–3590.

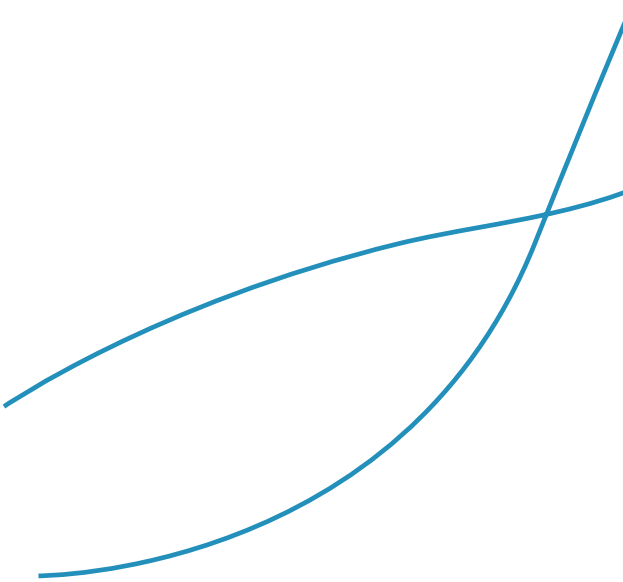

CHAPTER 6

Tmem161b: a novel regulator of cardiac electrophysiology

Koopman CD, Verkerk AO, de Angelis JE, de Jonge B,
Onderwater Y, Smith KA[#], de Boer TP[#], Bakkers J[#]

[#] contributed equally

Abstract

The coordinated contraction of the heart relies on a proper generation and conduction of action potentials, which is regulated by the orchestrated opening and closing of cardiac ion channels. Channelopathies are a group of disorders in which ion channel function is disrupted. Patients with cardiac channelopathies may develop arrhythmias, which can result in sudden cardiac death. The identification of genetic factors that predispose individuals to arrhythmias is important as it enables genetic testing and may contribute to diagnosis, risk stratification and preventative treatment. The zebrafish *grime* mutant was identified in an ENU screen and presented with severe arrhythmias starting at 2 days post fertilization. Using whole genome sequencing based mapping, a nonsense mutation in *tmem161b* was found. *tmem161b* is a gene with unknown function and structure.

Methods: High-speed brightfield imaging was used to characterize arrhythmias, heart rate, and short-term variation (STV) in atrial contraction interval in *grime* mutants and siblings. To determine the effects of the *tmem161b* mutation on cardiac cellular electrophysiology, in vivo optogenetic imaging was performed at 2 and 3 dpf using the genetically encoded membrane voltage sensor VSFP-butterfly. Electrical conduction was visualized and parameters of action potential shape quantified, including upstroke time ($Up_{90\text{-}10}$), action potential duration (APD_{90}), repolarization time ($APD_{90\text{-}10}$) and amplitude. To validate the embryonic VSFP data, patch-clamping was performed on isolated adult wild-type and *tmem161b*$^{+/-}$ cardiomyocytes and action potentials measured. Subsequently, voltage-clamping was used to investigate which repolarizing currents contributed to the changes in AP shape. Intracellular Ca^{2+} transients were vizualised and analyzed in 3 dpf *tmem161b* hearts, using the genetically encoded Ca^{2+} sensor GCaMP6f. Different parameters were quantified, including Ca^{2+} transient upstroke speed, recovery speed, and amplitude.

Results: *grime* mutants showed a ±25% decrease in heart rate at 2-5 dpf, and presented with higher atrial contraction interval STV values and severe arrhythmias. The number of fish with arrhythmias as well as the complexity of arrhythmias increased significantly after 3 dpf. VSFP analysis revealed changes in conduction, prolonged APD_{90} and $APD_{90\text{-}10}$ values, and decreased action potential amplitudes. Patch-clamping confirmed VSFP findings, and demonstrated that the *tmem161b* mutation results in a faster and more pronounced phase 1 repolarization, a more negative and prolonged plateau phase, and EADs at lower frequencies. Voltage-clamping showed that $I_{Ca,L}$ and I_{Kr} were affected, and are likely responsible for the observed action potential changes. Analysis of Ca^{2+} transients in 3 dpf *tmem161b* confirmed the voltage-clamp findings, as Ca^{2+} transients showed distinct changes in *tmem161b*$^{-/-}$ hearts. The Ca^{2+} transient upstroke speed was increased (only in ventricle), the recovery phase prolonged (throughout the heart) and the amplitude increased (throughout the heart).

Conclusion: We identified Tmem161b as an important novel regulator of cardiac cellular electrophysiology, as zebrafish *tmem161b* mutants present with distinct changes in action potential repolarization and severe arrhythmias, likely due to disruption of $I_{Ca,L}$ and I_{Kr}. Future

research should focus on elucidating the role of Tmem161b within the cardiomyocyte proteome and the importance of TMEM161B in human cardiac electrophysiology.

Introduction

The coordinated contraction of the heart relies on a proper generation and conduction of action potentials (APs); electrical impulses that are formed by the orchestrated opening and closing of cardiac ion channels. A disruption of these highly coordinated processes can lead to arrhythmias and may even result in sudden cardiac death.[1] It is estimated that 5-15% of sudden cardiac deaths are caused by inherited arrhythmia syndromes, so-called 'channelopathies'.[2] Channelopathies are a heterogeneous group of disorders that are characterized by an electrically unstable substrate (disrupted ion channels) in a structurally normal heart.[3] The identification of genetic factors that predispose individuals to arrhythmias is important as it enables genetic testing and may contribute to diagnosis, risk stratification and preventative treatment. Much progress has already been made in this regard, which has led to progressive change in the approach of diagnosis and treatment of channelopathies.[4] At the same time, cardiac electrophysiology remains extremely complex and a further identification of electrophysiology genes will improve our understanding of the mechanisms that underlie arrhythmias.

Transmembrane proteins (TMEM) are proteins that are linked to and span across biological membranes. Within the TMEM class of proteins, there is also a TMEM family of proteins.[5] This family consists of approximately 310 different members that are predicted to be components of cell membranes, such as mitochondrial, lysosomal, Golgi, and plasma membranes. The biological function of most members of this family remains unknown, mostly due to difficulties in the extraction and purification of transmembrane proteins.[6] During recent years, the function of a number of TMEMs has been elucidated and it has become clear that this family is involved in many important physiological functions, such as epidermal keratinization (TMEM45a)[7], smooth muscle contraction and melatonin secretion (TMEM16a and TMEM16b)[8,9], protein glycosylation (TMEM165)[10], angiogenesis (TMEM215)[11] and lysosomal homeostasis (TMEM55B)[12]. Some TMEMs are known to function as channels to permit the transport of specific substances across membranes. An example of this is TMEM16, which was identified as a calcium-activated chloride channel.[13,14]

The zebrafish is increasingly being used as a model for disease due to their conserved organ physiology, also in studies of cardiac arrhythmias.[15-22] Certain aspects of zebrafish cardiac electrophysiology, like action potential shape and heart rate, are very similar to that of humans.[20] In addition, zebrafish are highly suitable for large-scale forward genetic screens, as they produce high numbers of offspring, and embryos develop rapidly and externally. N-ethyl-N-nitrosourea (ENU) is a chemical that can be used to effectively introduce random point-mutations on a genome-wide scale.[23] Studies using ENU mutagenesis have provided a wealth of knowledge on genotype-phenotype relationships, demonstrating that ENU is an efficient and reliable method to screen for novel genes.[24]

In this study we characterize the zebrafish *grime* mutant, which carries a nonsense mutation in *tmem161b*, a gene with unknown function and structure. The *grime* mutant was identified in

an ENU screen and presented with severe arrhythmias starting at 2 days post fertilization. Using in vivo imaging on transgenic embryos expressing a cardiac voltage sensitive fluorescence protein (VSFP) sensor or a cardiac Ca^{2+} sensor (GCaMP6f), and by performing patch-clamp experiments on isolated adult cardiomyocytes, we found that the *tmem161b* mutation affects the cardiac action potential shape by influencing Ca^{2+} and K^{+} currents. These findings implicate a novel role of Tmem161b in the modulation of ion channels that shape cardiac electrophysiology.

Materials and methods

Zebrafish husbandry

Fish used in this study were housed under standard conditions as previously described.[25] All experiments were conducted in accordance to the ethical guidelines and approved by the local ethics committee at the Royal Dutch Academy of Sciences (KNAW) and the University of Queensland.

Generation of mutant line

tmem161b fish were generated using N-ethyl-N-nitrosourea (ENU) mutagenesis as described before.[26] F1 progeny from mutagenized males were crossed to wild-type fish to produce F2 families. Subsequent incrossing of F2 progeny generated F3 embryos that were screened for cardiac arrhythmias during multiple time-points. To generate a stable *tmem161b* mutant line, the *grime* mutant was outcrossed multiple times.

RT-PCR.

RNA was isolated from whole embryos 4 days post fertilization (dpf) and from hearts of adult TL wild-type fish. Adult hearts were either processed as a whole (atrium and ventricle, but without the bulbus arteriosus, n=3) or separated into atrial (n=8) and ventricular (n=4) samples. *ef1α* was used as reference gene for the RT-PCR. Primers for *ef1α* were: forward primer GGCCACGTCGACTCCGGAAAGTCC, reverse primer: CTCAAAACGAGCCTGGCTGTAAGG. Primers for *tmem161b* were: forward primer ACCAACACCCCACAGAAGAC, reverse primer CTCCGCCACACAGAAGTACA, product size 272 bp.

High-speed brightfield imaging

Embryos were placed in 1-phenyl-2-thiourea (PTU) 20-24 hours post fertilization (hpf) to prevent pigmentation. 2-5 dpf embryos were embedded in 0.3% agarose prepared in E3 medium containing 16 mg/ml Tricaine. Recordings were performed at 150 fps using a high-speed inverted light microscope at 28°C. Heart rate measurements were analyzed using ImageJ (U. S. National Institutes of Health, Bethesda, Maryland, USA). Movies from offspring of 3 different breeding pairs were analyzed, to assess if changes were consistent between pairs, and data from all embryos

pooled. For each larvae 20 consecutive beats were analyzed. The STV of atrial contraction interval was determined by the following formula: (SUM ΔR-R)/(n*√2). Heart rates were considered bradycardic when they were 30% lower than the wild-type average heart rate (2 dpf <133 bpm, 3 dpf <145 bpm, 4 dpf <143 bpm, 5 dpf <154 bpm). This cut-off was chosen as in humans a heart rate of <40 beats per minute (bpm) is considered bradycardic, which is ±30% lower than a resting heart rate of 60 bpm. Hearts were considered to have sinoatroial node (SAN) irregulaties when the STV was ≥10% higher than the highest wild-type STV value (highest wild-type STV was 6.05 ms, an STV of ≥7.6 ms was considered irregular). AV-blocks were identified by eye, by observing the high-speed speed movies at a low speed. An arrhythmia was identified as an AV-block when a clearly visible coordinated atrial contraction was not followed by a ventricular contraction.

High-speed fluorescence imaging in embryos

Fish carrying the *tmem161b* mutation were crossed to the *tg(myl7:Gal4FF;UAS:GCaMP6f)* or *tg(myl7:chimeric VSFP-butterfly CY)* line.[27] A morpholino (MO) oligomer targeted against *tnnt2a* (5'-CATGTTTGCTCTGATCTGACACGCA-3') was used to uncouple contraction from excitation in *tmem161b* embryos carrying the VSFP-butterfly or GCaMP6f sensor, thereby preventing contraction artifacts in our recordings of cardiac action potentials (APs) and Ca^{2+} transients. This 'silent heart' ATG morpholino was applied as described previously.[28] At 24 hours post fertilization, embryos were placed in PTU to keep them transparent. Embryos at 2-3 dpf were embedded in 0.3% agarose prepared in E3 medium containing 16 mg/mL Tricaine and placed in a heated (28 °C) recording chamber. Recordings were performed using a custom-build upright widefield microscope (Cairn research, Kent, UK) equipped with a 20x 1.0 NA objective (Olympus XLUMPLFLN20X W). For VSFP imaging white LED excitation light was filtered using a 438/24 nm filter (Semrock FF02-438/24-25) and reflected towards the objective using a 458 nm dichroic mirror (Semrock FF458-Di02-25x36). Emitted fluorescence was directed to an emission splitter unit (OptoSplit II ByPass Image Splitter) fitted with a 509 nm dichroic mirror (Semrock FF509-FDi01-25x36) and 483/32 nm and 514 long-pass emission filters (Semrock FF01-483/32-25 and LP02-514RU-25, respectively). For GCaMP6f imaging blue LED excitation light (470 nm) was filtered using a 470/40 nm filter (Chroma ET470/40x) and reflected towards the objective using a 515 nm dichroic mirror (Chroma T515lp). Emitted fluorescence was filtered by a 514 long-pass filter (Semrock LP02-514RU). Images were projected on a high-speed camera (Andor Zyla 4.2 plus sCMOS). Recordings were performed at 100 fps, for 1000-2000 frames. Recordings were analyzed using ImageJ and Matlab (Version R2015a, Mathworks, Natick, MA, USA). Line plots (Figure 3B-G) were obtained by drawing a line over the atrial and ventricular wall, straightening out this line, and plotting the signals along this line (1 pixel wide) versus time (10 seconds). The average graphs in Figure 4F-G were obtained by averaging five representative APs from the same fish into one AP, and plotting this average AP from all fish with the same genotype into one graph.

Whole mount embryo immunostaining

Embryos for immunocytochemistry were fixed in 2% paraformaldehyde containing glycerol (overnight at 4°C), and washed with PBS containing 0.1% Tween (PBST) the following day. Embryos were permeabilized using Proteinase K. The primary antibody used was mouse anti-Isl1 (Developmental Studies Hybridoma Bank, Iowa City, IA, USA, clone 39.4D5, 1:100). The secondary antibody used was Cy3 (Thermo Fisher Scientific, Waltham, MA USA, 1:2000). Embryos were mounted and imaged ventrally using an inverted Leica TCS SP8 confocal laser-scanning microscope (Leica microsystems, Wetzlar, Germany) with a 20x objective.

Cellular Electrophysiology

Cell Preparation. Single ventricular cells were isolated by an enzymatic dissociation procedure as described previously.[29] For this, ventricles from 3 adult fishes were pooled and stored at RT in a modified Tyrode's solution containing (in mmol/L): NaCl 140, KCl 5.4, $CaCl_2$ 1.8, $MgCl_2$ 1.0, glucose 5.5, HEPES 5.0; pH 7.4 (set with NaOH). Subsequently, the ventricles were cut in small pieces, which were transferred to Tyrode's solution with 10 µmol/L $CaCl_2$ (30°C). The solution was refreshed one time before the addition Liberase TM research grade (final concentration 0.038 mg/mL (Roche Diagnostics, GmbH, Mannheim, Germany)) and Elastase from porcine pancreas (final concentration 0.01 mg/mL (Bio-Connect B.V., Huissen, Netherlands)) for 12–15 min. During the incubation period, the tissue was triturated through a pipette (tip diameter: 2.0 mm). The dissociation was stopped by transferring the ventricle pieces into a modified Kraft-Brühe solution (30°C) containing (in mmol/L): KCl 85, K_2HPO_4 30, $MgSO_4$ 5.0, glucose 5.5, pyruvic acid 5.0, creatine 5.0, taurine 30, β-hydroxybutyric acid 5.0, succinic acid 5.0, BSA 1%, Na_2ATP 2.0; pH 6.9 (set with KOH). The tissue pieces were triturated (pipette tip diameter: 0.8 mm) in Kraft-Brühe solution (30°C) for 4 min to obtain single cells. The cells were stored for at least 45 min in modified Kraft-Brühe solution before they were put into a recording chamber on the stage of an inverted microscope (Nikon Diaphot), and superfused with Tyrode's solution (28 °C). Quiescent single cells with smooth surfaces were selected for electrophysiological measurements.

Data acquisition. Action potentials (APs) and net membrane currents were recorded using the amphotericin-B perforated patch-clamp technique and an Axopatch 200B amplifier (Molecular Devices, Sunnyvale, CA, USA). Voltage control, data acquisition, and analysis were realized with custom-made software. Pipettes (resistance 3–4 MΩ) were pulled from borosilicate glass capillaries (Harvard Apparatus, UK) using a custom-made microelectrode puller, and filled with solution containing (in mmol/L): 125 K-gluconate, 20 KCl, 10 NaCl, 0.44 amphotericin-B, 10 HEPES; pH 7.2 (KOH). Potentials were corrected for the calculated liquid junction potential.[30] Signals were low-pass-filtered with a cutoff of 5 kHz and digitized at 40 and 5 kHz for APs and membrane currents, respectively. Cell membrane capacitance (C_m) was estimated by dividing the time constant of the decay of the capacitive transient in response to 5 mV hyperpolarizing voltage clamp steps from -40 mV by the series resistance.

Action potentials. APs were elicited at 0.2, 1, 2, and 3 Hz by 3-ms, ~1.2× threshold current pulses through the patch pipette. As depicted in Figure 5A, APs were characterized by resting membrane potential (RMP), maximum AP amplitude (APAmax), AP duration at 20, 50 and 90% of repolarization (APD_{20}, APD_{50}, APD_{90} respectively), maximal upstroke velocity (dV/dt_{max}), and plateau amplitude (APA_{plat}; measured 50 ms after the AP upstroke). Averages were taken from 10 consecutive APs.

Membrane currents. The AP measurements were alternated by a general voltage clamp protocol to elucidate the ionic mechanism underlying the AP changes. Therefore, 500 ms depolarizing and hyperpolarizing voltage clamp steps were applied from a holding potential of -50 mV with a cycle length of 2 sec (Figure 7A). To ensure that the remaining cardiomyocytes in the recording chamber stay undistorted for biophysical analysis, our voltage clamp measurements were performed without specific channel blockers or modified solutions. Inward rectifier K^+ current (I_{K1}) and rapid delayed rectifier K^+ current I_{Kr} were defined as the quasi steady-state current at the end of the voltage-clamp steps at potentials negative or positive to -30 mV, respectively. The L-type Ca^{2+} current ($I_{Ca,L}$) was defined as the difference between peak current and steady-state current at potentials of -50 mV and more positive. Current densities were obtained by normalizing to C_m. Gating properties of $I_{Ca,L}$ were measured with a two-pulse voltage clamp protocol (Figure 7D) or with a double-pulse protocol with variable interpulse intervals (Figure 7F).

6

Statistical analysis

Cellular Electrophysiology data. Data is presented as mean ± SEM. Statistical analysis was carried out with SigmaStat 3.5 software. Normality and equal variance assumptions were tested with the Kolmogorov-Smirnov and the Levene median test, respectively. Two groups were compared with unpaired t-test or with two-way repeated measures ANOVA followed by pairwise comparison using the Student–Newman–Keuls test. $P < 0.05$ defines statistical significance.

Other data. Data was analyzed blinded. Statistical analysis and drawing of graphs and plots were carried out in GraphPad Prism (version 6 for Mac OS X, GraphPad Software, San Diego California USA). Differences between two groups were analyzed using the paired Student's t-test, and comparisons between experimental groups were analyzed by one-way ANOVA for non-parametric variables with Tukey's post-test for intergroup comparisons. All data is presented as mean ± SD unless indicated otherwise, and $p<0.05$ was considered significant. * $p\leq0.05$, ** $p\leq0.01$, *** $p\leq0.001$, **** $p\leq0.0001$, n.s. $p>0.05$. n denotes the number of fish used per dataset.

Results

The *grime* mutant was identified in an ENU screen and displays severe arrhythmias

In an effort to identify new genes that are involved in cardiac form and function, an N-ethyl-N-nitrosourea (ENU) forward genetic screen was performed in zebrafish (Figure 1A). Male zebrafish

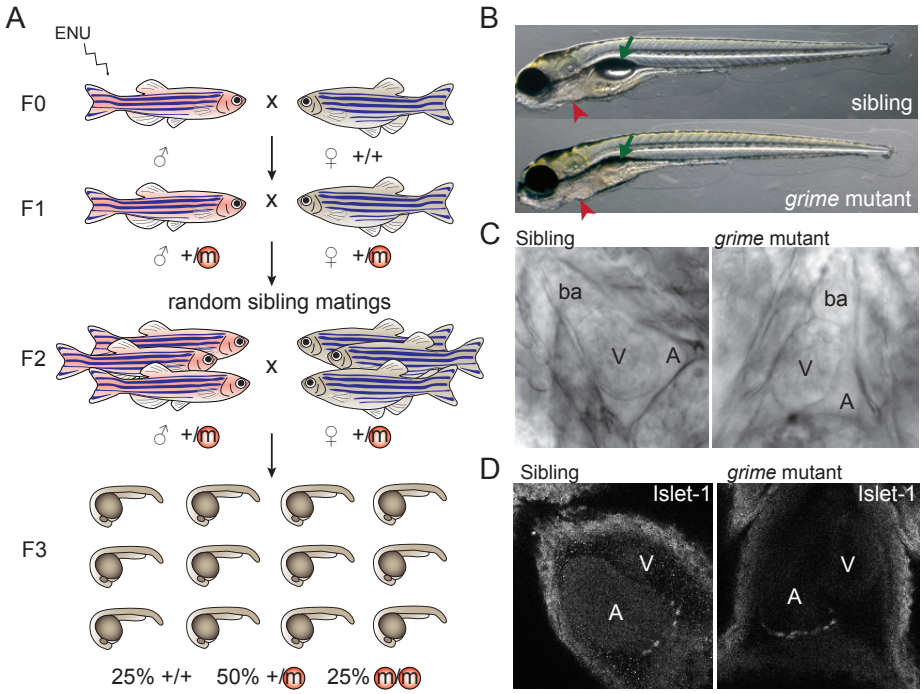

Figure 1. Characterization of the zebrafish grime mutant. (A) Schematic diagram of the ENU-based forward genetic screen that led to the identification of the grime mutant. Male founders were mutagenized with ENU and outcrossed to wild-type females. Progeny of this cross was raised and incrossed to generate F2 families. Fish from these families were randomly incrossed and F3 embryos were screened for cardiac phenotypes that occurred in ±25% of the embryos, indicating Mendelian inheritance. (B) Side view of a 5-day-old sibling and grime mutant larvae. The grime mutant displays a normal body plan, but fails to inflate its swim bladder. The green arrows indicate the location of the swim bladder, the red arrowheads the location of the heart. (C) High-speed imaging stills of a sibling and grime mutant heart at 5 days post fertilization. A: atrium, V: ventricle, ba: bulbus arteriosus. (D) 3-day-old *grime* mutant and wild-type heart immuno-stained for Islet-1, a transcription factor marking pacemaker cells. The pacemaker cells are clearly visible as a ring-like structure at the base of the atrium.

founders (F0) were mutagenized with ENU for several weeks and then outcrossed to wild-type females. Progeny of this cross was raised and incrossed to generate F2 families. Fish from F2 families were incrossed and F3 embryos were collected and screened for defects in cardiac morphology or function. The *grime* mutant (named after the *grime* music genre) was one of the mutants identified in this screen, as it presented with severe arrhythmias at 4-5 days post fertilization (dpf) and died between 7-15 dpf. We observed strong effects in the sinoatrial node (SAN) and atrioventricular canal (AVC), as hearts seemed to beat slower, more irregular and atrial contraction was not always followed by ventricular contraction. Next to the arrhythmic phenotype, *grime* mutants had no apparent morphological defects in body plan and cardiac structure (Figure 1B-C). However, many mutants (± 90-100%) did fail to inflate their swim bladder by 5 dpf (Figure

1B). In addition, some fish with arrhythmias developed (severe) cardiac edema, likely in response to changes in circulation and blood pressure. Immunostaining of the pacemaker cells, using an antibody against islet-1 (a transcription factor marking pacemaker cells), ruled out that the arrhythmias we observed were a result of poorly defined or absent pacemaker cells (Figure 1D, S1A), as *grime* mutants displayed no changes in the structure and number of pacemaker cells compared to their siblings.

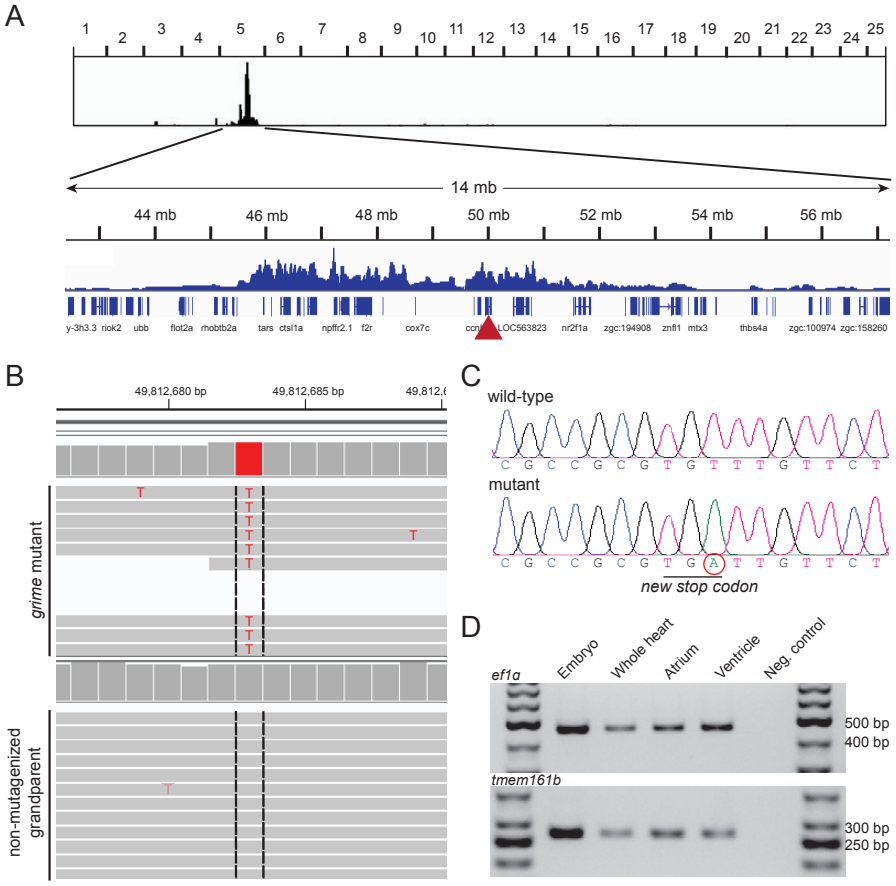

Figure 2. Identification of a *tmem161b* mutation in the grime mutant. (A) Graph showing a homozygosity peak on chromosome 5, following whole genome sequencing, and a zoom-in of the linked region. The red arrowhead indicates the *tmem161b* gene. (B) Sequencing reads from a mutant showing a homozygous mutation in *tmem161b* that is absent in a direct, non-mutagenized ancestor. (C) Sequencing profiles showing part of the *tmem161b* gene sequence in wild-type and *tmem161b* mutants. The red circle highlights the location of the T>A mutation. The mutation introduces a new stop codon. (D) RT-PCR data showing *tmem161b* expression in 4 dpf whole embryos (n=100-200), whole hearts (n=3), only atria (n=8) and only ventricles (n=4). *ef1α* was used as control gene. A 50 bp ladder was added on both sides of the samples, the size of each band is indicated on the side. Neg: negative.

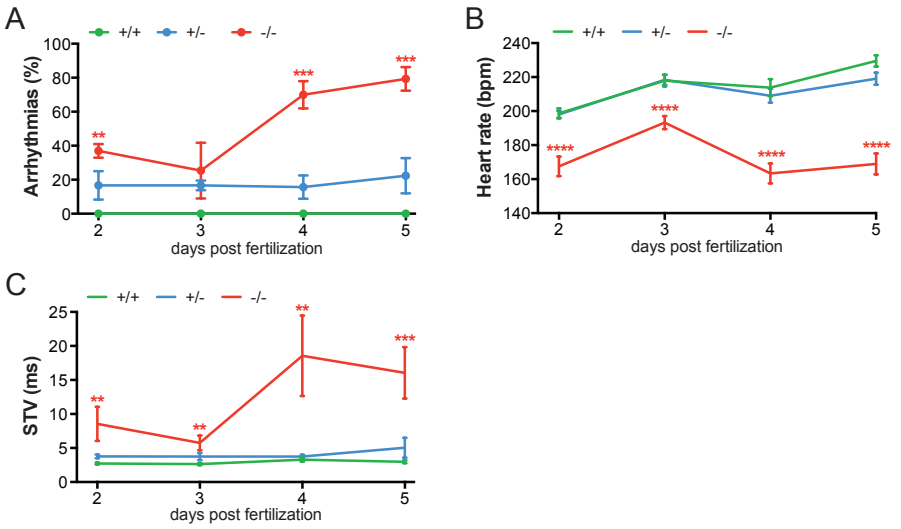

Figure 3. Characterization of arrhythmias in the *tmem161b* mutant. (A-C) Graphs of wild-type, heterozygous and homozygous *tmem161b* mutants at 2-5 dpf (mean ± SEM, n=3 different pairs)(** p≤0.01, *** p≤0.001, **** p≤0.0001), showing (A) the % of embryos presenting with arrhythmias, (B) heart rates, and (C) the short-term variation (STV) in atrial contraction interval. Bpm: beats per minute.

Arrhythmias in the *grime* mutant are due to a nonsense mutation in *tmem161b*

To determine which mutation was linked to the arrhythmic phenotype that we observed in the *grime* mutant, whole genome sequencing based mapping was performed. The genomes of *grime* mutants, non-mutagenized wild-type ancestors, and the ENU treated ancestor were analyzed and variants (SNPs) were identified. Subsequently, the mutant genome was scanned for SNPs that were ENU derived and homozygous. A unique homozygosity peak was identified on chromosome 5 (Figure 2A) and within this linked region two candidate genes presented themselves: the novel transmembrane domain protein *tmem161b* and the nuclear receptor protein *nr2f1a*. Given that a zebrafish mutant for nr2f1a had already been reported with vascular defects[31] and the *grime* mutant showed no vascular anomalies, our attention was directed to *tmem161b*. The homozygous *tmem161b* SNP encoded for a nonsense mutation (c.1398T>A), which introduced a new stop codon resulting in the loss of the last 19 amino acids (aa 466 – 484, p.C466*)(Figure 2B-C, S2A). To confirm that mutation of *tmem161b* was the cause of the arrhythmia phenotype, genome editing of *tmem161b* was performed using Crispr/cas9 technology. Complementary analysis using Crispr/cas9 edited F0 founder fish crossed with a *grime/tmem161b* heterozygous carrier resulted in embryos in which the arrhythmia phenotype, as well as the absence of a swim bladder was reproduced. In the rest of this study we will refer to the *grime* mutant as the *tmem161b* mutant. We found that Tmem161b is highly conserved between zebrafish and man (Figure S2B), but humans express multiple isoforms of TMEM161B, while in zebrafish only one isoform has been

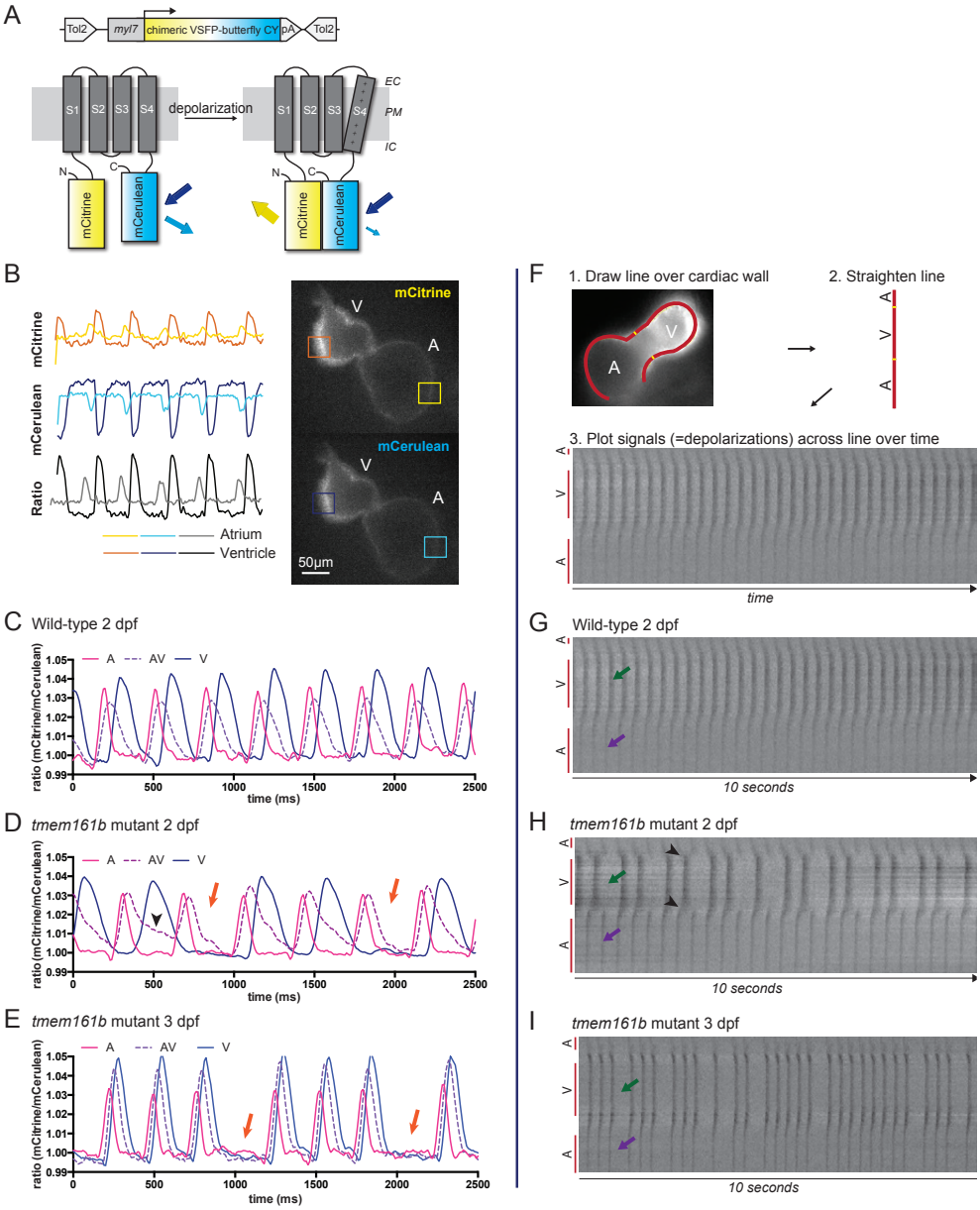

Figure 4. Action potential conduction in *tmem161b* embryos. (A) DNA construct and concept of the sensing mechanism of chimeric VSFP-butterfly CY. The *myl7* promoter restricts VSFP expression to the heart. The sensor consists of a voltage sensitive domain with transmembrane segments S1-S4, sandwiched between a FRET pair of mCitrine and mCerulean. Movement of S4 upon membrane depolarization translates into a change of FRET efficiency. pA: poly-A, EC: extracellular, PM: plasma membrane, IC: intracellular. (B) Movies of 2-3 dpf non-contracting VSFP hearts were recorded. An increase in mCitrine (top panel) and decrease in mCerulean (bottom panel) is visible every consecutive excitation cycle, starting in the atrium and followed by the ventricle. From these signals, a ratiometric

signal can be calculated that reflects action potential shape. Squared boxes indicate the region of measurement. A: atrium, V: ventricle. (C-E) Action potential graphs showing atrial, AV-canal and ventricular activations over time. Examples of a wild-type heart in sinus rhythm, and *tmem161b* mutant hearts with AV-block or with sinoatrial irregularities are shown. Orange arrows indicate missing activations, the black arrowhead prolonged repolarization of an AV-canal action potential. AV: atrioventricular. (F) Line plots were generated by drawing a line across the cardiac wall (red), straightening the line, and plotting the fluorescence signals across this line over time. A change from light grey to darker grey in each line plot indicates depolarization. (G-I) Line plots showing depolarizations across the entire cardiac wall over time. Examples of a wild-type heart in sinus rhythm, and *tmem161b* mutant hearts with AV-block or with sinoatrial irregularities are shown. The purple and green arrows indicate atrial and ventricular depolarization, respectively, or the location where this depolarization should have taken place. The black arrowheads indicate broad AVC depolarizations that extend into the consecutive depolarization.

identified (source: NCBI and Ensembl databases). Reverse Transcription (RT)-PCR data revealed that *tmem161b* is expressed in zebrafish embryos and throughout the adult zebrafish heart (Figure 2D), confirming a possible role of Tmem161b in cardiac function.

Arrhythmias in the *tmem161b* mutant increase in frequency and complexity over time

Using high-speed imaging we studied the arrhythmias that were present in *tmem161b* mutants. Overall, we found arrhythmias in approximately 30-40% of the embryos at 2 dpf (Figure 3A). This number slightly decreased at 3 dpf, but increased drastically at 4-5 dpf to >60%. Strikingly, heterozygous fish also presented with arrhythmias, although the frequency of arrhythmias was much lower and more or less constant over time at 15-25%. Analysis of heart rate revealed that *tmem161b* mutants had an approximately 25% lower heart rate compared to wild-type siblings at 2 and 3 days post fertilization (dpf), which decreased further at 4-5 dpf (Figure 3B). Heart rates of heterozygous fish did not significantly differ from wild-type siblings, but a slight trend towards a lower heart rate was visible at 4-5 dpf. To investigate the regularity of sinoatrial node (SAN) firing, we measured short-term variation (STV) of the interval between atrial contractions as an indication of SAN beat-to-beat variation (Figure 3C). *tmem161b* mutants displayed significantly higher atrial STV values at 2-5 dpf, with a dip at 3 dpf and a drastic increase at 4-5 dpf, indicating that SAN firing was more irregular compared to wild-type siblings. We grouped the observed arrhythmias into 6 different classes based on our findings, containing one or more of the following components (table S1): (1) bradycardia, defined as a ≥30% decrease in heart rate compared to the average wild-type heart rate, (2) SAN irregularities, defined by an STV that showed a ≥10% increase compared to the highest wild-type STV value, and (3) AV-block, defined as an atrial contraction that was not followed by a ventricular contraction. Some hearts were too arrhythmic to classify, so we defined those as completely irregular (class 7). The severity and complexity of arrhythmias increased over time, and by day 5 many larvae were severely affected (table S1).

In vivo analysis of action potentials reveals abnormal conduction patterns in *tmem161b* mutants

As *tmem161b* mutants presented with arrhythmias, we focused to analyze the effects of the mutation on cardiac electrophysiology. To this end, we crossed *tmem161b* fish with fish carrying an optogenetic cardiac-targeted voltage sensor *tg(myl7:VSFP-butterfly)*.[27] VSFP-butterfly allows the in vivo analysis of action potential (AP) shape and propagation and consists of a transmembrane voltage sensitive domain, which is sandwiched between a mCitrine and mCerulean fluorescence resonance energy transfer (FRET) pair. Upon membrane depolarization, the voltage sensitive domain changes conformation, which is translated into a change of FRET efficiency (Figure 4A). We recorded mCitrine and mCerulean signals of *tmem161b* VSFP-butterfly hearts at 2 dpf and 3 dpf using high-speed wide-field fluorescence microscopy. Fluorescent signals were analyzed in two different ways: 1) through AP graphs (Figure 4B-E): ratiometric analysis of mCitrine/mCerulean FRET signals in different regions of the heart allowed us to compare atrial, AV-canal and ventricular activations over time, and 2) through line plots (Figure 4F-I): analysis of depolarizations (here mCerulean signals) over the cardiac wall over time allowed us to visualize conduction over the entire heart. Conduction patterns in *tmem161b*$^{+/+}$ embryos were very regular (Figure 4C,G), but we could clearly observe AV-blocks and SAN irregularities in a small group of *tmem161b*$^{+/-}$ embryos and a large group of *tmem161b*$^{-/-}$ embryos, which was in line with our findings of high-speed brightfield imaging (Figure 3A). AV-blocks appeared in our analysis as clear atrial and AV-canal activations, without a subsequent ventricular activation (Figure 4D, orange arrows; Figure 4H, green and purple arrows). In hearts with AV-block arrhythmias, we could regularly observe broad AV-canal signals (Figure 4D,H, black arrowheads), which extended into the following AV-canal depolarization. SAN irregularities appeared in our analysis as gaps between consecutive atrial/AV-canal/ventricular activations (Figure 4E, orange arrows; Figure 4I, green and purple arrow).

In vivo analysis of action potential shape demonstrates a prolongation of repolarization and a decrease in signal amplitude

Since we observed changes in heart rhythm and APs between wild-type and *tmem161b* mutants (Figure 4) we examined atrial, AVC, and ventricular AP shape in more detail. Analyzed AP parameters included upstroke time (Up_{90}-Up_{10}, time between 10% and 90% of full depolarization), action potential duration (APD_{90}, the time from the start of the AP to the moment when 90% of full repolarization is reached), repolarization time (APD_{90}-APD_{10}), and signal amplitude (Figure 5A). Upstroke time was not affected at 2 dpf, but at 3 dpf *tmem161b*$^{-/-}$ displayed a significantly slower atrial AP upstroke compared to *tmem161b*$^{+/+}$ and *tmem161b*$^{+/-}$ siblings (Figure 5B,G). Strikingly, action potential duration and repolarization time were significantly prolonged throughout the heart in mutants, both at 2 dpf and 3 dpf (Figure 5C-D, F-G). To determine whether APD_{90} prolongation was a consequence of the decreased heart rate in *tmem161b*$^{-/-}$ embryos (Figure 3B), we plotted APD_{90} against heart rate (Figure S3A-B). The correlation plots demonstrated that APD_{90} and heart rate are poorly correlated for all genotypes at 2-3 dpf (R^2 values all <0.4). Also,

linear regression in *tmem161b*$^{-/-}$ was clearly distinct from *tmem161b*$^{+/+}$ and *tmem161b*$^{+/-}$ siblings, indicating that APD_{90} prolongation was not indirectly caused by the decreased heart rate. Next to APD_{90} prolongation, signal amplitude was also affected as 3 dpf mutants showed a decrease in signal amplitude throughout the heart (Figure 5E-G). In conclusion, these results point to a role of Tmem161b in the repolarization of cardiomyocytes

Isolated cardiomyocytes from adult heterozygous *tmem161b* fish have distinct changes in action potential phase-1 repolarization and the plateau phase

In order to validate our in vivo findings, we attempted patch clamp studies using *tmem161b*$^{-/-}$ cardiomyocytes (CMs). One issue was that *tmem161b*$^{-/-}$ larvae didn't survive past 15 dpf and that the isolation of CMs from embryonic mutant hearts was technically very challenging. For that reason, we decided to isolate and analyze CMs from adult *tmem161b*$^{+/-}$ fish. We hypothesized that heterozygous fish were also affected by the mutation, at least to a certain extent, as a small percentage of the *tmem161*$^{+/-}$ embryos presented with arrhythmias (Figure 3A). Indeed, we found very distinct AP shape changes in adult ventricular *tmem161b*$^{+/-}$ CMs. APs were measured with 1 Hz pacing and parameters were analyzed as depicted in Figure 6A. Distinct changes in phase 1 repolarization and plateau phase could be observed (Figure 6B). Resting membrane potential (RMP), maximal action potential amplitude (APA_{max}), and the maximal upstroke speed (dV/dt_{max}) were not affected by the *tmem161b* mutation (Figure 6C,D). However, we observed a significant shortening of the first repolarization phase (reflected by a shorter APD_{20}) and a lowering of the plateau phase (APA_{plat},) while the action potential duration (APD_{50} and APD_{90}) was significantly prolonged (Figure 6C,E). The increase in APD_{90} was present at pacing frequencies of 2 Hz and lower (Figure 6F). Remarkable, almost all *tmem161b*$^{+/-}$ CMs showed early afterdepolarizations (EADs) at the slow pacing frequency of 0.2 Hz (Figure 6G). The observed AP phenotype in *tmem161b*$^{+/-}$ CMs, i.e., a faster phase 1 repolarization but increased action potential duration is relatively uncommon and suggests that Tmem161b is involved in interactions with multiple cardiac ion currents.

Major cardiac membrane currents I_{Kr} and $I_{Ca,L}$ are affected in *tmem161b*$^{+/-}$ cardiomyocytes

To investigate which changes in cardiac ion currents were responsible for the changes in AP shape, we next measured the major membrane currents responsible for AP repolarization in *tmem161b*$^{+/-}$ CMs.[17] I_{K1}, defined as a steady-state current at membrane voltages of -30 mV and lower (Figure 7A-B), was not significantly different between wild-type and *tmem161b*$^{+/-}$ zebrafish. However, we observed a larger outward steady-state current at 0 mV and higher test potentials in *tmem161b*$^{+/-}$ CMs compared to wild-type CMs (Figure 7A-B). When membrane potentials in zebrafish cardiomyocytes are in the 0-40 mV range, steady-state currents are mainly due to I_{Kr}.[17] The increase in I_{Kr} is compatible with the faster phase 1 repolarization (Figure 6B,E), but cannot explain the observed prolongation in APD_{50} and APD_{90} and the large amount of EADs (Figure 6E,G). Since changes in Ca^{2+} currents are often associated with EADs, we analyzed $I_{Ca,L}$. Indeed, a larger $I_{Ca,L}$ was measured in *tmem161b*$^{+/-}$ CMs compared to wild-type CMs (Figure 7C). Voltage gated

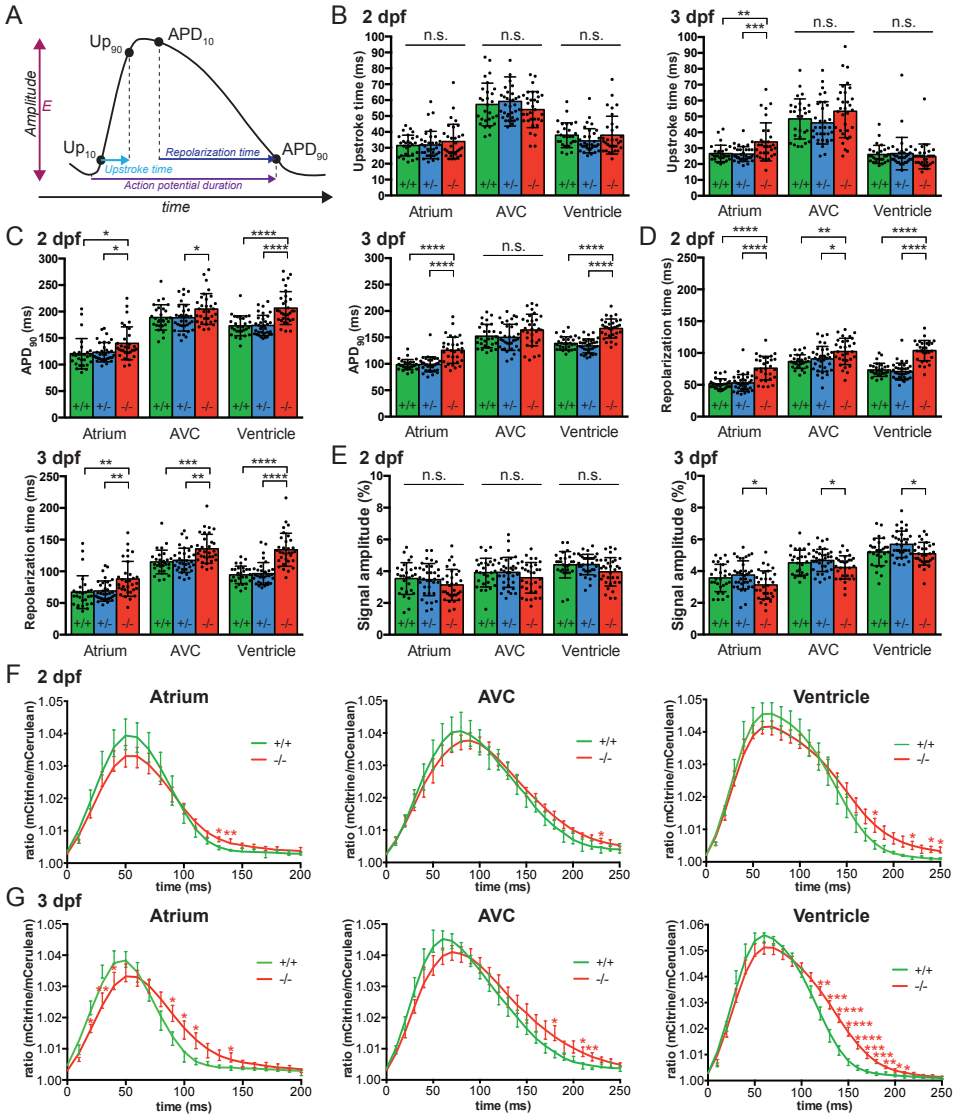

Figure 5. Action potential parameters in *tmem161b* embryos. (A) Action potential parameters analyzed. Up: transient upstroke, APD: action potential duration. (B-E) Action potential parameters of 2 and 3 dpf *tmem161b*$^{+/+}$, *tmem161b*$^{+/-}$ and *tmem161b*$^{-/-}$ embryos (mean ± SD, 2 dpf: +/+ n=28, +/- n=34, -/- n=32; 3 dpf: +/+ n=28, +/- n=34, -/- n=31) (* p<0.05, ** p≤0.01, *** p≤0.001, **** p≤0.0001). (B) Upstroke time at 2 dpf and 3 dpf, showing a significant increase of atrial upstroke time in *tmem161b*$^{-/-}$ at 3 dpf. (C) APD_{90} at 2 dpf and 3 dpf, demonstrating a significant action potential prolongation in *tmem161b*$^{-/-}$. (D) APD_{90}-APD_{10} (repolarization time) at 2 dpf and 3 dpf, demonstrating a significant prolongation of repolarization in *tmem161b*$^{-/-}$. (E) Signal amplitude at 2 dpf and 3 dpf, showing a significant decrease in amplitude in *tmem161b*$^{-/-}$ at 3 dpf. (F-G) Representative average atrial, AVC, and ventricular action potential curves of 2-3 dpf *tmem161b*$^{+/+}$ and *tmem161b*$^{-/-}$ siblings. Embryos are from one breeding pair.

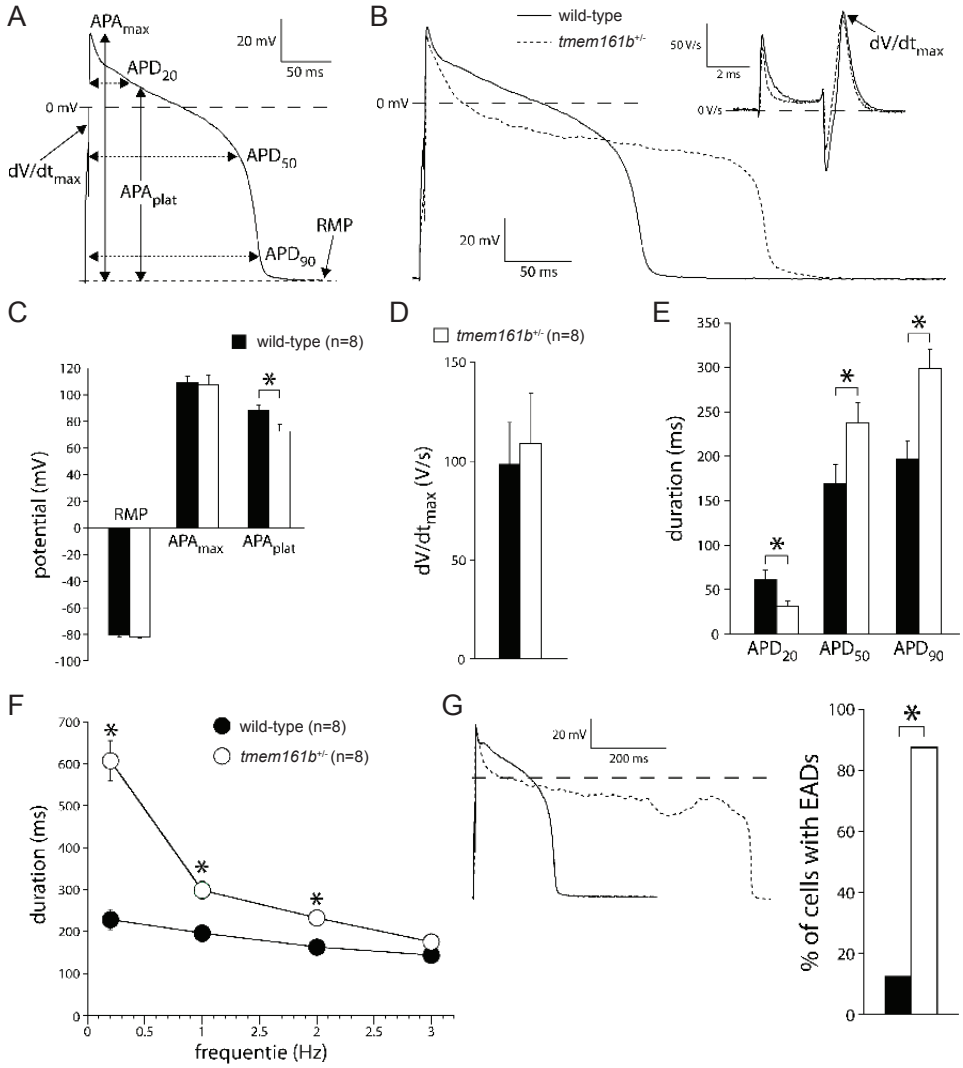

Figure 6. Action potentials changes in isolated adult *tmem161b*$^{+/-}$ cardiomyocytes. (A) Action potential parameters analyzed. APD: action potential duration, APA: action potential amplitude, RMP: resting membrane potential. (B) Typical action potentials of cells isolated from wild-type and *tmem161b*$^{+/-}$ fish. Inset: first derivative of the action potential upstroke. (C-E) Average action potential parameters (mean ± SEM, wild-type n=8, *tmem161b*$^{+/-}$ n=8, * p < 0.05) showing (C) Resting membrane potential (RMP), maximal action potential amplitude (APA$_{max}$) and plateau phase action potential amplitude (APA$_{plat}$), (D) maximal upstroke speed (dV/dt$_{max}$), and (E) action potential duration (APD$_{20}$, APD$_{50}$ and APD$_{90}$). (F) The action potential prolongation was most prominent at slow pacing frequencies. (G) Early afterdepolarizations (EADs) were frequently observed at 0.2 Hz in *tmem161b*$^{+/-}$ cells.

Ca^{2+} channels have three main gating transitions: closed to open (activation), open to inactivated (inactivation, the channel gets plugged), inactivated to closed (recovery). Reverse paths are also

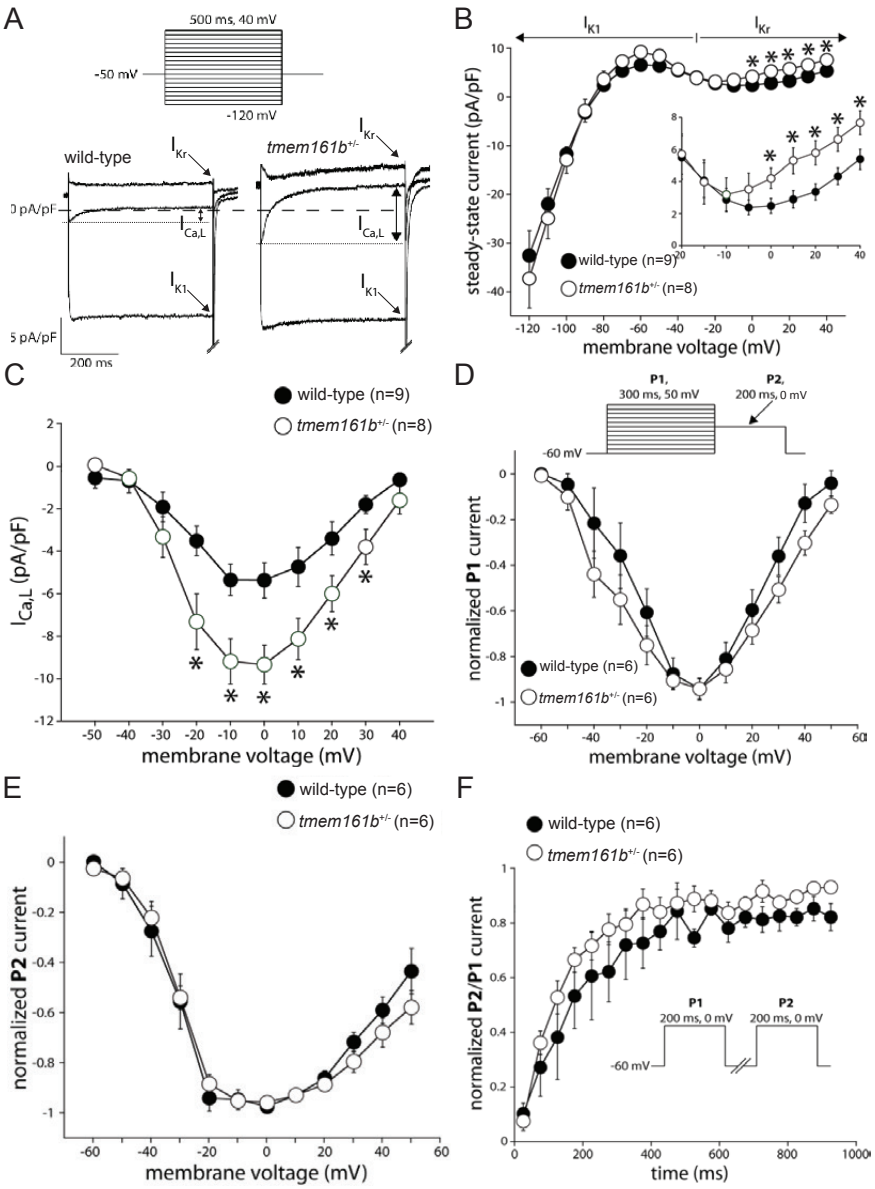

Figure 7. Membrane current changes in isolated adult *tmem161b*$^{+/-}$ cardiomyocytes. (A) Voltage clamp protocol and typical net membrane currents at -100 mV (I_{K1}), 0 mV ($I_{Ca,L}$), and +40 mV (I_{Kr}). pA/pF: picoampère per picofarad, current density. (B-C) Current-voltage (I-V) relationships of (B) I_{K1}, I_{Kr} and (C) $I_{Ca,L}$. Negative current densities indicate a net inward current, positive current densities a net outward current. (D) Normalized I-V relationships of $I_{Ca,L}$ measured at P1 during a two-pulse voltage clamp protocol (inset). The curves are virtually overlapping indicating that the voltage dependency of activation is not affected by *tmem161b*$^{+/-}$. (E) Normalized I-V relationships of $I_{Ca,L}$ measured at P2 during a two-pulse voltage clamp protocol (inset). The curves are virtually

overlapping indicating that the voltage dependency of inactivation is not affected in *tmem161b*$^{+/-}$ cardiomyocytes. (F) Normalized $I_{Ca,L}$ measured with a double-pulse protocol with variable interpulse intervals. The curves are virtually overlapping indicating that the recovery from inactivation is not affected in *tmem161b*$^{+/-}$ cardiomyocytes.

possible, for example from an inactivated to an open state channel (reactivation, or 'recovery from inactivation').[32] To examine whether the higher Ca^{2+} current densities where a consequence of altered gating properties of the L-type Calcium Channel (LTCC), we measured the transitions that could lead to an increased open state of the LTCC. These included activation, inactivation and recovery from inactivation. The larger current density of $I_{Ca,L}$ we observed was not accompanied by changes in activation and inactivation properties of LTCC because the normalized current-voltage relationships measured with a two-pulse voltage clamp protocol (Figure 7D-E) were not significantly different between wild type and *tmem161b*$^{+/-}$ CMs. Recovery from inactivation measured with a double-pulse protocol with variable interpulse intervals was also not affected by the *tmem161b* mutation (Figure 7F). Together, these findings indicate that under healthy conditions Tmem161b negatively regulates I_{Kr} and $I_{Ca,L}$ in CMs. Tmem161b likely does not affect LTCC conformation as the gating properties of LTCCs were unaffected in *tmem161b*$^{+/-}$ CMs.

In vivo imaging of Ca^{2+} transients shows that Ca^{2+} handling is affected in *tmem161b* embryos as well

As patch clamp experiments indicated that Ca^{2+} and K^+ currents were affected in adult *tmem161b*$^{+/-}$ CMs we investigated whether Ca^{2+} transient changes were involved in the in vivo AP effects we observed in embryos (Figure 4), especially in homozygous *tmem161b* mutants. For intracellular Ca^{2+} transient measurements we crossed the *tmem161b* mutant line with a transgenic line carrying an optogenetic cardiac-targeted Ca^{2+} sensor (*tg(myl7:gal4FF;UAS:GCaMP6f)*).[27] GCaMP6f consists of a circularly permutated enhanced green fluorescence protein (cpEGFP) fused to calmodulin (CaM) and the M13 peptide (Figure 8A). When intracellular Ca^{2+} rises, CaM binds to M13, causing increased brightness of cpEGFP. Analysis of cpEGFP signal intensity over time in 3 dpf embryos allowed examination of Ca^{2+} transient upstroke time (intracellular Ca^{2+} release), Ca^{2+} transient recovery time (reuptake/clearance of Ca^{2+}) as well as maximal Ca^{2+} transient amplitudes (Figure 8B). Upstroke time was significantly shorter in the ventricle of *tmem161b*$^{-/-}$ embryos, compared to *tmem161b*$^{+/-}$ and *tmem161b*$^{+/+}$ siblings (Figure 8C,H), indicating faster Ca^{2+} release. In line with the patch-clamp data, Ca^{2+} transient amplitude was higher in the atrium and ventricle of *tmem161b*$^{-/-}$ embryos, indicating that more Ca^{2+} entered the CM cytosol (Figure 8D,F,H). However, Ca^{2+} transient amplitude was not affected in *tmem161b*$^{+/-}$ embryos (Figure 8D). Ca^{2+} transient recovery was prolonged throughout the heart of *tmem161b*$^{-/-}$ embryos compared to their wild type siblings, but not in *tmem161b*$^{+/-}$ siblings (Figure 8E-H). Overall this data indicates that Ca^{2+} release in 3 dpf *tmem161b*$^{-/-}$ embryos is faster and larger in comparison to wild-type siblings, leading to prolonged recovery times.

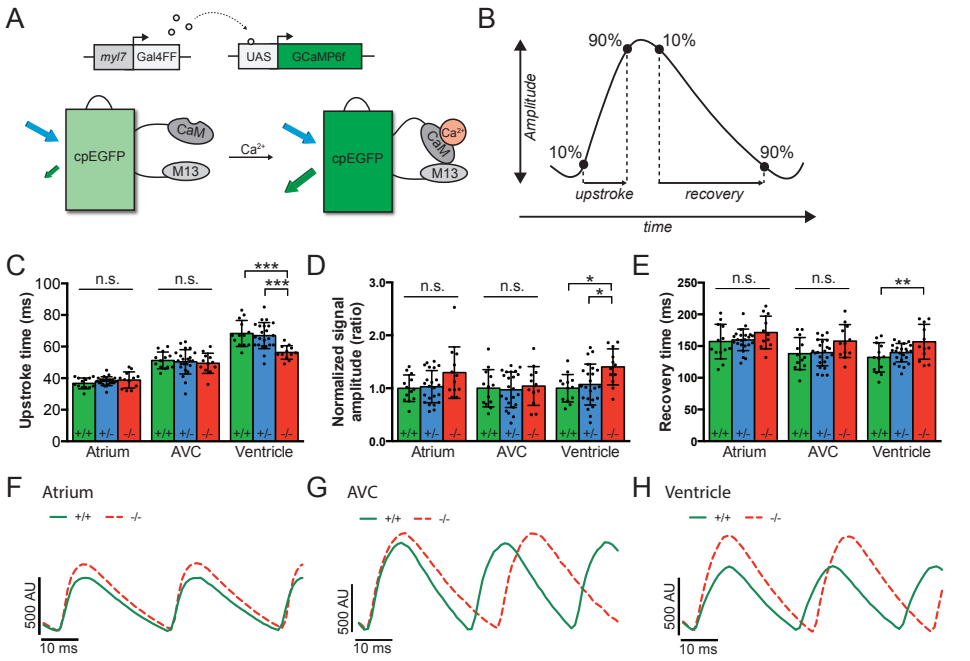

Figure 8. Ca^{2+} transient parameters in *tmem161b* embryos. (A) DNA construct and sensor dynamics of GCaMP6f. The *myl7* promoter restricts GCaMP6f expression to the heart The Gal4FF-UAS system amplifies the sensor expression. GCaMP6f consists of a circularly permutated enhanced green fluorescence protein (cpEGFP) fused to calmodulin (CaM) and the M13 peptide. When intracellular Ca^{2+} rises, CaM binds to M13, causing increased brightness of cpEGFP. (B) Ca^{2+} transient parameters analyzed. (C-E) Ca^{2+} transient parameters in 3 dpf *tmem161b*$^{+/+}$, *tmem161b*$^{+/-}$ and *tmem161b*$^{-/-}$ embryos from 3 different breeding pairs (mean ± SD, +/+ n=13, +/- n=23, -/- n=12) (* p<0.05, ** p≤0.01, *** p≤0.001, **** p≤0.0001). (C) Transient upstroke time, showing a faster upstroke in the ventricle of *tmem161b*$^{-/-}$ embryos. N.s.: non-significant, AVC: atrioventricular canal. (D) GCaMP6f signal amplitude, demonstrating a higher atrial and ventricular Ca^{2+} transient amplitude in *tmem161b*$^{-/-}$. (E) Ca^{2+} recovery time, demonstrating a slower reuptake/efflux of Ca^{2+} in *tmem161b*$^{-/-}$ hearts. (F-H) Representative Ca^{2+} transients from the (F) atrium, (G) AVC, and (H) ventricle of *tmem161b*$^{+/+}$ and *tmem161b*$^{-/-}$ embryos. AU: arbitrary units.

Discussion

Approximately 5-15% of all sudden cardiac deaths are caused by inherited 'channelopathies', disorders in which the function of ion channels is disrupted. The identification of genetic factors that predispose individuals to arrhythmias and sudden cardiac death is essential as it enables genetic testing and may contribute to diagnosis, risk stratification and preventative treatment. In this study we identify Tmem161b as a novel regulator of cardiac cellular electrophysiology, as zebrafish carrying a mutation in *tmem161b* show severe arrhythmias and have distinct changes in K^+ and Ca^{2+} currents.

The rhythmicity of the heart is governed by the orchestrated opening and closing of cardiac

ion channels. The cardiac action potential (AP) is shaped by different ion currents and the AP repolarization phase mainly depends on outward K^+ currents and inward Ca^{2+} currents.[37] In this study, we show that *tmem161b*$^{-/-}$ embryonic hearts and *tmem161b*$^{+/-}$ adult cardiomyocytes (CMs) display characteristic changes in AP repolarization, including a faster and more pronounced AP phase 1 repolarization, a lower plateau phase (running at negative potentials), and a prolonged action potential duration (APD). In addition, isolated CMs are sensitive for early after depolarizations (EADs) at lower frequencies. These findings can largely be explained by the marked changes we find in K^+ and Ca^{2+} currents, encompassing an increased I_{Kr} and $I_{Ca,L}$. The channel that conducts I_{Kr} is the human ether-à-go-go-related gene (hERG) channel. Strikingly, human gain-of-function mutations in the hERG channel (increasing I_{Kr}) are associated with short QT syndromes.[38,39] Short QT syndrome indicates that the cardiac repolarization is shorter, which is in conflict with the APD and repolarization prolongation that we observe in *tmem161b*$^{-/-}$ embryonic hearts and *tmem161b*$^{+/-}$ CMs. However, gain of function mutations in the L-type Calcium channel (increasing $I_{Ca,L}$) are associated with the Timothy Syndrome, a rare multisystem disorder in which patients present with an extreme prolongation of the QT interval.[40] Measurements on induced pluripotent stem cell CMs from Timothy patients show APs up to three times as long as those of control cells.[41] It is likely that the increase in $I_{Ca,L}$ in *tmem161b* mutants has a more dominant effect than the increase in I_{Kr}, and therefore results in a net prolongation of AP repolarization. The only AP change in *tmem161b* mutants that we cannot explain with our current data is the faster and more pronounced phase 1 repolarization. This repolarization is likely the result of an increased K^+ efflux, however we have not measured currents that are active during this phase of the action potential.

Interestingly, many Timothy syndrome patients present with bradycardia and atrioventricular block[40], which are arrhythmic phenotypes that we also find in the *tmem161b* mutants. For this reason, it is likely that the arrhythmias we observe in *tmem161b* mutants are in part the effect of increased $I_{Ca,L}$. Atrio-ventricular blocks arise when the ventricular effective refractory period increases to such an extent that CMs are still recovering from a previous depolarization when the next action potential arrives. This was observed in *tmem161b* mutant hearts showing AV block due to failure of ventricular excitation (Figure 4H) and significantly prolonged APs. How the *tmem161b* mutation causes bradycardia and sinoatrial node irregularities is more difficult to explain, and requires additional measurements on pacemaker cells. It is possible that Tmem161b regulates the funny current (I_f), the main depolarizing pacemaker current, in addition to $I_{Ca,L}$ and I_{Kr}.

In this study we observed distinct changes in AP characteristics of isolated adult *tmem161b*$^{+/-}$ CMs, but not in *tmem161b*$^{+/-}$ embryonic hearts. It is possible that heterozygous mutants develop electrophysiological changes at a later age, as wild-type Tmem161b protein may be able to compensate for the mutated protein. Also, the role of Tmem161b may be become more essential with age. However, this would not explain why *tmem161b*$^{+/-}$ fish present with arrhythmias at the embryonic stages, similar to *tmem161b*$^{-/-}$ embryos. Another explanation could be the difference in techniques that were used to measure APs. Fluorescent recordings are less sensitive when compared to patch clamp recordings, possibly obscuring slight differences in AP characteristics

between *tmem161b*$^{+/-}$ and wild-type embryos. On the other hand, ex vivo recordings using patch clamping do not incorporate potential extracardiac compensatory mechanism, which are present in vivo. For a better understanding of the role of Tmem161b in development of cardiac excitability, additional measurements are required that use identical experimental approaches at all ages, for example through the patch clamp analysis of CMs from younger *tmem161b*$^{+/-}$ zebrafish, or VSFP imaging of adult *tmem161b*$^{+/-}$ hearts.

While the effects of the *tmem161b* mutation were largely unraveled in this study, we did not address how and where Tmem161b exerts its function within cardiomyocytes. Based on the fact that Tmem161b affects multiple cardiac ion currents, and the fact that the gating properties of $I_{Ca,L}$ are not disrupted, we hypothesize that Tmem161b is part of macromolecular signaling complexes that regulate cardiac ion channel activity or membrane expression.[42] How Tmem161b would fit in those complexes and how the protein could aid in ion channel regulation is something we cannot explain at this point. For this we need more information on the whereabouts of Tmem161b within the cardiomyocyte and on its interacting partners.

To our knowledge, our study demonstrates for the first time that Tmem161b is an important regulator of cardiac cellular electrophysiology. Studies mentioning TMEM161B are very rare. The protein has been indicated in patients with large chromosomal deletions in chromosome 5q14.3q15, which in some cases contained the *TMEM161B* gene.[33-36] Patients with these deletions present with mental retardation, seizures and hypotonia, but symptoms were linked to a haploinsufficiency of *MEF2C* and not to *TMEM161B*.[33] Interestingly, one of the children with a deletion including the *TMEM161B* gene was born through induced labor at 41 weeks of gestation because of an abnormal fetal cardiac rhythm, which was not further specified.[34] In the other patient cases, cardiac parameters were not described, so it is unclear if cardiac electrophysiology was examined. For this reason, we cannot draw any conclusions concerning the role of TMEM161B in human cardiac electrophysiology based on these studies. It does however demonstrate that the loss of one *TMEM161B* allele is not lethal.

In conclusion, we identified Tmem161b as a novel component of cardiac cellular electrophysiology. Mutation of *tmem161b* in the zebrafish results in severe arrhythmias and pronounced AP repolarization changes, due to changes in I_{Kr} and $I_{Ca,L}$ Further research is required to elucidate the role of Tmem161b within the cardiomyocyte proteome and the importance of TMEM161B in human cardiac electrophysiology.

References

1. Lodder EM, Bezzina CR. Genomics of cardiac electrical function. *Brief Funct Genomics* 2014 Jan;13(1):39–50
2. Napolitano C, Bloise R, Monteforte N, Priori SG. Sudden cardiac death and genetic ion channelopathies: long QT, Brugada, short QT, catecholaminergic polymorphic ventricular tachycardia, and idiopathic ventricular fibrillation. *Circulation* 2012 Apr;125(16):2027–34.
3. Novelli V, Gambelli P, Memmi M, Napolitano C. Challenges in Molecular Diagnostics of Channelopathies in the Next-Generation Sequencing Era: Less Is More? *Front Cardiovasc Med* 2016;3(12):29.
4. Wilde AAM, Amin A. Channelopathies, genetic testing and risk stratification. *Int J Cardiol* 2017 Jun;237:53–5.
5. Schmit K, Michiels C. TMEM Proteins in Cancer: A Review. *Front Pharmacol* 2018;9:1345.
6. Wrzesiński T, Szelag M, Cieślikowski WA, Ida A, Giles R, Zodro E, et al. Expression of pre-selected TMEMs with predicted ER localization as potential classifiers of ccRCC tumors. *BMC Cancer* 2015 Jul;15(1):518.
7. Hayez A, Malaisse J, Roegiers E, Reynier M, Renard C, Haftek M, et al. High *TMEM45A* expression is correlated to epidermal keratinization. *Exp Dermatol* 2014 May;23(5):339–44.
8. Thomas-Gatewood C, Neeb ZP, Bulley S, Adebiyi A, Bannister JP, Leo MD, et al. TMEM16A channels generate Ca^{2+}-activated Cl^- currents in cerebral artery smooth muscle cells. *Am J Physiol Heart Circ Physiol* 2011 Nov;301(5):H1819–27.
9. Yamamura H, Nishimura K, Hagihara Y, Suzuki Y, Imaizumi Y. TMEM16A and TMEM16B channel proteins generate Ca^{2+}-activated Cl^- current and regulate melatonin secretion in rat pineal glands. *J Biol Chem* 2018 Jan;293(3):995–1006.
10. Foulquier F, Amyere M, Jaeken J, Zeevaert R, Schollen E, Race V, et al. TMEM165 deficiency causes a congenital disorder of glycosylation. *Am J Hum Genet* 2012 Jul;91(1):15–26.
11. Liu Y, Zheng Q, He G, Zhang M, Yan X, Yang Z, et al. Transmembrane protein 215 promotes angiogenesis by maintaining endothelial cell survival. *J Cell Physiol* 2018 Oct 28;8:464.
12. Hashimoto Y, Shirane M, Nakayama KI. TMEM55B contributes to lysosomal homeostasis and amino acid-induced mTORC1 activation. *Genes Cells* 2018 Jun;23(6):418–34.
13. Terashima H, Picollo A, Accardi A. Purified TMEM16A is sufficient to form Ca^{2+}-activated Cl^- channels. *Proc Natl Acad Sci U.S.A.* 2013 Nov;110(48):19354–9.
14. Ishihara K, Suzuki J, Nagata S. Role of $Ca(^{2+})$ in the Stability and Function of TMEM16F and 16K. *Biochemistry* 2016 Jun 14;55(23):3180–8.
15. Huttner IG, Trivedi G, Jacoby A, Mann SA, Vandenberg JI, Fatkin D. A transgenic zebrafish model of a human cardiac sodium channel mutation exhibits bradycardia, conduction-system abnormalities and early death. *J Mol Cell Cardiol* 2013 Aug;61:123–32.
16. Arnaout R, Ferrer T, Huisken J, Spitzer K, Stainier DYR, Tristani-Firouzi M, et al. Zebrafish model for human long QT syndrome. *Proc Natl Acad Sci U.S.A.* 2007 Jul 3;104(27):11316–21.
17. Verkerk AO, Remme CA. Zebrafish: a novel research tool for cardiac (patho)electrophysiology and ion channel disorders. *Front Physiol* 2012;3:255.
18. Nemtsas P, Wettwer E, Christ T, Weidinger G, Ravens U. Adult zebrafish heart as a model for human heart? An electrophysiological study. *J Mol Cell Cardiol* 2010 Jan;48(1):161–71.

19. Langenbacher AD, Dong Y, Shu X, Choi J, Nicoll DA, Goldhaber JI, et al. Mutation in sodium-calcium exchanger 1 (NCX1) causes cardiac fibrillation in zebrafish. *Proc Natl Acad Sci U.S.A.* 2005 Dec;102(49):17699–704.
20. Pott A, Rottbauer W, Just S. Functional genomics in zebrafish as a tool to identify novel antiarrhythmic targets. *Curr Med Chem* 2014;21(11):1320–9.
21. Vornanen M, Hassinen M. Zebrafish heart as a model for human cardiac electrophysiology. *Channels* 2016;10(2):101–10.
22. van Opbergen CJM, van der Voorn SM, Vos MA, de Boer TP, van Veen TAB. Cardiac Ca^{2+} signalling in zebrafish: Translation of findings to man. *Prog Biophys Mol Biol* 2018 Oct;138:45-58
23. Knapik EW. ENU mutagenesis in zebrafish--from genes to complex diseases. *Mamm Genome* 2000 Jul;11(7):511–9.
24. Haffter P, Granato M, Brand M, Mullins MC, Hammerschmidt M, Kane DA, et al. The identification of genes with unique and essential functions in the development of the zebrafish, *Danio rerio*. *Development* 1996 Dec;123:1–36.
25. Westerfield M. The Zebrafish Book. 4 ed. University of Oregon Press, Eugene.
26. Wienholds E, Schulte-Merker S, Walderich B, Plasterk RHA. Target-selected inactivation of the zebrafish *rag1* gene. *Science* 2002 Jul;297(5578):99–102.
27. van Opbergen CJM, Koopman CD, Kok BJM, Knöpfel T, Renninger SL, Orger MB, et al. Optogenetic sensors in the zebrafish heart: a novel in vivo electrophysiological tool to study cardiac arrhythmogenesis. *Theranostics* 2018;8(17):4750–64.
28. Sehnert AJ, Huq A, Weinstein BM, Walker C, Fishman M, Stainier DYR. Cardiac troponin T is essential in sarcomere assembly and cardiac contractility. *Nature Genetics* 2002 May;31(1):106–10.
29. Tessadori F, van Weerd JH, Burkhard SB, Verkerk AO, de Pater E, Boukens BJ, et al. Identification and functional characterization of cardiac pacemaker cells in zebrafish. *PLoS ONE* 2012;7(10):e47644.
30. Barry PH, Lynch JW. Liquid junction potentials and small cell effects in patch-clamp analysis. *J Membr Biol* 1991 Apr;121(2):101–17.
31. Wu BJ, Chiu CC, Chen CL, Wang WD, Wang JH, Wen ZH, et al. Nuclear receptor subfamily 2 group F member 1a (nr2f1a) is required for vascular development in zebrafish. *PLoS ONE* 2014;9(8):e105939.
32. Hinard V, Britan A, Rougier JS, Bairoch A, Abriel H, Gaudet P. ICEPO: the ion channel electrophysiology ontology. *Database* 2016 Apr;2016.
33. Nowakowska BA, Obersztyn E, Szymańska K, Bekiesińska-Figatowska M, Xia Z, Ricks CB, et al. Severe mental retardation, seizures, and hypotonia due to deletions of MEF2C. *Am J Med Genet B Neuropsychiatr Genet* 2010 Jul;153B(5):1042–51.
34. Le Meur N, Holder-Espinasse M, Jaillard S, Goldenberg A, Joriot S, Amati-Bonneau P, et al. MEF2C haploinsufficiency caused by either microdeletion of the 5q14.3 region or mutation is responsible for severe mental retardation with stereotypic movements, epilepsy and/or cerebral malformations. *J Med Genet* 2010 Jan;47(1):22–9.
35. Engels H, Wohlleber E, Zink A, Hoyer J, Ludwig KU, Brockschmidt FF, et al. A novel microdeletion syndrome involving 5q14.3-q15: clinical and molecular cytogenetic characterization of three patients. *Eur J Hum Genet* 2009 Dec;17(12):1592–9.

36. Cardoso C, Boys A, Parrini E, Mignon-Ravix C, McMahon JM, Khantane S, et al. Periventricular heterotopia, mental retardation, and epilepsy associated with 5q14.3-q15 deletion. *Neurology* 2009 Mar;72(9):784–92.
37. Grant AO. Cardiac ion channels. *Circ Arrhythm Electrophysiol* 2009 Apr;2(2):185–94.
38. Butler A, Zhang Y, Stuart AG, Dempsey CE, Hancox JC. Action potential clamp characterization of the S631A hERG mutation associated with short QT syndrome. *Physiol Rep* 2018 Sep;6(17):e13845.
39. El Harchi A, Melgari D, Zhang YH, Zhang H, Hancox JC. Action potential clamp and pharmacology of the variant 1 Short QT Syndrome T618I hERG K^+ channel. *PLoS ONE* 2012;7(12):e52451.
40. Splawski I, Timothy KW, Decher N, Kumar P, Sachse FB, Beggs AH, Sanguinetti MC, Keating MT. Severe arrhythmia disorder caused by cardiac L-type calcium channel mutations. *Proc Natl Acad Sci U.S.A*. 2005 Jun;102(23):8089–96
41. Yazawa M, Hsueh B, Jia X, Pasca AM, Bernstein JA, Hallmayer J, Dolmetsch RE. Using induced pluripotent stem cells to investigate cardiac phenotypes in Timothy syndrome. *Nature* 2011 Mar;471(7337):230–4.
42. Soni S, Scholten A, Vos MA, van Veen TAB. Anchored protein kinase A signalling in cardiac cellular electrophysiology. *J Cell Mol Med* 2014 Nov;18(11):2135–46.

Supplemental Figures

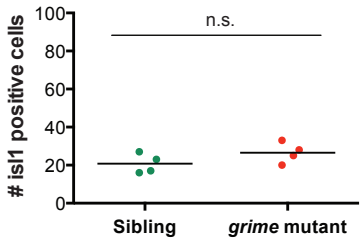

Figure S1. Characterization of the grime mutant. The number of islet-1 positive cells in the sinoatrial node of *grime* mutants (n=4) and siblings (n=4). N.s.: non-significant.

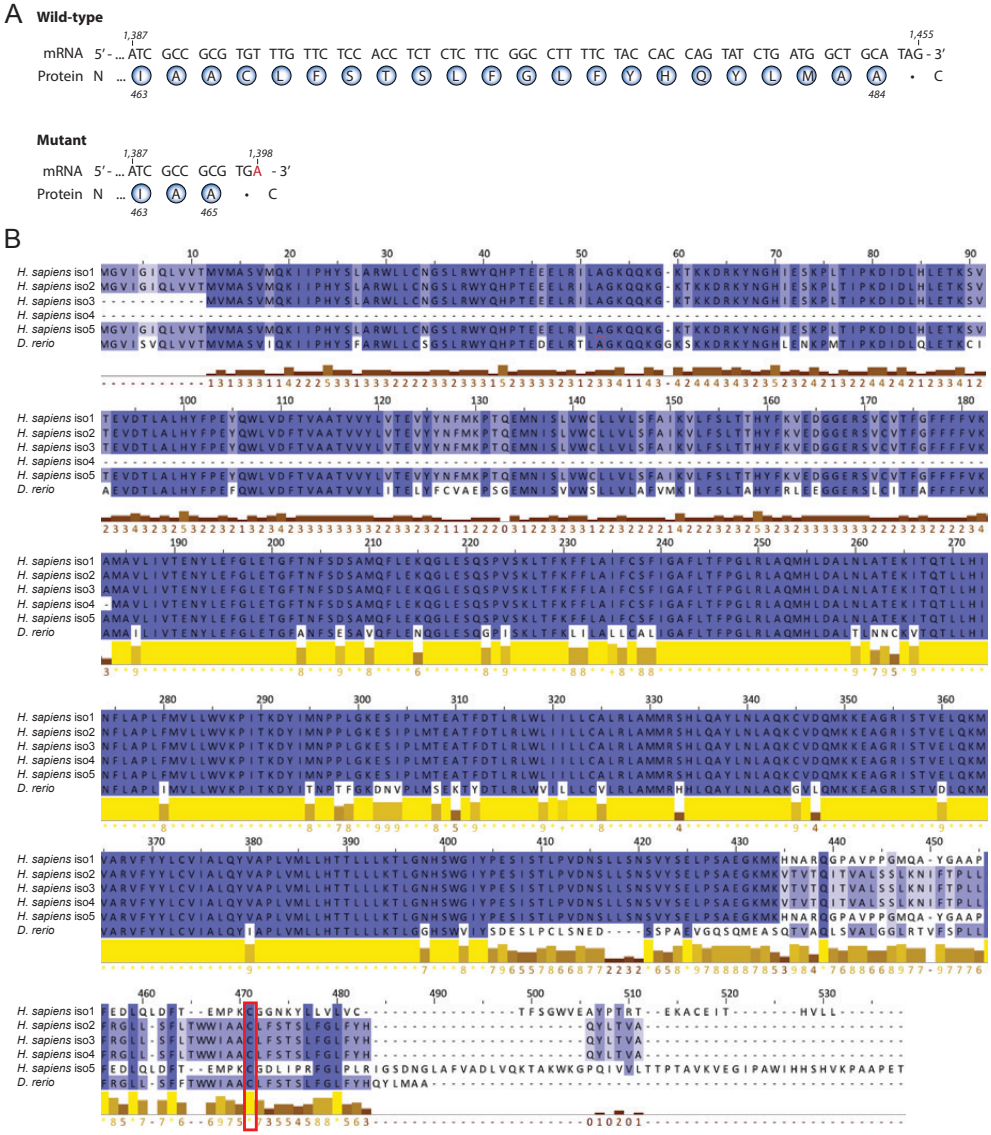

Figure S2. Mutation effects and Tmem161b protein conservation. (A) Schematic of the wild-type and *tmem161b* mutant mRNA and protein sequences (only sequence ends depicted). The mutation found in the *grime* mutant is a T>A transition at position 1,398 on the coding sequence, which encodes a novel stop codon and results in the loss of the last 19 amino acids. (B) Tmem161b conservation scores between human (Homo sapiens) isoforms and the zebrafish (Danio Rerio) protein. Darker blue indicates a higher conservation. Conservation scores are noted below the sequences, * indicates a perfect overlap in amino acid sequence. The red box indicates the mutation site.

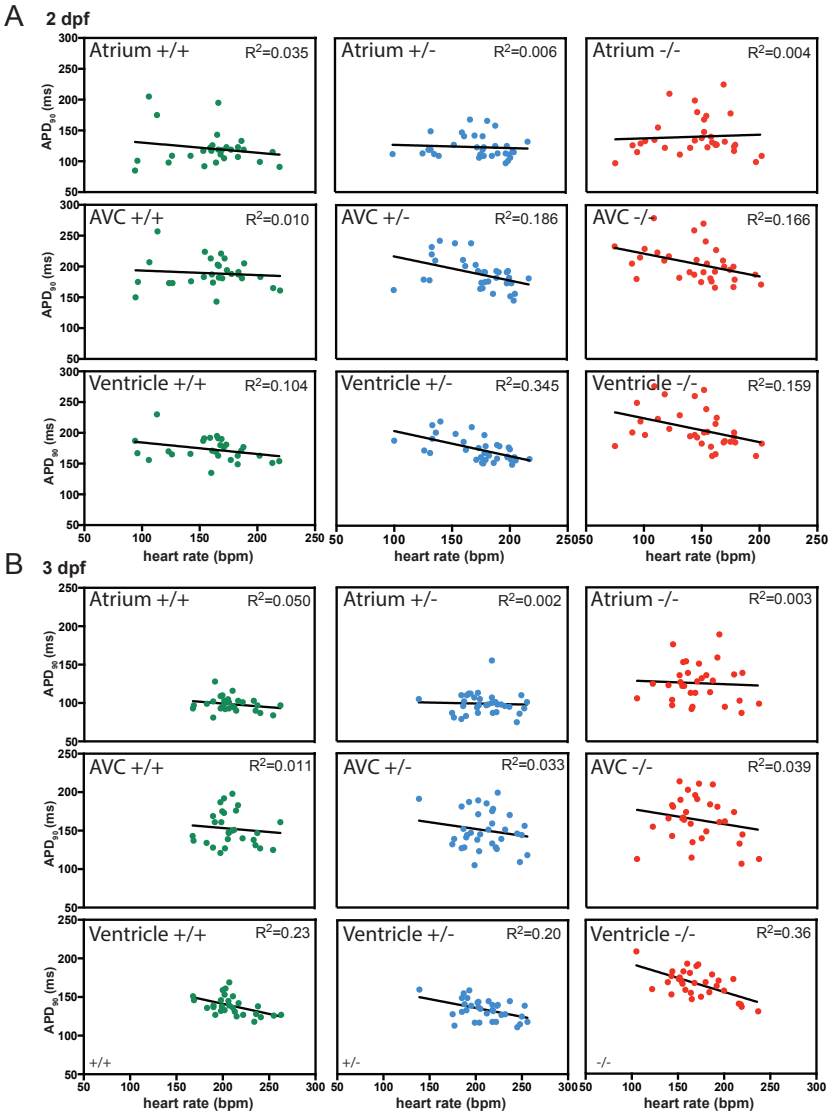

Figure S3. Correlation between heart rate and action potential duration. (A-B) Correlation plots in which the heart rate and APD_{90} of 2 and 3 dpf *tmem161b*$^{+/+}$, *tmem161b*$^{+/-}$ and *tmem161b*$^{-/-}$ hearts are plotted against each other (2 dpf: +/+ n=28, +/- n=34, -/- n=32; 3 dpf: +/+ n=28, +/- n=34, -/- n=31). (A) 2 dpf correlation plots. (B) 3 dpf correlation plots.

	2 dpf			3 dpf			4 dpf			5 dpf		
	+/+ n=23	+/- n=47	-/- n=23	+/+ n=22	+/- n=44	-/- n=24	+/+ n=20	+/- n=40	-/- n=28	+/+ n=22	+/- n=44	-/- n=27
Sinus rhythm	**23** (100%)	**41** (87%)	**14** (61%)	**22** (100%)	**37** (84%)	**17** (71%)	**20** (100%)	**35** (88%)	**9** (32%)	**22** (100%)	**35** (80%)	**5** (19%)
Bradycardia	-	-	-	-	**1** (2%)	-	-	-	-	-	-	-
SAN irregularities	-	-	**2** (9%)	-	-	**1** (4%)	-	**1** (3%)	**2** (7%)	-	**1** (2%)	**2** (7%)
AV block	-	**4** (9%)	**4** (17%)	-	**3** (7%)	**3** (12.5%)	-	3 (8%)	**8** (29%)	-	**7** (16%)	4 (15%)
Bradycardia + SAN irregularities	-	-	**1** (4%)	-	-	-	-	-	**2** (7%)	-	-	**1** (4%)
SAN irregularities + AV block	-	**2** (4%)	**2** (9%)	-	**3** (7%)	**3** (12.5%)	-	-	**5** (18%)	-	-	**7** (26%)
Bradycardia + SAN irregularities + AV-block	-	-	-	-	-	-	-	**1** (3%)	**2** (7%)	-	**1** (2%)	4 (15%)
Completely irregular	-	-	-	-	-	-	-	-	-	-	-	**4** (15%)

Table S1. Characterization of arrhythmias in the *tmem161b* mutant. Table showing the different types of arrhythmias found within *tmem161b*$^{+/+}$, *tmem161b*$^{+/-}$ and *tmem161b*$^{-/-}$ fish between 2-5 dpf.

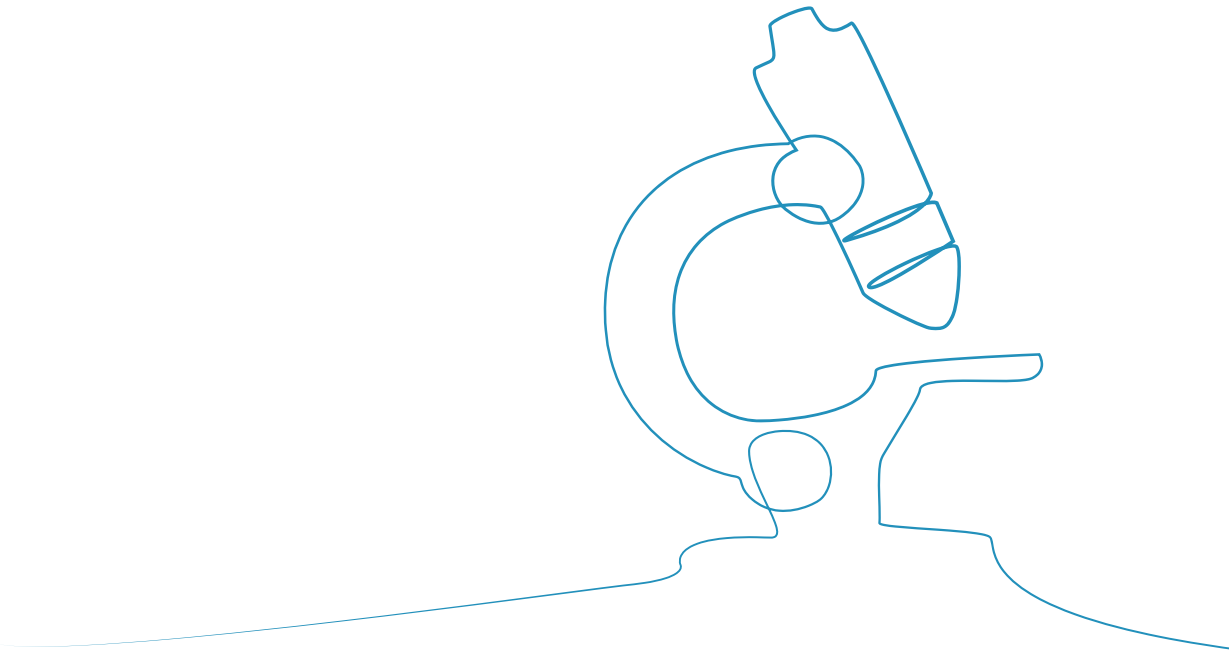

CHAPTER 7

A zebrafish model to study the human phospholamban R14del mutation

Koopman C.D.*, van Opbergen C.J.M.*, Kamel S.M.*, Chocron S., Polidoro Pontalti C., Onderwater, Y., Vos, M.A., van Veen A.A.B., de Boer T.P.#, Bakkers J.#

*# contributed equally

Abstract

The phospholamban R14 deletion (PLN R14del) is a Dutch founder mutation, found in 10-15% of all Dutch patients diagnosed with dilated cardiomyopathy and arrhythmogenic right ventricular cardiomyopathy. Overall, heterozygous carriers have a high risk of developing malignant ventricular arrhythmias and end-stage heart failure, resulting in a high mortality and poor prognosis. Despite decades of research into PLN function, very little is known about how PLN R14del can cause cardiomyopathy. To enable detailed investigation of the pathogenic effects of PLN R14del over time, we generated a Pln R14del zebrafish model and carefully validated cardiac function in embryos and cardiac morphology in adult fish.

Methods: Zebrafish carry two copies of the *pln* gene, one on chromosome 17 (*plna*) and one on chromosome 20 (*plnb*). We recently introduced the R14del mutation in *plnb* using homologous recombination and CRISPR/Cas9. Here, we assessed three groups of embryos (all *plna* wild-type): *plnb*$^{+/+}$ *plnb*$^{R14/+}$ or *plnb*$^{R14/R14}$. High-speed epifluorescence microscopy was used to visualize Ca^{2+} transients in Pln R14del embryos expressing the fluorescent cytoplasmic Ca^{2+} sensor GCaMP6f. High-speed brightfield imaging was used to assess basic contractile and hemodynamic parameters at baseline and after treatment with isoproterenol, a β-adrenergic agonist. To analyze heart morphology and tissue composition in adult Pln R14del fish, we isolated and stained the hearts of 2-year-old *plnb*$^{R14/R14}$ fish and a severely sick 9.5-month-old *plnb*$^{R14/R14}$ fish. Hearts were assessed on overall morphology, fibrin/collagen content, fat deposits, and *myl7*, *tbx18*, *grn1* and *postn* expression.

Results: Pln R14del embryos with cardiac-targeted GCaMP6f (*plnb*$^{R14/+}$ and *plnb*$^{R14/R14}$) presented with a decrease in diastolic Ca^{2+} levels, peak Ca^{2+} levels, and Ca^{2+} transient amplitude, while upstroke and recovery time were not affected compared to wild-type siblings. Heart rate, contractility dynamics, and hemodynamic parameters were similar between wild-type and Pln R14del mutant embryos (*plnb*$^{R14/+}$ and *plnb*$^{R14/R14}$) at baseline and after treatment with isoproterenol. Approximately 25% of isolated adult 2-year-old Pln R14del hearts showed severe morphological changes. A thick layer of cells covered the Pln R14 hearts, which expressed the embryonic epicardial gene *tbx18*. In addition, we observed an accumulation of immune cells, fibroblasts and fat in the epicardial regions of the PLN R14del hearts.

Conclusion: By introducing the R14del mutation on *plnb* in zebrafish we generated a novel in vivo PLN R14del animal model. Pln R14del embryos display differences in cardiac Ca^{2+} handling, but no changes in contraction dynamics were observed. Hemodynamic parameters like cardiac output were not affected, indicating that embryos can (still) compensate for any effects of Pln R14del. The morphological changes in the adult Pln R14del hearts displayed some classical hallmarks of human PLN R14del disease, such as fibrofatty infiltrates. Further research is necessary to establish how well the zebrafish model recapitulates the human phenotype and if this model can be used to unravel human PLN R14del pathology.

Keywords: phospholamban, PLN, R14del mutation, zebrafish model, contractility, Ca^{2+} dynamics, cardiomyopathy, morphological changes

Introduction

The phospholamban Arginine-14 deletion (PLN R14del) is a Dutch founder mutation and the most prevalent cardiomyopathy-related mutation in the Netherlands. It is found in 10-15% of all Dutch patients diagnosed with dilated cardiomyopathy (DCM) and arrhythmogenic right ventricular cardiomyopathy (ARVC)[1], but has also been found in several other countries, including the USA, Canada, Spain, Germany, and Greece.[2-5] Up to today, only heterozygous individuals have been identified.[6] Patient phenotypes are very heterogeneous, not only between families but also within families.[7,8] Overall, carriers have a high risk of developing malignant ventricular arrhythmias and end-stage heart failure, resulting in a high mortality and poor prognosis.[9] End-stage PLN R14del hearts show pronounced fibrosis and fatty changes in the left and right ventricular myocardial wall.[10]

Phospholamban (PLN; encoded by the *PLN* gene) is a small 52 amino-acid transmembrane sarcoplasmic reticulum (SR) protein and a crucial regulator of SR function and cardiac contractility as it can reversibly inhibit the sarco(endo)plasmic reticulum Ca^{2+}-ATPase (SERCA2a).[11] PLN consists of three domains: a cytoplasmic domain (Ia), a linker domain (Ib), and a SR transmembrane domain (II).[12] Two crucial phosphorylation sites are located within the cytoplasmic Ia domain of PLN; one at Ser^{16} which can be phosphorylated by protein kinase A (PKA), and one at Thr^{17} which can be phosphorylated by Ca^{2+}/calmodulin-dependent protein kinase II (CaMKII).[13] Under healthy conditions, non-phosphorylated PLN actively inhibits SERCA activity, while phosphorylation of PLN during β-adrenergic stimulation releases its inhibition on SERCA, allowing more Ca^{2+} to flow into the SR. This is required to normalize cytosolic Ca^{2+} levels and to allow faster relaxation of the myofilaments at faster heart rates. Initially, it was believed that the function of PLN was restricted to this simple interaction with SERCA. However, it has become increasingly clear that PLN affects many more processes in the cell and is in fact part of a multimeric regulatome, with interacting partners like HAX-1, Hsp90, Gm, AKAP, PP1, I-1, and Hsp20.[14] Due to the complex role of PLN in cardiomyocytes, it is difficult to explain how PLN R14del exerts its pathogenic effects. At the level of PLN-SERCA interaction, it appears that PLN R14del cannot release it inhibition on SERCA2a, likely due to disruption of the phosphorylation motif involving Ser^{16}.[15] Impaired SR Ca^{2+} reuptake, intracellular Ca^{2+} overload and activation of pathologic Ca^{2+} signaling pathways (via CAMKII) have been suggested to play an important role in the development of disease in patients. However, many questions still remain and the generation of suitable animal models is essential.

Different research models to study PLN R14del pathology have already been developed. In 2006, Haghighi et al. introduced a mouse model overexpressing PLN R14del. These mice developed a cardiac phenotype that was very similar to patients, including ventricular dilatation, fibrosis and early death.[2] In 2012, a second transgenic mouse was introduced by the same research group, but this time PLN R14del was inserted in a PLN null background. Interestingly, characterization of this model indicated that PLN did not co-localize with SERCA2a, but instead was misrouted to the plasma membrane.[6] It is possible that wild-type PLN is required for the pathogenic effect of PLN

R14del on SERCA2a, as wild-type PLN transports the mutant protein to the SR membrane. Next to these mouse models, induced pluripotent stem cells (iPSCs) were used in a recent study as a model to investigate PLN R14del effects. iPSCs were generated from patient dermal fibroblasts and differentiated into cardiomyocytes (iPSC-CMs). These PLN R14del iPSC-CMs showed distinct Ca^{2+} handling abnormalities, electrical instability, abnormal cytoplasmic distribution of the PLN protein and increased markers of cardiac hypertrophy. Genetic correction of the mutation resulted in a marked improvement of the phenotypes.[16]

While these studies have provided important insights in PLN R14del disease, the use of mice and iPSC-CMs has some drawbacks. The use of iPSC-CMs is a cell-based approach, which eliminates the effects of signaling cues from the rest of the organism. In contrast, mouse models have the advantage of organism complexity, but mice are difficult to use in a high-throughput manner, and in vivo cellular measurements on the heart are extremely difficult. In addition, the PLN R14del mouse models that are described were generated using gene-overexpression methods. Mutagenesis of one of the endogenous *PLN* genes would reflect the patient situation more accurately, in terms of wild-type to mutated protein ratio.

During the past decades, the zebrafish (Danio rerio) has emerged as a powerful, cost-efficient, and easy-to-use vertebrate model to study human disease.[17] In contrast to the mammalian heart, fish only have one atrium and one ventricle. Nevertheless, human and zebrafish adult hearts resemble each other in many aspects, including basic contractile dynamics, beating rates, the shape of APs and of electrocardiograms. In addition, humans and zebrafish have a high degree of genetic homology.[18] Zebrafish have been widely used to study gene function using morpholino knock-down studies, and more recently using CRISPR/Cas9 knock-out and knock-in studies. It is now even possible to generate fish carrying patient-specific mutations.[19] Especially appealing for cardiovascular research is the high number of experimental animals that can be used and the fact that early cardiac defects can be easily observed in vivo. In addition, we recently developed a novel approach to study in vivo voltage and Ca^{2+} dynamics in the zebrafish heart.[20] Heart disease in zebrafish can be easily tracked into adulthood and monitored using traditional techniques like electrocardiography[10,21], echography[22,23] and histology. Also, zebrafish provide an efficient platform to screen chemical compounds[24], which allows fast and economical surveys to identify novel compounds that could benefit patients, including PLN R14del patients.

In this study we present the Pln R14del zebrafish as an interesting new model to study human PLN R14del disease. Embryonic in vivo Ca^{2+} dynamics, as well as contractility responses at baseline and to ß-adrenergic stimulation were measured. We observed a decrease in diastolic Ca^{2+} levels, peak Ca^{2+} levels, and Ca^{2+} transient amplitudes. We did not observe differences in contractility dynamics or hemodynamics between Pln R14del mutants and wild-type embryos at baseline or after treatment with isoproterenol. In addition to the embryonic data, we found that approximately 25% of isolated adult Pln R14del hearts presented with severe morphological changes. A thick layer of cells covered these hearts, which expressed the embryonic epicardial gene *tbx18*, and showed an accumulation of immune cells, fibroblasts and fat.

Materials and methods

Zebrafish husbandry

Fish used in this study were housed under standard conditions as previously described.[25] All experiments were conducted in accordance to the ethical guidelines and approved by the local ethics committee at the Royal Dutch Academy of Sciences (KNAW).

Generation of mutant line

pln R14del fish were generated as described before.[19] Mutations were generated in wild-type Tupfel Longfin (TL) strain zebrafish using CRISPR/Cas9. One-cell-stage zebrafish embryos were microinjected with an injection mixture consisting of (final concentrations): 150 ng/µl nuclear Cas9 (nCas9) mRNA, 20-40 ng/µl sgRNA, 10% (v/v) Phenol Red and 25 ng/µl template oligo. sgRNA sequences can be provided upon request.

RT-PCR

RNA was isolated from whole embryos 4 days post fertilization (dpf) and from hearts of adult TL wild-type fish. Adult hearts were either processed as a whole (atrium and ventricle, but without the bulbus arteriosus, n=3) or separated into atrial (n=8) and ventricular (n=4) samples. *ef1α* was used as reference gene for the RT-PCR. Primers for *ef1α* were: forward primer GGCCACGTCGACTCCGGAAAGTCC, reverse primer: CTCAAAACGAGCCTGGCTGTAAGG, product size 465 bp. Primers for *pln* on chromosome 17 (*plna*) were: forward primer AAATCGATCCCCGAGTCTTT, reverse primer CCTGGGACGTATTTTGTGCT, product size 254 bp. Primers for *pln* on chromosome 20 (*plnb*) were: forward primer GCAGGAGCTCTTCGTCAACT, reverse primer GCATGAGCAGTAGAGCCACA, product size 291 bp.

High-speed brightfield imaging

Embryos were placed in 1-phenyl-2-thiourea (PTU) 20-24 hours post fertilization (hpf) to prevent pigmentation. 5 dpf embryos were embedded in 0.3% agarose prepared in E3 medium containing 16 mg/ml Tricaine. Recordings were performed at 150 fps using a high-speed inverted light microscope at 28°C. We recorded hearts at baseline first. Subsequently 3 mL of 100 µM Isoproterenol hydrochloride (ISO; Sigma-Aldrich 1351005) in E3-Tricaine solution was added, incubated for 30 min, and hearts were recorded for a second time. Heart rate measurements and contractility parameters were analyzed from these recordings using ImageJ (U. S. National Institutes of Health, Bethesda, Maryland, USA). Contraction time, relaxation time and systolic duration were analyzed by going through the recorded movies frame by frame, and by noting (1) the moment the ventricular wall moved inwards and the ventricle started expelling blood (start of contraction), (2) the moment the ventricular wall moved back outwards (start of relaxation), and (3) the moment that the ventricular wall was back at its most dilated position (maximum relaxation). This process was repeated 3 times for each heart. Values were averaged and relaxation

time and contraction time were corrected for heart rate (HR) using the formula: time/√(beat to beat interval). From the systolic time we calculated the systolic fraction: (systolic time*HR)/60.000 The hemodynamic parameters such as surface area and volumes were analyzed using imageJ by drawing an ellipse on top of the ventricle at end diastole and end systole. Per heart 6 ellipses were analyzed: 3 at diastole, and 3 at systole. Values were averaged. ImageJ provided the values for the minor and major axis of each ellipse. Diastolic and systolic surface areas were calculated using the following formula: (0.5*major axis)*(0.5*minor axis)*π. Fractional area change (FAC) was calculated by: (area diastole–area systole)/(area diastole). End diastolic and end systolic volume (EDV/ESV) were calculated by: (1/6)*(π)*(major axis)*(minor axis^2). Stroke volume (SV) by: EDV-ESV. Ejection fraction (EF) by: SV/EDV. Cardiac output (CO) by: SV*Heart rate.

High-speed fluorescence imaging

pln R14del fish were crossed to *tg(myl7:Gal4FF; UAS:GCaMP6f)* fish[20] to obtain *pln* R14del fish with a genetically encoded intracellular cardiac Ca^{2+} sensor. For each experiment we used the offspring of the same breeding pair, to limit variation in sensor expression between embryos. A morpholino (MO) oligomer targeted against *tnnt2a* (5'-CATGTTTGCTCTGATCTGACACGCA-3') was injected at the 1-cell stage to uncouple contraction from excitation in embryos, thereby preventing contraction artifacts in our recordings of intracellular cardiac Ca^{2+} handling. This 'silent heart' ATG morpholino was applied as described previously.[26] Embryos were placed in PTU after 20-24 hours to keep them transparent. 3 dpf embryos were embedded in 0.3% agarose prepared in E3 medium containing 16 mg/ml Tricaine and placed in a heated (28°C) recording chamber. Recordings were performed using a custom-build upright widefield microscope (Cairn research, Kent, UK) equipped with a 20x 1.0 NA objective (Olympus XLUMPLFLN20X W). Blue LED excitation light (470 nm) was filtered using a 470/40 nm filter (Chroma ET470/40x) and reflected towards the objective using a 515 nm dichroic mirror (Chroma T515lp). Emitted fluorescence was filtered by a 514 long-pass filter (Semrock LP02-514RU) and Images were projected on a high-speed camera (Andor Zyla 4.2 plus sCMOS). Recordings were performed at 100 fps, for 1000 frames. Recordings were analyzed using ImageJ and Matlab (Version R2015a, Mathworks, Natick, MA, USA).

Adult heart staining

For paraffin sections, adult zebrafish hearts were dissected and fixed in 4% paraformaldehyde (dissolved in phosphate buffer containing 4% sucrose) at 4^{o}C overnight, washed twice in PBS, dehydrated in EtOH, and embedded in paraffin. Serial sections were made at 10 µm using a microtome (Leica RM2035). For cryosections, zebrafish hearts were extracted and fixed in 4% paraformaldehyde (in Phosphate buffer) for 4 hours at room temperature. Three washes of 10 minutes were performed using 4% sucrose (in Phosphate buffer) followed by an overnight incubation at 4ºC in 30% sucrose (in Phosphate buffer). Hearts were embedded in tissue freezing medium (Leica), frozen on dry ice and kept at -80ºC. Cryo-sectioning using Cryostar NX70 (Thermo Scientific) was performed to obtain 10 µm thin sections.

In situ hybridization (ISH) was performed on paraffin sections as previously described[27] with the exception that the hybridization buffer did not contain heparin and yeast total RNA. Primers for the *grn1* probe were: forward primer TCCCGGTGGAGACTGTAGAC, reverse primer AATGACGGTGCATTTTGACA. Primers for the *postnb* probe were: forward primer AGAGGTTCTGGACAGGCTCA, reverse primer AAGGCACCATTTTTCACCAG. The *myl7* and *tbx18* ISH probes were described before.[28,29] Hematoxylin and Eosin (H&E) staining was performed on paraffin sections according to standard laboratory protocols. Acid fuchsin-orange G (AFOG) and Oil Red O stainings were performed on cryosections as previously described.[30,31] Imaging of stained sections was performed using a Leica DM4000 B LED upright automated microscope.

Statistical analysis

Data was analyzed blinded, with the exception of the adult heart tissue, as the phenotype was very apparent. Statistical analysis and drawing of graphs and plots were carried out in GraphPad Prism (version 6 for Mac OS X, GraphPad Software, San Diego California USA). Differences between two groups were analyzed using the paired Student's t-test, and comparisons between experimental groups were analyzed by one-way ANOVA for non-parametric variables with Tukey's post-test for intergroup comparisons. All data is presented as mean ± SD unless indicated otherwise, and $p \leq 0.05$ was considered significant. * $p \leq 0.05$, ** $p \leq 0.01$, *** $p \leq 0.001$, **** $p \leq 0.0001$, n.s. $p > 0.05$. n denotes the number of fish used per dataset.

7

Results

Zebrafish have two *pln* genes that are both expressed in the heart

To model the PLN R14del mutation, we first characterized the genetics of *pln* in the zebrafish. While humans only carry one *PLN* gene, two gene copies were identified in the zebrafish (source: NCBI and Ensembl databases): one is present on chromosome 17, which we referred to as '*plna*', and one on chromosome 20, which we referred to as '*plnb*' (Figure 1A). Human *PLN* encodes for a 52 amino acid (aa) protein, *plna* and *plnb* for a 52 aa and a 57 aa protein, respectively (Figure 1A,C). To test whether both *pln* genes are actively transcribed in the zebrafish we performed reverse transcription (RT)-PCR on whole embryos, whole adult hearts, only atria and only ventricles. We found strong RNA expression of both *plna* and *plnb* in all these tissues, indicating that both genes are transcribed, already during development (Figure 1B). Alignment of the annotated human and zebrafish protein sequences revealed a high level of identity between zebrafish and human proteins: *plna* 67.3% and *plnb* 75.0%. More importantly, a full conservation of the R14 region in the zebrafish was observed (Figure 1C).

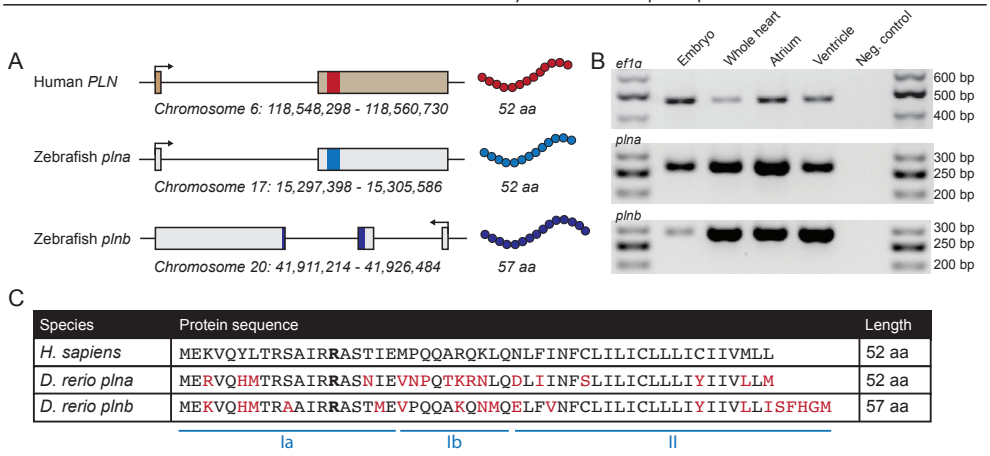

Figure 1. Genetics and expression of *pln* in the zebrafish. (A) In contrast to humans, zebrafish carry two *pln* genes instead of one. One gene is located on chromosome 17 (***plna***) and one on chromosome 20 (***plnb***). The R14del mutation was introduced in ***plnb***. aa: amino acids. (B) RT-PCR data shows *pln* Chr 17 (***plna***) and Chr 20 (***plnb***) expression in 4 dpf whole embryos (n=100-200), whole hearts (n=3), only atria (n=8) and only ventricles (n=4). ***ef1α*** was used as control gene. A 50 bp ladder was added on both sides of the samples, the size of each band is indicated on the side. Neg: negative. (C) Alignment of the human (H. sapiens) and zebrafish (D. rerio) protein sequences. Differences in amino acid sequence are indicated in red. The R14 site is indicated in bold. The different protein domains are indicated by Ia (cytosolic), Ib (linker) and II (transmembrane).

Diastolic and peak Ca^{2+} levels, as well as maximal Ca^{2+} transient amplitudes are decreased in Pln R14del embryos

We previously described how the R14del mutation was successfully introduced on *plnb* by injecting a short template oligonucleotide template containing the mutation together with Cas9/sgRNAs (Figure S1 from Tessadori et al 2018[19]). We were unable to introduce the R14del mutation in *plna*, as PAM sites and effective CRISPR/Cas9 sgRNA sequences were all too far away from the R14 site (a requirement for efficient knock-in using CRISPR/Cas9). In this study we used embryos carrying either a heterozygous or homozygous R14del mutation on *plnb* and compared these to their wild-type siblings. As all zebrafish were wild-type for *plna*, we only refer to the *plnb* genotype from this point on. Embryos carrying the R14del mutation ($plnb^{R14/+}$ or $plnb^{R14/R14}$) displayed no morphological changes at 5 days post fertilization (dpf) (Figure 2A), appeared healthy and could be raised to adulthood. As the mutated PLN protein is known to affect SERCA2a activity, we first studied the effects of the R14del mutation on Ca^{2+} transients. To this end, we crossed *tg(myl7:Gal4FF UAS:GCaMP6f)* zebrafish[20] with the *pln* R14del line, resulting in *pln* R14del fish carrying the intracellular Ca^{2+} sensor GCaMP6f. GCaMP6f consists of a circularly permutated enhanced green fluorescence protein (cpEGFP) fused to calmodulin and the M13 peptide. When intracellular Ca^{2+} rises, calmodulin binds to M13, causing increased brightness of cpEGFP (Figure 2B). Analysis of cardiac GCaMP6f (cpEGFP) signal intensity over time allowed examination of the speed of Ca^{2+} transient upstroke (intracellular Ca^{2+} release), Ca^{2+} transient recovery (Ca^{2+} reuptake/

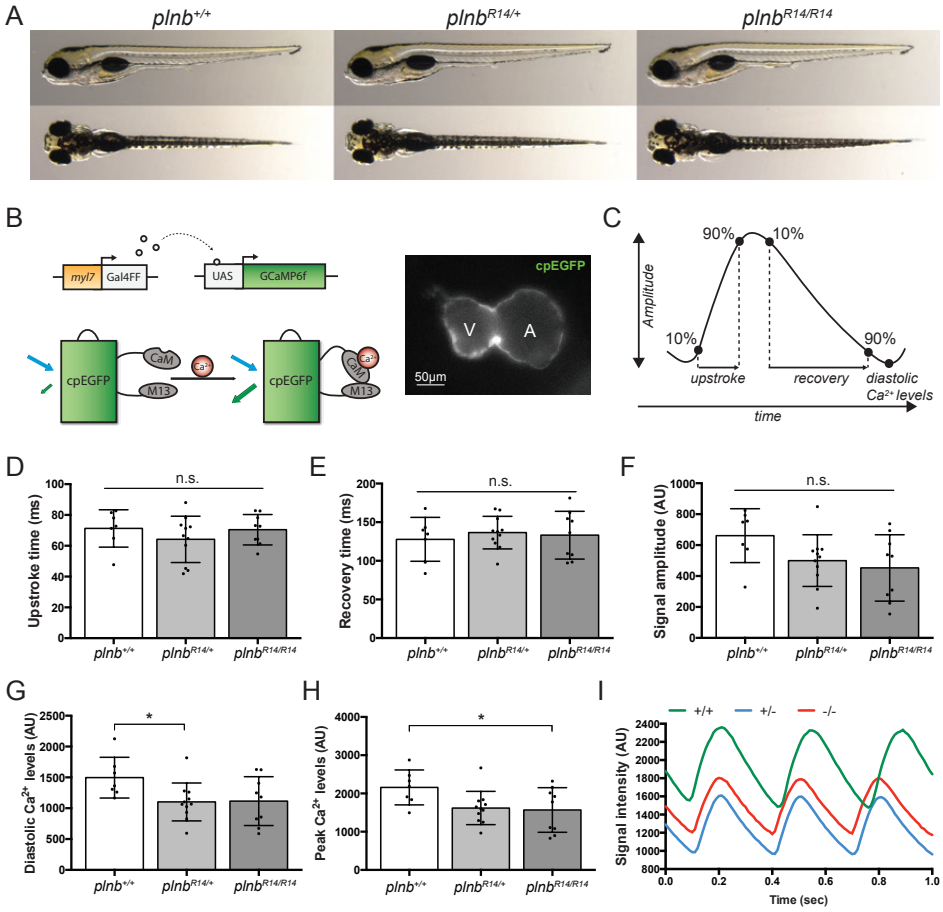

Figure 2. Intracellular Ca^{2+} dynamics in hearts of Pln R14del embryos. (A) Side and top views of 5 dpf embryos that are wild-type for ***plna***, and wild-type, heterozygous or homozygous for the R14del mutation on ***plnb***. All embryos are from the same clutch. (B) The DNA construct and sensor dynamics of GCaMP6f. GCaMP6f is placed behind the ***myl7*** promoter, which restricts its expression to the heart. The Gal4FF-UAS system amplifies its expression. GCaMP6f consists of a circularly permutated enhanced green fluorescence protein (cpEGFP) fused to calmodulin (CaM) and the M13 peptide. When intracellular Ca^{2+} rises, CaM binds to M13, causing increased brightness of cpEGFP. cpEGFP expression can be clearly observed in a widefield fluorescence image of an embryonic heart. A: atrium, V: ventricle. (C) Schematic representation of analyzed Ca^{2+} transient parameters. (D-H) Bar graphs of Ca^{2+} transient parameters (mean ± SD, ***plnb***$^{+/+}$ n=7, ***plnb***$^{R14/+}$ n=11, ***plnb***$^{R14/R14}$ n=9), including (D) upstroke time, (E) recovery time, (F) signal amplitude, (G) diastolic Ca^{2+} levels, and (H) peak Ca^{2+} levels. AU: arbitrary units, n.s.: non-significant. (I) Representative Ca^{2+} transients from ***plnb***$^{+/+}$, ***plnb***$^{R14/+}$ and ***plnb***$^{R14/R14}$ embryos, demonstrating reduced diastolic Ca^{2+} levels, peak Ca^{2+} levels, and Ca^{2+} signal amplitudes in ***plnb***$^{R14/+}$ and ***plnb***$^{R14/R14}$ embryos compared to wild-type siblings.

clearance), diastolic and peak Ca^{2+} levels, as well as maximal Ca^{2+} transient amplitudes (Figure 2C). Surprisingly, we observed no significant differences in upstroke time and recovery time

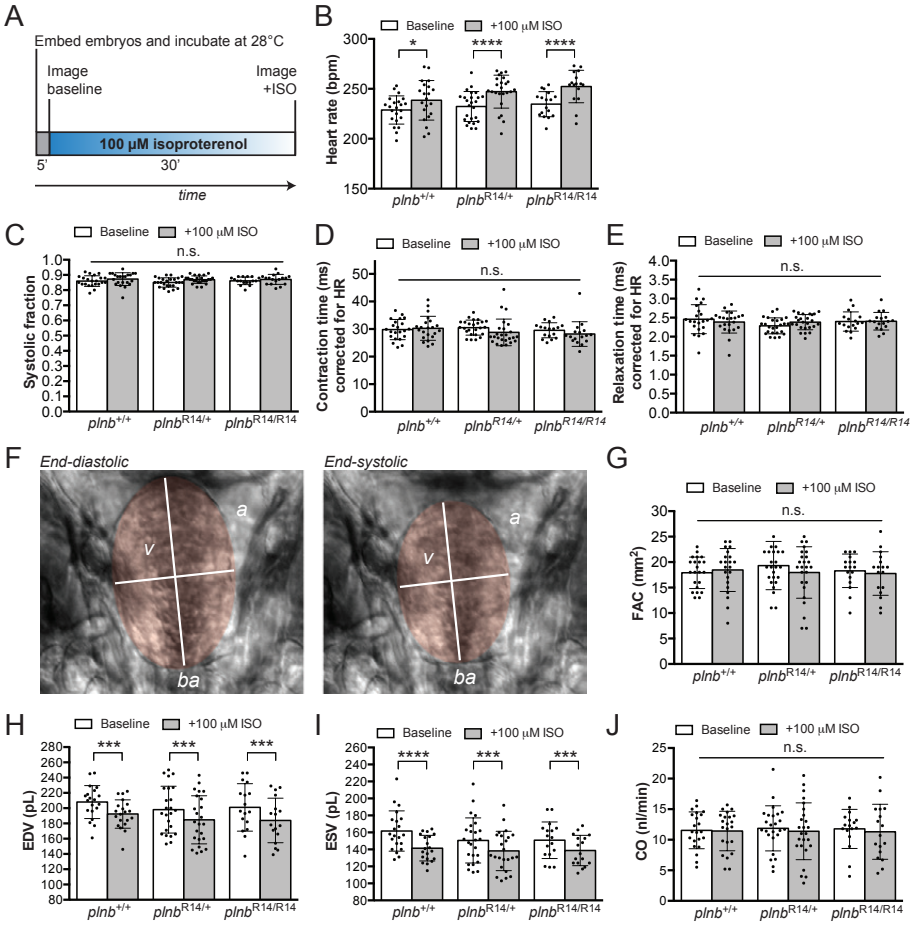

Figure 3. Cardiac function in Pln R14del embryos. (A) Overview of the experimental setup. Embryos were embedded in agarose and incubated for 5 minutes at 28°C. Baseline measurements were performed, embryos were incubated with 100 µM isoproterenol (ISO) for 30 min, and imaged again. (B-E) Bar graphs of contractility parameters at baseline and after incubation with 100 µM isoproterenol (mean ± SD, *plnb*$^{+/+}$ n=22, *plnb*$^{R14/+}$ n=25, *plnb*$^{R14/R14}$ n=17)(** p≤0.01, **** p≤0.0001), including (B) heart rate, (C) systolic fraction, (D) contraction time, and (E) relaxation time. (F) To measure hemodynamic parameters we used imageJ to fit an ellipse over the ventricle in every recording, both at end-diastole (left) and end-systole (right). The long axis and short axis values were used to measure surface and volume. a: atrium, v: ventricle, ba: bulbus arteriosus. (G-J) Bar graphs of hemodynamic parameters at baseline and after incubation with 100 µM isoproterenol (mean ± SD, ***plnb***$^{+/+}$ n=22, ***plnb***$^{R14/+}$ n=25, ***plnb***$^{R14/R14}$ n=17)(*** p≤0.001, **** p≤0.0001), including (G) fractional area change (FAC), (H) end-diastolic volume (EDV), (I) end-systolic volume (ESV), and (J) cardiac output (CO). No significant differences in could be observed between ***plnb***$^{+/+}$, ***plnb***$^{R14/+}$ and ***plnb***$^{R14/R14}$ embryos.

when comparing 3 dpf *plnb*$^{R14/+}$ and *plnb*$^{R14/R14}$ embryos with their wild-type siblings (Figure 2D-E), indicating that R14del embryos had a normal speed of Ca^{2+} release and reuptake/clearance

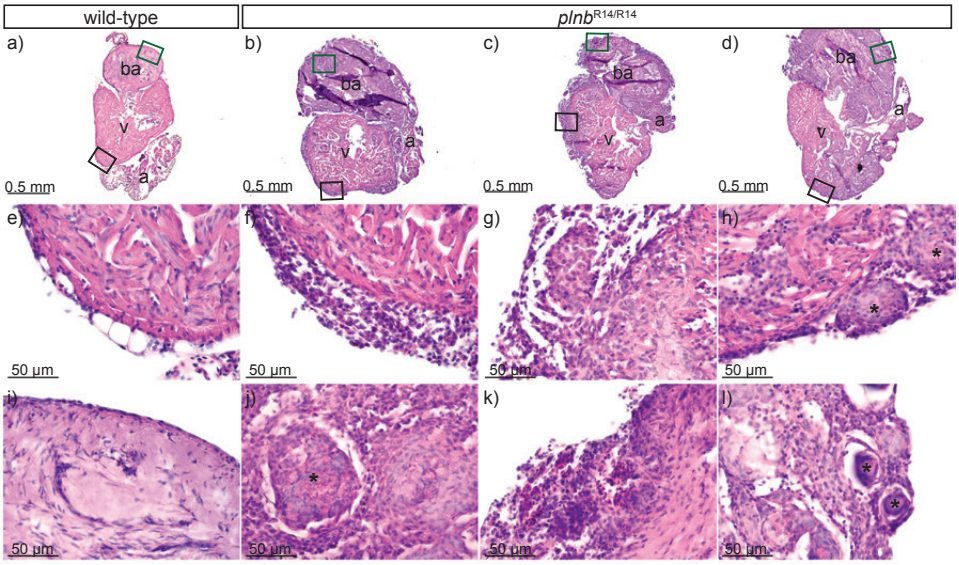

Figure 4. Histology of adult Pln R14del zebrafish hearts. H&E staining demonstrating distinct morphological changes in R14del fish (n=3) compared to wild-type (n=1). The top panels (a-d) show an overview of the total heart, the bottom panels show a zoom in of the indicated regions (e-l). The regions indicated by the black rectangles are at panel e-h, and the regions indicated by the green rectangles are at panel i-l. In panel h, j and l distinct sphere-like structures are indicated with asterisks. a: atrium, v: ventricle, ba: bulbus arteriosus.

from the cytosol despite of the mutation. In contrast, diastolic and peak Ca^{2+} levels, as well as Ca^{2+} transient amplitudes showed a clear decrease of approximately 25-35% within *plnb*$^{R14/+}$ and *plnb*$^{R14/R14}$ embryos (Figure 2F-H). These changes could also clearly be observed in representative Ca^{2+} transients from *plnb*$^{+/+}$, *plnb*$^{R14/+}$ and *plnb*$^{R14/R14}$ embryos (Figure 2I).

Contraction dynamics and hemodynamics are not affected in Pln R14del embryos

To analyze whether the differences in cytosolic calcium levels affected cardiac contractility, we measured contraction dynamics and hemodynamics in 5 dpf embryos. These parameters were measured at baseline and after 30 min treatment with 100 µM of the β-adrenergic agonist isoproterenol (ISO) (Figure 3A), as this drug is known to affect PLN/SERCA2a function through PLN phosphorylation by PKA. We first analyzed heart rate, as a standard parameter of cardiac function. At baseline, heart rates did not differ significantly between groups, and in response to 100 µM ISO all groups displayed an increase in heart rate of approximately 4-8% (Figure 3B). Next, we analyzed the ability of the ventricular wall to contract and release its contraction. We measured systolic fraction (=the fraction of time the heart is in systole), contraction time (=time from max. relaxation to max. contraction), and relaxation time (=time from max. contraction to max. relaxation). Since heart rates were similar, but not equal between all groups (Figure 3B), and heart rate can have a significant impact on contraction time and relaxation time, we corrected

these parameters for heart rate. At baseline and after ISO treatment, systolic fraction, contraction time and relaxation time did not significantly differ between *plnb*$^{+/+}$, *plnb*$^{R14/+}$ and *plnb*$^{R14/R14}$ hearts (Figure 3C-E). Next, we examined hemodynamic parameters, to determine if Pln R14del affects cardiac pump function. The ventricular surface area was measured by fitting an ellipse shape on the ventricular region in high speed imaging recordings of the zebrafish heart, both at diastole and systole (Figure 3F). Surface and volume parameters were calculated by extrapolating values of the long and short ellipse axis into a 3D volume, making use of existing mathematical formulas.[32] We examined diastolic and systolic surface area, fractional area change (FAC), end-diastolic volume (EDV), end-systolic volume (ESV), stroke volume (SV), ejection fraction (EF), and cardiac output (CO). No differences were found in FAC, SV and EF between *plnb*$^{+/+}$, *plnb*$^{R14/+}$ and *plnb*$^{R14/R14}$ hearts, at baseline or after treatment with ISO (Figure 3G, Figure S2A-B). Diastolic and systolic surface area, EDV and ESV were comparable between groups at baseline, but did significantly decrease with approximately 5-15% ($p \leq 0.001$) in all groups after treatment with ISO (Figure 3H-I, Figure S2C-D), indicating that the ventricle remained in a more contracted state in the presence of ISO. As

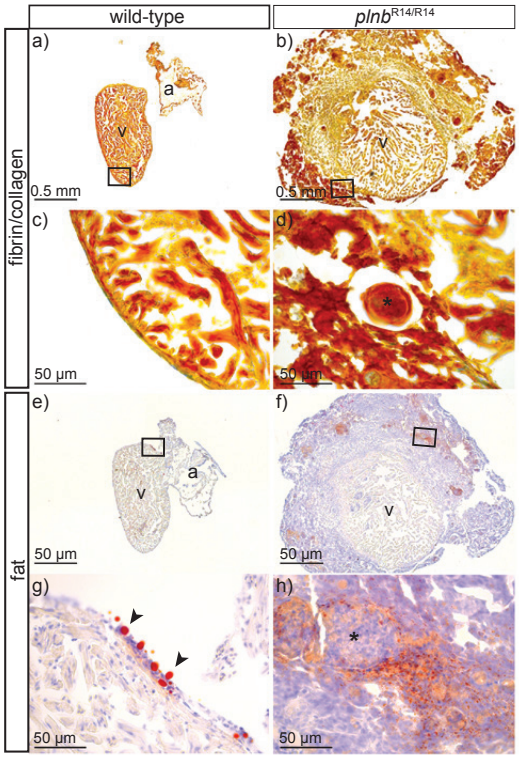

Figure 5. Fibrin/collagen and fat staining of adult Pln R14del zebrafish hearts. (a-d) AFOG and (e-h) Oil Red O staining demonstrating fibrin and fat deposits in the extra tissue layer present in Pln R14del zebrafish. The bottom panels (c-d, g-h) show a zoom in of the indicated rectangular regions. Distinct sphere-like structures are indicated with asterisks, and appear positive for fibrin and fat. Arrows indicate fat droplets in wild-type fish. a: atrium, v: ventricle, ba: bulbus arteriosus. Figure 5. Fibrin/collagen and fat staining of adult Pln R14del zebrafish hearts. (a-d) AFOG and (e-h) Oil Red O staining demonstrating fibrin and fat deposits in the extra tissue layer present in Pln R14del zebrafish. The bottom panels (c-d, g-h) show a zoom in of the indicated rectangular regions. Distinct sphere-like structures are indicated with asterisks, and appear positive for fibrin and fat. Arrows indicate fat droplets in wild-type fish. a: atrium, v: ventricle, ba: bulbus arteriosus. Figure 5. Fibrin/collagen and fat staining of adult Pln R14del zebrafish hearts. (a-d) AFOG and (e-h) Oil Red O staining demonstrating fibrin and fat deposits in the extra tissue layer present in Pln R14del zebrafish. The bottom panels (c-d, g-h) show a zoom in of the indicated rectangular regions. Distinct sphere-like structures are indicated with asterisks, and appear positive for fibrin and fat. Arrows indicate fat droplets in wild-type fish. a: atrium, v: ventricle, ba: bulbus arteriosus.

a consequence, CO did not significantly increase in any of the groups after ISO treatment (Figure 3J).

Age-related cardiac remodeling in Pln R14del zebrafish

PLN R14del-related symptoms usually develop later during life at a mean age of 44.4 years.[8] To investigate whether Pln R14del zebrafish develop changes in heart morphology we isolated the hearts of older (2 years of age) wild-type controls and *plnb*$^{R14/R14}$ fish. Strikingly 6 out of 25 pln R14del fish (23%) displayed severe cardiac morphological changes, compared to 0 out of 20 (0%) wild-type fish. In addition, we identified a severely sick 9.5-month-old fish (same genotype) with an enlarged heart. This isolated heart displayed highly similar morphological changes when compared to the affected 2-year-old hearts, confirming our earlier phenotypic findings. By eye, affected hearts appeared larger and were covered in a white flocculent layer of tissue. Histological analysis demonstrated that affected Pln R14del hearts had an extra layer of tissue surrounding

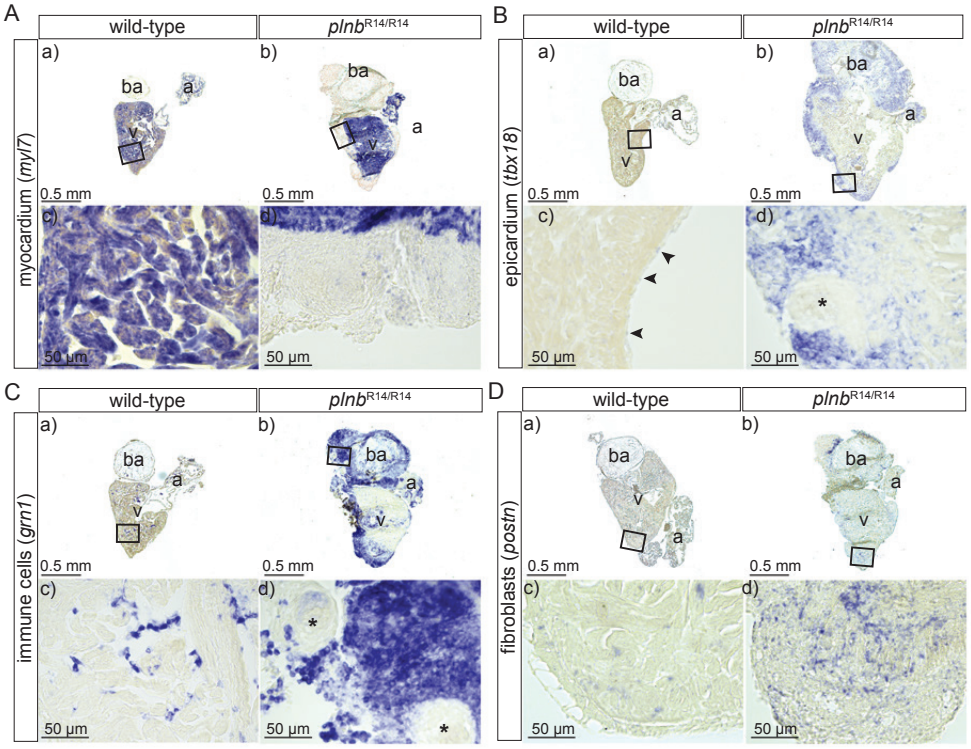

Figure 6. In situ hybridization on adult Pln R14del zebrafish hearts. (A) *myl7* staining to indicate the myocardial cells, (B) *tbx18* staining to indicate the epicardial cells, (C) *grn1* staining to indicate immune cells, and (D) *postn* staining to indicate fibroblasts. The bottom panels (c-d) show a zoom in of the indicated regions. Distinct sphere-like structures are indicated with asterisks, and are negative for *myl7, tbx18, grn1* and *postn*. Arrows indicate *tbx18* positive epicardial cells in a wild-type fish. a: atrium, v: ventricle, ba: bulbus arteriosus.

the ventricle and bulbus arterious (Figure 4), which appeared to be fused to or originate from the outer cardiac layer. The extra layer was characterized by a high density of cell nuclei (Figure 4 panel b-d, f-h, j-l) and the presence of typical sphere-like structures (Figure 4 panel h,j,l indicated by asterisks).

In PLN patients, the changes in the cardiac wall are characterized by fibrofatty replacement of myocardial tissue. To explore whether similar processes occurred in the zebrafish we performed AFOG and Oil Red O staining, to visualize fibrin/collagen and fat (Figure 5). These stainings were performed on the 9.5-month-old Pln R14del heart and compared with a 2-year-old wildtype control. We did not find large collagen deposits, but the Pln R14del mutant fish did show relatively high fibrin levels in the extra tissue layer. Especially the sphere-like structures appeared positive for fibrin (Figure 5 panel b,d indicated by asterisks). The wild-type heart displayed overall higher levels of fibrin in the cardiomyocytes, compared to the 9.5-month-old heart (Figure 5 panel a,c), therefore myocardial fibrin deposits might increase with age. In addition to the higher levels of fibrin in the extra tissue layer of the Pln R14del heart, we also observed prominent fat deposits that were spread throughout this layer (Figure 5 panel f,h). Strikingly, also the sphere-like structures appeared to be positive for fat, indicating that both fat and fibrin are present within these structures (Figure 5, panel h). Fat deposits were nearly absent in the wildtype control heart (Figure 5, panel e,g).

To explore if myocardial or epicardial cells contributed to the extra tissue layer, we stained for *myl7* (myocardial marker) and *tbx18* (epicardial marker) using in situ hybridization (ISH) (Figure 6A-B). These stainings revealed a clear expression of *tbx18* in the extra tissue, but a complete absence of *myl7* expression (Figure 6A-B panels a-d), indicating that the extra tissue might have an epicardial origin. The sphere-like structures were completely devoid of any *tbx18* staining (Figure 6B panel b,d). As the extra tissue displayed a high density of cell nuclei and increased levels of fibrin, we also explored the possibility of immune cell and fibroblast infiltration, by staining for *grn1* and *postn* respectively (Figure 6C,D). While wild-type hearts already expressed the *grn1* immune cell marker (Figure 6C panel a,c), Pln R14del hearts showed a massive increase of immune cells, especially in the extra tissue surrounding the heart (Figure 6C panel b,d). Also, we observed a clear infiltration of fibroblasts in the extra tissue layer (Figure 6D, panel b.d), while fibroblast staining was nearly absent in the wild-type control heart (Figure 6D, panel a,c). The sphere-like structures were completely devoid of any staining for *grn1* or *postn*.

Discussion

The phospholamban (PLN) R14del mutation is a Dutch founder mutation and the most prevalent single cardiomyopathy-related mutation identified in the Netherlands. Many carriers develop malignant ventricular arrhythmias and end-stage heart failure. However, it remains unclear how exactly PLN R14del can lead to such severe cardiac changes, and suitable animal models to study

PLN R14del pathology over time are lacking. In this study we introduce the zebrafish as a possible model to study PLN R14del disease. We show that Pln R14del embryos display distinct changes in Ca^{2+} dynamics, but have no changes in contractility. In addition, approximately 25% of 2-year-old adult Pln R14del fish developed severe cardiac morphological changes, in the form of an extra tissue layer covering the heart.

In this study, we established an overview of early and late Pln R14del phenotypes in the zebrafish. In PLN R14del patients, myocardial fibrosis is one of the early disease features. However, it was recently found that fibrosis is independently associated with ventricular arrhythmias[33], suggesting that distinct processes are involved in the development of arrhythmias in PLN patients. Studies using induced pluripotent stem cell cardiomyocytes have shown that PLN R14del causes Ca^{2+} overload, which may lead to activation of malignant Ca^{2+}-related signaling pathways, peri-nuclear protein aggregates and eventually cardiomyocyte damage.[16,34] In this study we examined in vivo intracellular Ca^{2+} dynamics in Pln R14del fish, making use of the GCaMP6f sensor. We found that diastolic Ca^{2+} levels, peak Ca^{2+} levels, and Ca^{2+} transient amplitudes were markedly decreased in *plnb*$^{R14/+}$ and *plnb*$^{R14/R14}$ embryonic cardiac hearts compared to wild-type siblings. Of note, differences in sensor expression between embryos may (in part) attribute to the differences we find in diastolic and peak Ca^{2+} levels, therefore it is difficult to draw any conclusions based on this data alone. However, as the changes in signal intensity are correlated to genotype, we can conclude that it is a Pln R14del specific effect. In theory, a reduction in SR Ca^{2+} reuptake and SR Ca^{2+} content could affect systolic Ca^{2+} levels, as less Ca^{2+} is released into the cytosol during calcium-induced calcium release (CICR). An alternative explanation for a reduction of systolic Ca^{2+} levels would be a decrease in L-type calcium channel peak Ca^{2+} current, but to our knowledge no link has been described between PLN R14del and the L-type calcium channel. Increased diastolic Ca^{2+} levels have been associated with PLN R14del disease as a reduced SR Ca^{2+} reuptake can lead to a reduced clearance of intracellular Ca^{2+}.[16] However, we found the opposite effect in zebrafish embryos, as diastolic Ca^{2+} levels were decreased. In contrast to their less substantial role in human cardiomyocytes, NCX pumps play a very prominent role in Ca^{2+} efflux in zebrafish cardiomyocytes.[35] Changes in intracellular diastolic Ca^{2+} levels due to impaired SR Ca^{2+} reuptake may therefore result in enhanced NCX activity, triggered by a larger Ca^{2+} gradient between cytoplasm and extracellular space, and ultimately lower diastolic Ca^{2+} levels. However, such effects are at this point speculation. To gain more insight into the effects of Pln R14del on in vivo Ca^{2+} dynamics in our zebrafish model, it would be ideal to directly measure SR Ca^{2+} content in *pln* R14del mutants, making use of a specific SR Calcium sensor (D1ER/D4ER).[36]

Calcium is an important regulator of cardiomyocyte contractility, as free cytosolic Ca^{2+} ions bind troponin, causing contraction of the cardiomyocyte. PLN activity is tightly regulated via β-adrenergic signaling, as PKA activation (via cAMP) causes phosphorylation and deactivation of PLN. Reduced inhibition of SERCA results in an increased Ca^{2+} reuptake into the SR, improving contractility as Ca^{2+} is removed more efficiently from the cytosol and the myofilaments and more SR Ca^{2+} is available for the next contraction.[37] In this study we demonstrate that zebrafish carrying

the *pln* R14del mutation display no or minimal changes in cardiac contractility at baseline and after treatment with the β-adrenergic agonist isoproterenol. It is possible that the time resolution (frame rate) of our recordings is too low to detect small changes in contraction and relaxation time, especially since relaxation time in zebrafish embryos is quite rapid (±35-45ms). However, it is also not surprising if zebrafish embryos can compensate for the Pln R14del mutation, as PLN R14del patients only present with contractile dysfunction during later stages of the disease.[33] Of note, EDV and ESV did significantly decrease in all groups after treatment with isoproterenol, indicating that the ventricle remained in a more contracted state during β-adrenergic stimulation. This is probably caused by the negative force-frequency of the zebrafish heart, which is in contrast to dynamics of myocardial contraction in mammals.[38] Regarding future experiments, it would be interesting to see how contractility parameters change in older Pln R14del fish, and if the differences we have found become more pronounced.

It is important to mention that Ca^{2+} transients do not directly reflect dynamics of cardiac contractility, as myofilament affinity for Ca^{2+} needs to be taken into account. The efficiency of Ca^{2+}-binding to the myofilaments depends on the myofilament Ca^{2+} sensitivity.[39] Therefore Ca^{2+} transients and contractility measurements cannot be compared one on one. Zebrafish have the ability to adapt their myofilament Ca^{2+} sensitivity extensively, to maintain cardiac function under a large range of temperatures (6-38°C), demanding a high Ca^{2+} buffering capacity in the cell.[40] These factors can explain why we find differences in the Ca^{2+} transients, while contractility dynamics and hemodynamics are not affected.

PLN R14del patients start to develop R14del-related symptoms later during life at a mean age of 44.4 years.[8] Therefore we examined cardiac morphology in an older Pln R14del zebrafish population. Adult zebrafish hearts respond to the *pln* R14del mutation with striking changes in heart morphology. In line with the variable phenotypes in patients, we observe a very heterogeneous effect of Pln R14del, as some zebrafish appear completely healthy while others display end-stage cardiac disease. At the same time, there are some significant differences between patients and Pln R14del zebrafish. In PLN R14del patients, myocardial fibrosis is predominantly located in the left posterolateral wall of the heart and to a lesser extent in the right ventricle. Fat infiltration is most pronounced in the right ventricular wall[10,21] Pln R14del zebrafish display changes throughout the whole heart, showing distinct extra tissue layers at the atrium, as well as the ventricle and the bulbus arteriosus. This may very well be a consequence of a difference in cardiac anatomy, as zebrafish only have one atrium and one ventricle, resulting in a different distribution of hemodynamic forces. Another interesting observation is that in zebrafish the epicardial layer mainly seems to be affected, whereas in patients fibrofatty infiltrates are located in the posterolateral region of the left ventricular myocardium, right underneath the epicardium. Despite differences in the precise regions that are affected, the underlying processes involved in the development of these morphological changes might be similar. The importance of paracrine signaling between epicardial and subepicardial cells, as driver of morphologic changes in the subepicardial region, is increasingly recognized.[22,23] In fact, it was shown that fat cells can derive from epicardial cells by

mesenchymal transformation and PPARγ activation.[41] Specific remodeling of the epicardial region in PLN R14del patients may point towards an epicardial origin, but this has not been studied yet. Another factor that makes a direct comparison between zebrafish and human PLN R14del disease challenging is the fact that human hearts contain more myocardial fat tissue than zebrafish hearts. Therefore Pln R14del zebrafish hearts may develop less pronounced fat deposits.

We observed distinct sphere-like structures, and vast immune cell infiltrations and fibrin deposits in Pln R14del zebrafish hearts. The sphere-like structures stained negative for inflammatory, myocardial and epicardial markers, but positive for fat and fibrin. Structures like this have never been observed in PLN R14del patients, but if these fibrofatty infiltrates develop in a similar fashion as myocardial fibrofatty infiltrates in patients, they might be interesting to explore. The extra tissue in the Pln R14del zebrafish hearts is also infiltrated with large amounts of inflammatory cells. Immune cells are already clearly present in the 2-year old wildtype hearts, but as the heart is a blood infiltrated organ, immune cells will always be present to some extent. Involvement of inflammation in progression of structural heart disease in arrhythmogenic cardiomyopathy is well known[24], but to our knowledge myocardial inflammation has not yet been examined in PLN R14del patients. For future experiments, it would be interesting to perform RNA sequencing on Pln R14del zebrafish hearts of different ages and to study how transcriptome profiles change over time. This could identify factors that are important in the development of the morphological changes we observed.

In this study, we established an overview of early and late Pln R14del phenotypes in the zebrafish. Based on the data presented in this chapter, we can state that the Pln R14del zebrafish is a novel and interesting model to study PLN R14del disease. We show that Pln R14del embryos present with changes in Ca^{2+} handling, but have normal contractility dynamics. In addition, we demonstrate that adult fish develop changes in cardiac morphology, related to what is observed in patients. Extrapolation of our findings to the human situation should be done cautiously, as there are known differences between human and zebrafish in Ca^{2+} handling and cardiac anatomy, but also because the effects of PLN R14del on human cardiomyocyte physiology are still uncertain. In order to fully appreciate the Pln R14del zebrafish model to study PLN R14del disease and to test possible treatments that may benefit patients, additional studies are required.

References

1. van der Zwaag PA, van Rijsingen IAW, Asimaki A, Jongbloed JDH, van Veldhuisen DJ, Wiesfeld ACP, et al. Phospholamban R14del mutation in patients diagnosed with dilated cardiomyopathy or arrhythmogenic right ventricular cardiomyopathy: evidence supporting the concept of arrhythmogenic cardiomyopathy. *Eur J Heart Fail* 2012 Nov;14(11):1199–207.
2. Haghighi K, Kolokathis F, Gramolini AO, Waggoner JR, Pater L, Lynch RA, et al. A mutation in the human phospholamban gene, deleting arginine 14, results in lethal, hereditary cardiomyopathy. *Proc Natl Acad Sci U.S.A*. 2006 Jan;103(5):1388–93.
3. DeWitt MM, MacLeod HM, Soliven B, McNally EM. Phospholamban R14 deletion results in late-onset, mild, hereditary dilated cardiomyopathy. *J Am Coll Cardiol* 2006 Oct;48(7):1396–8.
4. Posch MG, Perrot A, Geier C, Boldt LH, Schmidt G, Lehmkuhl HB, et al. Genetic deletion of arginine 14 in phospholamban causes dilated cardiomyopathy with attenuated electrocardiographic R amplitudes. *Heart Rhythm* 2009 Apr;6(4):480–6.
5. López-Ayala JM, Boven L, van den Wijngaard A, Peñafiel-Verdú P, van Tintelen JP, Gimeno JR. Phospholamban p.arg14del mutation in a Spanish family with arrhythmogenic cardiomyopathy: evidence for a European founder mutation. *Rev Esp Cardiol* 2015 Apr;68(4):346–9.
6. Haghighi K, Pritchard T, Bossuyt J, Waggoner JR, Yuan Q, Fan G-C, et al. The human phospholamban Arg14-deletion mutant localizes to plasma membrane and interacts with the Na/K-ATPase. J Mol Cell Cardiol 2012 Mar;52(3):773–82.
7. Rijdt Te WP, van der Klooster ZJ, Hoorntje ET, Jongbloed JDH, van der Zwaag PA, Asselbergs FW, et al. Phospholamban immunostaining is a highly sensitive and specific method for diagnosing phospholamban p.Arg14del cardiomyopathy. *Cardiovasc Pathol* 2017 Oct;30:23–6.
8. van der Zwaag PA, van Rijsingen IAW, de Ruiter R, Nannenberg EA, Groeneweg JA, Post JG, et al. Recurrent and founder mutations in the Netherlands-Phospholamban p.Arg14del mutation causes arrhythmogenic cardiomyopathy. *Neth Heart J* 2013 Jun;21(6):286–93.
9. van Rijsingen IAW, van der Zwaag PA, Groeneweg JA, Nannenberg EA, Jongbloed JDH, Zwinderman AH, et al. Outcome in phospholamban R14del carriers: results of a large multicentre cohort study. *Circ Cardiovasc Genet* 2014 Aug;7(4):455–65.
10. Gho JMIH, van Es R, Stathonikos N, Harakalova M, Rijdt Te WP, Suurmeijer AJH, et al. High resolution systematic digital histological quantification of cardiac fibrosis and adipose tissue in phospholamban p.Arg14del mutation associated cardiomyopathy. *PLoS ONE* 2014;9(4):e94820.
11. MacLennan DH, Kranias EG. Phospholamban: a crucial regulator of cardiac contractility. *Nat Rev Mol Cell Biol* 2003 Jul;4(7):566–77.
12. Traaseth NJ, Shi L, Verardi R, Mullen DG, Barany G, Veglia G. Structure and topology of monomeric phospholamban in lipid membranes determined by a hybrid solution and solid-state NMR approach. *Proc Natl Acad Sci U.S.A*. 2009 Jun;106(25):10165–70.
13. Chu G, Lester JW, Young KB, Luo W, Zhai J, Kranias EG. A single site (Ser^{16}) phosphorylation in phospholamban is sufficient in mediating its maximal cardiac responses to beta -agonists. *J Biol Chem* 2000 Dec;275(49):38938–

43.

14. Kranias EG, Hajjar RJ. The Phospholamban Journey 4 Decades After Setting Out for Ithaka. *Circ Res* 2017 Mar;120(5):781–3.
15. Vostrikov VV, Soller KJ, Ha KN, Gopinath T, Veglia G. Effects of naturally occurring arginine 14 deletion on phospholamban conformational dynamics and membrane interactions. *Biochim Biophys Acta* 2015 Jan;1848(1 Pt B):315–22.
16. Karakikes I, Stillitano F, Nonnenmacher M, Tzimas C, Sanoudou D, Termglinchan V, et al. Correction of human phospholamban R14del mutation associated with cardiomyopathy using targeted nucleases and combination therapy. *Nat Commun* 2015 Apr 29;6(1):6955.
17. Lieschke GJ, Currie PD. Animal models of human disease: zebrafish swim into view. *Nat Rev Genet* 2007 May;8(5):353–67.
18. Howe K, Clark MD, Torroja CF, Torrance J, Berthelot C, Muffato M, et al. The zebrafish reference genome sequence and its relationship to the human genome. *Nature* 2013 Apr;496(7446):498–503.
19. Tessadori F, Roessler HI, Savelberg SMC, Chocron S, Kamel SM, Duran KJ, et al. Effective CRISPR/Cas9-based nucleotide editing in zebrafish to model human genetic cardiovascular disorders. *Dis Model Mech* 2018 Oct;11(10):dmm035469.
20. van Opbergen CJM, Koopman CD, Kok BJM, Knöpfel T, Renninger SL, Orger MB, et al. Optogenetic sensors in the zebrafish heart: a novel in vivo electrophysiological tool to study cardiac arrhythmogenesis. *Theranostics* 2018;8(17):4750–64.
21. Sepehrkhouy S, Gho JMIH, van Es R, Harakalova M, de Jonge N, Dooijes D, et al. Distinct fibrosis pattern in desmosomal and phospholamban mutation carriers in hereditary cardiomyopathies. *Heart Rhythm* 2017 Jul;14(7):1024–32.
22. Matthes SA, Taffet S, Delmar M. Plakophilin-2 and the migration, differentiation and transformation of cells derived from the epicardium of neonatal rat hearts. *Cell Commun Adhes* 2011 Aug;18(4):73–84.
23. Dubash AD, Kam CY, Aguado BA, Patel DM, Delmar M, Shea LD, et al. Plakophilin-2 loss promotes TGF-β1/p38 MAPK-dependent fibrotic gene expression in cardiomyocytes. *J Cell Biol* 2016 Feb;212(4):425–38.
24. Asimaki A, Tandri H, Duffy ER, Winterfield JR, Mackey-Bojack S, Picken MM, et al. Altered desmosomal proteins in granulomatous myocarditis and potential pathogenic links to arrhythmogenic right ventricular cardiomyopathy. *Circ Arrhythm Electrophysiol* 2011 Oct;4(5):743–52.
25. Westerfield M. The Zebrafish Book. 4 ed. University of Oregon Press, Eugene.
26. Sehnert AJ, Huq A, Weinstein BM, Walker C, Fishman M, Stainier DYR. Cardiac troponin T is essential in sarcomere assembly and cardiac contractility. *Nature Genetics* 2002 May;31(1):106–10.
27. Moorman AF, Houweling AC, de Boer PA, Christoffels VM. Sensitive nonradioactive detection of mRNA in tissue sections: novel application of the whole-mount in situ hybridization protocol. *J Histochem Cytochem* 2001 Jan;49(1):1–8.
28. Yelon D, Horne SA, Stainier DY. Restricted expression of cardiac myosin genes reveals regulated aspects of heart tube assembly in zebrafish. *Dev Biol* 1999 Oct;214(1):23–37.
29. Begemann G, Gibert Y, Meyer A, Ingham PW. Cloning of zebrafish T-box genes tbx15 and tbx18 and their expression during embryonic development. *Mech Dev* 2002 Jun;114(1-2):137–41.

30. Poss KD, Wilson LG, Keating MT. Heart regeneration in zebrafish. *Science* 2002 Dec;298(5601):2188–90.
31. Bancroft JD, Stevens A. Theory and Practice of Histological Techniques. 4 ed. Churchill Livingstone.
32. Yalcin HC, Amindari A, Butcher JT, Althani A, Yacoub M. Heart function and hemodynamic analysis for zebrafish embryos. *Dev Dyn* 2017 Nov;246(11):868–80.
33. Rijdt Te WP, Sande Ten JN, Gorter TM, van der Zwaag PA, van Rijsingen IA, Boekholdt SM, et al. Myocardial fibrosis as an early feature in phospholamban p.Arg14del mutation carriers: phenotypic insights from cardiovascular magnetic resonance imaging. *Eur Heart J Cardiovasc Imaging* 2018 Apr;14:1199.
34. Rijdt Te WP, van Tintelen JP, Vink A, van der Wal AC, de Boer RA, van den Berg MP, et al. Phospholamban p.Arg14del cardiomyopathy is characterized by phospholamban aggregates, aggresomes, and autophagic degradation. *Histopathology* 2016 Oct;69(4):542–50.
35. van Opbergen CJM, van der Voorn SM, Vos MA, de Boer TP, van Veen TAB. Cardiac Ca^{2+} signalling in zebrafish: Translation of findings to man. *Prog Biophys Mol Biol* 2018 Oct;138:45-58
36. Greotti E, Wong A, Pozzan T, Pendin D, Pizzo P. Characterization of the ER-Targeted Low Affinity Ca($^{2+}$) Probe D4ER. *Sensors* 2016 Sep;16(9):1419.
37. Li L, Desantiago J, Chu G, Kranias EG, Bers DM. Phosphorylation of phospholamban and troponin I in beta-adrenergic-induced acceleration of cardiac relaxation. *Am J Physiol Heart Circ Physiol* 2000 Mar;278(3):H769–79.
38. Haustein M, Hannes T, Trieschmann J, Verhaegh R, Köster A, Hescheler J, et al. Excitation-contraction coupling in zebrafish ventricular myocardium is regulated by trans-sarcolemmal Ca^{2+} influx and sarcoplasmic reticulum Ca^{2+} release. *PLoS ONE* 2015;10(5):e0125654.
39. Chung JH, Biesiadecki BJ, Ziolo MT, Davis JP, Janssen PML. Myofilament Calcium Sensitivity: Role in Regulation of In vivo Cardiac Contraction and Relaxation. *Front Physiol* 2016;7(Pt 1):562.
40. Stevens CM, Rayani K, Genge CE, Singh G, Liang B, Roller JM, et al. Characterization of Zebrafish Cardiac and Slow Skeletal Troponin C Paralogs by MD Simulation and ITC. *Biophys J* 2016 Jul;111(1):38–49.
41. Yamaguchi Y, Cavallero S, Patterson M, Shen H, Xu J, Kumar SR, et al. Adipogenesis and epicardial adipose tissue: a novel fate of the epicardium induced by mesenchymal transformation and PPARγ activation. *Proc Natl Acad Sci U.S.A*. 2015 Feb;112(7):2070–5.

Supplemental figures

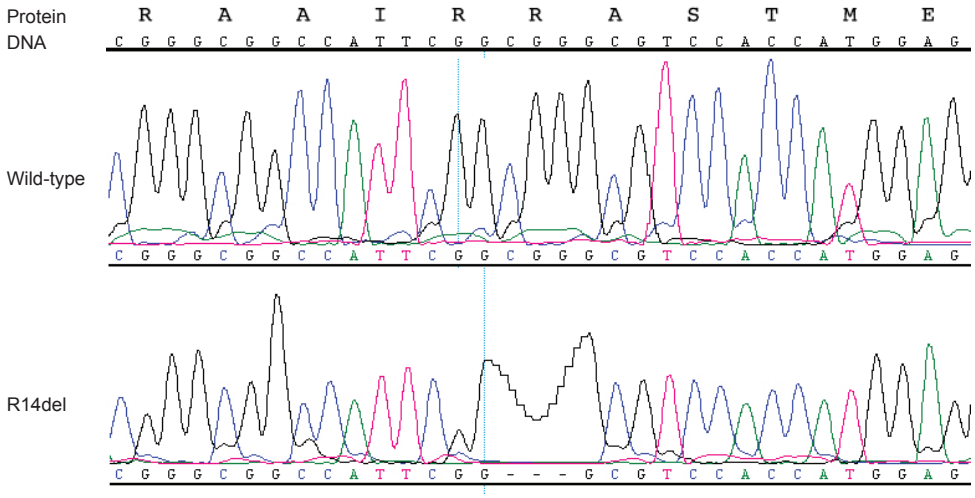

Figure S1. Sequencing peaks of *plnb* showing the R14del mutation. Sequencing peaks from a wild-type and a *pln* R14del fish. In the R14del fish, the arginine on amino acid location 14 has evidently been deleted.

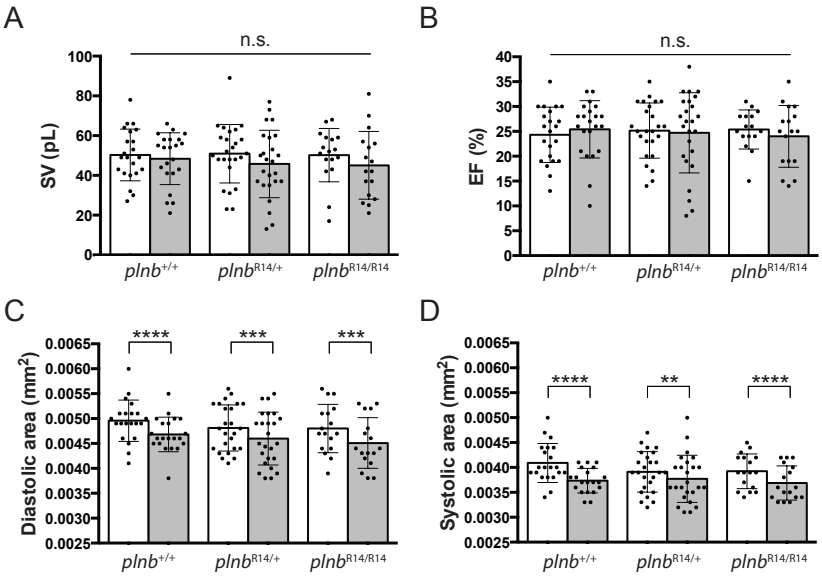

Figure S2. Cardiac hemodynamics in Pln R14del embryos. Complementary to figure 3, demonstrating additional bar graphs of hemodynamic parameters at baseline and after incubation with 100 µM isoproterenol (mean ± SD, *plnb*$^{+/+}$ n=22, *plnb*$^{R14/+}$ n=25, *plnb*$^{R14/R14}$ n=17) (** p≤0.01, *** p≤0.001, **** p≤0.0001), including (A) stroke volume (SV), (B) ejection fraction (EF), (C) diastolic area, and (D) systolic area.

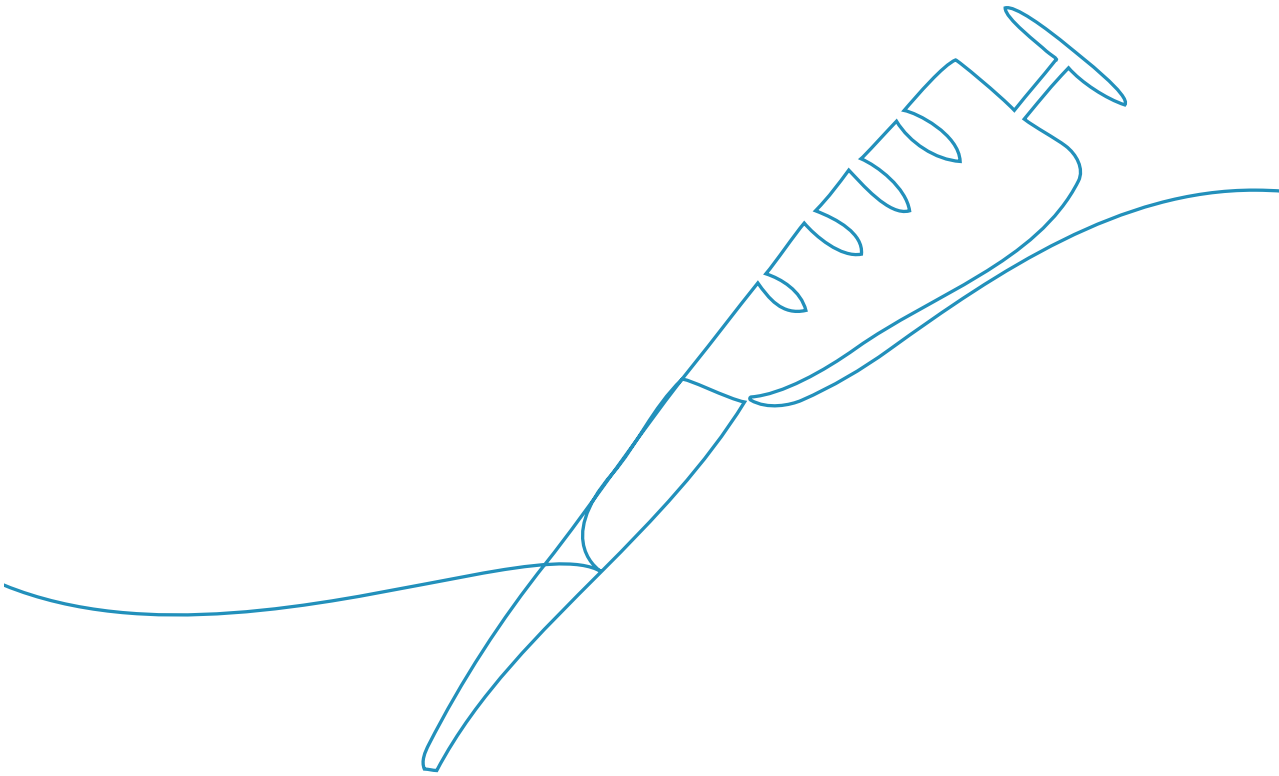

CHAPTER 8

General Discussion

The heart is one of the first organs to develop during embryonic development, illustrating its importance in maintaining life. The fundamental function of the heart is to pump blood throughout the body, allowing the delivery of oxygen and nutrients to tissues and the disposal of waste products from the body. This pumping function relies on the highly coordinated contraction of individual cardiac muscle cells, which is triggered by the heart's electrical system. Electrical conduction starts at the top of the right atrium, where highly specialised cardiomyocytes called 'pacemaker cells' are located. Pacemaker cells are capable of rhythmically producing electrical impulses, which trigger neighbouring cardiomyocytes to contract. The electrical impulses are then passed along from cardiomyocyte to cardiomyocyte, inducing contraction along the way and resulting in a sequential contraction of the atria and the ventricles. The processes of electrical conduction and cardiomyocyte contraction rely heavily on intricate signal conduction cascades that are regulated by cardiac ion channels and ions like Na^+, K^+ and Ca^{2+}.

Disruptions in cardiac electrical conduction can result in arrhythmias; a condition in which the heart beats irregular, too fast or too slow. Arrhythmias can be life threatening as they may cause a complete arrest of the heartbeat. Unfortunately, sudden cardiac arrest occurs out-of-hospital in the vast majority of cases, and although resuscitation rates are increasing, the majority of individuals do not survive.[1] As a consequence, sudden cardiac death (SCD) accounts for approximately 15-20% of mortality in the general population.[1,2] Different cardiac pathologies underlie SCD, and there are various risks and predisposing factors that determine the likelihood of developing fatal arrhythmias, making it extremely difficult to diagnose and prevent this disease.[1] The identification of genetic factors that underlie SCD has the benefit of providing molecular leads that can result in an increased understanding of disease pathways.[2] In addition it enables genetic testing and can contribute to diagnosis, risk stratification and preventative treatment. Fortunately, due to advancing genetic techniques, much progress has already been made over the past years. However, many question remain and further identification of genes that are involved in cardiac electrophysiology is necessary.

The zebrafish has gained increasing interest as a model organism to study human disease, including cardiac arrhythmias. Certain aspects of zebrafish cardiac electrophysiology, like action potential shape and heart rate, are very similar to that of humans. In addition, zebrafish are highly suitable for medium to large-scale forward and reverse genetic screens, as they can be easily genetically manipulated, produce high numbers of offspring, and embryos develop rapidly and externally.[3] For this reason we implemented the zebrafish as a model to screen for genes that affect cardiac electrophysiology. We were able to address different questions:

1. Can we generate novel tools to study cardiac cellular electrophysiology in an in vivo setting, and use these tools to examine the cardiac changes in zebrafish mutants?
2. Can we identify new genes that are important in cardiac cellular electrophysiology using the zebrafish?
3. Can we use zebrafish to model known human heart disease, and study disease mechanisms?

And then there was light.

Is optogenetics a useful technique in the study of in vivo cardiac cellular electrophysiology?
Cellular electrophysiological measurements are often performed on isolated hearts or isolated cardiomyocytes. Undeniably, in vivo experiments provide a better understanding of the complex physiology of the heart and the way it functions within the context of the whole body. Optogenetics is a relatively new technique that combines genetic engineering with optics to observe and/or control the function of genetically targeted groups of cells with light.[4] The technique is widely and successfully being applied in neuroscience, but has so far gained limited ground in cardiac research. This is mostly due to the gross movements of the heart and the location of the heart within the thorax. In chapter 2 we provide an overview of how optogenetic sensors can be useful tools to study the dynamics of cardiac molecules at a cellular level. In chapter 3 we implement optogenetic sensors for membrane voltage (chimeric VSFP-butterfly) and cytosolic Ca^{2+} (GCaMP6f) in the zebrafish heart. Excitingly, using embryos of these zebrafish we were able to study in vivo cardiac membrane depolarizations and cytosolic Ca^{2+} dynamics in a spatiotemporal manner. We were able to prevent movement of the heart with a knockdown approach using a silent heart (tnnt2a) morpholino, which enable us to look at fluorescent signals without movement artefacts. As embryos are transparent, recording of fluorescence signals was possible without the use of invasive procedures. We validated the reliability and robustness of both the VSFP-butterfly and GCaMP6f sensor and show that both sensors accurately reflect cardiac electrophysiology. Therefore, parallel use of these zebrafish lines provides a powerful new tool to study in vivo excitation-contraction coupling. We were also able to measure GCaMP6f signals in older larvae of 14 days old, making use of the transparent casper fish[5] and treatment with the non-toxic drug 'para-amino-blebbistatin' to block contraction.[6]

This study in **chapter 3** demonstrates that the optogenetic VSFP-butterfly and GCaMP6f fish lines provide excellent tools to study membrane voltage and Ca^{2+} transients in vivo in embryonic and larval zebrafish. However, as cardiac cellular electrophysiology is extremely complex and many molecules are involved in maintaining a proper conduction and contraction, it is compelling to generate more optogenetic zebrafish lines in the future. Especially since we now have the complete toolset to analyse such lines. New optogenetic fish could provide a more comprehensive view of the in vivo effects of for example genetic mutations. In this regard, it would be very interesting to study molecule dynamics (e.g. Ca^{2+}) at additional locations within cardiomyocytes, such as the sarcoplasmic reticulum, and to combine different optogenetic sensors in one fish line. This would allow either the simultaneous analysis of different molecules at a similar/different cellular location, or the simultaneous analysis of the same molecule at different cellular locations, and would eliminate the influence of inter-animal variability on measurements, including genetic influences and heart rate differences. It is relatively easy to target genetically encoded sensors to a specific location within the cell, by implementing a localization motif.[7] However, the sensor itself also has to be equipped for the specific subcellular conditions. When the concentration

of a molecule is high for example, the sensor requires different kinetics compared to when a molecule has a low concentration.[8] Ideally, sensors should exhibit strong fluorescence, high signal to noise ratio, fast kinetics, not interfere with local processes, and possess a suitable affinity for the molecule of interest at the specific subcellular location. Fortunately, the optogenetic research field is very dynamic, and new sensors with optimized characteristics are constantly being developed.

There are also some important limitations to the in vivo use of optogenetics. In zebrafish embryos, the heart can be easily observed through the skin, as the skin is transparent. However, a contraction block (using a tnnt2a knockdown approach or treatment with para-amino-blebbistatin) is still necessary to visualise cardiac optogenetic signals and eliminate movement artefacts. Blocking contraction will however interfere with normal hemodynamics and could affect certain aspects of heart physiology.[9] Obviously, an approach where there is minimal interference with heart physiology would be preferable. The development of software and/or microscope systems that can correct for cardiac movement, but still provide detailed beat-to-beat information, would therefore definitely move the field forward. Unfortunately, such systems are extremely complex and will likely not be realised within the next couple of years. Another limitation is the age at which we can analyse optogenetic sensors in fish or other animals. At the moment, we can only image young zebrafish, as they are less dependent on a functional circulation and their skin is still thin enough to penetrate with excitation light. However, older animals have a more developed heart and measurements may therefore reflect the human situation more accurately. For now, measurements in older animals are only possible using invasive techniques or in vitro experiments.

The optogenetic field is moving rapidly and gaining more and more interest. Next to its usefulness as a tool in research, it even has the potential to be used as a therapy in the clinic. Researchers have for example been able to restore sight in blind rodents[10] and have stopped seizures in epileptic animals.[11] All this has been achieved by controlling cells with optogenetics. While this was not the focus of my research, and it may be a long road before such a treatment will be applied in the clinic, there may be a unique potential of optogenetics for cardiac therapies, including cardiac pacing and resynchronization therapies.[12] Optogenetic pacing strategies may also be interesting for future experiments, as it could eliminate experimental variation that is caused by heart rate differences between animals.

Fishing for new genes.

GNB5, the brake of the cardiac parasympathetic system

Heterotrimeric G proteins are important for signal transduction as they are associated with G protein-coupled receptors (GPCRs) and modulate a vast array of cellular functions. G proteins are composed of α, β, and γ subunits. Guanine nucleotide-binding protein subunit β5 (GNB5/Gβ5) is one of the different β-subunits. A role of GNB5 in neurological and ophthalmologic function was reported previously[13-17], and in **chapter 4** and **chapter 5** we identify GNB5 as an important regulator

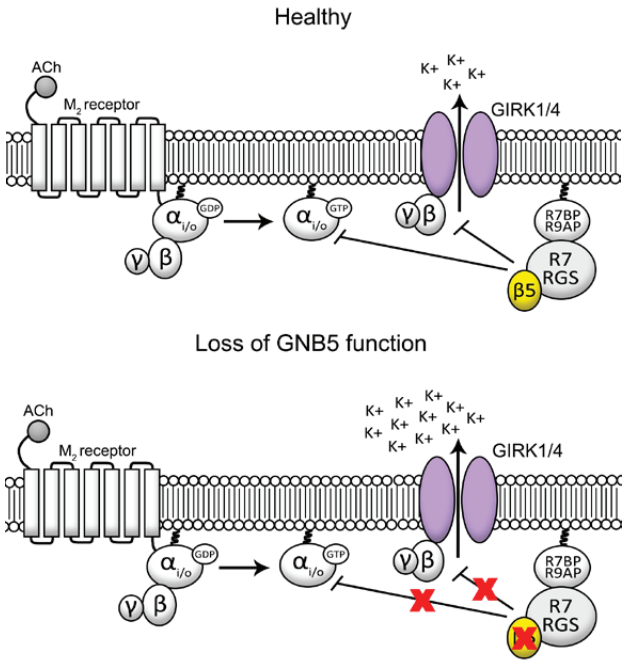

Figure 1. The role of GNB5 in the cardiac parasympathetic signalling cascade. Acetylcholine (ACh) is released by the post-ganglionic parasympathetic nerves and binds to the M2 receptor on pacemaker cells and atrial cardiomyocytes. The M2 7-transmembrane receptor changes conformation and the coupled G protein is activated, dissociating into Gα and Gβγ. The Gβγ complex in turn activates the GIRK1/4 channel, resulting in an efflux of K+ and hyperpolarization of the cell membrane. This renders the cell less susceptible to new electrical stimuli and thereby lowers the heart rate. Under healthy conditions, GNB5 (Gβ5) inhibits the βγ-GIRK1/4 interaction, and provides a brake to the parasympathetic response. When GNB5 function is lost, the parasympathetic response results in an extreme hyperpolarization of the cell membrane and the heart becomes bradycardic.

of parasympathethic activation of the heart. We show that mutations in *GNB5* are associated with a multisystem syndrome in which affected individuals present with a clinical overlap of neurological and cardiac conduction defects, including heart-rate disturbances, eye disease, intellectual disability, gastric problems, hypotonia, and seizures. In our study, nine affected individuals from six different families were identified. After publication, additional cases have been reported[18-21], which brings the total identified GNB5 patients to 21, originating from 9 different families. The zebrafish has two *GNB5* paralogs as a result of an ancient genome duplication event. Using CRISPR/Cas9 we developed a *gnb5a/gnb5b* knockout zebrafish, which shows altered responses to touch, impaired ocular movement, and cardiac sinus node dysfunction, thus recapitulating the patient phenotypes. This provided evidence that *GNB5* is indeed the disease-causing gene in this disorder. It also demonstrates that the *gnb5* knockout zebrafish is an excellent model to study molecular mechanisms of GNB5 disease.

It has been reported that GNB5 has an inhibitory effect on G protein-coupled inwardly rectifying K^+ (GIRK) channels.[22,23] In the heart, this channel is predominantly expressed in pacemaker cells and atrial myocytes, and consists of heterotetramers of GIRK1 (Kir3.1) and GIRK4 (Kir3.4) subunits. The GIRK1/4 channel underlies the acetylcholine (ACh)-activated K^+ current ($I_{K,Ach}$), which is important for the parasympathetic responsiveness of the heart. During rest, ACh is released from post-ganglionic parasympathetic neurons and binds to the G-protein coupled M_2 muscarinic receptors on pacemaker cells and atrial cardiomyocytes. Binding of ACh triggers the activation of heterotrimeric G-proteins that dissociate into Gα-GTP and Gβγ subunits (this complex does not contain GNB5, but possibly GNB2[24]). The Gβγ complex binds and activates the cardiac GIRK channel, resulting in K^+ efflux and membrane hyperpolarization, slowing depolarization in pacemaker cells and atrial cardiomyocytes. This decreases spontaneous pacemaker cell activity and atrial cardiomyocyte responsiveness. In contrast to other β-subunits, β5 binds to the RGS family of proteins and has an inhibitory effect on GIRK, which dampens the parasympathetic response (Figure 1). In chapter 5 we show that the S81L *GNB5* mutation, a mutation that we frequently observed in GNB5 patients, results in an increased $I_{K,ACh}$ density and in excessive slowing of spontaneous activity upon stimulation with the cholinergic agonist carbachol (CCh) in human induced pluripotent stem cell cardiomyocytes (hiPSC-CMs). Zebrafish with a loss of function of Gnb5, show a highly similar response as heart rates decrease drastically in response to cholinergic stimulation with CCh. We demonstrate that the bradycardic phenotype can be reversed by specifically blocking $I_{K,ACh}$, both in hiPSC-CMs and in the *gnb5* zebrafish mutant.

Overall, our studies in chapter 4 and chapter 5 reveal an important role of GNB5 in cardiac parasympathetic regulation, and unravel the molecular mechanism of cardiac GNB5 function to a large extent. At the same time, it would be interesting to explore the role of GNB5 even further. At this point, it remains unclear how $I_{K,Ach}$ density increases in iPSC-CMs with the S81L *GNB5* mutation, and if this effect is similar in other *GNB5* mutations or with a full loss of GNB5. Also, the GNB5-RGS complex may have additional effects within cardiomyocytes. Interestingly, a recent publication demonstrated that GNB5 may be involved in cardiac Ca^{2+} signalling, in a process that is referred to as store-operated calcium entry (SOCE).[25] SOCE refers to the replenishment of (sarco) endoplasmic reticulum Ca^{2+} stores by specialised Ca^{2+} channels, such as Stim1-Orai1 complexes. Cells expressing GNB5 showed an enhanced store-operated calcium entry (SOCE) when Stim1-Orai1 complexes were also present. This is intriguing, as SOCE has been associated with chronic cardiac disease development.[26-28]

In chapter 4 and chapter 5 we mainly focussed on the molecular mechanisms of GNB5 in cardiac function. However, as the *gnb5* knockout zebrafish recapitulates many patient symptoms, it would be interesting to exploit this model also for detailed research into neurologic and ophthalmologic GNB5 pathways. In addition, we can use *gnb5* knockout zebrafish to screen for drugs that can interfere with disease processes. In the end, that is the main goal of developing animal disease models: to understand human disease and identify pathways for therapeutic intervention. We have demonstrated that inhibition of the cardiac-specific GIRK1/4 channels

can rescue the bradycardic phenotype in both zebrafish and iPSC-CMs. As GNB5 also regulates GIRK channels in neurons, it would be interesting to explore general GIRK channel blockers as a potential therapy for GNB5 patients. To our knowledge, there are no FDA approved drugs that specifically target GIRK-channels, but certain antidepressants (e.g. imipramine, desipramine, amitriptyline and citalopram) can block GIRK channels in addition to their primary effects.[29] While such drugs will undeniable produce side effects, it will be interesting to determine if the most debilitating symptoms in GNB5 patients, such as mental retardation, hypotonia and bradycardia can be alleviated using antidepressants. Promisingly, a study using mice with constitutively active GIRK2 demonstrated that antidepressants (here desipramine and fluoxetine) can indeed restore motor disturbances.[30]

Tmem161b, the versatile electrophysiological newbie

Transmembrane (TMEM) proteins are proteins that are linked to and span across biological membranes. Within the TMEM class of proteins, there is also a TMEM family of proteins. Interestingly, the biological function of most members of this family remains unknown, mostly due to difficulties in the extraction and purification of transmembrane proteins. In **chapter 6** we identify Tmem161b as a novel regulator of cardiac ion channels as *tmem161b*$^{-/-}$ zebrafish embryos present with severe arrhythmias that increase in frequency and severity over time. These arrhythmias include sinoatrial node irregularities, bradycardia and/or atrioventricular-block. Tmem161b has a completely unknown function, but its sequence is highly conserved between zebrafish and human. We used the chimeric VSFP-butterfly sensor and the patch clamp technique to study action potential (AP) morphology and ion channel currents in *tmem161b* mutants. In vivo APs of *tmem161b*$^{-/-}$ mutant embryos show a significantly prolonged action potential duration (APD) compared to wild-type siblings. As *tmem161b*$^{-/-}$ fish generally die between 7-14 days post fertilization we decided to isolate cardiomyocytes from adult heterozygous fish. In these cardiomyocytes, we observed APs with a more pronounced and faster phase 1 repolarization, a severely prolonged and lower plateau phase, and early after depolarisations at lower pacing frequencies. Subsequent voltage clamp experiments showed that I_{Kr} and $I_{Ca,L}$ are increased in response to the *tmem161b* mutation. This indicates that more K^+ is leaving the cell via hERG channels during repolarization, and that more Ca^{2+} enters the cell via L-type calcium channels during depolarization/repolarization. We postulate that the increase in $I_{Ca,L}$ has a dominant effect over the increase in I_{Kr}, as an increase in I_{Kr} would normally result in a shorter repolarization phase. Also, arrhythmias in the *tmem161b* zebrafish mutants show remarkable similarities to the arrhythmic phenotype observed in Timothy Syndrome patients, who carry a gain-of-function mutation in the L-type calcium channel. Unfortunately, we were unable to address how and where Tmem161b exerts its function within cardiomyocytes. Based on the fact that Tmem161b affects multiple cardiac ion currents, and the fact that the gating properties of $I_{Ca,L}$ are not affected, we hypothesize that Tmem161b is part of macromolecular signalling complexes that regulate cardiac ion channel activity or membrane expression.

Excitingly, our first results indicate that Tmem161b is an important novel regulator of cardiac electrophysiology. We have however only scratched the surface when it comes to Tmem161b function, and further research is necessary to fully determine the importance of this protein, also within the human heart. Many questions remain, including: what causes the pronounced phase 1 repolarization we observe in isolated mutant *tmem161b* cardiomyocytes? Where is Tmem161b located within cardiomyocytes? Which proteins does Tmem161b bind? How can Tmem161b affect both I_{Kr} and $I_{Ca,L}$? How does loss of Tmem161b result in an increase of I_{Kr} and $I_{Ca,L}$? Are other currents affected in *tmem161b* mutant fish? What is the function of Tmem161b in the sinoatrial node? Does it regulate the funny current (If)? Do mutations of *TMEM161B* also cause arrhythmias in humans?

In order to determine if TMEM161B is important in human electrophysiology, it would be interesting to see if hiPSC-CMs carrying a mutation in *TMEM161B* display similar changes in AP morphology as we observed in zebrafish. Also, the analysis of *TMEM161B* expression and *TMEM161B* mutations in healthy and diseased human heart tissue may provide important information on TMEM161B function in the human heart. To answer the question of were in the cell Tmem161b is active, it would be interesting to develop a transgenic zebrafish model with fluorescently tagged Tmem161b. Also transfecting hiPSC-CMs with fluorescently tagged TMEM161B could provide more details on where the protein is expressed within human cardiomyocytes. It will likely be difficult to isolate TMEM161B protein for co-immunoprecipitation or mass spectrometry, as transmembrane proteins are notoriously difficult to isolate.[31] This would however, provide important information on the binding partners of TMEM161B and provide a link for further research.

The zebrafish. A fintastic model.

Modelling PLN R14del, a mutation with Dutch roots, in the zebrafish

The phospholamban Arginine-14 deletion (PLN R14del) is the most prevalent cardiomyopathy-related mutation in the Netherlands, as it is found in 10-15% of all Dutch patients diagnosed with dilated cardiomyopathy (DCM) and arrhythmogenic right ventricular cardiomyopathy (ARVC). Interestingly the origin of the mutation has been traced back to a Dutch founder from Friesland (a province in the north of the Netherlands) that lived approximately 600-800 years ago.[32] As a result, most carriers of the PLN R14del mutation still live in the northern part of the Netherlands. The mutation has also been found in several other countries, including the USA, Canada, Spain and Germany, likely due to immigration of Dutch inhabitants.[33-36] Patient phenotypes are highly heterogeneous, but overall, carriers of the PLN R14del mutation have a high risk of developing malignant ventricular arrhythmias and end-stage heart failure, resulting in a high mortality and poor prognosis.[37] End-stage PLN R14del hearts show pronounced fibrosis and fatty changes in the left and right ventricular myocardial wall.[38]

PLN is a small 52 amino-acid transmembrane sarcoplasmic reticulum (SR) protein and a crucial regulator of SR function and cardiac contraction. Under basal conditions, non-phosphorylated PLN inhibits SERCA2a activity, the ion pump that is responsible for Ca^{2+} reuptake into the SR. During β-adrenergic stimulation, PLN is phosphorylated and releases its inhibition of SERCA2a. This allows more Ca^{2+} to flow into the SR, resulting in a faster relaxation of cardiomyocytes and enhanced contractility due to an increased calcium-induced calcium release. It is a generally accepted that PLN R14del cannot release its inhibition of SERCA2a due to a disruption of the PKA phosporylation motif on PLN. However, the pathologic role of PLN R14del likely extends beyond its interaction with SERCA, as PLN is in fact part of a multimeric regulatome, with various interacting partners. To study the effects of the mutation in more detail and to get a better understanding of disease mechanisms, we developed a pln R14del zebrafish using a CRISPR/Cas9 knock-in strategy. In **chapter 7** we show that this zebrafish is an interesting new model to study human PLN R14del disease. Embryos display changes in cytosolic Ca^{2+} dynamics, but not in contractility and hemodynamic parameters. This is not surprising as patients usually develop mutation-related phenotypes much later during life, at a mean age of 44.4 years.[32] In line with patients, cardiac disease in adult fish is very heterogeneous, and approximately 25% of older Pln R14del zebrafish present with severe morphological changes of the heart, in the form of a thick layer of cells that covers the heart. This layer expresses the embryonic epicardial gene *tbx18* and shows an accumulation of immune cells, fibrin, fibroblasts and fat. Despite of differences in the affected heart region in zebrafish and human, the processes that underlie the development of the cardiac morphological changes might be very similar.

In this study, we have tried to provide an overview of cardiac function in Pln R14del zebrafish, but there are some fundamental questions that remain. At this point, we have only examined early-stage and late-stage animals. However, the early-stage animals do not have a clear contractility phenotype despite of changes in cytosolic Ca^{2+} dynamics and analysis of end-stage hearts will likely only provide limited answers as to how R14del disease can develop, since many compensatory pathways will be activated. Therefore it would be interesting to trace disease progression over time. When do R14del zebrafish start to develop contractility problems? How do Ca^{2+} dynamics change after the embryonic stages? How is structural remodelling of the heart induced? Contractility of the heart can be traced for example by echography, and Ca^{2+} dynamics can be measured using in vitro experiments with Pln R14del GCaMP6f hearts or isolated cardiomyocytes. To explore detailed cellular responses over time, mRNA sequencing on hearts from different ages could be a good approach, as it will provide a complete overview of transcriptome changes and may identify novel targets that are involved in R14del disease progression. A recent study with iPSC-CMs demonstrated that PLN R14del also results in changes in action potential shape.[39] It would therefore be useful to measure action potentials in isolated zebrafish cardiomyocytes, as this would allow the detailed detection of electrophysiological changes over time. This may be an important parameter, as PLN R14del patients can develop fatal arrhythmias also in the absence of structural heart disease.[37]

We observed that the extra tissue layer in Pln R14del mutants is positive for the epicardial marker *tbx18*. This could indicate that epicardial cells have an important impact on R14del disease progression. Interestingly, a role of paracrine signalling between epicardial and subepicardial cells, as driver of morphologic changes in the subepicardial region, is recognized.[40,41] It was even demonstrated that fat cells can derive from epicardial cells by mesenchymal transformation and PPARγ activation.[42] To investigate epicardial involvement, it would be interesting to trace the epicardial cells over time. A zebrafish line with inducible Cre-recombinase activity in endocardial cells has been described before (the *tg(tcf21:CreErt)*^{pd42} zebrafish line)[43] and would be highly useful for such experiments. A final but important question that needs to be addressed is the heterogeneity of Pln disease, both in zebrafish and patients. Why do some zebrafish/patients develop heart failure, while others do not? At this point it is very difficult to answer such a question, as we do not fully understand Pln pathology. Hopefully, mRNA sequencing data or data from other experiments can give us clues for future research.

For now, it is good to be cautious with the extrapolation of our findings to the human situation. There are known differences between human and zebrafish in Ca^{2+} handling and cardiac anatomy, but we also do not fully understand the effects of PLN R14del on human cardiomyocyte physiology. Hopefully, additional studies will provide a better overview of the potential of this zebrafish model to study PLN R14del disease and to test possible treatments that may benefit patients.

Final remarks

In this thesis, I have organized almost 5 years worth of data. I hope that my work demonstrates how versatile the zebrafish is as a model organism, and how useful this vertebrate can be for genetics screens and to model human disease. Overall, we were able to develop new tools to study in vivo cardiac cellular electrophysiology, we identified two novel genes that are involved in cardiac electrophysiology, and we developed a zebrafish model of human heart disease. In addition to the zebrafish lines that have been described in this thesis, I generated more mutant zebrafish lines (e.g. sphkap and flot2). Unfortunately, I was unable to characterize these mutants during my PhD due to time limitations. I hope that my work will be continued and that what we have learned about cardiac electrophysiology will inspire other researchers and will someday benefit patients in the clinic.

References

1. Hayashi M, Shimizu W & Albert CM. The spectrum of epidemiology underlying sudden cardiac death. *Circulation Research* 2015;116:1887–1906.
2. Bezzina CR, Lahrouchi N & Priori SG. Genetics of sudden cardiac death. *Circulation Research* 2015;116:1919–1936.
3. Lieschke GJ & Currie PD. Animal models of human disease: zebrafish swim into view. *Nat Rev Genet* 2007;8:353–367.
4. Miesenbock G. The Optogenetic Catechism. *Science* 2009;326:395–399.
5. D'Agati G et al. A defect in the mitochondrial protein Mpv17 underlies the transparent casper zebrafish. *Dev Biol* 2017;430:11–17.
6. Várkuti BH et al. A highly soluble, non-phototoxic, non-fluorescent blebbistatin derivative. *Sci Rep* 2016;6:26141.
7. Pendin D, Greotti E, Lefkimmiatis K & Pozzan T. Exploring cells with targeted biosensors. *J Gen Physiol* 2017;149:1–36.
8. Tang S et al. Design and application of a class of sensors to monitor Ca^{2+} dynamics in high Ca^{2+} concentration cellular compartments. *Proc Natl Acad Sci U.S.A.* 2011;108:16265–16270.
9. Takahashi K, Kakimoto Y, Toda K & Naruse K. Mechanobiology in cardiac physiology and diseases. *J Cell Mol Med* 2013;17:225–232.
10. Sato M et al. Visual Responses of Photoreceptor-Degenerated Rats Expressing Two Different Types of Channelrhodopsin Genes. *Sci Rep* 2017;7:41210.
11. Henderson KW et al. Long-term seizure suppression and optogenetic analyses of synaptic connectivity in epileptic mice with hippocampal grafts of GABAergic interneurons. *J Neurosci* 2014;34:13492–13504.
12. Nussinovitch U & Gepstein L. Optogenetics for in vivo cardiac pacing and resynchronization therapies. *Nat Biotechnol* 2015;33:750–754.
13. Ostrovskaya O et al. RGS7/Gβ5/R7BP complex regulates synaptic plasticity and memory by modulating hippocampal GABABR-GIRK signaling. *Elife* 2014;3:e02053.
14. Liang JJ, Cockett M & Khawaja XZ. Immunohistochemical localization of G protein beta1, beta2, beta3, beta4, beta5, and gamma3 subunits in the adult rat brain. *J Neurochem* 1998;71:345–355.
15. Krispel CM, Chen CK, Simon, MI & Burns ME. Prolonged photoresponses and defective adaptation in rods of $Gbeta5^{-/-}$ mice. *J Neurosci* 2003;23:6965–6971.
16. Rao A, Dallman R, Henderson S & Chen CK. Gbeta5 is required for normal light responses and morphology of retinal ON-bipolar cells. *J Neurosci* 2007;27:14199–14204.
17. Zhang JH et al. Knockout of G protein β5 impairs brain development and causes multiple neurologic abnormalities in mice. *J Neurochem* 2011;119:544–554.
18. Vernon H et al. Intellectual developmental disorder with cardiac arrhythmia syndrome in a child with compound heterozygous *GNB5* variants. *Clin Genet* 2018;93:1254–1256.
19. Shamseldin, HE et al. *GNB5* mutation causes a novel neuropsychiatric disorder featuring attention deficit hyperactivity disorder, severely impaired language development and normal cognition. *Genome Biol*

2016;17:195.

20. Malerba N et al. A NGS-Targeted Autism/ID Panel Reveals Compound Heterozygous *GNB5* Variants in a Novel Patient. *Front Genet* 2018;9:626.
21. Turkdogan D, Usluer S, Akalin F, Agyuz U & Aslan ES. Familial early infantile epileptic encephalopathy and cardiac conduction disorder: A rare cause of SUDEP in infancy. *Seizure* 2017;50:171–172.
22. Xie K et al. Gbeta5 recruits R7 RGS proteins to GIRK channels to regulate the timing of neuronal inhibitory signaling. *Nat Neurosci* 2010;13:661–663.
23. Zhou H et al. GIRK channel modulation by assembly with allosterically regulated RGS proteins. *Proc Natl Acad Sci U.S.A.* 2012;109:19977–19982.
24. Stallmeyer B et al. A Mutation in the G-Protein Gene *GNB2* Causes Familial Sinus Node and Atrioventricular Conduction Dysfunction. *Circ Res* 2017;120:e33–e44.
25. Kang N, Kang JY, Park S & Shin DM. Increased store-operated Ca^{2+} entry mediated by GNB5 and STIM1. *Korean J Physiol Pharmacol* 2018;22:343–348.
26. Eder P & Molkentin JD. TRPC channels as effectors of cardiac hypertrophy. *Circ Res* 2011;108:265–272.
27. Hulot JS et al. Critical role for stromal interaction molecule 1 in cardiac hypertrophy. *Circulation* 2011;124:796–805.
28. Luo X et al. STIM1-dependent store-operated Ca^{2+} entry is required for pathological cardiac hypertrophy. *J Mol Cell Cardiol* 2012;52:136–147.
29. Kobayashi T, Washiyama K & Ikeda K. Inhibition of G protein-activated inwardly rectifying K^+ channels by various antidepressant drugs. *Neuropsychopharmacology* 2004;29:1841–1851.
30. Takahashi T et al. G protein-activated inwardly rectifying K^+ channel inhibition and rescue of weaver mouse motor functions by antidepressants. *Neurosci Res* 2006;54:104–111.
31. Schmit K & Michiels C. TMEM Proteins in Cancer: A Review. *Front Pharmacol* 2018;9:1345.
32. van der Zwaag PA et al. Recurrent and founder mutations in the Netherlands-Phospholamban p.Arg14del mutation causes arrhythmogenic cardiomyopathy. *Neth Heart J* 2013;21:286–293.
33. Haghighi K et al. A mutation in the human phospholamban gene, deleting arginine 14, results in lethal, hereditary cardiomyopathy. *Proc Natl Acad Sci U.S.A.* 2006;103:1388–1393.
34. DeWitt MM, MacLeod HM, Soliven B & McNally EM. Phospholamban R14 deletion results in late-onset, mild, hereditary dilated cardiomyopathy. *J Am Coll Cardiol* 2006;48:1396–1398.
35. Posch MG et al. Genetic deletion of arginine 14 in phospholamban causes dilated cardiomyopathy with attenuated electrocardiographic R amplitudes. *Heart Rhythm* 2009;6:480–486.
36. López-Ayala JM et al. Phospholamban p.arg14del mutation in a Spanish family with arrhythmogenic cardiomyopathy: evidence for a European founder mutation. *Rev Esp Cardiol* 2015;68:346–349.
37. van Rijsingen IAW et al. Outcome in phospholamban R14del carriers: results of a large multicentre cohort study. *Circ Cardiovasc Genet* 2014;7:455–465.
38. Gho JMIH et al. High resolution systematic digital histological quantification of cardiac fibrosis and adipose tissue in phospholamban p.Arg14del mutation associated cardiomyopathy. *PLoS ONE* 2014;9:e94820.
39. Karakikes I et al. Correction of human phospholamban R14del mutation associated with cardiomyopathy using targeted nucleases and combination therapy. *Nat Commun* 2015;6:6955.

40. Matthes SA, Taffet S & Delmar M. Plakophilin-2 and the migration, differentiation and transformation of cells derived from the epicardium of neonatal rat hearts. *Cell Commun Adhes* 2011;18:73–84.
41. Dubash AD et al. Plakophilin-2 loss promotes TGF-β1/p38 MAPK-dependent fibrotic gene expression in cardiomyocytes. *J Cell Biol* 2016;212:425–438.
42. Yamaguchi Y et al. Adipogenesis and epicardial adipose tissue: a novel fate of the epicardium induced by mesenchymal transformation and PPARγ activation. *Proc. Natl. Acad. Sci. U.S.A.* 2015;112:2070–2075.
43. Kikuchi K et al. tcf21+ epicardial cells adopt non-myocardial fates during zebrafish heart development and regeneration. *Development* 2011;138:2895–2902.

Appendix

Nederlandse samenvatting
Dankwoord
Curriculum vitae
List of publications

Nederlandse samenvatting

Hartritmestoornissen

Het hart slaat ongeveer 100.000 keer per dag en pompt daarmee zo'n 7.500 liter bloed door het lichaam. Dit is belangrijk voor het leveren van zuurstof aan organen en het afvoeren van afvalstoffen uit het lichaam. Het hart bestaat uit miljoenen hartspiercellen die heel gecoördineerd en ritmisch samentrekken. Om dit voor elkaar te krijgen heeft het hart een pacemaker; een groepje zeer gespecialiseerde hartcellen. Deze pacemakercellen kunnen elektrische pulsen (actiepotentialen) produceren en doorgeven aan de rest van het hart. Wanneer een elektrische puls een hartspiercel (cardiomyociet) bereikt, zorgt dit ervoor dat deze cel gaat samentrekken. Uiteindelijk trekt zo het hele hart samen en wordt het bloed uit het hart gestuwd.

Het is niet moeilijk om voor te stellen dat een verstoring in de productie en/of de voortgeleiding van deze elektrische pulsen kan leiden tot hartritmestoornissen, ook wel aritmieën genoemd. Hierbij slaat het hart te snel (tachycardie), te langzaam (bradycardie), of onregelmatig. Dit kan levensgevaarlijk zijn, omdat het bloed soms nog maar amper rondgepompt wordt. Aritmieën kunnen er zelfs voor zorgen dat het hart helemaal stopt met kloppen.

Per jaar overlijden miljoenen mensen wereldwijd aan plotselinge hartdood, maar helaas weten we nog te weinig van hartritmestoornissen om dit aantal flink te laten dalen. Dat komt omdat de onderliggende oorzaak erg complex kan zijn. We kunnen daarom slecht voorspellen welke personen een hartritmestoornis gaan ontwikkelen en hoe we deze personen het beste (preventief) kunnen behandelen. In het onderzoek van dit proefschrift hebben we geprobeerd meer inzicht te krijgen in de genetische achtergrond van hartritmestoornissen. Als bekend is welke genen belangrijk zijn voor de elektrische functie van het hart, kunnen we beter voorspellen welke personen risico lopen en krijgen we meer inzicht in de processen die belangrijk zijn voor het ontstaan van hartritmestoornissen. Voor dit promotieonderzoek hebben we de zebravis gebruikt als een model voor de mens.

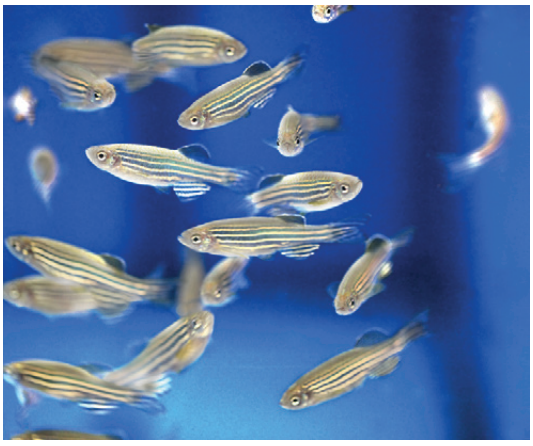

Figuur 1. Een groep zebravissen. Bron: www.tuebingen.mpg.de

Zebravissen en genetisch onderzoek

De zebravis is een tropisch visje uit India van ongeveer 2-5 cm groot met blauwe strepen. Hij wordt veel gebruikt in wetenschappelijk onderzoek, bijvoorbeeld voor onderzoek naar embryonale ontwikkeling of naar genetische ziektes. Deze populariteit heeft de zebravis vooral te danken aan de volgende factoren: 1) het feit dat hij klein is, 2) weinig kost, 3) makkelijk in grote aantallen te houden is, en 4) dat de embryos en larven zich buiten de moeder ontwikkelen, doorzichtig zijn (o.a. het hart is door de huid heen te zien) en makkelijk genetisch te manipuleren zijn. Hoewel zebravissen op het eerste oog niet erg op mensen lijken, hebben ze meer overeenkomsten dan je zou verwachten. Toen onderzoekers een directe vergelijking maakten van het genoom van de mens en het genoom van de zebravis (het genoom is alle erfelijke informatie in een cel), zagen ze dat ongeveer 70% van alle genen in de mens ook terug te vinden zijn in de zebravis. Ook vonden ze maar liefst 82% van alle ziekte veroorzakende genen in mensen terug in de zebravis. Daarnaast hebben zebravissen volledig herkenbare organen, zoals hart, lever, nieren en alvleesklier, en hebben deze organen een heel vergelijkbare functie met die van de mens.

Hoofdstuk 1 is een algemene introductie waarin we de elektrische functie van het hart en het gebruik van de zebravis in de wetenschap uitgebreid beschrijven.

Optogenetische sensoren

In de literatuurstudie in **hoofdstuk 2** geven we een overzicht van verschillende optogenetische sensoren die gebruikt kunnen worden om moleculaire processen in het hart te bestuderen. “Opto-” staat voor “optic” en geeft aan dat deze sensoren werken met behulp van licht. De sensoren bevatten namelijk fluorescente eiwitten. “-genetisch” geeft aan dat deze sensoren als code ingebouwd kunnen worden in het DNA. DNA wordt door de cel gelezen en vertaald in eiwitten. Door de toevoeging van een extra stukje code (bijvoorbeeld een promotor sequentie) kunnen optogenetische sensors heel specifiek tot expressie gebracht worden in cellen van het lichaam, bijvoorbeeld in de hartspiercellen. Op die manier kunnen bepaalde moleculaire processen zichtbaar gemaakt worden in deze specifieke cellen. Denk hierbij aan veranderingen in calcium (Ca^{2+}), actiepotentialen, en andere moleculaire processen die we normaal met het oog niet kunnen waarnemen. Dit kan veel inzicht geven in de manier waarop het hart werkt en hoe dit wordt verstoord bij ziekte.

In **hoofdstuk 3** passen we twee optogenetische sensors toe in de hartspiercellen van zebravissen: één die calcium meet (GCaMP6f) en één die voltage meet (chimeric VSFP-butterfly CY). Calcium en elektrische signalen zijn belangrijk voor een goede functie van het hart. We laten zien dat we zonder invasieve methoden de fluorescentie van de sensors kunnen meten. Dit is belangrijk omdat we op deze manier processen die in het hart plaatsvinden, in de context van het lichaam kunnen meten. Weefsels en organen in het hele lichaam kunnen namelijk met elkaar communiceren en elkaars functie beïnvloeden. We valideerden de werking van de sensoren door de zebravissen te behandelen met verschillende medicijnen (met een bekende werking op het hart). Propranolol is bijvoorbeeld een b-blokker en verlaagt de hartslag. Dit was, zoals

verwacht, zichtbaar met onze sensoren in de vorm van een lagere signaalfrequentie van de sensor. Isoproterenol daarentegen is een b-agonist en verhoogt de hartslag. Ook dit was zichtbaar met onze sensoren in de vorm van een hogere signaalfrequentie van de sensor. Het doel van deze studie was om een nieuw onderzoeksmodel te introduceren dat gebruikt kan worden voor de studie van hartritmestoornissen.

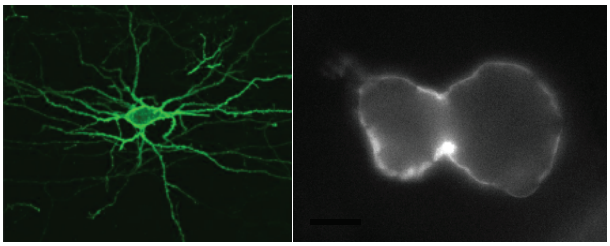

Figuur 2. Links een voorbeeld van een optogenetische sensor in een neuron en rechts in een zebravis hartje. In dit geval zijn het sensors die spanning/voltage (links) en Ca^{2+} concentraties (rechts) kunnen meten. Bron: www.sciencedaily.com en onze eigen data.

Patiënten met een trage hartslag en ontwikkelingsproblemen

Soms komt een zeldzame ziekte bij één of meerdere kinderen van een gezin voor. Dat kan komen omdat een verandering in een gen (een zogenaamde mutatie) bij zowel de moeder als de vader voorkomt en vervolgens doorgegeven wordt aan een kind. In **hoofdstuk 4** beschrijven we een nieuw syndroom dat voorkomt bij kinderen uit zes gezinnen. Deze kinderen vertonen allemaal hetzelfde spectrum aan symptomen, waaronder een pathologische verlaging van de hartslag, toevallen, oogproblemen, ontwikkelingsproblemen en problemen met de spieraansturing. Door het genoom van de patiënten en ouders te bestuderen, werden mutaties in het *GNB5*-gen gevonden. Om te controleren of dit gen inderdaad verantwoordelijk is voor het syndroom, hebben we vergelijkbare mutaties aangebracht in het *GNB5*-gen van zebravissen. Vervolgens hebben we gekeken naar de symptomen die deze vissen vertoonden en zagen dat deze voor een groot deel overlapten met die van de patiënten. Zo hadden vissen met een *GNB5* mutatie moeite om te zwemmen, problemen om licht te volgen met hun ogen, en een pathologisch verlaagde hartslag. Dit bevestigt dat mutaties in het *GNB5*-gen verantwoordelijk zijn voor dit zeldzame syndroom.

Om meer te leren over de functie van GNB5 in het hart, hebben we in **hoofstuk 5** verder gekeken naar GNB5 met behulp van losse hartspiercellen (zogenaamde human-induced pluripotent stem cell-derived cardiomyocytes) in kweek. Deze hartspiercellen bevatten gezond *GNB5* of gemuteerd *GNB5*. Hartspiercellen hebben allerlei ion-kanalen. Dat zijn poortjes waarbij ionen, bijvoorbeeld calcium (Ca^{2+}) of kalium (K^{+}), naar binnen en/of naar buiten kunnen stromen. Op die manier kan een hartspiercel heel nauwkeurig regelen hoeveel er van elk ion in de cel aanwezig is. Met behulp van de techniek “patch-clamp” kan de beweging van ionen door de kanalen gemeten worden.

Uit onze metingen bleek dat een mutatie in *GNB5* zorgt voor een verandering in een uitwaartse kalium stroom ($I_{K,ACh}$) die erg belangrijk is voor het verlagen van de hartslag tijdens rust. Er lijkt bij de mutatie meer kalium door de $I_{K,ACh}$ kanalen te stromen, omdat er meer $I_{K,ACh}$ kanalen aanwezig zijn. Dit komt mogelijk omdat GNB5 dit kanaal normaal gesproken remt, maar dat door de mutatie niet meer kan. Door de toegenomen uitwaartse kaliumstroom, kan de cel minder goed geprikkeld worden door elektrische signalen en wordt de hartslag van patiënten soms gevaarlijk. We laten in deze studie ook zien dat behandeling met een medicijn dat het $I_{K,ACh}$ kanaal remt (XEN-R0703) een lage klopfrequentie kan voorkomen, zowel in losse hartspiercellen als in de zebravissen met een *GNB5*-mutatie.

Een zebravis met hartritmestoornissen

In **hoofdstuk 6** beschrijven we een nieuw gen dat waarschijnlijk belangrijk is voor de elektrische functie van het hart: *TMEM161B*. In een genetische screen in zebravissen, waarbij willekeurig mutaties worden gemaakt over het hele DNA, viel het op dat een bepaalde groep vissen ernstige hartritmestoornissen had. Na een analyse van het genoom, bleek er een mutatie in het *TMEM161B*-gen te zitten. We hebben de optogenetische sensoren van hoofdstuk 3 en de patch-clamp techniek gebruikt om te onderzoeken wat er op moleculair niveau fout gaat bij deze mutatie. Uit deze metingen blijkt dat TMEM161B een aantal belangrijke ion-stromen in hartspiercellen reguleert, waaronder calcium ($I_{Ca,L}$) en kalium (I_{Kr}), die betrokken zijn bij de vorming van actiepotentialen (elektrische pulsen). Hoe TMEM161B deze ion-stromen precies reguleert en of TMEM161B ook belangrijk is in het menselijke hart kunnen we naar aanleiding van deze studie helaas nog niet zeggen.

Een zebravis met een patiënten-mutatie

De PLN-R14del-mutatie is een relatief veelvoorkomende mutatie in Nederland. In het noorden van Nederland heeft naar verwachting ongeveer 1 op 1500 mensen deze mutatie. Dit komt waarschijnlijk omdat ±700 jaar geleden een gen-mutatie is opgetreden in een Friese voorouder. Deze mutatie is doorgegeven van generatie op generatie en is zo steeds meer verspreid over Nederland en ook over andere landen. Helaas kan het dragen van een kopie van de mutatie leiden tot ernstige veranderingen in de hartspierwand (cardiomyopathie) en tot aritmieën. Veel patiënten hebben op den duur zelfs een harttransplantatie nodig. Hoewel de R14del-mutatie in het PLN-gen dus relatief veel voorkomt in Nederland, is de mutatie nog redelijk onbekend en weten we eigenlijk niet goed hoe de mutatie leidt tot zo'n ernstig ziektebeeld. Om die reden hebben we in de studie in **hoofdstuk 7** precies dezelfde mutatie aangebracht in het PLN-gen van de zebravis. We hebben deze vissen vervolgens een tijd lang gevolgd en zagen dat deze vissen soms ook ernstige veranderingen in het hart ontwikkelden. We weten dat het PLN-eiwit belangrijk is voor de calciumhuishouding van hartspiercellen en hebben daarom de calcium sensor uit hoofdstuk 3 ook toegepast in PLN-R14del-vissen. Uit metingen met deze sensor bleek dat de hartspiercellen van PLN-R14del-vissen inderdaad al in een vroeg stadium veranderingen laten zien. Helaas kunnen we

met de resultaten uit hoofdstuk 7 nog geen grote conclusies trekken, maar het laat wel zien dat de PLN-R14del-zebravis in vervolgonderzoek mogelijk kan bijdragen aan een beter begrip van het PLN-R14del-ziektebeeld in patiënten.

Conclusie

Hoofdstuk 8 is de algemene discussie van dit proefschrift. Hierin discussiëren we over de resultaten die we in dit proefschrift presenteren en bekijken we deze resultaten in een bredere context. Ook kijken we hoe onderzoek naar aritmieën in de toekomst aangepakt kan worden. In het kort concluderen we in dit proefschrift dat optogenetische sensors nuttig kunnen zijn in moleculaire studies van het hart. Daarnaast hebben we in dit proefschrift een aantal nieuwe genen geïdentificeerd en nieuwe zebravismodellen geïntroduceerd. Hopelijk zal deze nieuwe kennis en zullen deze nieuwe zebravismodellen in de toekomst bijdragen aan een beter begrip van hartritmestoornissen en een vermindering van het aantal slachtoffers door plotselinge hartdood.

Curriculum Vitae

Charlotte (Lotte) Dieudonée Koopman was born on the 28th of May 1988 in Rhenen and grew up in Veenendaal. She obtained her VWO diploma in 2006 at the Ichthus college in Veenendaal. Due to her fascination for nature, biology and animals she started Veterinary Medicine at the University of Utrecht in the same year. After discovering that she was mostly interested in fundamental biology, Lotte switched to Biomedical Sciences at the University of Utrecht in 2009. She received her BSc degree in March 2011. During the master's program of Biology of Disease, she performed her 9-month research project at the department of Clinical Chemistry and Haematology at University Medical Center Utrecht under the supervision of Eelo Gitz and dr. Rolf Urbanus. For her minor research project, she traveled to San Francisco and performed research at the University of California, San Francisco under the supervision of dr. Vicki Plaks and prof. dr. Zena Werb. After receiving her MSc degree November 2013, Lotte started her PhD research in April 2014 at the UMC Utrecht (department of Medical Physiology) and the Hubrecht Institute (Bakkers Group) under the supervision of prof. dr. Marc Vos, dr. Teun de Boer and prof. dr. Jeroen Bakkers. Her thesis is the result of this PhD project. On February 1st 2019 she started as lab manager NGS at the Hubrecht Institute spinoff company Single Cell Discoveries.

List of publications

1. Gitz E, **Koopman CD**, Giannas A, Koekman CA, van den Heuvel DJ, Deckmyn H, Akkerman JW, Gerritsen HC, Urbanus RT (2013). Platelet interaction with von Willebrand factor is enhanced by shear-induced clustering of glycoprotein Ibα. *Haematologica* 98(11):1810-8

2. Plaks V, **Koopman CD**, Werb Z (2013). Cancer. Circulating tumor cells. *Science* 341(6151):1186-8

3. Lodder EM*, De Nittis P*, **Koopman CD***, Wiszniewski W, Moura de Souza CF, Lahrouchi N, Guex N, Napolioni V, Tessadori F, Beekman L, Nannenberg EA, Boualla L, Blom NA, de Graaff W, Kamermans M, Cocciadiferro D, Malerba N, Mandriani B, Akdemir ZHC, Fish RJ, Eldomery MK, Ratbi I, Wilde AAM, de Boer T, Simonds WF, Neerman-Arbez M, Sutton VR, Kok F, Lupski JR, Reymond A#, Bezzina CR#, Bakkers J#, Merla G# (2016). GNB5 Mutations Cause an Autosomal-Recessive Multisystem Syndrome with Sinus Bradycardia and Cognitive Disability. *America Journal of Human Genetics* 99(3):704-710

4. **Koopman CD**, Zimmermann WH, Knöpfel T, de Boer TP (2017). Cardiac optogenetics: using light to monitor cardiac physiology. *Basic Research in Cardiology* 112(5):56

5. van Opbergen CJM*, **Koopman CD***, Kok BJM, Knöpfel T, Renninger SL, Orger MB, Vos MA, van Veen TAB, Bakkers J#, de Boer TP# (2018). Optogenetic sensors in the zebrafish heart: a novel in vivo electrophysiological tool to study cardiac arrhythmogenesis. *Theranostics* 8(17):4750-4764.

6. Sala L, van Meer BJ, Tertoolen LGJ, Bakkers J, Bellin M, Davis RP, Denning C, Dieben MAE, Eschenhagen T, Giacomelli E, Grandela C, Hansen A, Holman ER, Jongbloed MRM, Kamel SM, **Koopman CD**, Lachaud Q, Mannhardt I, Mol MPH, Mosqueira D, Orlova VV, Passier R, Ribeiro MC, Saleem U, Smith GL, Burton FL, Mummery CL (2018). MUSCLEMOTION: A Versatile Open Software Tool to Quantify Cardiomyocyte and Cardiac Muscle Contraction In Vitro and In Vivo. *Circulation Research* 122(3):e5-e16.

7. Christiaan C. Veerman*, Isabella Mengarelli*, **Charlotte D. Koopman**, Ronald Wilders, Shirley C. van Amersfoorth, Diane Bakker, Rianne Wolswinkel, Mariam Hababa, Teun P. de Boer, Kaomei Guan, James Milnes, Elisabeth M. Lodder, Jeroen Bakkers, Arie O. Verkerk#, Connie R. Bezzina# (2019). Genetic variation in GNB5 causes bradycardia by increasing $I_{K,ACh}$ augmenting cholinergic response. *Under revision*

*# contributed equally